

DISCRETE ELEMENT BASED ANALYSES OF STRUCTURE-RESERVOIR  
PROBLEM FOR GRAVITY DAMS

A THESIS SUBMITTED TO  
THE GRADUATE SCHOOL OF NATURAL AND APPLIED SCIENCES  
OF  
MIDDLE EAST TECHNICAL UNIVERSITY

BY

BERAT FEYZA SOYSAL ALBOSTAN

IN PARTIAL FULFILLMENT OF THE REQUIREMENTS  
FOR  
THE DEGREE OF DOCTOR OF PHILOSOPHY  
IN  
CIVIL ENGINEERING

JANUARY 2021



Approval of the thesis:

**DISCRETE ELEMENT BASED ANALYSES OF STRUCTURE-  
RESERVOIR PROBLEM FOR GRAVITY DAMS**

submitted by **BERAT FEYZA SOYSAL ALBOSTAN** in partial fulfillment of the requirements for the degree of **Doctor of Philosophy in Civil Engineering, Middle East Technical University** by,

Prof. Dr. Halil Kalıpçılar  
Dean, Graduate School of **Natural and Applied Sciences**

Prof. Dr. Ahmet Türer  
Head of the Department, **Civil Engineering**

Prof. Dr. Yalın Arıcı  
Supervisor, **Civil Engineering, METU**

**Examining Committee Members:**

Prof. Dr. Kağan Tuncay  
Civil Engineering, METU

Prof. Dr. Yalın Arıcı  
Civil Engineering, METU

Assoc. Prof. Dr. Ercan Gürses  
Aerospace Engineering, METU

Prof. Dr. Hilmi Luş  
Civil Engineering, Boğaziçi University

Assoc. Prof. Dr. Cemalettin Dönmez  
Civil Engineering, İzmir Institute of Technology

Date: 25.01.2021

**I hereby declare that all information in this document has been obtained and presented in accordance with academic rules and ethical conduct. I also declare that, as required by these rules and conduct, I have fully cited and referenced all material and results that are not original to this work.**

Name, Last name : Berat Feyza Soysal Albostan

Signature :



## **ABSTRACT**

### **DISCRETE ELEMENT BASED ANALYSES OF STRUCTURE- RESERVOIR PROBLEM FOR GRAVITY DAMS**

Soysal Albostan, Berat Feyza  
Doctor of Philosophy, Civil Engineering  
Supervisor : Prof. Dr. Yalın Arıcı

January 2021, 223 pages

The prediction of the nonlinear behavior of gravity dams under seismic actions is challenging. Firstly, a clear damage indicator to quantify the performance limits of such structures is limited. Besides, a proper numerical model producing reliable results both in the linear and nonlinear ranges for the dam body has to be established, coupled with its surrounding reservoir. This study is focused on damage assessment of gravity dams with the goal of determining seismic and post-seismic behavior considering crack propagation, crack openings, and leakage estimations through these cracks. A robust discrete element-based methodology, the modified applied element method (MAEM), was first developed, accurately simulating the behavior of plain concrete structures, representing a variety of Poisson's ratio. Having validated this methodology under various loading conditions, the successful coupling of MAEM with the implemented fluid finite elements was shown. Incremental dynamic analyses (IDA) were then conducted on concrete and roller-compacted concrete (RCC) gravity dam-reservoir systems to assess the damage. The damage on the dam body was evaluated first by utilizing fragility curves considering

crack propagation. Then, crack widths on the upstream faces were computed as a new damage indicator, and the leakage through these cracks was estimated for the post-seismic state. A relationship between ground motion intensity measures and maximum crack widths were sought. The results show that although cracking was more pronounced in the RCC dam due to weak lift joints, the crack opening and leakage were more critical for the concrete dam.

Keywords: Modified Applied Element Method, Displacement/Pressure Based Mixed Finite Element, Explicit Nonlinear Dynamic Analyses, RCC Dam-Reservoir System, Seismic Performance Limits

## ÖZ

### REZERVUAR-YAPI İLİŞKİSİNİN AĞIRLIK BARAJLARI İÇİN AYRIK ELEMEN TABANLI ANALİZLERİ

Soysal Albostan, Berat Feyza  
Doktora, İnşaat Mühendisliği  
Tez Yöneticisi: Prof. Dr. Yalın Arıcı

Ocak 2021, 223 sayfa

Ağırlık barajlarının sismik yükler altında doğrusal olmayan davranışını tahmin etmek zorludur. Öncelikle bu tür yapıların performanslarını ölçen net bir hasar göstergesi mevcut değildir. Buna ek olarak, baraj gövdesi için hem doğrusal hem de doğrusal olmayan aralıklarda güvenilir sonuçlar veren uygun bir sayısal modelin çevresindeki rezervuar ile birlikte kurulması gerekmektedir. Bu çalışma, çatlak ilerlemesi, çatlak açıklıkları ve bu çatlaklar üzerinden sızıntı tahminlerini dikkate alarak deprem ve deprem sonrası davranışın belirlenmesi ve ağırlık barajlarında hasar değerlendirilmesine odaklanmıştır. İlk olarak, beton yapıların davranışını doğru bir şekilde simüle eden ve çeşitli Poisson oranlarını da temsil ederek modelleyen modifiye edilmiş uygulamalı eleman yöntemi (MAEM) ismi verilen sağlam bir ayırık eleman tabanlı metodoloji geliştirilmiştir. Bu metodoloji çeşitli yükleme koşulları altında doğruladıktan sonra, MAEM'in entegre edilmiş su sonlu elemanları ile uyumlu bir şekilde çalıştığı gösterilmiştir. Daha sonra, artımlı dinamik analiz (IDA) yöntemi kullanılarak beton ve silindirle sıkıştırılmış beton (SSB) ağırlık baraj-rezervuar sistemleri üzerinde oluşan hasar değerlendirilmiştir. Bunun için önce çatlak ilerlemesi dikkate alınarak oluşturulan kırılma eğrileri kullanılmış, daha sonra ise barajların memba yüzlerindeki çatlak genişlikleri yeni bir hasar göstergesi

olarak hesaplanmıştır. Deprem sonrası durum için bu çatlaklarda beklenen sızıntı hesaplanmıştır. Analizlerde belirlenen maksimum çatlak genişlikleri ile deprem kayıtlarının şiddet ölçümleri arasındaki ilişki incelenmiştir. Sonuçlar, SSB barajda yatay döküm derzlerindeki zayıflıktan dolayı çatlakların daha fazla olmasına rağmen, çatlak açılmasının ve sızıntının beton baraj için daha kritik olduğunu göstermiştir.

Anahtar Kelimeler: Modifiye Edilmiş Uygulamalı Eleman Yöntemi, Deplasman/Basınca Dayalı Karma Sonlu Eleman, Belirtik Doğrusal Olmayan Dinamik Analiz, SSB Baraj-Rezervuar Sistemleri, Sismik Performans Limitleri

To My Family

## ACKNOWLEDGMENTS

I wish to express my utmost gratitude to my supervisor Prof. Dr. Yalın Arıcı, for his guidance, advice, criticism, support, encouragement, and insight throughout the research. He has been a great supervisor and mentor.

I would like to express my appreciation to the members of my Ph.D. monitoring committee: Assoc. Prof. Dr. Ercan Gürses and Prof. Dr. Kağan Tuncay. I wish to offer special thanks to Prof. Dr. Kağan Tuncay for being part of my committee, but also for his motivation, guidance, and feedback throughout my Ph.D.

I would like to thank my coworkers in METU Civil Engineering Department when I was working as a research assistant.

I would also like to thank my friends for standing next to me during this challenging process.

I am grateful for all the continuous support, understanding, and encouragement I have received from all of my family members.

This dissertation is literally possible with the continuous support and patience of my husband and my best friend, Utku. You always believed in me. I cannot thank you enough for the continuous support and endless patience throughout this study and in all aspects of my life.

This study had been conducted with the funding provided by the Scientific and Technological Research Council of Turkey (TUBITAK) under the grant 116M524.

## TABLE OF CONTENTS

ABSTRACT.....	v
ÖZ.....	vii
ACKNOWLEDGMENTS.....	x
TABLE OF CONTENTS.....	xi
LIST OF TABLES.....	xvi
LIST OF FIGURES.....	xvii
CHAPTERS	
1 INTRODUCTION.....	1
1.1 Motivation.....	1
1.2 Literature Review.....	3
1.2.1 Numerical Methods for Modeling of Crack Propagation.....	3
1.2.1.1 Continuum Based Methods.....	4
1.2.1.2 Discrete Element Based Methods.....	5
1.2.2 Applied Element Method.....	5
1.2.3 Dam-Reservoir Interaction on Seismic Behavior of Concrete Dams.....	8
1.2.4 Nonlinear Analyses of Concrete Dams.....	10
1.3 Objectives.....	15
1.4 Outline.....	17
2 THEORETICAL BACKGROUND.....	21
2.1 Introduction.....	21
2.2 Review of Applied Element Method.....	22
2.3 Modified Applied Element Method.....	23

2.3.1	Theory and Formulation in Elastic Range .....	24
2.3.2	Stress Tensor in Arbitrary Directions .....	31
2.3.2.1	Tensile Loading in Both Directions .....	32
2.3.2.2	Shear Loading .....	36
2.3.3	Theory and Formulation for Cracked Media .....	37
2.3.4	Mass and Damping Matrices.....	41
2.4	Finite Elements for Modeling Fluids .....	42
2.4.1	Fluid Element Formulation .....	42
2.4.2	Displacement/Pressure Based Mixed Finite Element Formulation .....	43
2.4.3	Radiation Boundary Condition .....	47
2.5	The Developed Software .....	48
2.5.1	Solvers.....	49
2.5.1.1	Linear Static Solver.....	49
2.5.1.2	Nonlinear Static Solver .....	51
2.5.1.3	Linear Dynamic Solver .....	54
2.5.1.3.1	Implicit Solution Algorithm.....	56
2.5.1.3.2	Explicit Solution Algorithm.....	57
2.5.1.4	Nonlinear Explicit Dynamic Solver .....	59
2.5.1.5	Modal Analysis .....	62
2.5.2	Mass Scaling Technique .....	62
2.5.3	Loading Types.....	63
3	VALIDATION STUDIES .....	65
3.1	Introduction.....	65
3.2	Validation of the Modified Applied Elements in Linear Range.....	67



3.2.1	Linear Static Analysis of a Cantilever Column .....	67
3.3	Wall and Frame Problems: The Convergence Rate of MAEM.....	70
3.4	Validation of the Modified Applied Elements in the Nonlinear Range ...	76
3.4.1	Direct Tension Simulation.....	76
3.4.2	Uniaxial Tension Test.....	78
3.4.3	Splitting Tension Test.....	81
3.4.4	Push-Over Loading Problem of a Notched Model Concrete Dam .....	83
3.5	Validation of the Mixed u/p Fluid Finite Elements.....	86
3.5.1	Water Tank under Self-Weight.....	86
3.5.2	Modal Analysis of a Water Column .....	87
3.6	Frequency Response of a Full-Scale Dam-Reservoir System.....	89
3.7	Nonlinear Dynamic Analysis of Koyna Dam-Reservoir System.....	94
3.8	The Effect of Poisson’s Ratio on Results.....	96
3.8.1	Linear Static Analysis of a Cantilever Column .....	99
3.8.2	Uniaxial Tension Test.....	100
3.8.3	Splitting Tension Test.....	101
3.8.4	Push-Over Loading Problem of a Notched Model Concrete Dam .....	102
3.9	Computational Aspects of MAEM.....	105
3.10	Summary .....	107
3.10.1	Summary – Linear Validations.....	107
3.10.2	Summary – Nonlinear Validations .....	111
4	NONLINEAR BEHAVIOR OF CONCRETE AND ROLLER- COMPACTED CONCRETE GRAVITY DAM-RESERVOIR SYSTEMS DURING SEISMIC EXCITATION.....	117

4.1	Introduction.....	117
4.2	Simulation Models.....	120
4.2.1	Finite Element Method Model .....	121
4.2.2	Modified Applied Element Method Model I .....	122
4.2.3	Modified Applied Element Method Model II .....	123
4.2.4	Modal Properties of FEM and MAEM Models .....	124
4.3	Analysis Technique.....	125
4.3.1	Incremental Dynamic Analysis .....	125
4.3.2	Fragility Analysis .....	128
4.3.3	Limit States .....	129
4.4	Results from the Incremental Dynamic Analysis .....	130
4.4.1	Comparison of MAEM and Finite Element Simulations.....	132
4.4.2	Comparison of the Gravity Dam vs. RCC Dam with Weak Joints....	136
4.4.3	Cracking in the Upstream Face as a Performance Indicator .....	141
4.4.4	Cracking on Monoliths: Relationship to Seismic Intensity Measures	147
4.4.5	Leakage through a Monolith as a Performance Indicator .....	152
4.5	Summary.....	160
5	SUMMARY, CONCLUSIONS AND FUTURE EXTENSIONS .....	167
5.1	Executive Summary .....	167
5.2	Summary.....	168
5.3	Concluding Remarks.....	171
5.4	Future Extensions .....	177
	REFERENCES .....	181
	APPENDICES	

A.	Cracking Scheme and Run Time Comparisons.....	195
B.	Incremental Dynamic Analyses Results.....	197
C.	Assessment of the Use of Damaged State Models for Determination of the Post-Earthquake Response.....	219
	CURRICULUM VITAE.....	221

## LIST OF TABLES

### TABLES

Table 2.1 Parameters for elasticity tensor calculation.....	28
Table 2.2 Integral points and weights.....	47
Table 3.1 Splitting tensile strengths for different Poisson's ratio .....	102
Table 3.2 Total spring numbers .....	106
Table 4.1 Modal properties of FEM and MAEM models .....	125
Table 4.2 Selected ground motions for IDA .....	127

## LIST OF FIGURES

### FIGURES

Figure 2.1 Applied element method.....	23
Figure 2.2 Modified applied element method.....	24
Figure 2.3 Directionality and elements' orientation for applied element models...	32
Figure 2.4 Displacements of springs due to tensile loading in x and y directions..	32
Figure 2.5 Local displacements of springs.....	33
Figure 2.6 Displacements of springs due to shear loading .....	36
Figure 2.7 Maekawa tension softening model and fracture energy .....	38
Figure 2.8 Mixed finite element (Özmen, 2016) .....	46
Figure 2.9 Flowchart of linear static analysis .....	50
Figure 2.10 Flowchart of nonlinear static analysis .....	52
Figure 2.11 Flowchart of linear dynamic analysis.....	55
Figure 2.12 Flowchart of nonlinear dynamic analysis.....	61
Figure 3.1 Linear static analysis of a cantilever column, error with respect to the theoretical solution.....	69
Figure 3.2 Normal and shear stress distributions for case II loading.....	70
Figure 3.3 Benchmark problems for the convergence rate .....	71
Figure 3.4 Finite element solutions.....	72
Figure 3.5 Shear wall problem.....	74
Figure 3.6 Tall frame problem .....	76
Figure 3.7 Direct tension simulation.....	78
Figure 3.8 Uniaxial tension test .....	79
Figure 3.9 Splitting tension test models.....	82
Figure 3.10 MAEM results of push-over loading problem.....	86
Figure 3.11 Water tank example under self-weight.....	87
Figure 3.12 Modal analysis of a water column.....	88
Figure 3.13 Full-scale dam reservoir system .....	90
Figure 3.14 Transfer function estimation.....	91

Figure 3.15 Frequency response comparison .....	93
Figure 3.16 Effect of largest finite element size.....	94
Figure 3.17 Cracking pattern of Koyna Dam .....	96
Figure 3.18 Lateral displacement comparison for axial loading .....	99
Figure 3.19 Stress-displacement response for different $\nu$ .....	101
Figure 3.20 Load-CMOD response for different $\nu$ .....	104
Figure 3.21 Deformed shapes for different $\nu$ .....	104
Figure 3.22 Koyna Dam models.....	105
Figure 3.23 Solution time comparison .....	106
Figure 4.1 Dam-reservoir models.....	121
Figure 4.2 Frequency response comparison of MAEM models.....	124
Figure 4.3 Acceleration response spectra of the selected ground motions.....	127
Figure 4.4 Graphical description of limit states (Soysal et al., 2016) .....	130
Figure 4.5 Cracking scheme comparison for FEM and MAEM models for selected results.....	132
Figure 4.6 Fragility curves for FEM and MAEM Model I.....	135
Figure 4.7 Cracking schemes of MAEM models at selected times.....	137
Figure 4.8 Deformed shapes of MAEM models at selected times .....	139
Figure 4.9 Fragility curves for MAEM Model I and II .....	141
Figure 4.10 Crack width and leakage amount estimations.....	144
Figure 4.11 Maximum crack widths.....	145
Figure 4.12 Intensity measures vs. maximum base crack width (black concrete dam, cyan RCC dam) .....	149
Figure 4.13 Intensity measures vs. total maximum crack width (black concrete dam, cyan RCC dam) .....	151
Figure 4.14 Leakage amount estimations for residual crack factor 0.2.....	157
Figure 4.15 Mean leakage amount comparison of residual crack width factor 0.2 (black) and 0.1 (gray) .....	158
Figure 4.16 Computed residual crack width factors.....	160
Figure A.1 Cracking schemes of MAEM models .....	195

Figure A.2 Cracking schemes of MAEM models with different spring numbers.	196
Figure B.1 Cracking scheme comparison for FEM and MAEM models .....	197
Figure C.1 Damaged State Modeling with MAEM.....	220





# CHAPTER 1

## INTRODUCTION

### 1.1 Motivation

The prediction of the behavior of concrete gravity dams is an interesting and daunting task that has been the subject of theoretical and experimental research in the last 6 decades. The importance of these structures to the civil infrastructure is kept aside; the problem is a significant engineering challenge, requiring the combination of two very important phenomena, namely the crack propagation in a brittle media like concrete and the complex reservoir-soil-structure interaction, in the analytical simulation of the behavior. Analytical approaches have been developed to address the latter issue with high computational costs. The large size of the systems precludes experimentation and model calibration for the latter. Consequently, a combined, accurate simulation of a dam-reservoir system is still a significant challenge in contrast to the detailed analysis and decision frameworks developed for reinforced concrete or steel frame buildings in the last two decades.

The nonlinear analyses of plain concrete structures have been studied since the 1960s with interest in the performance of nuclear bunkers and gravity dams. The complex structural response of concrete in the nonlinear range is challenging to simulate: in order to evaluate the performance of such structures, the crack locations and the propagation should be adequately determined. The continuum-based finite element method (FEM) was first utilized to model the cracking phenomenon employing fracture mechanics and the introduction of crack models. Several drawbacks of this method on the fracture simulation of plain concrete structures have been reported. In order to improve the methodology, different types of FEM were developed; however, by its nature, the continuum-based methods are not very convenient for modeling the cracking phenomenon. The counterpart of the continuum-based methods assuming a

continuous (interpolated) displacement field are techniques modeling systems as a combination of discrete elements/points and discontinuous displacement fields. There exist many methods to predict the nonlinear behavior of structures with discrete elements as the discrete nature is more suitable to model element separation and the gain of kinetic energy. However, these methods have problems with simulations in the conventional elastic range regarding accuracy in the small displacement range and the representation of Poisson's ratio an issue. Stresses and strains, as we are used to, are difficult to obtain in these discrete methods. On the other hand, finite element methods are advantageous in simulating potential energy stored within the media.

The use of nonlinear structural analysis tools on the seismic behavior of dam structures began in the 1990s, building on the former studies in the elastic domain studying soil-structure-reservoir interaction. The complex problem includes modeling highly nonlinear behavior of plain concrete as in the form of discrete crack propagation on the dam body as well as the simulation of its surrounding environment, i.e., the dam reservoir. The compressibility of water and the effect of hydrodynamic forces on the dam body are essential for the accurate prediction of the seismic response of dam-reservoir systems. Reservoir effects are modeled exactly in the elastic domain: a combination with the nonlinear behavior, therefore, requires simplification of the theory or the use of large models and often both, with clear effects on the behavior.

Facing these difficulties, research is still ongoing for the accurate simulation of the seismic response and the determination of seismic limit states of concrete dams. In order to predict the behavior of dam-reservoir systems accurately, the concrete dam body should be modeled with a robust technique to account for the formation and propagation of cracks. Given the limitations of FEM to model the cracking phenomenon, it is more advantageous that the dam body is modeled with discrete element techniques. Still, the utilized discrete methodology should be robust so that the results in the small displacement range, as well as the simulation of highly nonlinear response, are both reliable. A nonlinear concrete material model for

cracking in plain concrete structures should be implemented with the parameters representing the global material parameters correctly. In addition, it is essential that the fluid elements are implemented in the model representing the behavior of the reservoir. Only with the combination of these two domains, as well as their interaction, an accurate prediction of dam-reservoir behavior, which can be used to investigate the seismic limit states, can be obtained. This work has been conducted for the development of these tools for the aforementioned purpose. Before presenting the objectives and limitations of this study, a review of the literature pertaining to the seismic analysis of gravity monoliths is presented below.

## **1.2 Literature Review**

The extensive work on predicting the seismic behavior of gravity dam monoliths is summarized under two main headings in this section. First, the advances of numerical methods focusing on the simulation of nonlinear concrete behavior are presented, comparing continuum and discrete element techniques with a particular focus on the utilized applied element method. Next, research on modeling concrete dams and the effect of the reservoir under seismic loading are provided together with the development of the fluid elements. The combined applications for predicting the behavior of concrete dams are summarized along with the studies on the proposed performance limits of concrete dams.

### **1.2.1 Numerical Methods for Modeling of Crack Propagation**

The increase in computational power leads to an increase in the usage of numerical simulations to assess the structural behavior. To this end, many techniques were developed to simulate a variety of problems with different materials under various loading conditions. Given a problem, based on the capabilities and limitations of the structural analysis method, the numerical simulations should be carried out.

The structural analysis techniques for modeling engineering structures can broadly be classified as continuum methods and discrete element-based techniques. Together with their advantages and drawbacks, the development of the methods is explained in the following sections.

### **1.2.1.1 Continuum Based Methods**

In the continuum-based methods, the structure is analyzed as a continuum with continuous shape functions. The most commonly used numerical tool almost by every engineer is the finite element method (FEM). The method was initially developed to find approximate solutions to boundary value problems, and for the simulation of cracking, some modifications were introduced. In the 1960s, fracture mechanics theory was used for crack propagation prediction (Barenblatt, 1962; Dugdale, 1960). Then, the crack models, namely the discrete crack approach (Ngo & Scordelis, 1967) and the smeared crack approach (Rashid, 1968), were developed. The main drawback of the discrete crack method is that the crack location has to be known a priori, and re-meshing is required for the crack propagation (Rots, 1988). The most significant issues regarding the smeared crack approach, on the other hand, are the mesh bias and the diffused crack profiles. Furthermore, by its nature, the collapse of structures cannot be predicted by FEM (Meguro & Tagel-Din, 2000). In order to overcome the difficulties of crack simulation phenomenon, techniques to enhance FEM such as the strong discontinuity approach (Simo et al., 1993), generalized FEM, GFEM (Strouboulis et al., 2000), extended FEM, XFEM (Belytschko et al., 2003) and cohesive segments (Remmers et al., 2008) techniques were developed. Although these methods have the advantage of mesh independence and re-meshing is not required for crack propagation, the global stiffness matrix may become ill-conditioned, causing loss of accuracy in the solutions.

### **1.2.1.2 Discrete Element Based Methods**

The second group of analysis techniques is discrete element-based methods. Many methodologies such as the distinct element method, DEM (Cundall, 1971), smoothed particle hydrodynamics (Gingold & Monaghan, 1977; Lucy, 1977), the rigid body and spring model, RBSM (Kawai, 1986), the particle model (Bažant et al., 1990), lattice models (Van Mier, 1997), peridynamics (Silling, 2000) and the applied element method (Meguro & Tagel-Din, 2000) were developed. Due to the discrete elements, crack initiation, propagation, and highly nonlinear behavior such as element separation can be simulated. While these methods are attractive, there are several disadvantages reported in the literature. These methods are generally very costly; oftentimes, they are inapplicable to practical modeling of real-size structures such as buildings, bridges, or dams (Lilliu & van Mier, 2003). Most of these methods focus on failure behavior; predicting displacement and stresses in typical operative ranges (i.e., small-displacement range) falls short of finite element techniques. The Poisson's effect is often neglected,  $\nu=0$ , (Meguro & Tagel-Din, 2000), or incorporated as a singular value for all materials as  $\nu=0.25$  and  $\nu=0.33$  for 3D and 2D cases, respectively, in the lattice models (Zhao et al., 2011).

### **1.2.2 Applied Element Method**

The applied element method, a discrete element based technique, was proposed in the late 1990s by Meguro & Tagel-Din (1997) with the goal of enabling the simulation of the behavior of structures from the small displacement range to the collapse (Meguro & Tagel-Din, 2000), combining the advantages of the finite element and discrete element based simulation techniques. Many studies were conducted by the authors to verify and to develop the AEM further. This method has been adopted by a wide range of researchers in various fields for simulations of seismic loads, demolition, blast loading, and progressive collapse analysis. It has

been used for concrete, reinforced concrete, masonry, and steel structures with success.

The idea of AEM was developed and improved by Meguro and Tagel-Din in stages comprising a work over a couple of years. It was first introduced for structural analysis of linear materials under static loading conditions (Meguro & Tagel-Din, 2000). Then, dynamic large deformation analysis was conducted for the simulation of collapse of a reinforced concrete (RC) frame, and the crack initiation, propagation, reinforcement failure, separation, and rigid body motion of members after failure was obtained (Tagel-Din & Meguro, 2000). Collision and recontact of elements were introduced in Tagel-Din & Meguro (1999). The nonlinear material model was verified by Meguro & Tagel-Din (2001) under static loading by investigating the behavior of RC structures and the obtained cracking patterns. Large deformation analysis under static loading conditions was investigated for buckling and post-buckling simulations (Meguro & Tagel-Din, 2002).

The first of many application areas of AEM is the seismic analysis of concrete and masonry structures. The behavior of clay brick masonry walls subjected to lateral loads was investigated (Pandey & Meguro, 2004). Nonlinear large deformation analysis of RC bare frames subjected to earthquake excitation was conducted by Raparla & Ramancharla (2012). Fragility curves of an existing industrial masonry building were obtained via push-over and incremental dynamic analysis within the scope of performance-based evaluation (Karbassi & Nolle, 2008, 2013). The inelastic behavior of RC frames with and without brick infill under lateral loading was compared by Dongre & Ramancharla (2012). The pounding effect of adjacent buildings was also examined by carrying out nonlinear dynamic analysis (Ehab et al., 2014). Recently, the dynamic response of a full-scale unreinforced masonry building specimen was investigated, and the damage and failure modes were evaluated by Malomo et al. (2019).

Demolition and blast scenarios could be simulated with the use of AEM. The controlled demolition of an RC structure by a single column removal was

investigated by Lupoae & Bucur (2009). While the demolition of an RC hospital building was simulated by Helmy et al. (2012a), the demolition of an industrial building based on controlled blasting was conducted by Simion & Dragomir (2013). Structural identification of a masonry infill wall in an industrial building was performed by Kernicky et al. (2015) with internal blast loading. The global response of steel frame structures and masonry structures subjected to blast loading was studied by Coffield and Adeli (2016) and Keys and Clubley (2017), respectively.

With the recontact and separation capabilities, progressive collapse analysis (coupled with blast or demolition loads) is an established AEM field. The response of different types of structures such as RC bridges (Lau & Wibowo, 2010), steel structures (Dinu et al., 2015; Khalil, 2012), post-tensioned box girder bridges (Ibarhim et al., 2012), and RC structures (Helmy et al., 2012b, 2015; Lupoae et al., 2012) were assessed for the progressive collapse analyses. The commercial software Extreme Loading for Structures (ASI, 2014), specialized in progressive collapse, appears to be a popular tool for designing/predicting the demolition of buildings in urban areas.

AEM has been rigorously used for the simulation of highly nonlinear behavior of structures, as given above. However, in common with other discrete element methods, one particular difficulty with the original formulation is neglecting the Poisson's ratio on the behavior. In order to simulate this effect, one alternative was developed by transforming the rigid elements into deformable bodies; hence, additional two degrees of freedom accounting for the relative deformations between the horizontal and vertical edges were introduced (Meguro & Tagel-Din, 2000). The increase in the number of degrees of freedom of an element from 3 to 5 led to increased computational cost. Therefore, a second approach to account for Poisson's effect was utilized. In this approach, without increasing the degrees of freedom number, the stiffness matrix of adjacent elements were correlated so that the assembly of elements would be deformable (Meguro & Tagel-Din, 2000). The proposed methodology was verified for the solution of linear elastic problems; on the other hand, in the nonlinear simulations, the Poisson's effect was neglected. This

material property affects the stress and displacement fields as well as the loading direction. Ignoring the effect of Poisson's ratio by neglecting it or taking it as a fixed value implies directionality in the analysis, which is a disadvantage in the application of loads in multiple load cases as well as problems in stress and displacement predictions in orthogonal directions (Gao & Klein, 1998; Liu & Hong, 2012; Zhao et al., 2011).

### **1.2.3 Dam-Reservoir Interaction on Seismic Behavior of Concrete Dams**

The seismic analysis of concrete dams is a challenging task requiring the consideration of the complex soil-structure and structure-reservoir interactions. Work on the numerical simulation of these phenomena dates back to the 1960s, coinciding with the proper development of finite element tools. As dams are massive, vital structures for hydropower, water supply, and flood control, considerable research to accurately predict the seismic response of dams has been conducted, taking the dam-reservoir interaction into account. The importance of hydrodynamic effects on the seismic response of dams was first acknowledged by Westergaard (Westergaard, 1933). Assuming the reservoir as incompressible and the dam as rigid, the hydrodynamic forces acting on the upstream face of the dam were represented by added mass on the dam upstream face. Although his work was later improved (Kotsubo, 1957; Zangar, 1959) and is practical for engineering purposes, it yielded conservative results (Fok & Chopra, 1986a). For constructing proper analytical models of dams subjected to seismic loading, the need for the simulation of the wave propagation in the reservoir has been recognized by Chopra and his coworkers. Accordingly, the water compressibility and radiation damping at the far end of the reservoir were taken into account in the simulations, and the phenomenon was solved in the frequency domain with the substructure method (Fenves & Chopra, 1985; Fok & Chopra, 1986b, 1987; Hall & Chopra, 1983). Similarly, solutions of dam-reservoir systems in the frequency domain were performed utilizing the boundary element method; however, this methodology was computationally costly (Domínguez &



Maeso, 1993; Maeso & Dominguez, 1993; Medina et al., 1990). One limitation of these techniques is that simulations require linear elastic analysis since the formulation is in the frequency domain. In order to account for nonlinearity, hybrid frequency-time domain procedures were proposed with certain assumptions and simplifications (Chàvez & Fenves, 1995). Still, solutions in the time domain were developed to consider the nonlinearities in the concrete dam body.

In the time-domain solution, on the other hand, the general modeling of hydrodynamic behavior requires the solution of nonlinear Navier-Stokes equations. Given the massive scale of dam-reservoir problems, the solution of these nonlinear equations is problematic, requiring considerable computational power for the simulations (Demirel & Aydin, 2016). Consequently, solutions are often done in simplified versions of the flow equations, such as pure displacement formulations (Bathe & Hahn, 1979; Belytschko, 1980; Olson & Bathe, 1983), the displacement potential and pressure formulation (Morand & Ohayon, 1979), and the velocity potential formulation (Everstine, 1981; Olson & Bathe, 1985). Pure pressure formulations cannot include the effect of viscosity in the formulation, unlike displacement-based techniques. Pure displacement-based elements have the main advantage of the direct connection of fluid elements to the structural counterparts as well as side advantages such as being able to simulate the surface waves. However, numerical problems such as spurious zero-energy modes and locking emerge in the applications. While improved formulations were proposed to eliminate these spurious modes in pure displacement formulations (Chen & Taylor, 1990; Wilson & Khalvati, 1983), it was shown that the formulations that do not satisfy the inf-sup condition led to spurious zero-energy modes (X. Wang & Bathe, 1997). Accordingly, a displacement/pressure (u/p) based mixed finite element formulation satisfying the inf-sup condition and eliminating the spurious zero-energy modes was proposed by Wang & Bathe (1997).

#### 1.2.4 Nonlinear Analyses of Concrete Dams

The performance evaluation of new dams and existing, aging dam stock is a significant issue that would require nonlinear analyses for increased seismic hazard. Therefore, the prediction of damage on the concrete dam body through the crack simulation was investigated extensively in the literature. The majority of these studies focused on verifying the nonlinear concrete material model used in the analytical simulations by investigating the cracking profile of Koyna Dam. This dam suffered severe damage during the 1967 Koyna Earthquake, and cracking occurred at the base of the upstream face and the abrupt slope change in the downstream side (i.e., the neck portion) (Chopra & Chakrabarti, 1973). Utilizing the discrete crack approach, the damage of Koyna Dam was obtained, and results were compared with the smeared crack approach, showing that both methods predicted the cracks at the actual crack locations (Skrikerud & Bachmann, 1986). Similarly, the cracking of Koyna Dam at the neck portion was predicted using the discrete crack method (Ayari & Saouma, 1990). The main drawback of the discrete crack method is the pre-definition of the crack location (Rots, 1988) and the remeshing requirement (Skrikerud & Bachmann, 1986). With the development of smeared crack tools, which considerably simplified the analyses, smeared crack models were also utilized for the simulation of the Koyna Dam response: The cracking profile of Koyna Dam at the base and the neck was obtained by Bhattacharjee & Léger (1993) in addition to localized spurious deformations observed at the neck of the dam. A co-axial rotating crack model was verified with the seismic analysis of Koyna Dam by simulating the cracks at the base and the neck of the dam (Mirzabozorg & Kianoush, 2008). The major problem with the smeared crack models is that although a singularity in the model, such as the neck portion of Koyna Dam, exists, diffused cracking patterns are observed. Mesh bias is another significant issue regarding the smeared crack approaches.

The modeling approach to predict the cracking of roller-compacted concrete (RCC) dams was similar to the approach followed for the concrete gravity dams. However,

there is a significant difference in the construction methodology of RCC dams: they are constructed in thin horizontal layers (lifts), ranging from 0.15 m to 1 m, and compacted by rollers (USACE, 2000). Despite the significant weakness in the contact between these horizontal layers, the modeling and analysis approaches have been identical for concrete gravity and RCC dams. Research on RCC dams has been conducted in the last decade on case studies of new dams mainly built in the developing world, such as China, Malaysia, Iran, and Turkey. A case study to assess the seismic failure process of an RCC dam in China was conducted by taking the heterogeneity of concrete into account, ignoring the effect of lift joints (Zhong et al., 2012). The nonlinear seismic analysis of an RCC dam located in Malaysia was conducted utilizing concrete damaged plasticity model and considering the reservoir effects (Ghaedi et al., 2016), underlining the effects of size and shape of galleries on the crack patterns and propagation. Five typical failure modes were described based on the cracks observed at the upstream and downstream slopes, dam heel, top of the corridor, and the concrete partition interface (Chen et al., 2019) using incremental dynamic analysis of an RCC dam using the concrete damaged plasticity model. All these studies ignored the horizontal layering associated with the RCC construction technique, and the diffused cracking patterns are typical, as the previous studies on concrete gravity dams.

With the advance of computational power, the 3D nature of the dam response was recognized, leading to the use of 3D finite element models to investigate the behavior. The seismic response of arch dams was the first concern in this regard. Cracking patterns of a 130 m high arch dam located in Iran were obtained using smeared crack and elasto-plastic models, and it was recommended that the fracture based models should be utilized for dynamic analysis of concrete arch dams (Espandar & Lotfi, 2003). The double curvature Morrow Point arch dam with dam-reservoir interaction was analyzed with the smeared crack approach leading to a crack profile deemed reasonable (Mirzabozorg & Ghaemian, 2005). One particular concern for RCC dams is, in contrast to former generations of concrete dams generally built in wide canyons, RCC gravity dams are built even in narrow valleys

that may require the consideration of 3D effects (Bybordiani & Arici, 2017). Consequently, gravity dams were also studied in a 3D setting to compare the 2D and 3D modeling approaches. A 56 m high concrete gravity dam located in Turkey was simulated with smeared rotating crack and utilizing the Westergaard added mass approach (Akpinar et al., 2013), showing that the cracking locations were highly dependent on the modeling approach (i.e., 2D or 3D). Similarly, the investigation of the seismic performance of a tall RCC dam in Turkey with smeared rotating crack concrete model and added mass approach to account for hydrodynamic effects showed that the 3D behavior differed substantially from 2D monolith by means of base and body cracks (Arici et al., 2014). The performance of Dez Dam was evaluated using a 3D model and various damage indices by Hariri-Ardebili et al. (2016). A probabilistic-based correlation between linear and nonlinear analyses was performed by correlating the overstressed area and damage index based on cracking (Hariri-Ardebili et al., 2016). Validating a complete fluid-soil-structure interaction analysis approach, the Morrow Point dam was modeled utilizing the concrete damaged plasticity model simulating the tensile cracking on the system (Løkke & Chopra, 2017). From these studies, it can be deduced that in 3D models, the diffusion of cracking is even more prominent since the finite element sizes are much larger than the 2D models.

The seismic response of dams is highly affected by the surrounding medium, i.e., reservoir and foundation. The coupling of dams with the reservoir utilizing nonlinear mechanics requires analyses in the time domain. Hence, modeling the reservoir to account for the hydrodynamic effects has been investigated with many different approaches, such as the Westergaard added mass approach, Lagrangian formulation, and the mixed Lagrangian-Eulerian formulations. These modeling approaches of the reservoir on the cracking behavior of Koyna Dam were compared either with each other or to results obtained without considering the reservoir. As early as 1986, it was reported that the Westergaard approach, which is based on an incompressible fluid assumption, generally led to erroneous results in contrast to the approaches where water compressibility is taken into account (Chopra, 1986). Still, using

Westergaard added mass approach for reservoir modeling, and utilizing the rate-independent plastic damage model, the stability of the neck portion of Koyna Dam was investigated, showing a stable rocking behavior of the upper portion of the dam (Lee & Fenves, 1998). The earthquake damage response of Koyna Dam employing the continuum damage model was compared with two modeling approaches for the reservoir, namely Westergaard technique and Lagrangian formulations, and the damage propagation was obtained differently for the two reservoir modeling approaches (Calayir & Karaton, 2005a). Another study on determining the cracking of Koyna Dam was conducted using the co-axial rotating crack model with Lagrangian reservoir formulation; the cracks at the heel and the neck matched with the observed damage (Calayir & Karaton, 2005b). The Lagrangian-Eulerian formulation was used with the smeared crack model in a study conducted by Mansouri et al. (2011), showing that ignoring the reservoir effects led to conservative results. Omidi et al. (2013) compared the cracking profile of Koyna Dam with the reservoir modeled with the Lagrangian-Eulerian formulation and the Westergaard approach concluding better estimation of cracking at the neck with the Lagrangian-Eulerian reservoir elements. Lagrangian formulation was used for obtaining the sliding fragility at the base and at the neck of a dam located in Eastern Canada studied to improve the development of fragility curves for concrete gravity dams (Bernier et al., 2016a; Bernier et al., 2016b). The Lagrangian- Eulerian approach was utilized in some of the simulations by Hariri-Ardebili et al. (2016; 2018) for uncertainty quantification of concrete gravity dams under seismic actions. Nevertheless, Westergaard added mass technique is still used commonly due to its simplicity with the modeling interest concentrating on other simulation aspects. The effect of ground motion duration on Koyna Dam response was investigated using the Westergaard added mass technique and the concrete damaged plasticity model showing an increase in strong motion duration led to more accumulated damage Zhang et al. (2013). The wavelet analysis method was utilized to evaluate the overall damage degree of the Koyna Dam using similar analysis assumptions by Sun & Ren (2016).

Determining the performance limits of dams is an ongoing research subject (Léger, 2007; Pekau & Zhu, 2006). Most early works focused on the use of stress and stress exceedance to quantify the behavior of dams in the nonlinear range (Tekie & Ellingwood, 2003). Stress and strain-based quantifications are based on the cumulative inelastic duration (CID) approach proposed by Ghanaat (2004) and adopted in the USACE recommendations (USACE, 2003). While the relationship between CID and the damaged state is not clear, this index is still continued to be used in detailed simulations (Hariri-Ardebili et al., 2016). The crest displacement was used as a damage indicator (and for defining performance limits) by Alembagheri & Ghaemian (2013) and Hariri-Ardebili & Saouma (2015); however, a relationship between damage on the dam body and the crest displacement could not be set (Soysal et al., 2016). Crack profiles on damaged systems are also used to set performance limits: Zhong et al. (2012) proposed five earthquake damage states for gravity dams as basic intact, slight damage, moderate damage, severe damage, and dam failure according to the cracking profiles obtained from dynamic simulations. Four states were suggested in Soysal et al. (2016) based on concerns on post-earthquake performance. The crack profiles presented by Chen et al. (2019) are similar to these previous work: concentrated cracking at the upstream toe and slope change locations for smaller excitations followed by large, smeared cracks in strong excitations. While cracking is generally detected, extensive simulations on Koyna Dam have also shown that a joined crack at the crest is not necessarily an ultimate state of a dam and the stability of the crest was maintained (Lee and Fenves, 1998, Jiang & Du, 2012; Pekau & Yuzhu, 2004).

Although much work has been performed on seismic analysis of concrete dams, performance criteria are still not clear, and performance limits on dams for highly nonlinear behavior are still not set. For RCC dams, the effect of lift joints on the global seismic performance is not known. Furthermore, collapse scenarios could not be simulated with continuum models, but discrete element techniques enable these simulations where crack propagation and element separation are modeled naturally with these tools. With these limitations in mind, the investigation of the highly

nonlinear behavior of RCC dams should be simulated with proper numerical techniques, which led to the work undertaken in this dissertation.

### 1.3 Objectives

As explained in detail in the previous section, the majority of research on the seismic performance of concrete dams is based on determining the damage on the dam body rather than setting performance limits within the framework of performance-based design. While the finite element method (FEM) is a commonly utilized tool to predict damage on concrete dam bodies, diffused cracking patterns have been reported as a significant disadvantage in fracture simulation. Moreover, due to the limitations of the finite element methodology, most of these works ignore the effect of the layered structure of the RCC material: all gravity dams of the last 2 decades were built with RCC, conventional concrete is reserved only for arch dams. With these limitations in mind, a comprehensive review of the modeling techniques of gravity dams yielded the following motivations for this study:

- The continuum-based finite element method was mostly utilized in the simulations, in which the collapse behavior of structures can hardly be simulated.
- The effect of the reservoir on the seismic performance of gravity dams was acknowledged; however, mostly, simplified techniques such as the added mass approach or pressure-based formulations have been utilized.
- The effect of lift joints in RCC dams was not considered in the nonlinear analyses.

Given these shortcomings of the literature on nonlinear seismic performance of dam-reservoir systems, the objectives of this study were set as:

- Developing a robust discrete element tool based on the applied element technique to accurately simulate the behavior of a concrete monolith from small displacement range until the collapse state,

- Conducting a realistic analysis of dams with discrete cracks and assessing their behavior in the highly nonlinear range,
- Investigating the performance limits of concrete and RCC gravity dam-reservoir systems under seismic loading based on discrete cracks and analyzing the effect of lift joints on the global performance of RCC dams.

The following tasks were undertaken to reach these goals within this work:

- Development and proof of the modification of the applied element technique enabling the representation of any Poisson's ratio as well as direction independence,
- Implementation of a cyclic, hysteretic, nonlinear concrete tension material model representing the global material parameters,
- Implementation of displacement/pressure based mixed fluid elements and combination with discrete elements accurately representing their interaction,
- Implementation of dynamic implicit and explicit time-stepping techniques along with mass-scaling enabling the time history analysis with MAEM combined with reservoir elements,
- Incremental dynamic analysis of a concrete and an RCC monolith with lift joints for the investigation of crack propagation and distribution,
- Characterization of the seismic behavior of concrete and RCC monoliths using fragility curves and crack width based measures.

In order to achieve the objectives, a computer program with several modules was developed in FORTRAN. The details of the work on the developed and implemented routines are explained in the forthcoming chapter. The program can be further developed by implementing other methodologies to solve multi-physics problems similar to the dam-reservoir systems. It should be noted that the main objective of this study is to perform simulations of the concrete gravity mass and the corresponding crack propagation in continuous brittle media; therefore, the dam-foundation interaction is kept beyond the scope of this research, and only dam-reservoir interaction is accounted for in the 2D simulations.



## 1.4 Outline

The outline of this dissertation is as follows:

Chapter 2 presents a review of the applied element technique for the modeling of continuum structures such as gravity dam monoliths:

The proposed methodology, i.e., the modified applied element method, is introduced. The theory and formulation in linear and nonlinear range with the introduction of the Poisson's ratio to the modeling are shown. The direction independence of the proposed methodology is shown by using strain energy in the domain. Implementation of post-peak behavior using fracture energy to the modified applied element models is introduced, providing element size-dependent model parameters. The formulation for the fluid finite element, the radiation boundary condition at the far end of the reservoir, the utilized mass scaling technique, and their implementation to the computer program is presented in detail.

Chapter 3 focuses on the validation studies of the developed tools:

Validation tests for the modified applied elements are performed for linear and nonlinear static problems, and the results are compared to theoretical and experimental counterparts for verification. Firstly, linear static analyses of a cantilever column under different loading conditions are conducted to demonstrate the robustness of the proposed methodology by comparing the results with theoretical solutions. Later, the convergence rate of MAEM is investigated considering a shear dominant structural member and a bending dominant frame; the results are compared to their counterparts based on FEM solutions. Next, the loading, unloading, and reloading branches of the implemented nonlinear material model is demonstrated. Then, a direct tension test, splitting tension test, and the push-over analyses of a scaled concrete dam model experiment are performed in the nonlinear static setting. For the three simulations, the analytical results are compared with the experimental outcomes by means of cracking simulation and prediction of load-displacement behavior. The validation of fluid elements follows this section by

conducting the static analysis of a water tank under self-weight and the modal analysis of a water column. The analysis results are compared with theoretical solutions. The combined performance of the MAEM and reservoir elements, together with the radiation boundary condition defined at the truncated far end of the reservoir, are validated, simulating the dynamic behavior of a dam-reservoir system to obtain the frequency response compared with solutions performed in the frequency domain. Then, the nonlinear explicit dynamic simulation of the Koyna Dam-reservoir system is presented, verifying the coupling of modified applied-finite elements in the nonlinear dynamic setting through crack simulation on the dam body. This chapter is concluded with the study on the effect of Poisson's ratio on the same MAEM validation tests, demonstrating the significance of modeling the Poisson's effect in discrete element models.

Chapter 4 presents the results for nonlinear dynamic simulations of concrete and RCC gravity dam-reservoir systems using the modified applied elements technique:

Firstly, the numerical models of the concrete gravity and RCC gravity dam-reservoir systems, with identical geometries for the dam body, are introduced. The modeling approach to consider the lift joints for the simulation of the RCC dam is explained. In order to assess the performance of these systems under seismic actions, IDA is conducted on a ground motion set comprised of 21 motions, each scaled to 17 different intensity levels leading to 357 nonlinear transient analyses for each model. After the utilized ground motion set is explained together with the IDA procedure, the fragility analysis and the limit states used to construct these fragility functions are introduced. The first set of analyses presented in this chapter are those for the concrete dam whose results are compared with counterparts based on FEM. The cracking schemes and fragility curves are investigated in detail, accounting for different modeling approaches on the nonlinear analysis results. Next, IDA analyses conducted on the MAEM model for the RCC dam is presented. The cracking distribution of the dam body is compared with that of the concrete dam model. The evolution of damage and the discrete crack propagation on the dam body for the two models are investigated thoroughly. The damage on the dam body for the two

MAEM models is compared qualitatively and quantitatively utilizing fragility curves considering the extent of cracks. In addition to the fragility functions, crack widths on the upstream faces of the dam monoliths are computed as a new damage indicator. The variation of the maximum base and total crack widths are studied to set a relationship between ground motion IMs and the damage on the dam bodies. Lastly, the leakage through the upstream cracks are estimated related to the residual opening of the crack as well as crack geometrical properties like depth and length. The effect of residual crack widths on the leakage estimations is studied considering 4 different residual crack width factors.

Chapter 5 summarizes this study, and conclusions are drawn. Based on the work conducted and the limitations of this study, future avenues for research are discussed.



## CHAPTER 2

### THEORETICAL BACKGROUND

#### 2.1 Introduction

A new methodology based on an existing discrete technique called the applied element method (AEM) is proposed and coupled with a fluid finite element to investigate the seismic performance limits of dam-reservoir systems within the framework of performance-based design. AEM was modified to obtain a more robust methodology and to include the effect of Poisson's ratio on the numerical simulations. Cauchy-Born rule and hyperelastic theory were utilized to construct the constitutive relation in the proposed methodology, which is the modified applied element method (MAEM). The reservoir, on the other hand, was modeled with displacement/pressure (u/p) based mixed finite element formulation.

In this chapter, first, a brief review of classical AEM is presented. Then, to overcome some limitations of the method, the proposed technique MAEM is introduced. The theory and formulation for elastic range and cracked media are presented together with the theoretical representation of accounting for Poisson's effect. The formulation of fluid finite element to model fluid-structure interaction problems and the implemented radiation boundary condition at the far end of the reservoir are explained.

Finally, the implementation of the methodology in a computer program written in FORTRAN language is presented in detail in this chapter. The linear and nonlinear static solvers, linear implicit and explicit dynamic solution algorithms, and nonlinear explicit dynamic solver are explained in detail. The utilized mass scaling technique, a procedure to decrease the computational cost in explicit dynamic analyses, is

introduced. The loading types, namely nodal load, body forces, and earthquake loading, implemented in the program, are presented at the end of this chapter.

## 2.2 Review of Applied Element Method

Applied Element Method (AEM) (Meguro & Tagel-Din, 2000) is a discrete element based technique in which the domain is modeled via rigid square elements that are connected by a number of normal and shear spring pairs between the boundaries of each element (Figure 2.1a). The number of spring pairs is defined by the user, and they can be selected as any number such as 1, 2, 5, 10, or 20 pairs. The spring pairs represent the deformation of a tributary area of two connecting elements based on their location (Figure 2.1b). The stiffness of springs is determined as if they are truss elements; accordingly, normal spring stiffness,  $k_n$  and shear spring stiffness,  $k_s$  are given in Equation (2.1).

$$k_n = \frac{Edt}{a}, k_s = \frac{Gdt}{a} \quad (2.1)$$

where  $E$  and  $G$  are the elasticity and shear modulus, respectively,  $d$  is the distance between spring pairs (Figure 2.1b),  $t$  is the thickness of the model and  $a$  is the length of the rigid element (Figure 2.1b).

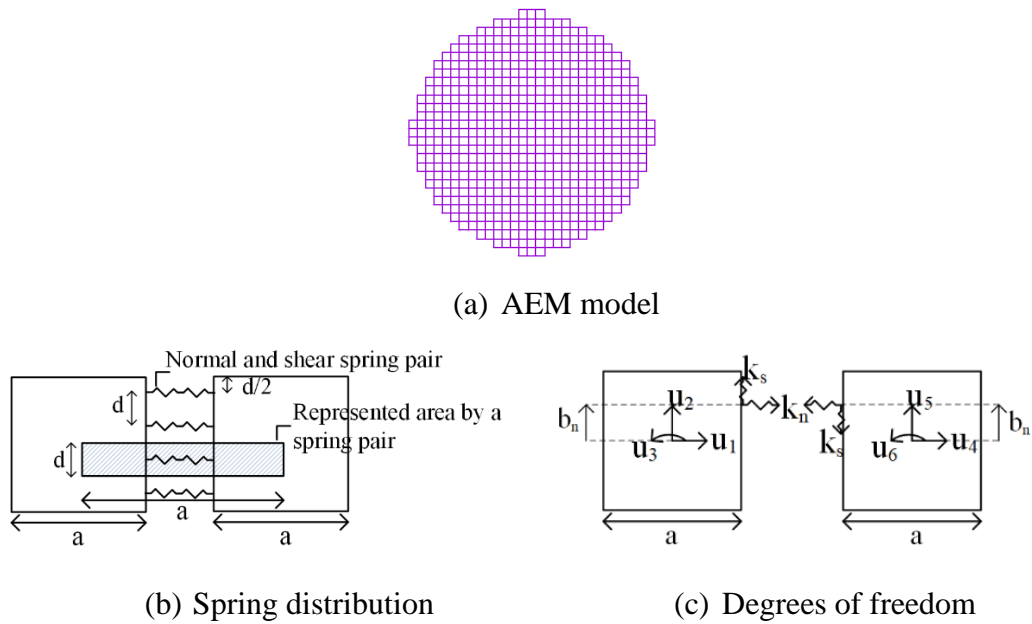


Figure 2.1 Applied element method

The rigid elements have three degrees of freedom (DOF) located at their centroids, which are two translational and one rotational DOF representing the rigid body motion (Figure 2.1c). Although elements are rigid, the deformation along each element is calculated from the corresponding surrounding springs' deformation.

### 2.3 Modified Applied Element Method

In accordance with AEM, the modified applied element method (MAEM) also models the structure by rigid square elements with three degrees of freedom. In addition to the normal and shear spring pairs connecting the elements, in the modified approach, the model is enriched by introducing two diagonal springs that make  $135^\circ$  and  $45^\circ$  angle with respect to horizontal, as illustrated in Figure 2.2a.

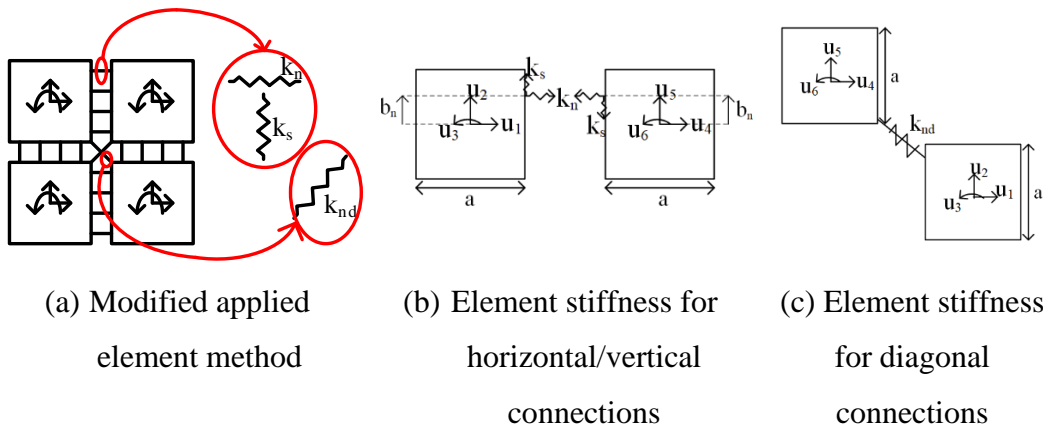


Figure 2.2 Modified applied element method

In this methodology, the stiffness of springs is calculated by the Cauchy-Born rule and hyperelastic theory, satisfying Hooke's law. The stiffness matrix formulation, in addition to the spring stiffness constant calculations, are presented in the next section.

### 2.3.1 Theory and Formulation in Elastic Range

The particular strength of the applied element formulation is the use of spring deformations directly to obtain forces at the degrees of freedom by simple equilibrium equations and the simplicity of using one-dimensional relations for spring pairs to that end. For each element connection (i.e., horizontal, vertical, and two diagonal cases), the element stiffness matrix is obtained via the general stiffness method (i.e., by applying unit displacement to each DOF and calculating the corresponding force at each spring). For the element pair, the force at each spring is summed up to obtain the local element stiffness matrix. After the transformation of element stiffness matrices to the global coordinates, the system stiffness matrix of the overall structure is assembled.

For a horizontal/vertical connection, there may be a number of spring pairs that have distance  $d$  in between, and from the edges, the first and last spring are located at



distance  $d/2$  (Figure 2.1b). It can be seen from Figure 2.2b that  $b_n$  is the distance of a spring from element's centroid, hence  $b_{n,i}$  for each spring,  $i$ , is calculated as in Equation (2.2).

$$b_{n,i} = \frac{a}{2} - \frac{d}{2} - d(i - 1) \quad (2.2)$$

where  $a$  is the element length, and  $i$  is the spring number that starts from 1 until the number of connecting springs in between the two elements. It should be noted that for the springs located below the centroid,  $b_{n,i}$  is negative.

For the horizontal/vertical connection, the 6x6 local element stiffness matrix,  $\mathbf{k}_{el}$ , for a single spring pair is presented (Equation (2.3)).

$$\mathbf{k}_{el} = \begin{bmatrix} k_n & 0 & -k_n b_n & -k_n & 0 & k_n b_n \\ 0 & k_s & k_s \frac{a}{2} & 0 & -k_s & k_s \frac{a}{2} \\ -k_n b_n & k_s \frac{a}{2} & k_n b_n^2 + k_s \left(\frac{a}{2}\right)^2 & k_n b_n & -k_s \frac{a}{2} & -k_n b_n^2 + k_s \left(\frac{a}{2}\right)^2 \\ -k_n & 0 & k_n b_n & k_n & 0 & -k_n b_n \\ 0 & -k_s & -k_s \frac{a}{2} & 0 & k_s & -k_s \frac{a}{2} \\ k_n b_n & k_s \frac{a}{2} & -k_n b_n^2 + k_s \left(\frac{a}{2}\right)^2 & -k_n b_n & -k_s \frac{a}{2} & k_n b_n^2 + k_s \left(\frac{a}{2}\right)^2 \end{bmatrix} \quad (2.3)$$

In the above element stiffness matrix,  $k_n$  and  $k_s$  are the spring stiffness constants of normal and shear springs, respectively.

Similarly, for the diagonal connections (Figure 2.2c), the 6x6 element stiffness matrix,  $\mathbf{k}_{el}$ , is obtained as presented in Equation (2.4). In this equation,  $k_{nd}$  is the spring stiffness constant for diagonal springs.

$$\mathbf{k}_{el} = \begin{bmatrix} k_{nd} & 0 & 0 & -k_{nd} & 0 & 0 \\ 0 & 0 & 0 & 0 & 0 & 0 \\ 0 & 0 & 0 & 0 & 0 & 0 \\ -k_{nd} & 0 & 0 & k_{nd} & 0 & 0 \\ 0 & 0 & 0 & 0 & 0 & 0 \\ 0 & 0 & 0 & 0 & 0 & 0 \end{bmatrix} \quad (2.4)$$

After the local element stiffness matrix,  $\mathbf{k}_{el}$ , is obtained by summing up the local element matrices for each connecting spring pair, the transformation to global coordinates,  $\mathbf{K}_{global}$ , are made via the rotation matrix,  $\mathbf{R}$ , as in Equation (2.5).

$$\mathbf{K}_{global} = \mathbf{R}^T \mathbf{k}_{el} \mathbf{R} \quad \mathbf{R} = \begin{bmatrix} c & s & 0 & 0 & 0 & 0 \\ -s & c & 0 & 0 & 0 & 0 \\ 0 & 0 & 1 & 0 & 0 & 0 \\ 0 & 0 & 0 & c & s & 0 \\ 0 & 0 & 0 & -s & c & 0 \\ 0 & 0 & 0 & 0 & 0 & 1 \end{bmatrix} \quad (2.5)$$

$$c = \cos(\theta), s = \sin(\theta)$$

where  $\theta$  is the counterclockwise angle with respect to the horizontal such that it is  $0^\circ$ ,  $90^\circ$ ,  $135^\circ$  and  $45^\circ$  for horizontal, vertical, and the two diagonal connections, respectively.

The simulation of a continuum using discrete techniques requires determining the model's elastic constants (i.e., the spring constants) corresponding to the proper representation of strain energy distribution in the system. Accordingly, for the two-dimensional (2D) plane stress condition., the relationship between macro material constants such as elasticity modulus,  $E$ , and Poisson's ratio,  $\nu$ , and the micro spring parameters  $k_n$ ,  $k_s$  and  $k_{nd}$ , which are the spring stiffness constants for normal, shear, and diagonal springs, respectively, are calculated based on the Cauchy-Born rule and hyperelastic theory (Zhao et al., 2011) using the concept of strain energy. For a 2D system, the total strain energy per the domain volume,  $\Pi$ , is the summation of the potential energy stored in the normal, shear and the diagonal springs (Equation (2.6)).

$$\Pi = \frac{\sum \Pi_b}{V} = \frac{\sum (k_n \mathbf{u}^n \cdot \mathbf{u}^n + k_s \mathbf{u}^s \cdot \mathbf{u}^s + k_{nd} \mathbf{u}^{nd} \cdot \mathbf{u}^{nd})}{2V} \quad (2.6)$$

where  $\mathbf{u}^n = (\mathbf{u} \cdot \mathbf{n})\mathbf{n}$  and  $\mathbf{u}^s = \mathbf{u} - \mathbf{u}^n$  are the normal and shear components of the displacement vector,  $\mathbf{u}$ ,  $\mathbf{n}$  is the unit normal vector, and  $V$  is the total volume of the

modeled structure. The total strain energy can also be expressed in terms of strains (Equation (2.7)).

$$\Pi = \sum \frac{l^2(k_n \xi_i \varepsilon_{ij} \xi_j \xi_n \varepsilon_{nm} \xi_m + k_s(\varepsilon_{kl} \xi_l - \xi_i \varepsilon_{ij} \xi_j \xi_k)(\varepsilon_{km} \xi_m - \xi_n \varepsilon_{nm} \xi_m \xi_k) + k_{nd} \xi_i \varepsilon_{ij} \xi_j \xi_n \varepsilon_{nm} \xi_m)}{2V} \quad (2.7)$$

In the above equation,  $\varepsilon_{ij}$  represents the strain tensor,  $\xi_i$  is the  $i^{\text{th}}$  component of the unit normal vector  $\mathbf{n}$  and  $l$  is the length of the spring. The elasticity tensor,  $C_{ijnm}$  can be obtained by taking the second derivative of the total strain energy per volume,  $\Pi$  with respect to the strain tensor that is presented in Equation (2.8).

$$\begin{aligned} C_{ijnm} &= \frac{\partial^2 \Pi}{\partial \varepsilon_{ij} \partial \varepsilon_{nm}} \\ &= \sum \frac{l^2(k_n \xi_i \xi_j \xi_n \xi_m + k_s(\delta_{in} \xi_j \xi_m - \xi_i \xi_j \xi_n \xi_m) + k_{nd} \xi_i \xi_j \xi_n \xi_m)}{V} \end{aligned} \quad (2.8)$$

In Equation (2.8),  $\delta_{in}$  stands for the Kronecker symbol. For 2D problems, the elasticity tensor  $C_{ijnm}$  in matrix format,  $\mathbf{C}$  is given in Equation (2.9).

$$\mathbf{C} = \begin{bmatrix} C_{1111} & C_{1122} & 1/2(C_{1111} + C_{1121}) \\ C_{2211} & C_{2222} & 1/2(C_{2212} + C_{2221}) \\ C_{1211} & C_{1222} & 1/2(C_{1212} + C_{1221}) \end{bmatrix} \quad (2.9)$$

For a plane stress problem, the elasticity tensor should approximate the analytical solution. According to Hooke's Law, the elasticity tensor in terms of  $E$  and  $\nu$  in the plane stress and plane strain settings are presented in Equation (2.10a) and Equation (2.10b), respectively.

$$\mathbf{C} = \frac{E}{1-\nu^2} \begin{bmatrix} 1 & \nu & 0 \\ \nu & 1 & 0 \\ 0 & 0 & \frac{1-\nu}{2} \end{bmatrix} \quad (2.10a)$$

$$\mathbf{C} = \frac{E}{(1+\nu)(1-2\nu)} \begin{bmatrix} 1-\nu & \nu & 0 \\ \nu & 1-\nu & 0 \\ 0 & 0 & \frac{1-2\nu}{2} \end{bmatrix} \quad (2.10b)$$

It should be noted that the unit normal vector,  $\mathbf{n}$ , its components,  $\xi_i$ , and the spring length,  $l$  differ with respect to the spring types (Table 2.1).

Table 2.1 Parameters for elasticity tensor calculation

Spring type	$\mathbf{n}$	$\xi$	$l$
Horizontal normal-shear pair	$\mathbf{n} = [1 \ 0]$	$\xi_1 = 1, \xi_2 = 0$	$l = a$
Vertical normal-shear pair	$\mathbf{n} = [0 \ 1]$	$\xi_1 = 0, \xi_2 = 1$	$l = a$
Diagonal with 135°	$\mathbf{n} = [-\sqrt{2} \ \sqrt{2}]$	$\xi_1 = -\sqrt{2}, \xi_2 = \sqrt{2}$	$l = a\sqrt{2}$
Diagonal with 45°	$\mathbf{n} = [\sqrt{2} \ \sqrt{2}]$	$\xi_1 = \sqrt{2}, \xi_2 = \sqrt{2}$	$l = a\sqrt{2}$

Given these parameters, the components of the elasticity tensor are calculated (Equations (2.11)-(2.15)).

$$C_{1111} = \frac{s(n_x - 1)n_y a^2 k_n}{V} + \frac{(n_x - 1)(n_y - 1)a^2 k_{nd}}{V} \quad (2.11)$$

$$C_{2222} = \frac{s(n_y - 1)n_x a^2 k_n}{V} + \frac{(n_x - 1)(n_y - 1)a^2 k_{nd}}{V} \quad (2.12)$$

$$C_{1122} = C_{2211} = \frac{(n_x - 1)(n_y - 1)a^2 k_{nd}}{V} \quad (2.13)$$

$$C_{1112} = C_{1121} = C_{2212} = C_{2221} = C_{1211} = C_{1222} = 0 \quad (2.14)$$

$$1/2(C_{1212} + C_{1221}) = \frac{s_y(n_y - 1)n_x a^2 k_s}{2V} + \frac{(n_x - 1)(n_y - 1)a^2 k_{nd}}{V} \quad (2.15)$$

In the above equations,  $n_x$  and  $n_y$  are the number of modified applied elements in horizontal and vertical directions, respectively,  $s$  is the number of spring pairs between the elements,  $a$  is the element side length, and  $V$  is the total volume of the structure that can be approximated as  $V = n_x n_y a^2 t$ , with thickness  $t$ . It is important to note here that in the absence of diagonal springs, as in the case of AEM, the elasticity tensor components  $C_{1122}$  and  $C_{2211}$  (Equation (2.13)) would be zero, violating the plane stress and plane strain elasticity tensor formulations (Equation (2.10a)).

For the plane stress conditions, equating Equations (2.9) and (2.10a) and substituting the elasticity tensor components given in Equations (2.11)-(2.15), the spring stiffness constants are calculated (Equations (2.16)-(2.18)).

$$C_{1111} = \frac{s(n_x - 1)n_y a^2 k_n}{V} + \frac{(n_x - 1)(n_y - 1)a^2 k_{nd}}{V} = \frac{E}{1 - \nu^2} \quad (2.16)$$

$$C_{1122} = \frac{(n_x - 1)(n_y - 1)a^2 k_{nd}}{V} = \frac{E\nu}{1 - \nu^2} \quad (2.17)$$

$$1/2(C_{1212} + C_{1221}) = \frac{s(n_y - 1)n_x a^2 k_s}{2V} + \frac{(n_x - 1)(n_y - 1)a^2 k_{nd}}{V} = \frac{E(1 - \nu)}{2(1 - \nu^2)} \quad (2.18)$$

Solving the above three equations simultaneously leads to the three spring stiffness constants in plane stress setting as given in Equations (2.19)-(2.21).

$$k_n = \frac{E}{1 + \nu} \frac{V}{s_x(n_x - 1)n_y a^2} \quad (2.19)$$

$$k_s = \frac{E(1 - 3\nu)}{1 - \nu^2} \frac{V}{s_y(n_y - 1)n_x a^2} \quad (2.20)$$

$$k_{nd} = \frac{E\nu}{1 - \nu^2} \frac{V}{(n_x - 1)(n_y - 1)a^2} \quad (2.21)$$

Assuming that the model is constituted of infinitesimal elements such that  $n_x - 1$  and  $n_y - 1$  would converge to  $n_x$  and  $n_y$ , respectively, the normal,  $k_n$ , shear,  $k_s$  and diagonal,  $k_{nd}$  spring stiffness constants for plane stress problems simplify to terms presented in Equations (2.22)-(2.24).

$$k_n = \frac{Et}{(1 + \nu)s} \quad (2.22)$$

$$k_s = \frac{Et(1 - 3\nu)}{(1 - \nu^2)s} \quad (2.23)$$

$$k_{nd} = \frac{Et\nu}{(1 - \nu^2)} \quad (2.24)$$

For plane strain condition, the same procedure is valid and equating Equations (2.9) and (2.10b) and substituting the elasticity tensor components given in Equations (2.11)-(2.15), the spring stiffness constants are simplified as given in Equations (2.28)-(2.30).

$$k_n = \frac{Et}{(1 + \nu)s} \quad (2.25)$$

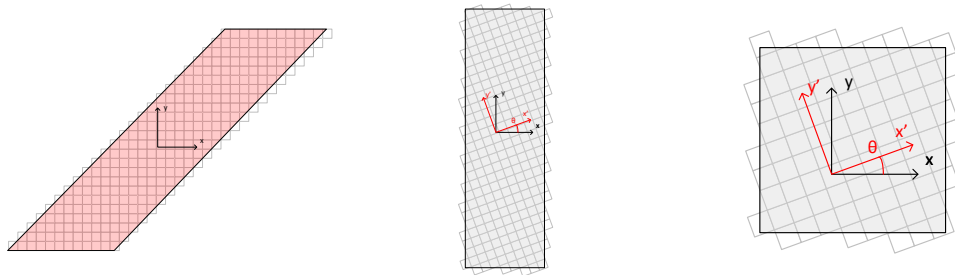
$$k_s = \frac{Et(1 - 4\nu)}{(1 + \nu)(1 - 2\nu)s} \quad (2.26)$$

$$k_{nd} = \frac{Et\nu}{(1 + \nu)(1 - 2\nu)} \quad (2.27)$$

The formulations, as given above, enable the representation of Poisson's ratio in AEM, in contrast to other techniques based on discrete elements which simulate the deformation fields for continuous media without rigorous consideration of the Poisson effect; the effect of Poisson's ratio is often ignored, or the technique involves an intrinsic Poisson ratio assumption. The proof of the representation of Poisson's effect in any direction within the continuum is presented in the next section.

### 2.3.2 Stress Tensor in Arbitrary Directions

A major limitation of AEM for the simulation of the mechanics of large, continuum bodies like gravity dam monoliths is the lack of the Poisson's effect. Accordingly, problems may arise while modeling complex geometries, arbitrarily inclined elements, or loading conditions. An inclined monolith formed with applied elements in a classical setting is shown in Figure 2.3a. The square elements are always horizontal regardless of the component shape or size; while leading to ease of discretization, this setup leads to directionality in the model for component angles between  $0^\circ$  and  $90^\circ$ . For elements of acceptably small sizes, the model of a column, as given in Figure 2.3b, should yield similar results regardless of the element orientations, i.e., the plane stress conditions should be satisfied irrespective of the elements' angles. A rigorous proof of close form approximation of the exact plane stress elasticity condition requires the elasticity tensor for the methodology to be obtained for arbitrary rotations of the Cartesian coordinates as well for general loading conditions, i.e., independently for normal and shear dominated problems. This condition is checked for the modified methodology using the generic setup given in Figure 2.3c showing the spring stiffness constants obtained in the preceding section meet the plane stress condition regardless of the direction for small element sizes. The modification enables modeling Poisson's ratio irrespective of the direction; the proofs under tensile and shear loadings are presented in the following sections, respectively.

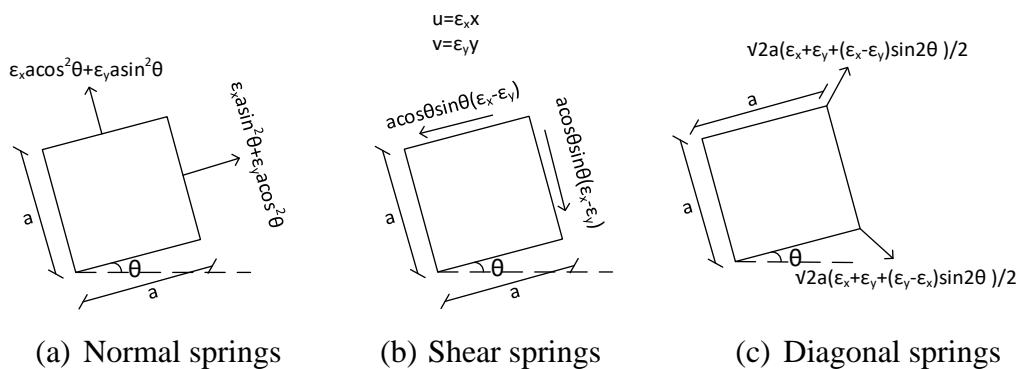


(a) An inclined monolith with applied elements      (b) A column with inclined AEs      (c) A domain with arbitrarily inclined modified AEs

Figure 2.3 Directionality and elements' orientation for applied element models

### 2.3.2.1 Tensile Loading in Both Directions

A domain under bi-directional tensile loading was assumed to be modeled as given in Figure 2.3c with a rotated configuration of modified applied elements which make an angle  $\theta$  from the horizontal  $x$ -direction. For pure tensile loading in the horizontal ( $x$ ) and vertical ( $y$ ) directions, the strain field at any point in the body is assumed to be expressed conventionally in terms of the strains  $\epsilon_x$  and  $\epsilon_y$ , respectively. For this strain field, the displacements imposed on the springs of a single element of size 'a' and unit thickness is presented in Figure 2.4. For simplicity, a single normal-shear spring pair is assumed between the elements.



(a) Normal springs      (b) Shear springs      (c) Diagonal springs

Figure 2.4 Displacements of springs due to tensile loading in  $x$  and  $y$  directions

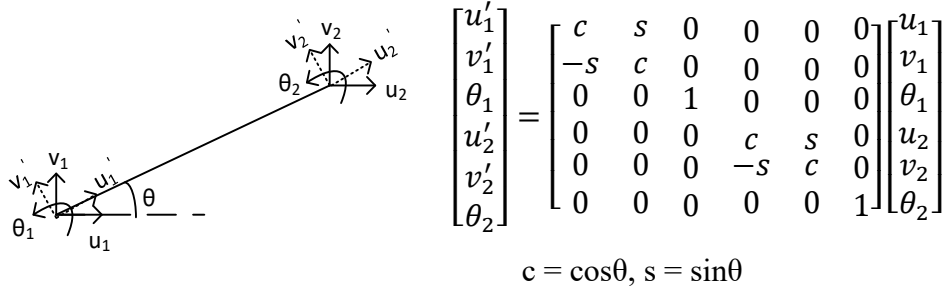


The displacements in global coordinates,  $\mathbf{u}_{global}$ , are transformed into the local coordinate system ( $\mathbf{u}_{local}$ ) via the rotation matrix,  $\mathbf{R}$  (Equation (2.5)), as presented in Equation (2.28) and Figure 2.5. The local forces in springs are then obtained by Equation (2.29).

$$\mathbf{u}_{local} = \mathbf{R}\mathbf{u}_{global} \quad (2.28)$$

$$\mathbf{k}_{el}\mathbf{u}_{local} = \mathbf{F}_{local} \quad (2.29)$$

$$\mathbf{k}_{el}\mathbf{R}\mathbf{u}_{global} = \mathbf{F}_{local}$$



$$\begin{bmatrix} u'_1 \\ v'_1 \\ \theta'_1 \\ u'_2 \\ v'_2 \\ \theta'_2 \end{bmatrix} = \begin{bmatrix} c & s & 0 & 0 & 0 & 0 \\ -s & c & 0 & 0 & 0 & 0 \\ 0 & 0 & 1 & 0 & 0 & 0 \\ 0 & 0 & 0 & c & s & 0 \\ 0 & 0 & 0 & -s & c & 0 \\ 0 & 0 & 0 & 0 & 0 & 1 \end{bmatrix} \begin{bmatrix} u_1 \\ v_1 \\ \theta_1 \\ u_2 \\ v_2 \\ \theta_2 \end{bmatrix}$$

c = cos $\theta$ , s = sin $\theta$

(a) Local and global displacements

(b) Rotation matrix

Figure 2.5 Local displacements of springs

Under the implied strains on this element, the potential energy,  $U$ , stored in the normal ( $U_{normal}$ ), shear ( $U_{shear}$ ) and the diagonal springs ( $U_{diagonal}$ ) around the element can be calculated from Equations (2.30)-(2.32).

$$U_{normal} = \frac{1}{2} k_n a^2 \left[ (\varepsilon_x \cos^2 \theta + \varepsilon_y \sin^2 \theta)^2 + (\varepsilon_x \sin^2 \theta + \varepsilon_y \cos^2 \theta)^2 \right] \quad (2.30)$$

$$U_{shear} = \frac{1}{2} k_s a^2 \left( \frac{\sin 2\theta}{2} (\varepsilon_x - \varepsilon_y) \right)^2 \quad (2.31)$$

$$U_{diagonal} = \frac{1}{2} k_{nd} \frac{a^2}{2} \left[ (\varepsilon_x + \varepsilon_y + (\varepsilon_x - \varepsilon_y) \sin 2\theta)^2 + (\varepsilon_x + \varepsilon_y + (\varepsilon_y - \varepsilon_x) \sin 2\theta)^2 \right] \quad (2.32)$$

The total potential energy,  $U_{total}$ , is obtained by summing up the energy stored in three types of springs as given below in a simplified form (Equation (2.33)).

$$\begin{aligned}
U_{total} &= U_{normal} + U_{shear} + U_{diagonal} \\
U_{total} &= \frac{1}{2} k_n a^2 \left[ \varepsilon_x^2 + \varepsilon_y^2 - \frac{\sin^2 2\theta}{2} (\varepsilon_x - \varepsilon_y)^2 \right] \\
&\quad + \frac{1}{4} k_s a^2 \sin^2 2\theta (\varepsilon_x - \varepsilon_y)^2 \\
&\quad + \frac{1}{2} k_{nd} a^2 \left[ (\varepsilon_x + \varepsilon_y)^2 + (\varepsilon_x - \varepsilon_y)^2 \sin^2 2\theta \right]
\end{aligned} \tag{2.33}$$

The first derivative of potential energy with respect to strain yields stress terms. Assuming a unit size for the element as 1, the partial derivatives of the total potential energy are obtained in x- and y-directions yielding  $\sigma_x$  and  $\sigma_y$ , respectively, shown in Equation (2.34) and Equation (2.35).

$$\begin{aligned}
\sigma_x = \frac{\partial U_{total}}{\partial \varepsilon_x} &= \varepsilon_x \left[ k_n \left( 1 - \frac{\sin^2 2\theta}{2} \right) + k_s \frac{\sin^2 2\theta}{2} + k_{nd} (1 + \sin^2 2\theta) \right] \\
&\quad + \varepsilon_y \left[ k_n \left( \frac{\sin^2 2\theta}{2} \right) - k_s \frac{\sin^2 2\theta}{2} + k_{nd} (1 - \sin^2 2\theta) \right] \\
&= \varepsilon_x a_{11} + \varepsilon_y a_{12}
\end{aligned} \tag{2.34}$$

$$\begin{aligned}
\sigma_y = \frac{\partial U_{total}}{\partial \varepsilon_y} &= \varepsilon_x \left[ k_n \left( \frac{\sin^2 2\theta}{2} \right) - k_s \frac{\sin^2 2\theta}{2} + k_{nd} (1 - \sin^2 2\theta) \right] \\
&\quad + \varepsilon_y \left[ k_n \left( 1 - \frac{\sin^2 2\theta}{2} \right) + k_s \frac{\sin^2 2\theta}{2} + k_{nd} (1 + \sin^2 2\theta) \right] \\
&= \varepsilon_x b_{11} + \varepsilon_y b_{12}
\end{aligned} \tag{2.35}$$

The stress-strain relation is expressed in terms of multipliers of  $\varepsilon_x$  and  $\varepsilon_y$  depending on the spring stiffness and element orientation,  $\theta$ , as given above. Inserting the spring stiffness constants from the previous section (Equations (2.22)-(2.24)), the elasticity tensor should be obtained irrespective of angle  $\theta$ . In order to obtain Hooke's Law, these multipliers should be independent of orientation. The

coefficients  $a_{11}$  and  $a_{12}$  of stress terms  $\varepsilon_x$  and  $\varepsilon_y$  for Equation (2.34) are simplified using the spring constants from before in Equations (2.36)-(2.37). The use of trigonometric identities yields orientation independent stress values. The symmetric components of stress tensor for Equation (2.35) is obtained in a similar fashion in Equations (2.38)-(2.39). The coefficients obtained in these below equations are consistent with Hooke's Law (Equation (2.10a)) and are not dependent on element orientation  $\theta$ .

$$\begin{aligned}
a_{11} &= k_n \left( 1 - \frac{\sin^2 2\theta}{2} \right) + k_s \frac{\sin^2 2\theta}{2} + k_{nd}(1 + \sin^2 2\theta) \\
&= \frac{E(1-\nu)}{1-\nu^2} \left( 1 - \frac{\sin^2 2\theta}{2} \right) + \frac{E(1-3\nu)}{1-\nu^2} \frac{\sin^2 2\theta}{2} + \frac{E\nu}{1-\nu^2} (1 + \sin^2 2\theta) \quad (2.36) \\
&= \frac{E}{1-\nu^2}
\end{aligned}$$

$$\begin{aligned}
a_{12} &= k_n \frac{\sin^2 2\theta}{2} - k_s \frac{\sin^2 2\theta}{2} + k_{nd}(1 + \sin^2 2\theta) \\
&= \frac{E(1-\nu)\sin^2 2\theta}{2(1-\nu^2)} - \frac{E(1-3\nu)}{1-\nu^2} \frac{\sin^2 2\theta}{2} + \frac{E\nu(1-\sin^2 2\theta)}{1-\nu^2} \quad (2.37) \\
&= \frac{E\nu}{1-\nu^2}
\end{aligned}$$

$$\begin{aligned}
b_{11} &= k_n \frac{\sin^2 2\theta}{2} - k_s \frac{\sin^2 2\theta}{2} + k_{nd}(1 - \sin^2 2\theta) \\
&= \frac{E(1-\nu)\sin^2 2\theta}{2(1-\nu^2)} - \frac{E(1-3\nu)}{1-\nu^2} \frac{\sin^2 2\theta}{2} + \frac{E\nu(1-\sin^2 2\theta)}{1-\nu^2} \quad (2.38) \\
&= \frac{E\nu}{1-\nu^2}
\end{aligned}$$

$$\begin{aligned}
b_{12} &= k_n \left( 1 - \frac{\sin^2 2\theta}{2} \right) + k_s \frac{\sin^2 2\theta}{2} + k_{nd}(1 + \sin^2 2\theta) \\
&= \frac{E(1-\nu)}{1-\nu^2} \left( 1 - \frac{\sin^2 2\theta}{2} \right) + \frac{E(1-3\nu)}{1-\nu^2} \frac{\sin^2 2\theta}{2} + \frac{E\nu}{1-\nu^2} (1 + \sin^2 2\theta) \quad (2.39) \\
&= \frac{E}{1-\nu^2}
\end{aligned}$$

### 2.3.2.2 Shear Loading

Uniform shear strain,  $\gamma$ , was applied to the same model formed with modified applied elements at an angle of  $\theta$  from the horizontal x-direction (Figure 2.3c). The displacements imposed on the springs of a single element for this strain field is presented in Figure 2.6. Similar to the previous loading, the element's side length is 'a', unit thickness is assumed, and in between the elements, 1 normal-shear spring pair is modeled for simplicity. As before, the potential energy,  $U$ , stored in the normal ( $U_{normal}$ ), shear ( $U_{shear}$ ) and the diagonal springs ( $U_{diagonal}$ ) around the element are calculated as shown in Equations (2.40)-(2.42).

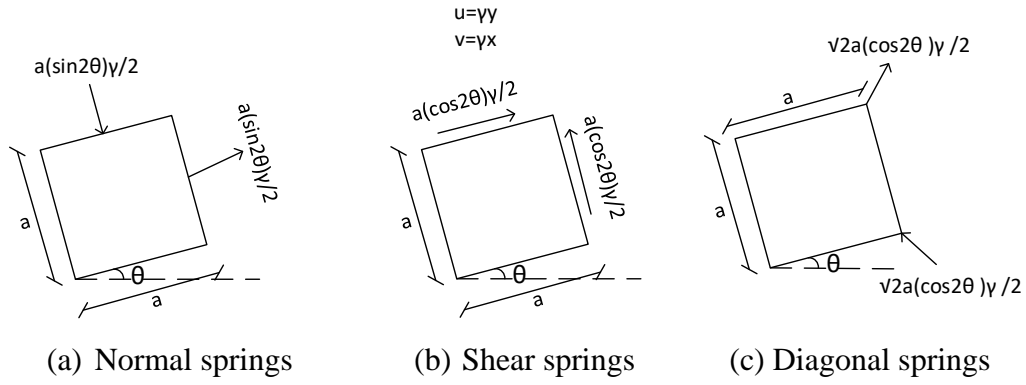


Figure 2.6 Displacements of springs due to shear loading

$$U_{normal} = \frac{1}{2} k_n a^2 \frac{\gamma^2}{4} (\sin^2 2\theta) 2 \quad (2.40)$$

$$U_{shear} = \frac{1}{2} k_s a^2 \frac{\gamma^2}{4} (\cos^2 2\theta) 2 \quad (2.41)$$

$$U_{diagonal} = \frac{1}{2} k_{nd} 2a^2 \frac{\gamma^2}{4} (\cos^2 2\theta) 2 \quad (2.42)$$

The total potential energy,  $U_{total}$ , is presented in Equation (2.43). The shear stress,  $\tau$ , is obtained by taking the first derivative of total potential energy with respect to

the shear strain,  $\gamma$  (Equation (2.44)). Substituting the spring stiffness constants (Equations (2.22)-(2.24)), assuming an element of unit size and making the necessary trigonometric simplifications, the following equation, consistent with Hooke's Law, can be obtained (Equation (2.45)). As before, the shear stress term is independent of the element orientation  $\theta$ , satisfying the plane stress conditions.

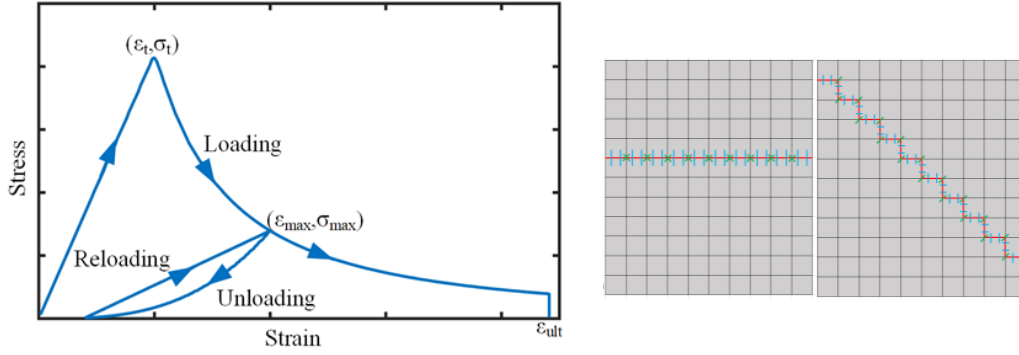
$$U_{total} = \frac{1}{4}k_n a^2 \gamma^2 (\sin^2 2\theta) + \frac{1}{4}k_s a^2 \gamma^2 (\cos^2 2\theta) + \frac{1}{2}k_{nd} a^2 \gamma^2 (\cos^2 2\theta) \quad (2.43)$$

$$\tau = \frac{\partial U_{total}}{\partial \gamma} = \frac{\gamma a^2}{2} (k_n \sin^2 2\theta + k_s \cos^2 2\theta + 2k_{nd} \cos^2 2\theta) \quad (2.44)$$

$$\tau = \frac{\gamma}{2} \left( \frac{E(\sin(2\theta))^2}{(1+\nu)} + \frac{E(1-3\nu)(\cos(2\theta))^2}{(1-\nu^2)} + \frac{2E\nu(\cos(2\theta))^2}{(1-\nu^2)} \right) = \frac{\gamma E}{2(1+\nu)} \quad (2.45)$$

### 2.3.3 Theory and Formulation for Cracked Media

The proper representation of strain energy in the elastic domain with the modified formulation is shown in the previous section. For modeling the complete range of behavior of brittle solids, the formulation should also be able to represent the fracture phenomena and fracture energy to avoid mesh dependence. A state of the art material model (Maekawa et al., 2003) is implemented for modeling the cracking of such brittle solids using the modified applied elements by introducing tension softening to the horizontal, vertical, and diagonal normal springs on the model. A linear elastic response is assumed until the cracking point  $(\varepsilon_t, \sigma_t)$ , and upon the exceedance of this limit, the loading curve has an exponential form. The unloading portion is also nonlinear, and reloading is a straight line between the initiation of the reloading point and the past maximum strain  $(\varepsilon_{max}, \sigma_{max})$  point (Figure 2.7a). The loading, unloading, and reloading portions are defined by Equations (2.46)-(2.48), respectively.



(a) Tensile behavior

(b) Crack orientation

Figure 2.7 Maekawa tension softening model and fracture energy

Loading:  $\epsilon > \epsilon_{max}$

$$\sigma = \begin{cases} \frac{\sigma_t}{\epsilon_t} \epsilon & \text{if } \epsilon \leq \epsilon_t \\ \sigma_t \left( \frac{\epsilon_t}{\epsilon} \right)^c & \text{if } \epsilon_t < \epsilon < \epsilon_{ult} \\ 0 & \text{if } \epsilon \geq \epsilon_{ult} \end{cases} \quad (2.46)$$

Unloading:  $\epsilon \leq \epsilon_{max}$  and  $\epsilon \leq \epsilon_0$

$$\sigma = E_{ul} \epsilon \alpha \quad (2.47)$$

where

$$E_{ul} = \frac{\sigma_{max}}{\epsilon_{max}} \text{ and } \alpha = \left( \frac{\sigma_0}{E_{ul} \epsilon} \right) \left( \frac{\epsilon}{\epsilon_0} \right)^3$$

Reloading:  $\epsilon \leq \epsilon_{max}$  and  $\epsilon > \epsilon_0$

$$\sigma = \sigma_{max} - (\sigma_{max} - \sigma_0) \left( \frac{\epsilon_{max} - \epsilon}{\epsilon_{max} - \epsilon_0} \right) \quad (2.48)$$

where  $\epsilon$  is the concrete tensile strain,  $\sigma$  is the corresponding tensile stress,  $\sigma_t$  is uniaxial tensile strength and  $\epsilon_t$  is the cracking strain. The softening parameter  $c$  defines the post-peak behavior in the tensile region.  $\epsilon_{max}$  represents the maximum tensile strain ever experienced with the corresponding tensile stress  $\sigma_{max}$ . The current stress and strain are expressed as  $\sigma_0$  and  $\epsilon_0$ , respectively, and the unloading stiffness is given by  $E_{ul}$  times the stiffness parameter  $\alpha$ .

Compressive behavior is assumed as linear for all springs. For the shear springs, on the other hand, a brittle behavior depending on the normal spring couple is defined. In this brittle behavior, when the normal spring pair reaches the nonlinear loading part (i.e., when tensile strain exceeds  $\varepsilon_t$ ), it is assumed that the shear spring pair can no longer carry any force or contribute to the stiffness of the system.

In contrast to finite element-based techniques, where mesh independence in smeared crack models requires fracture energy computation for elements, fracture energy is computed on discrete paths in this model. This is done for two idealized crack paths, a horizontal and a 45° inclined crack, on a continuum separately. In the fracture energy calculations, the normal (horizontal and/or vertical) and diagonal springs are considered, while the shear springs are ignored for simplicity (Figure 2.7b). The corresponding fracture energy value is mesh dependent: mesh independence of the models is assured by the selection of the softening parameter,  $c$ , and the ultimate tensile strain limit,  $\varepsilon_{ult}$ , to obtain the required fracture energy in accordance with the element size.

The calculation of fracture energy at each normal and diagonal spring requires the stress-strain curve based on the Maekawa material model to be converted into a force-displacement relationship. It should be noted that the strain-displacement and stress-force relations vary for normal and diagonal springs since their lengths and the tributary area are different. For an element with side length  $a$ , a uniform strain  $\varepsilon$  on the crack plane leads to local normal,  $u_n$  and diagonal displacements,  $u_d$  as given in Equation (2.49). The corresponding forces in the normal and diagonal springs,  $F_n$  and  $F_d$ , respectively, are calculated as follows (Equation (2.50)), where  $t$ ,  $s$  and  $\nu$  represent the model thickness, the number of connecting spring pairs between two rigid elements and the Poisson's ratio, respectively.

$$u_n = \varepsilon a \text{ and } u_d = \varepsilon a \sqrt{2} \quad (2.49)$$

$$F_n = \sigma \frac{at}{(1+\nu)s} \text{ and } F_d = \sigma \frac{a\sqrt{2}t\nu}{(1-\nu^2)} \quad (2.50)$$

After the calculation of the total area under the force-displacement curves of the normal and diagonal springs at the crack plane, the fracture energy on the crack plane  $G_f$  is obtained by dividing this total energy with the cross-sectional area at the crack plane. The fracture energy values for the horizontal and 45° inclined cracks are obtained (Equations (2.51) and (2.52), respectively) in terms of the element size, a Poisson's ratio,  $\nu$  along with the Maekawa tension model parameters  $\varepsilon_t$ ,  $\varepsilon_{ult}$ ,  $\sigma_t$  and  $c$ .

$$G_f = \left( \frac{\varepsilon_t \sigma_t}{2} + \frac{\varepsilon_t \sigma_t - \varepsilon_f \sigma_t \left( \frac{\varepsilon_t}{\varepsilon_f} \right)^c}{c - 1} \right) \left( \frac{a}{(1 + \nu)} + \frac{4a\nu}{(1 - \nu^2)} \right) \quad (2.51)$$

$$G_f = \left( \frac{\varepsilon_t \sigma_t}{2} + \frac{\varepsilon_t \sigma_t - \varepsilon_f \sigma_t \left( \frac{\varepsilon_t}{\varepsilon_f} \right)^c}{c - 1} \right) \left( \frac{a\sqrt{2}}{(1 + \nu)} + \frac{2\sqrt{2}a\nu}{(1 - \nu^2)} \right) \quad (2.52)$$

As given above, the fracture energy terms are obtained somewhat differently for two different crack orientations. While the terms appear different, closed-form calculations for different parameters such as  $\varepsilon_{ult}$ ,  $\sigma_t$ ,  $a$ ,  $\nu$  or  $c$  show that the maximum difference between the fracture energy values of the horizontal and 45° inclined crack cases is 6%; for  $\nu=0.2$ ,  $G_f$  calculated for the inclined crack case is 6% higher than the horizontal case and vice versa when  $\nu=1/3$ , which lies in an acceptable range. It is worth mentioning that the contributions of normal and diagonal springs to the fracture energy is identical for  $\nu=0.2$  for a horizontal crack, i.e.,  $\frac{a}{(1+\nu)} = \frac{4a\nu}{(1-\nu^2)}$ . The same condition is valid when  $\nu=1/3$  for the inclined crack, i.e.,  $\frac{a\sqrt{2}}{(1+\nu)} = \frac{2\sqrt{2}a\nu}{(1-\nu^2)}$ .



### 2.3.4 Mass and Damping Matrices

For problems in the dynamic setting, the mass and damping matrices are also required to be set up. The mass matrix of a single rigid element is calculated by assuming that the element mass and inertia are lumped at the centroid of the element for each degree of freedom (Tagel-Din & Meguro, 2000). For the square element with side length,  $a$ , thickness,  $t$ , and density,  $\rho$ , the local element mass matrix,  $\mathbf{m}_{el}$ , is obtained as in Equation (2.53) in matrix format. The first and second diagonal terms,  $m_{11}$  and  $m_{22}$ , of the mass matrix represent the element mass in horizontal and vertical directions, respectively. The last diagonal term,  $m_{33}$ , corresponds to the rotational moment of inertia with respect to the centroid. The global mass matrix is assembled similarly to the assembly of the global stiffness matrix (Equation (2.5)).

$$\mathbf{m}_{el} = \begin{bmatrix} a^2 t \rho & 0 & 0 \\ 0 & a^2 t \rho & 0 \\ 0 & 0 & \frac{a^4 t \rho}{6} \end{bmatrix} \quad (2.53)$$

Rayleigh damping is implemented to obtain the global damping matrix,  $\mathbf{C}$  (Chopra, 2015). In this methodology, the damping matrix is calculated by the summation of the global mass matrix,  $\mathbf{M}$ , and the global stiffness matrix,  $\mathbf{K}$ , that are multiplied by scalar coefficients  $\alpha$  and  $\beta$ , respectively (Equation (2.54)). The coefficients  $\alpha$  and  $\beta$  are computed such that the system will have the desired damping ratio,  $\xi$ , at the selected frequencies,  $\omega$ . The damping ratio,  $\xi$ , at the selected frequency,  $\omega$ , in terms of  $\alpha$  and  $\beta$  are calculated as in Equation (2.55). Then, two damping ratios  $\xi_1$  and  $\xi_2$  are selected at different frequencies  $\omega_1$  and  $\omega_2$ , and the coefficients  $\alpha$  and  $\beta$  are computed from Equation (2.56). It is a common practice to specify 5% damping ratio at the first and third modes of a regular concrete structure (Smyrou et al., 2011).

$$\mathbf{C} = \alpha \mathbf{M} + \beta \mathbf{K} \quad (2.54)$$

$$\xi = \frac{1}{2} \left( \frac{\alpha}{\omega} + \beta \omega \right) \quad (2.55)$$

$$\alpha = \frac{2\omega_1\omega_2(\xi_1\omega_2 - \xi_2\omega_1)}{(\omega_2^2 - \omega_1^2)} \quad \beta = \frac{2(\xi_2\omega_2 - \xi_1\omega_1)}{(\omega_2^2 - \omega_1^2)} \quad (2.56)$$

The energy dissipation of a structure due to viscoelastic behavior is the basis of the Rayleigh damping assumptions; however, the energy dissipation due to cracking or hysteretic material behavior is not considered. Still, the viscous damping approximation is shown to be sufficiently accurate (Cook et al., 2001).

## 2.4 Finite Elements for Modeling Fluids

### 2.4.1 Fluid Element Formulation

Reservoir-dam interaction should be properly considered for the accurate seismic simulation of dam systems. This has been recognized early by Westergaard (1933), proposing the added mass approach to represent the hydrodynamic effects on the upstream face of the dam, mimicking the inertial forces of water under seismic loading. Although practical, this approach yields conservative results (Fok & Chopra, 1986a). Effective solution in the elastic domain using boundary element and sub-structuring techniques was proposed by Fenves & Chopra (1985) and Hall & Chopra (1983). As the time-domain modeling of the interaction of fluids and structures became important, several fluid finite elements based on displacement formulations were developed by researchers. One of the most widely used elements in the literature is based on a pure displacement formulation (Wilson & Khalvati, 1983). These elements often suffer zero-energy modes since they do not satisfy the so-called inf-sup condition due to the high Poisson's ratio. A mixed displacement/pressure based finite element formulation eliminating the spurious zero-energy modes by fulfilling the inf-sup condition was developed by Wang & Bathe (1997). No interface elements are required at the dam-reservoir boundary

using these elements; the displacement and pressure fields in the reservoir are obtained directly. Given the advantages, in this study, the modified applied elements are coupled with displacement/pressure based mixed finite elements proposed by Wang & Bathe (1997).

#### 2.4.2 Displacement/Pressure Based Mixed Finite Element Formulation

The variational formulation,  $\Pi$ , according to the Hu-Washizu principle, is defined in Equation (2.57).

$$\Pi = \int_V \left[ \frac{p^2}{2\beta} - \mathbf{u} \cdot \mathbf{f}^B - \lambda_p \left( \frac{p}{\beta} + \nabla \cdot \mathbf{u} \right) \right] dV + \int_S \bar{p} u_n^S dS \quad (2.57)$$

where  $p$  is pressure,  $\beta$  is the bulk modulus,  $\mathbf{u}$  is displacement,  $\mathbf{f}^B$  is body force,  $\lambda_p$  is Lagrange multiplier,  $\bar{p}$  is pressure on the boundary and  $u_n^S$  is the normal displacement acting on the boundary. While the first part of this equation represents the strain energy in terms of pressure, the second part corresponds to the potential of external body forces, including gravitational effects. In the third part, the constitutive relation is presented, and the last part is the pressure acting on the boundary,  $S$ .

When the Lagrange multiplier is defined as the pressure, the stationarity of Equation (2.57) is imposed together with specifying the governing equation as  $\mathbf{f}^B = -\rho\ddot{\mathbf{u}}$ , conservation of momentum and mass equations are obtained as given in Equation (2.58) and Equation (2.59), respectively.

$$\nabla p + \rho\ddot{\mathbf{u}} = \mathbf{0} \quad (2.58)$$

$$\nabla \cdot \mathbf{u} + \frac{p}{\beta} = 0 \quad (2.59)$$

where  $\rho$  is density, and  $\ddot{\mathbf{u}}$  is acceleration.

The boundary conditions on displacement and pressure boundaries are defined in Equation (2.60).

$$\begin{aligned} \mathbf{u} \cdot \mathbf{n} &= \bar{u}_n \text{ on } S_u \\ p &= \bar{p} \text{ on } S_f \end{aligned} \quad (2.60)$$

If the surface gravity wave effects are ignored, the pressure  $\bar{p}$  is considered as zero on the free surface.

The formulation presented above is utilized in finite element by applying Galerkin discretization to displacement and pressure (Equation (2.61)).

$$\begin{aligned} \mathbf{u} &= \mathbf{H}\hat{\mathbf{U}} \\ p &= \mathbf{H}_p\hat{\mathbf{P}} \\ \nabla \cdot \mathbf{u} &= (\nabla \cdot \mathbf{H})\hat{\mathbf{U}} = \mathbf{B}\hat{\mathbf{U}} \end{aligned} \quad (2.61)$$

where  $\mathbf{H}$  and  $\mathbf{H}_p$  are the interpolation matrices of displacement and pressure, respectively,  $\hat{\mathbf{U}}$  and  $\hat{\mathbf{P}}$  are the solution vectors of displacement and pressure, respectively. Displacement/pressure based mixed finite element formulation in matrix format is presented in Equation (2.62).

$$\begin{bmatrix} \mathbf{M} & \mathbf{0} \\ \mathbf{0} & \mathbf{0} \end{bmatrix} \begin{bmatrix} \hat{\mathbf{U}} \\ \hat{\mathbf{P}} \end{bmatrix} + \begin{bmatrix} \mathbf{K}_{uu} & \mathbf{K}_{up} \\ \mathbf{K}_{pu} & \mathbf{K}_{pp} \end{bmatrix} \begin{bmatrix} \hat{\mathbf{U}} \\ \hat{\mathbf{P}} \end{bmatrix} = \begin{bmatrix} \mathbf{R} \\ \mathbf{0} \end{bmatrix} \quad (2.62)$$

The terms in the above equations are calculated by Equations (2.63)-(2.67).

$$\mathbf{M} = \int_V \rho \mathbf{H}^T \mathbf{H} dV \quad (2.63)$$

$$\mathbf{K}_{uu} = \int_V \mathbf{B}_D^T \mathbf{C}' \mathbf{B}_D dV \quad (2.64)$$

$$\mathbf{K}_{up} = \mathbf{K}_{pu}^T = - \int_V \mathbf{B}^T \mathbf{H}_p dV \quad (2.65)$$

$$\mathbf{K}_{pp} = - \int_V \frac{1}{\beta} \mathbf{H}_p^T \mathbf{H}_p dV \quad (2.66)$$

$$\mathbf{R} = - \int_S \mathbf{H}_n^{S^T} \bar{\rho} dS \quad (2.67)$$

It is important to note here that in the  $\mathbf{K}_{uu}$  term of the stiffness matrix, the deviatoric part of  $\mathbf{B}$  (i.e., the derivatives of interpolation/shape functions), denoted as  $\mathbf{B}_D$  is used, and  $\mathbf{C}'$  is the stress-strain matrix for the deviatoric stress and strain components (Bathe, 1996). For a finite bulk modulus, the pressure unknowns can be statically condensed out to simplify the solution of the equation (Equation (2.68)).

$$\mathbf{M}_{uu} \hat{\mathbf{U}} + \mathbf{S}_{uu} \hat{\mathbf{U}} = \mathbf{R} \quad (2.68)$$

where  $\mathbf{S}_{uu}$  is calculated as  $\mathbf{S}_{uu} = -\mathbf{K}_{up} \mathbf{K}_{pp}^{-1} \mathbf{K}_{pu}$ .

For an almost incompressible material (i.e., positive bulk,  $\beta$ , and shear modulus,  $G$ , with  $\beta \gg G$ ), the displacement/pressure based mixed formulation fulfills the inf-sup condition eliminating the spurious zero-energy modes (Wang & Bathe, 1997).

The implemented 2D displacement/pressure based mixed finite element is presented in Figure 2.8 (Figure from (Özmen, 2016)). In this figure, the nine displacement degrees of freedom are marked with circles, while the three pressure degrees of freedom are shown with triangles.

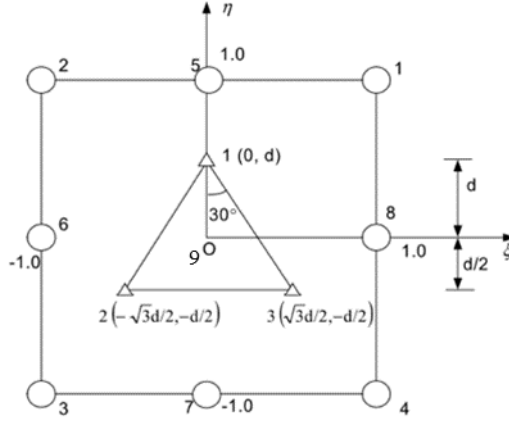


Figure 2.8 Mixed finite element (Özmen, 2016)

The shape functions,  $\mathbf{H}$ , for the displacement degrees of freedom are presented in Equation (2.69).

$$\begin{aligned}
 H_1 &= \frac{1}{4}(\xi^2 + \xi)(\eta^2 + \eta) & H_5 &= \frac{1}{2}(1 - \xi^2)(\eta^2 + \eta) \\
 H_2 &= \frac{1}{4}(\xi^2 - \xi)(\eta^2 + \eta) & H_6 &= \frac{1}{2}(\xi^2 - \xi)(1 - \eta^2) \\
 H_3 &= \frac{1}{4}(\xi^2 - \xi)(\eta^2 - \eta) & H_7 &= \frac{1}{2}(1 - \xi^2)(\eta^2 - \eta) \\
 H_4 &= \frac{1}{4}(\xi^2 + \xi)(\eta^2 - \eta) & H_8 &= \frac{1}{2}(\xi^2 + \xi)(1 - \eta^2) \\
 & & H_9 &= (1 - \xi^2)(1 - \eta^2)
 \end{aligned} \tag{2.69}$$

For the pressure degrees of freedom, areal coordinates are utilized. The coordinates  $(\xi, \eta)$  of pressure degrees of freedom and the shape functions ( $\mathbf{H}^p$ ) for  $d=0.5$  are given in Equation (2.70) and Equation (2.71), respectively.

$$(\xi_1, \eta_1) = (0, d) \tag{2.70}$$

$$\begin{aligned}
(\xi_2, \eta_2) &= \left( -\frac{\sqrt{3}d}{2}, -\frac{d}{2} \right) \\
(\xi_3, \eta_3) &= \left( \frac{\sqrt{3}d}{2}, -\frac{d}{2} \right) \\
H_1^p &= \frac{4}{3}\eta + \frac{1}{3} \\
H_2^p &= -\frac{2}{\sqrt{3}}\xi - \frac{2}{3}\eta + \frac{1}{3} \\
H_3^p &= \frac{2}{\sqrt{3}}\xi - \frac{2}{3}\eta + \frac{1}{3}
\end{aligned} \tag{2.71}$$

All the integrations are conducted by utilizing the 2x2 Gauss-Quadrature scheme. The integrals are mapped into the natural coordinate system, as illustrated for  $\mathbf{K}_{uu}$  in Equation (2.72), with  $t$  indicating the element thickness. The integral points and weights used in this study are tabulated in Table 2.2 (Bathe, 1996).

$$\mathbf{K}_{uu} = \int_V \mathbf{B}_D^T \mathbf{C}' \mathbf{B}_D dV = t \int_{-1}^1 \int_{-1}^1 \mathbf{B}_D^T \mathbf{C}' \mathbf{B}_D \det \mathbf{J} d\xi d\eta \tag{2.72}$$

Table 2.2 Integral points and weights

$\xi$	$\eta$	weight
$\mp \frac{1}{\sqrt{3}}$	$\mp \frac{1}{\sqrt{3}}$	1

### 2.4.3 Radiation Boundary Condition

For the analysis of dam-reservoir systems in the time domain, a radiation boundary condition is employed at the far end of the reservoir to account for the radiating waves. This boundary condition introduces damping to the system; hence, loss of

energy can be modeled by the outgoing waves (Küçükarslan et al., 2005). In this study, Sommerfeld radiation boundary condition is employed (Sommerfeld, 1949). Under horizontal ground acceleration, with the introduction of this boundary condition, the reflection of waves in the upstream boundary in the horizontal direction is prevented. It is a totally absorptive boundary condition with a damping coefficient,  $q_s$  and reflection coefficient,  $\alpha_s$  given in Equation (2.73) (Bouaanani & Lu, 2009).

$$q_s = \frac{1}{C_r}, \alpha_s = 0 \quad (2.73)$$

where  $C_r$  is the acoustic wave speed of water calculated as  $C_r = \sqrt{\beta/\rho}$  with bulk modulus,  $\beta$ , and density,  $\rho$  of water. In order to simulate the Sommerfeld radiation boundary condition, viscous dampers are defined at the far end of the reservoir (Bouaanani & Lu, 2009). If the distance between the two dampers are denoted by  $l^{(e)}$ , then the local damping terms,  $c_1^{(e)}$  and  $c_2^{(e)}$ , of these two successive damper elements are calculated as given in Equation (2.74).

$$c_1^{(e)} = \frac{1}{2}\rho C_r l^{(e)}, c_2^{(e)} = \frac{1}{2}\rho C_r l^{(e)} \quad (2.74)$$

## 2.5 The Developed Software

Within the scope of this research, a computer program is developed in FORTRAN language. The element library consists of the proposed modified applied element methodology together with the displacement/pressure based mixed finite element. In addition to the linear elastic material, the Maekawa tension softening model is also utilized to account for nonlinearities for concrete structures. In the software, a variety of solvers are implemented. This section begins with an explanation of the formulation and flowcharts of the solvers in detail. At the end of the section, the



utilized mass scaling technique and the implemented loading schemes are defined briefly.

## 2.5.1 Solvers

The solution algorithms for static and dynamic problems in the linear and nonlinear settings are presented herein. For the linear transient analysis, both implicit and explicit time-stepping schemes are implemented, and an explicit solver is employed for the solution of nonlinear dynamic problems. Furthermore, information on the solver used for performing modal analysis is given at the end of this section.

### 2.5.1.1 Linear Static Solver

The flowchart of the solution of static linear elastic problems is presented in Figure 2.9. Firstly, the input data such as the coordinates of nodes, element connectivity, the number of connecting spring pairs between the elements, thickness and density of elements, boundary conditions, material properties, loading, solution options, and output data are read. Then, the element stiffness matrix for every connection is calculated in the element stiffness matrix subroutine, and the global stiffness matrix is assembled in a different subroutine. It should be noted that in order to assemble and solve large-scale problems efficiently and fast, the global stiffness matrix is assembled in a compressed sparse row (csr) format. After the assembly of the sparse global stiffness matrix,  $\mathbf{K}_{global}$ , the global load vector,  $\mathbf{F}_{global}$ , is calculated in a subroutine and the global displacements,  $\mathbf{u}_{global}$ , are obtained by the solution of Equation (2.75).

$$\mathbf{F}_{global} = \mathbf{K}_{global}\mathbf{u}_{global} \quad (2.75)$$

For the solution of the above linear system of equations, Intel MKL PARDISO solver is utilized in the developed computer program (PARDISO, 2018). This package

enables the fast, robust, and efficient solution of large sparse linear systems. Firstly, the sparse global stiffness matrix,  $\mathbf{K}_{global}$ , is decomposed into upper and lower triangular matrices by the LU decomposition method. Then, fill-reduction analysis, symbolic factorization, and numeric factorization are performed. As a final step, the global displacements are obtained by forward and backward substitution. In this step, in order to increase the accuracy of the solution, iterative refinement is made.

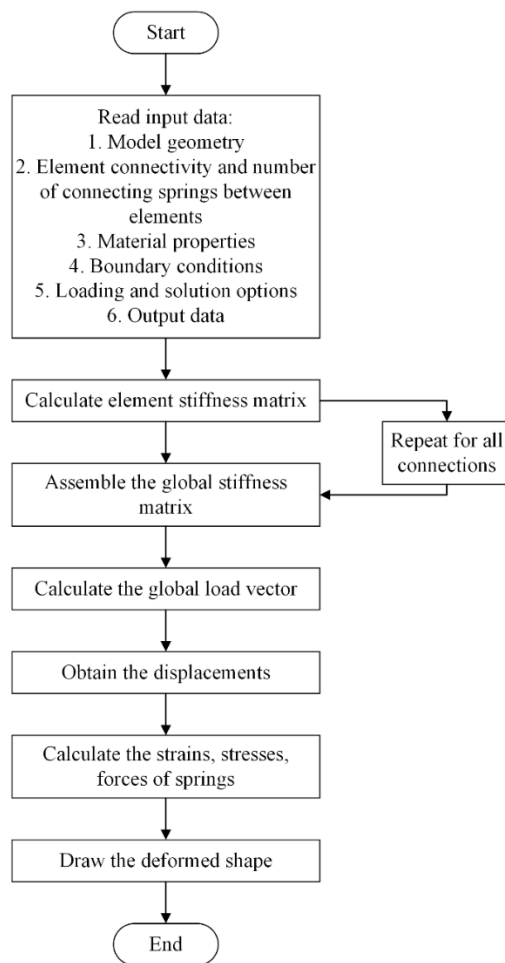


Figure 2.9 Flowchart of linear static analysis

### 2.5.1.2 Nonlinear Static Solver

For solving nonlinear static problems, the regular Newton-Raphson and the Modified Newton-Raphson iteration techniques are implemented. For displacement-based control of the loading in the static analysis, the arc-length method is also implemented. The flowchart of the solution of nonlinear static problems is outlined in Figure 2.10. The solution of incremental equilibrium equation with the Newton-Raphson method is presented in Equation (2.76). A linear approximation to the displacement increment  $\Delta \mathbf{u}$  is obtained using the tangent stiffness matrix  $\mathbf{K}_T$  from the residual force vector defined as the difference between the external applied load  $\mathbf{F}^{ext}$  and the internal resisting force  $\mathbf{F}^{int}$  vectors.

$$\mathbf{K}_T \Delta \mathbf{u} = \mathbf{F}^{ext} - \mathbf{F}^{int} \quad (2.76)$$

In the Newton-Raphson algorithm, incremental displacements,  $\Delta \mathbf{u}$  are obtained by the solution of Equation (2.76). Then, the displacement vector,  $\mathbf{u}$ , is updated  $\mathbf{u} = \mathbf{u} + \Delta \mathbf{u}$ . The convergence is checked by the Frobenius norms of displacement and force, as given in Equation (2.77). If the convergence criteria are not met, i.e., the norms are greater than the specified tolerance, then another iteration is performed. After a converged iteration, the next increment is performed until the load cycle is completed.

$$\begin{aligned} \text{Force norm} &= \frac{\|\mathbf{F}^{ext} - \mathbf{F}^{int}\|}{\|\mathbf{F}^{int}\|} \\ \text{Displacement norm} &= \frac{\|\Delta \mathbf{u}\|}{\|\mathbf{u}\|} \end{aligned} \quad (2.77)$$

Both Newton-Raphson and Modified Newton-Raphson methods are implemented in the software. In the Newton-Raphson method, the stiffness matrix is updated in each iteration, whereas, in the Modified Newton-Raphson algorithm, the tangent stiffness

matrix is calculated either at the beginning of the simulation or only at the beginning of each increment and kept constant through the iterations.

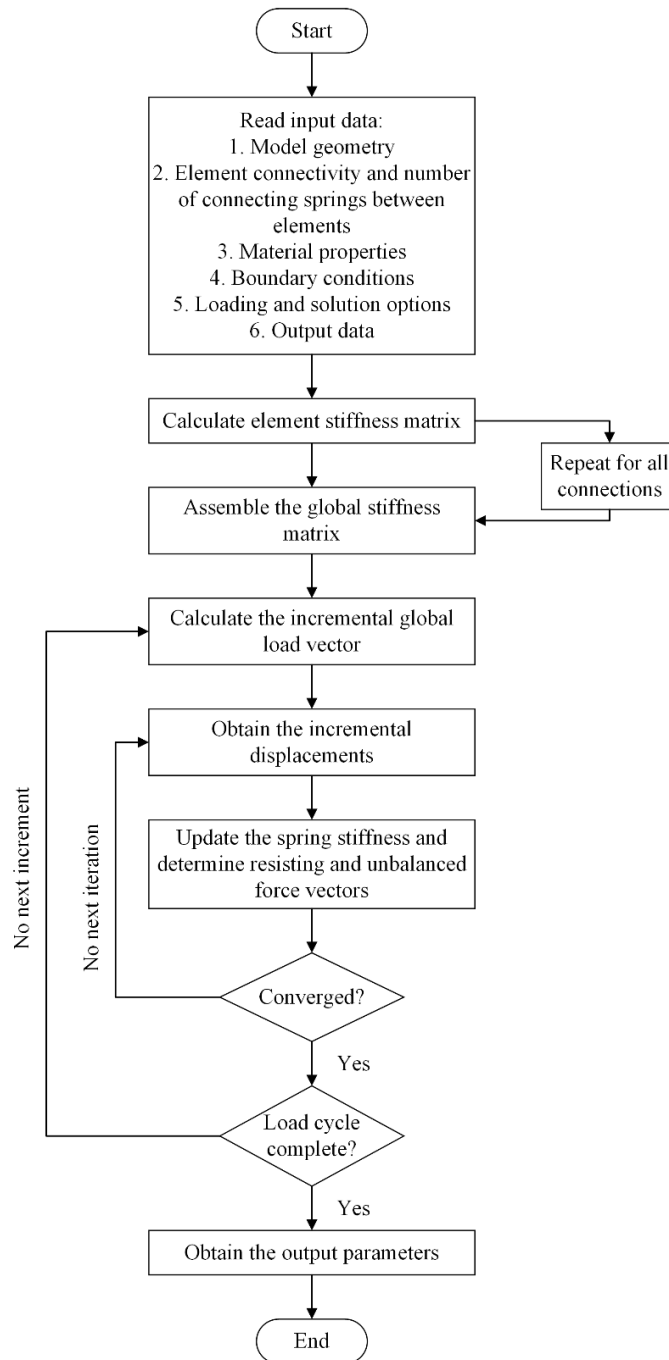


Figure 2.10 Flowchart of nonlinear static analysis

In the Newton family methods, the load factor increment,  $\Delta\lambda$ , is kept constant through the analysis. This condition leads to convergence problems for the simulation of complex behavior in the form of snap-through or snap-back. Accordingly, path following methods are introduced (de Borst et al., 2012). In this study, the arc-length method with updated normal plane is implemented to overcome this difficulty in obtaining the post-peak softening behavior in the brittle medium. In this solution algorithm, the load factor increment,  $\Delta\lambda$ , is considered as an additional unknown; hence, an additional constraint equation (Equation 2.78), with path length increment  $\Delta l$ , is supplied for the solution of the nonlinear system of equations. Although the procedure outlined in Figure 2.10 is still valid, additional computations are performed in the arc-length method during iteration,  $j$  (Equations (2.79)-(2.82)). In its most simple form, the load factor increment can be obtained to retain a fixed displacement increment at a node or between two nodes (also known as crack mode opening displacement), which is generally called the indirect displacement control.

$$g(\mathbf{u}, \Delta\lambda, \Delta\mathbf{u}, \delta\lambda, \Delta l) = 0 \quad (2.78)$$

$$\delta\mathbf{u}_{j+1}^I = \mathbf{K}_j^{-1} \widehat{\mathbf{F}}_{ext} \quad (2.79)$$

$$\delta\mathbf{u}_{j+1}^{II} = \mathbf{K}_j^{-1} (\Delta\lambda_j \widehat{\mathbf{F}}_{ext} - \mathbf{F}_{int,j})$$

$$\delta\lambda_{j+1} = -\frac{(\Delta\mathbf{u}_j)^T \delta\mathbf{u}_{j+1}^{II}}{(\Delta\mathbf{u}_j)^T \delta\mathbf{u}_{j+1}^I} \quad (2.80)$$

$$\Delta\mathbf{u}_{j+1} = \Delta\mathbf{u}_j + \delta\lambda_{j+1} \delta\mathbf{u}_{j+1}^I + \delta\mathbf{u}_{j+1}^{II} \quad (2.81)$$

$$\Delta\lambda_{j+1} = \Delta\lambda_j + \delta\lambda_{j+1} \quad (2.82)$$

In Equation (2.79), displacement prediction,  $\delta\mathbf{u}^I$ , for reference external force,  $\widehat{\mathbf{F}}_{ext}$ , and another displacement prediction,  $\delta\mathbf{u}^{II}$ , under residual force is done for the stiffness,  $\mathbf{K}$  in the iteration. The increment of the load factor increment,  $\delta\lambda_{j+1}$ , is calculated according to the updated normal plane constraint in Equation (2.80), based

on the incremental displacement,  $\Delta \mathbf{u}$ . Then, the incremental displacement and load factor increment are updated in Equation (2.81) and Equation (2.82), respectively.

In case of a physical nonlinearity such as damage or plasticity, instead of a global constraint equation, a constraint directly on the crack opening displacement can be used. If the nodes at both sides of a notch are labeled as  $m$  and  $n$ , then the constraint condition is given in Equation (2.83) (de Borst et al., 2012).

$$\delta u_m - \delta u_n = 0 \quad (2.83)$$

### 2.5.1.3 Linear Dynamic Solver

In Figure 2.11, the flowchart of the solution of linear problems in the dynamic setting is given. After the input data are read, element stiffness and mass matrices are calculated and assembled into global matrices in sparse format. If there exists a static loading before the transient analysis, such as self-weight, first, the static solution is performed, and the outputs are used as initial conditions in the dynamic analysis. If not, then the dynamic solution starts with at-rest initial conditions. Then, the damping matrix is assembled, and the dynamic force vector is calculated for each time step.

The equation of motion (Equation (2.84)) can be solved either with implicit or explicit solution algorithms, and hence, the displacement, velocity, and acceleration vectors are obtained. The solution of the equation of motion is conducted for each time step.

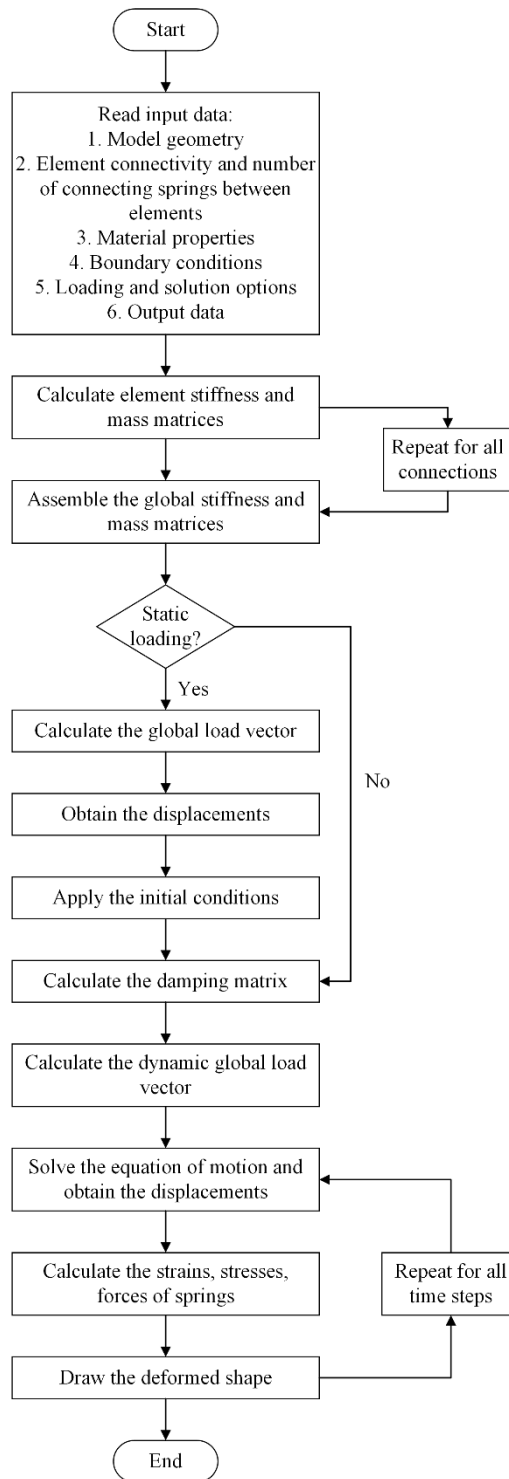


Figure 2.11 Flowchart of linear dynamic analysis

### 2.5.1.3.1 Implicit Solution Algorithm

The Newmark-Beta average acceleration method (Chopra, 2015) is implemented to solve the equation of motion (Equation (2.84)).

$$\mathbf{M}\ddot{\mathbf{u}}(t) + \mathbf{C}\dot{\mathbf{u}}(t) + \mathbf{K}\mathbf{u}(t) = \mathbf{P}(t) \quad (2.84)$$

where  $\mathbf{M}$ ,  $\mathbf{C}$  and  $\mathbf{K}$  are the mass, damping, and stiffness matrix, respectively.  $\ddot{\mathbf{u}}$ ,  $\dot{\mathbf{u}}$ , and  $\mathbf{u}$  are the acceleration, velocity, and displacement vector, respectively.  $\mathbf{P}$  is the dynamic loading vector, and  $t$  represents time.

The solution algorithm for Newmark-Beta average acceleration method ( $\gamma = \frac{1}{2}$ ,  $\beta = \frac{1}{4}$ ) is summarized below in Equation (2.85) (Chopra, 2015). The initial calculations for starting time stepping with selected time step  $\Delta t$  is given as follows:

$$\mathbf{M}\ddot{\mathbf{u}}_0 = \mathbf{P}_0 - \mathbf{C}\dot{\mathbf{u}}_0 - \mathbf{K}\mathbf{u}_0 \quad (2.85a)$$

$$\hat{\mathbf{K}} = \mathbf{K} + \frac{\gamma}{\beta\Delta t}\mathbf{C} + \frac{1}{\beta(\Delta t)^2}\mathbf{M} \quad (2.85b)$$

$$\mathbf{a} = \frac{1}{\beta\Delta t}\mathbf{M} + \frac{\gamma}{\beta}\mathbf{C} \quad \mathbf{b} = \frac{1}{2\beta}\mathbf{M} + \Delta t\left(\frac{\gamma}{2\beta} - 1\right)\mathbf{C} \quad (2.85c)$$

After the initial calculations, at each time step,  $i$ , the solution is obtained by using the dynamic stiffness matrix  $\hat{\mathbf{K}}$  and the equivalent force vector  $\Delta\hat{\mathbf{P}}_i$ . For avoiding iterations, the equations are written in terms of incremental terms. After obtaining the incremental displacement  $\Delta\mathbf{u}_i$  at each time step, velocity and acceleration increments  $\Delta\dot{\mathbf{u}}_i$  and  $\Delta\ddot{\mathbf{u}}_i$  are calculated to reach the current displacement, velocity, and acceleration values given in Equation (2.85h).

$$\Delta\hat{\mathbf{P}}_i = \Delta\mathbf{P}_i + \mathbf{a}\dot{\mathbf{u}}_i + \mathbf{b}\ddot{\mathbf{u}}_i \quad (2.85d)$$

$$\hat{\mathbf{K}}\Delta\mathbf{u}_i = \Delta\hat{\mathbf{P}}_i \quad (2.85e)$$



$$\Delta \dot{\mathbf{u}}_i = \frac{\gamma}{\beta \Delta t} \Delta \mathbf{u}_i - \frac{\gamma}{\beta} \dot{\mathbf{u}}_i + \Delta t \left( 1 - \frac{\gamma}{2\beta} \right) \ddot{\mathbf{u}}_i \quad (2.85f)$$

$$\Delta \ddot{\mathbf{u}}_i = \frac{1}{\beta (\Delta t)^2} \Delta \mathbf{u}_i - \frac{1}{\beta \Delta t} \dot{\mathbf{u}}_i - \frac{1}{2\beta} \ddot{\mathbf{u}}_i \quad (2.85g)$$

$$\mathbf{u}_{i+1} = \mathbf{u}_i + \Delta \mathbf{u}_i \quad \dot{\mathbf{u}}_{i+1} = \dot{\mathbf{u}}_i + \Delta \dot{\mathbf{u}}_i \quad \ddot{\mathbf{u}}_{i+1} = \ddot{\mathbf{u}}_i + \Delta \ddot{\mathbf{u}}_i \quad (2.85h)$$

The equations (2.85a) and (2.85e) are solved via the Intel MKL PARDISO solver. For the Newmark method, the results are stable when the condition in Equation (2.86) is met. For the average acceleration method ( $\gamma = \frac{1}{2}$ ,  $\beta = \frac{1}{4}$ ), the Newmark method is unconditionally stable, with  $T_n$  being the natural period of the structure.

$$\frac{\Delta t}{T_n} \leq \frac{1}{\pi \sqrt{2(\gamma - 2\beta)}} \quad (2.86)$$

### 2.5.1.3.2 Explicit Solution Algorithm

Equation of motion (Equation (2.84)) can also be solved with explicit direct integration methods. The half-time staggered central difference method is implemented in the developed software (Cook et al., 2001). As it is given in Equation (2.54), the damping matrix is a linear combination of mass and stiffness matrices. Therefore, the damping matrix is not diagonal but in a consistent format. The main advantage of the implemented solution algorithm is that the velocity vector is computed at half-time steps, and hence, the inverse of the damping matrix is not computed (Cook et al., 2001). After a brief review of the classical central difference method, the half-time staggered central difference method is presented.

The velocity and acceleration at time step  $i$ , with  $\Delta t$  time step, can be calculated with the classical central difference method (Equations (2.87)-(2.88)).

$$\dot{\mathbf{u}}_i = \frac{1}{2\Delta t} (\mathbf{u}_{i+1} - \mathbf{u}_{i-1}) \quad (2.87)$$

$$\ddot{\mathbf{u}}_i = \frac{1}{\Delta t^2} (\mathbf{u}_{i+1} - 2\mathbf{u}_i + \mathbf{u}_{i-1}) \quad (2.88)$$

Then, the solution of the equation of motion to obtain displacements,  $\mathbf{u}_{i+1}$ , is given in Equation (2.89).

$$\left( \frac{1}{\Delta t^2} \mathbf{M} + \frac{1}{2\Delta t} \mathbf{C} \right) \mathbf{u}_{i+1} = \mathbf{P}_i - \mathbf{K}\mathbf{u}_i + \frac{2}{\Delta t^2} \mathbf{M}\mathbf{u}_i - \left( \frac{1}{\Delta t^2} \mathbf{M} - \frac{1}{2\Delta t} \mathbf{C} \right) \mathbf{u}_{i-1} \quad (2.89)$$

In the half-step central difference method, the velocity vector is lagged by half a time step. Therefore, the velocity and acceleration are computed as in Equation (2.90) and Equation (2.91), respectively. The solution of the equation of motion is then conducted based on Equation (2.92) (Cook et al., 2001). In this equation, the damping matrix is on the right-hand side with the lagged velocity vector, enabling the solution of the whole system considering only the mass matrix on the right-hand side. If the mass matrix is diagonal, matrix inversion is no longer required.

$$\dot{\mathbf{u}}_{i-\frac{1}{2}} = \frac{1}{\Delta t} (\mathbf{u}_i - \mathbf{u}_{i-1}) \text{ and } \dot{\mathbf{u}}_{i+\frac{1}{2}} = \frac{1}{\Delta t} (\mathbf{u}_{i+1} - \mathbf{u}_i) \quad (2.90)$$

$$\ddot{\mathbf{u}}_i = \frac{1}{\Delta t} \left( \dot{\mathbf{u}}_{i+\frac{1}{2}} - \dot{\mathbf{u}}_{i-\frac{1}{2}} \right) = \frac{1}{\Delta t^2} (\mathbf{u}_{i+1} - 2\mathbf{u}_i + \mathbf{u}_{i-1}) \quad (2.91)$$

The explicit half-step central difference method for the solution of linear problems is presented in Equation (2.92), for each time step,  $i$  (Cook et al., 2001).

$$\frac{1}{\Delta t^2} \mathbf{M}\mathbf{u}_{i+1} = \mathbf{P}_i^{ext} - \mathbf{K}\mathbf{u}_i + \left( \frac{2}{\Delta t^2} \mathbf{M} - \frac{1}{\Delta t} \mathbf{C} \right) \mathbf{u}_i - \left( \frac{1}{\Delta t^2} \mathbf{M} - \frac{1}{\Delta t} \mathbf{C} \right) \mathbf{u}_{i-1} \quad (2.92)$$

The explicit solution algorithm for the half-step central difference method is presented below:

Calculations for each time step,  $i$ :

$$\mathbf{M}\ddot{\mathbf{u}}_i = \mathbf{P}_i - \mathbf{K}\mathbf{u}_i - \mathbf{C}\dot{\mathbf{u}}_{i-\frac{1}{2}} \quad (2.93a)$$

$$\dot{\mathbf{u}}_{i+\frac{1}{2}} = \dot{\mathbf{u}}_i\Delta t + \dot{\mathbf{u}}_{i-\frac{1}{2}} \quad (2.93b)$$

$$\mathbf{u}_{i+1} = \dot{\mathbf{u}}_{i+\frac{1}{2}}\Delta t + \mathbf{u}_i \quad (2.93c)$$

It should be noted that in Equations (2.93a) and (2.93b), for the first time step ( $i = 0$ ), the value of  $\dot{\mathbf{u}}_{i-\frac{1}{2}}$  is assumed to be equal to  $\dot{\mathbf{u}}_0$ . In explicit integration methods, the solution time step,  $\Delta t$ , should be selected smaller than the implicit methods, increasing the computational cost. Explicit methods are conditionally stable, and in order to obtain stable and accurate results, Equation (2.94) should be satisfied, with  $\omega_{max}$  being the highest natural frequency of the structure.

$$\Delta t < \frac{2}{\omega_{max}} \quad (2.94)$$

#### 2.5.1.4 Nonlinear Explicit Dynamic Solver

Both implicit and explicit solution algorithms explained in the previous section can be utilized for nonlinear problems. Although implicit methods require a larger time step for the solution of transient problems than explicit methods, explicit solution schemes are more suitable to model highly nonlinear behavior than implicit methods (Cook et al., 2001). Therefore, in this study, an explicit solution scheme is utilized to simulate nonlinear transient problems. It should be noted that nonlinearity is only accounted for in the stiffness matrix; the mass and damping matrices remain the same throughout the analysis (Cook et al., 2001).

The implemented half-step central difference method is presented in Equation (2.95), for each time step,  $i$  (Cook et al., 2001).

$$\frac{1}{\Delta t^2} \mathbf{M} \mathbf{u}_{i+1} = \mathbf{P}_i^{ext} - \mathbf{P}_i^{int} + \left( \frac{2}{\Delta t^2} \mathbf{M} - \frac{1}{\Delta t} \mathbf{C} \right) \mathbf{u}_i - \left( \frac{1}{\Delta t^2} \mathbf{M} - \frac{1}{\Delta t} \mathbf{C} \right) \mathbf{u}_{i-1} \quad (2.95)$$

In nonlinear solution algorithms, the global stiffness matrix is not assembled in each time step, instead based on the element forces, the internal force vector,  $\mathbf{P}_i^{int}$ , is assembled (Cook et al., 2001). The flowchart of the employed nonlinear explicit dynamic solution algorithm is provided in Figure 2.12.

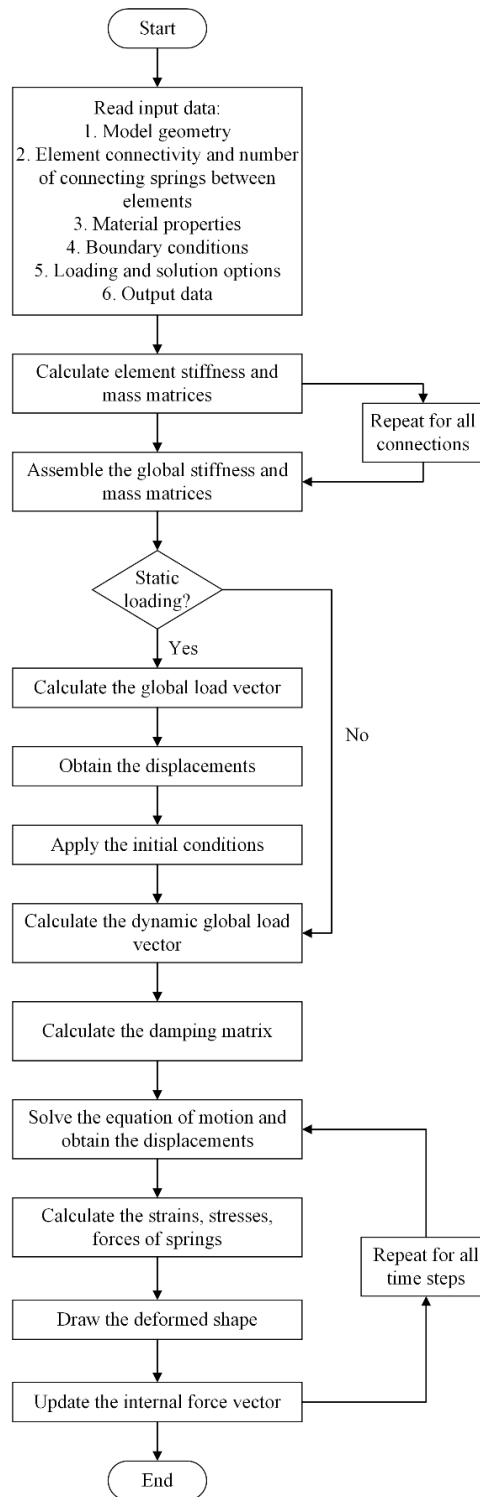


Figure 2.12 Flowchart of nonlinear dynamic analysis

### 2.5.1.5 Modal Analysis

The solution of eigenvalue problems (Equation (2.96)) is conducted by utilizing the FEAST eigenvalue solver (FEAST, 2015). Given a range of eigenvalues,  $\omega$ , the solver finds the eigenvectors,  $\Phi$ , for large scale problems, with mass and stiffness matrices assembled in sparse format. Developed in Polizzi Research Lab (Polizzi, 2009), the solver was included in the INTEL MKL library under ‘INTEL MKL Extended Eigensolver.’ Instead of traditional techniques such as Arnoldi and Lanczos algorithm or Davidson-Jacobi techniques, the method is inspired by the contour integration technique used in quantum mechanics. In the developed software, in addition to the sparse mass and stiffness matrices, the solution range and number of eigenvalues are given to perform modal analysis of structures.

$$K\Phi = \omega^2 M\Phi \quad (2.96)$$

### 2.5.2 Mass Scaling Technique

In the developed software, the mass scaling technique was implemented as well. This method is mainly utilized in explicit time stepping methods to increase the time step, and hence, to reduce the required total number of time steps. As given in Equation (2.94), the critical time step for explicit dynamic solution algorithm is inversely proportional to the maximum frequency of the system. As the mesh size decreases, the maximum stable time step is also decreased. In order to remediate for very small time steps, the mass scaling technique was proposed by introducing additional non-physical mass to the system (Olovsson et al., 2005). The key point of this method is to decrease the high frequencies while keeping the low frequencies unaffected from mass scaling so that the results are not affected by the scaling procedure (Olovsson et al., 2005). In this study, the mass scaling method introduced by Olovsson et al. (2005) was utilized. The global mass matrix is increased proportionally to the stiffness matrix by a positive scalar factor  $\alpha$  (Equation (2.97)).

$$\bar{\mathbf{M}} = \mathbf{M} + \alpha \mathbf{K} \quad (2.97)$$

where  $\bar{\mathbf{M}}$ ,  $\mathbf{M}$ ,  $\alpha$ , and  $\mathbf{K}$  are the modified global mass matrix, global mass matrix, stiffness multiplier, and global stiffness matrix, respectively.

### 2.5.3 Loading Types

Three different loading types can be defined in the program, namely, nodal loads, body forces, and earthquake loading.

In the nodal loading, force or displacement can be assigned to the nodes. The application of forces is straightforward as the force term in the related degree of freedom in the force vector is updated based on the magnitude and direction of loading. For assigning displacements, on the other hand, the Lagrange Multipliers Method is utilized to enforce constraints on the related degrees of freedom (Cook et al., 2001). The advantage of this method is that the original stiffness matrix,  $\mathbf{K}$ , is not altered but the size of the matrix is enlarged with the addition of constraint equations in the matrix format,  $\mathbf{C}$  (Equation (2.98)).

$$\begin{bmatrix} \mathbf{K} & \mathbf{C}^T \\ \mathbf{C} & \mathbf{0} \end{bmatrix} \begin{bmatrix} \mathbf{u} \\ \boldsymbol{\lambda} \end{bmatrix} = \begin{bmatrix} \mathbf{P} \\ \mathbf{Q} \end{bmatrix} \quad (2.98)$$

where  $\mathbf{Q}$  contains constants, and  $\boldsymbol{\lambda}$  contains as many Lagrange multipliers  $\lambda$  as there are constraint equations.

For the application of body forces,  $\mathbf{F}_b$ , such as the self-weight, the gravitational force,  $\mathbf{g}$ , is integrated over the volume,  $V$ , of each element, with  $\rho$  being the density of an element (Equation (2.99)).

$$\mathbf{F}_b = \iiint_V \rho \mathbf{g} dV \quad (2.99)$$

Uniform earthquake loading is defined in the program in a conventional way. The earthquake loading is applied to the nodes by calculating the effective force vector,  $\mathbf{F}^{eff}$ , using the mass of the structure  $\mathbf{m}$  and the ground acceleration  $\ddot{u}_g$  as given in Equation (2.100).

$$\mathbf{F}^{eff} = -\mathbf{m}\mathbf{l}\ddot{u}_g \quad (2.100)$$

In this equation, the influence vector  $\mathbf{l}$  takes on a value of unity for the degrees of freedom in the loading direction and is zero otherwise in accordance with uniform ground acceleration assumption (Chopra, 2015).



## CHAPTER 3

### VALIDATION STUDIES

#### 3.1 Introduction

Validation studies are conducted to show that a mathematical model can be used to simulate a physical phenomenon, and therefore, can be used as a prediction tool. Within the scope of this study, a combined mathematical model for accurate prediction of dam-reservoir systems is used to couple the modified applied elements with the displacement/pressure (u/p) based mixed finite elements. In order to show that both the behavior of the dam body and the reservoir, as well as the fluid-structure interaction, can be simulated successfully, a series of verification studies were conducted.

In this chapter, first, the validation tests for the modified applied element formulation are presented. The validation tests were conducted for linear and nonlinear response cases with the goal of demonstrating the robustness of the methodology and the behavior of the nonlinear material model, respectively. The robustness of the proposed technique was demonstrated by comparing the numerical results with the theoretical solutions to show that with the increase in the modeling details (i.e., increase in the mesh density and the connecting spring pair number), the results converged to the theoretical solutions. Besides, it was shown that the implemented nonlinear material model was capable of representing the nonlinear response of concrete structures by modeling experimental studies under various loading conditions such as direct tension, indirect tension, bending, and earthquake loading with a stable analysis response. The material model worked well in static and dynamic settings with both implicit and explicit time-stepping algorithms.

The first linear benchmark test was chosen identical to the test case used in the original proposal for the applied element method (Meguro & Tagel-Din, 2000) in

which static analysis of a cantilever column subjected to different loading conditions was conducted. Later, the convergence rate of MAEM was investigated considering two example problems with a shear dominant structural member and a bending dominant frame; the results were compared to their counterparts based on FEM solutions. In the nonlinear setting, a direct tension simulation was first conducted on a simple MAEM model to clearly illustrate the implemented Maekawa tension softening material model, demonstrating the loading, unloading, and reloading branches. Next, comparisons of numerical simulations with experimental studies were conducted, and the first validation test was the simulation of a direct tension test on a rectangular concrete prism specimen carried out by Gopalaratnam & Shah (1985). Then, the splitting tension experiment of Malárics & Müller (2010) was simulated. The last verification test in the nonlinear static setting was modeling the push-over loading of a scaled concrete dam model experiment conducted by Carpinteri et al. (1992). For all three simulations, the analytical results were compared with the experimental outcomes by means of cracking and prediction of load-displacement behavior.

The second set of validation tests were carried out using the utilized u/p fluid elements in order to verify the implementation as well as demonstrate the efficacy in simulation. The first verification was for a water tank under self-weight; the pressure distribution through the height was compared with the theoretical solution. The modal analysis of a water column was conducted, similar to Wang & Bathe (1997), and the eigenvalues and mode shapes were compared with the results obtained by the researchers. Next, the frequency response of a full-scale dam-reservoir system was investigated for the validation of both elements working together, as well as the verification of the radiation boundary condition modeled at the far end of the reservoir. The results were validated by the solutions performed with EAGD84 software. The effect of reservoir length and maximum size of water elements were investigated. Then, the dynamic simulation of the well-documented behavior of the Koyna Dam-reservoir system was conducted in order to demonstrate the behavior of the modified applied element methodology coupled with fluid finite elements in the

nonlinear dynamic setting, and the cracking pattern was compared with the actual observations.

Finally, a study on the effect of the Poisson's ratio on the same nonlinear static MAEM validation test results was presented in order to demonstrate the significance of modeling the Poisson's effect in such discrete element models. The effect of Poisson's ratio, together with the nonlinear material model parameters, on the behavior of concrete structures were investigated.

## **3.2 Validation of the Modified Applied Elements in Linear Range**

### **3.2.1 Linear Static Analysis of a Cantilever Column**

The cantilever column problem solved by Meguro & Tagel-Din (2000) using the original AEM was modeled for the axial load (Case I), lateral load (Case II), and in-plane moment (Case III) loadings to verify the proposed modified methodology in the linear elastic setting. The column width, height, and thickness were 1 m, 6 m, and 0.25 m, respectively (Figure 3.1a). The Young's modulus and Poisson's ratio were taken as 210 GPa and 0.2, respectively. In the plane stress setting, five models with different mesh densities were formed; the sizes of the elements of models MI, MII, MIII, MIV, and MV were 0.5 m, 0.25 m, 0.125 m, 0.0625 m, and 0.02 m, respectively. In order to investigate the effect of the number of connecting springs between elements, each model was analyzed with 1, 2, 5, 10, and 20 spring pairs. The relative error of the tip displacement of the column with respect to the theoretical solution was computed in Equation (3.1).

$$Error (\%) = \left| \frac{Disp_{MAEM} - Disp_{theo}}{Disp_{theo}} \right| \quad (3.1)$$

The uniformly distributed axial load was applied to all top nodes as equivalent point loads with the same magnitudes, and for this loading type (Case I), it can be seen

from Figure 3.1b that the vertical tip displacement can be obtained exactly (the relative error is less than 0.1%), for all cases. The minor difference in results for the coarsest mesh (Model I) with respect to different spring pairs was due to the rotation of elements. A single spring pair connection does not have a contribution to the rotational stiffness, whereas increasing the spring pairs connecting elements introduces rotational stiffness. For comparably large element sizes, rotational stiffness may affect the results; on the other hand, this effect vanished as the element sizes got smaller. It should also be noted that the tip displacements were predicted with identical accuracy for tensile loading as well. Therefore, a tension-compression asymmetry is not present in the numerical model.

The second loading case is a uniformly distributed lateral load at the column tip, and the equivalent nodal loads were applied as equal lateral loads and longitudinal couple to model the moment between the edge of the column and the centroid of the elements. For this loading case, the corresponding lateral displacement was compared with the theoretical solution using the Timoshenko beam theory (Figure 3.1c). As expected, the error prediction of the tip displacement was reduced as the number of elements and the number of spring pairs between elements increased; both enabled to capture the bending behavior more correctly (Figure 3.1c). It should be pointed out that compared to a model having a similar mesh density with 10 spring pairs in Meguro & Tagel-Din (2000), the error in the estimate was reduced from 12% to 6% in MAEM (MI, 10 spring pairs). The results were eventually similar for the most refined mesh; with the proposed methodology, the displacement was approximated with less than 1% error.

For this lateral load case, the normal and shear stress distributions at the column base were also calculated and compared with the theoretical stress distributions. The theoretical normal stress,  $\sigma$ , was calculated using the Euler-Bernoulli beam theory with normal stress  $\sigma = My/I$  written in terms of the bending moment  $M$ , distance from the neutral axis  $y$ , and moment of inertia  $I$ . The theoretical shear stress  $\tau = VQ/It$  was calculated using  $V$ ,  $Q$ , and  $t$  quantities representing the shear force, the

first moment of area, and the thickness, respectively. From Figure 3.2a, it can be concluded that regardless of the mesh density, the normal stress distribution was obtained very close to the theoretical solution. The shear stress in between any two modified applied elements is constant. Accordingly, by making the mesh more refined, as in the case of MV (Figure 3.2b), the theoretical shear stress distribution could be captured.

For the final in-plane moment loading case, similar results were obtained. The relative error of the axial tip displacement was reduced with the increase in the mesh density and the increase in the number of spring pairs between each element. The axial tip displacement could be approximated with less than 1% error.

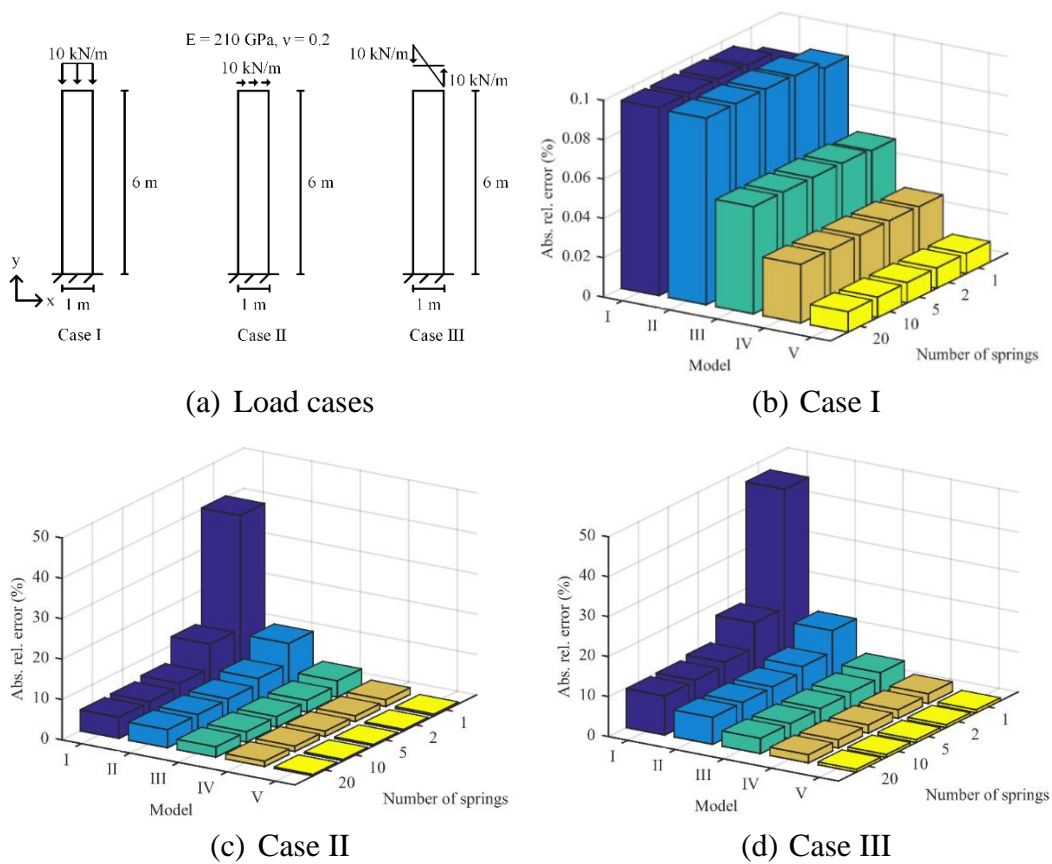
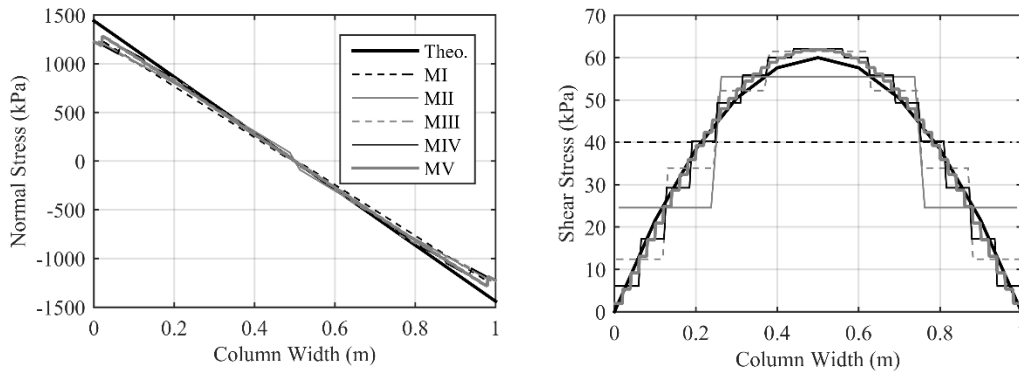


Figure 3.1 Linear static analysis of a cantilever column, error with respect to the theoretical solution



(a) Normal stress distribution

(b) Shear stress distribution

Figure 3.2 Normal and shear stress distributions for case II loading

For the static linear elastic problems of the cantilever column under three loading types, the robustness of MAEM was verified. As expected, the error in predicting the results compared to the theoretical solutions decreased with increasing mesh density. Moreover, the error decreased when the number of springs between elements increased, especially for coarse meshes. For the bending dominant problems, the increase of mesh density and spring pair number enabled to capture the bending behavior more correctly.

### 3.3 Wall and Frame Problems: The Convergence Rate of MAEM

The convergence rate of MAEM was investigated with two example plane stress problems, which are presented in Figure 3.3. A shear wall (Figure 3.3a) problem was selected to simulate shear dominant problems; whereas, bending dominant behavior was modeled by the bare tall frame problem (Figure 3.3b). The geometrical and material properties of these problems are given in Figure 3.3, together with the applied loadings. These benchmark problems were solved for two different Poisson's ratios,  $\nu = 0.2$ , and  $\nu = 0.33$ . Furthermore, to investigate the effect of the number of connecting spring pairs on the behavior of structures, 1 and 10 spring pairs were modeled for each problem. In addition to these, the MAEM models were generated

with various mesh densities, i.e., element side lengths,  $a$ , and the tip displacement results were compared with ‘converged’ finite element method (FEM) solutions.

The finite element models were formed with SAP2000 v20 (CSI, 2017) software utilizing thin shell elements with drilling degrees of freedom for the plane stress problems. In SAP2000, for the homogeneous shell elements, the in-plane displacements are quadratic, and out-of-plane displacements are cubic (CSI, 2017). For the simulation of these plane stress problems, the out-of-plane displacements were restrained. In order to obtain a ‘converged’ finite element solution, FEM models with different mesh densities were formed. The tip displacement equation with respect to mesh size was generated, and the ‘converged’ solution used for the comparisons was obtained for a nearly infinitesimal element.

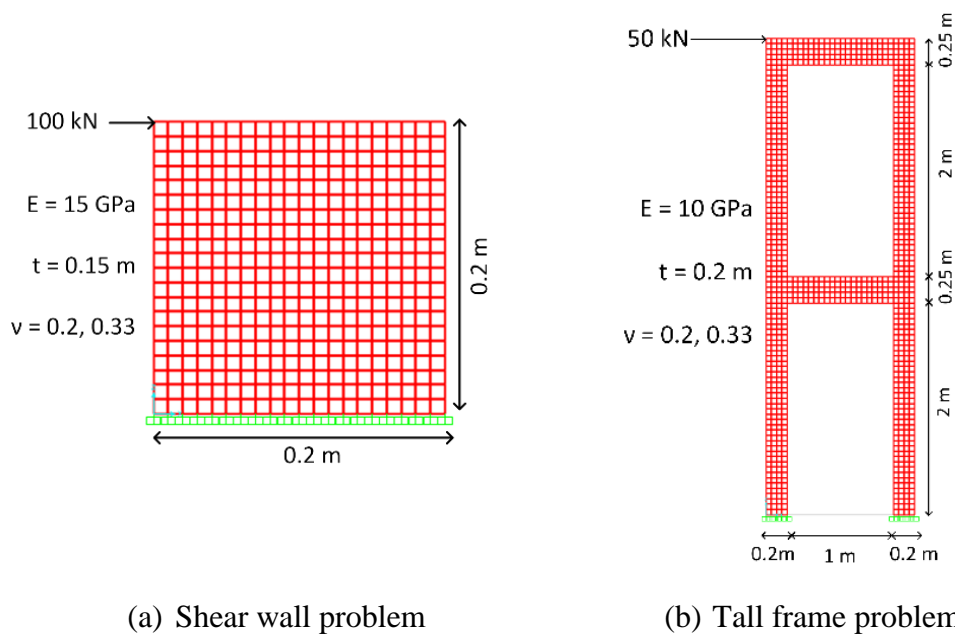
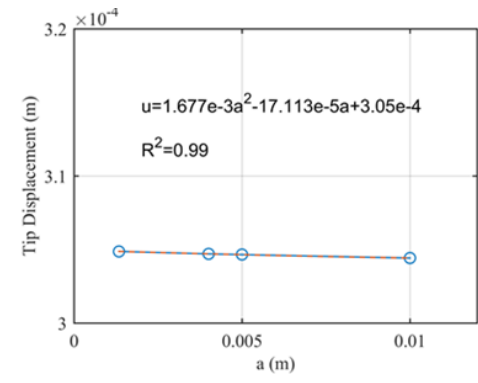


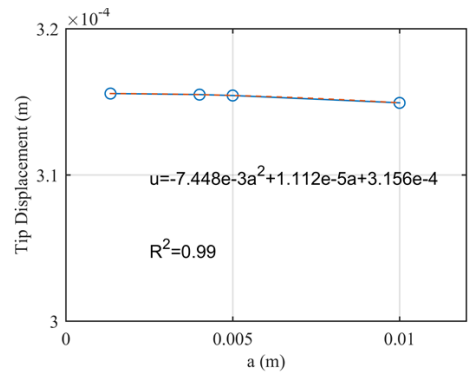
Figure 3.3 Benchmark problems for the convergence rate

The tip displacements,  $u$ , of the two benchmark problems with respect to the finite element model size,  $a$ , for  $\nu = 0.2$  and  $\nu = 0.33$  are presented in Figure 3.4. The analyses were conducted for  $a=0.01$ ,  $0.005$ ,  $0.004$ , and  $0.001$ m mesh sizes for the

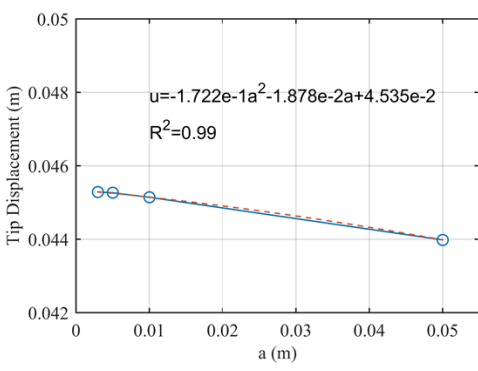
shear wall problem. The tall frame model sizes, on the other hand, were  $a=0.05, 0.01, 0.005,$  and  $0.003\text{m}$ . In this figure, the tip displacements are illustrated with circle markers and connected by solid lines. In order to estimate the ‘converged’ result, a quadratic polynomial was fitted, which is shown with dashed lines. The quadratic equations ( $u$ ) with respect to the finite element size ( $a$ ) and correlation coefficients ( $R^2$ ) are given in the figures as well. Accordingly, the ‘converged’ FEM results were assumed to be obtained for a nearly infinitesimal element size as  $3.050 \times 10^{-4} \text{ m}$  and  $3.156 \times 10^{-4} \text{ m}$  for the shear wall problem for  $\nu = 0.2$  and  $\nu = 0.33$  cases, respectively. Similarly, the ‘converged’ results of the tall frame problem were computed as  $4.535 \times 10^{-2} \text{ m}$  and  $4.536 \times 10^{-2} \text{ m}$  for  $\nu = 0.2$  and  $\nu = 0.33$  cases, respectively. The MAEM tip displacements were compared to these aforementioned results obtained for a nearly infinitesimal finite element size.



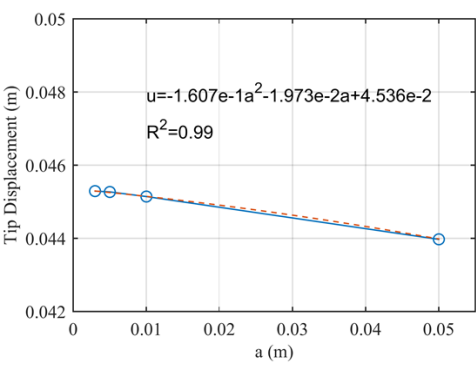
(a) Shear wall problem,  $\nu=0.2$



(b) Shear wall problem,  $\nu=0.33$



(c) Tall frame problem,  $\nu=0.2$



(d) Tall frame problem,  $\nu=0.33$

Figure 3.4 Finite element solutions



For the shear wall problem (Figure 3.3a), four different MAEM models with element length 0.01 m, 0.005 m, 0.0025 m and, 0.00125 m were generated, and the tip displacements were compared with the reported ‘converged’ FEM solutions obtained for an infinitesimal FE size (Figure 3.5). The absolute relative difference of tip displacement obtained by MAEM solution with respect to different element sizes,  $a$ , are presented in Figure 3.5a and Figure 3.5b, for  $\nu = 0.2$  and  $\nu = 0.33$ , respectively. For both Poisson’s ratio cases, the difference between the results of a coarse and fine mesh of an identical structure was higher in MAEM compared to FEM (Figure 3.5). The main reason for this difference is the boundary condition definitions in FEM and MAEM. In FEM, boundary conditions are assigned to a joint; therefore, the restrictions for the degrees of freedom influence only the points. Conversely, in MAEM, the degrees of freedom are located at the centroids of the elements, so when a boundary condition is assigned to a single element, the movement of the whole rigid element is restricted. This effect is especially significant for coarse meshes, as in this case, a larger part of the structure is restricted to move. By making the mesh finer, however, this effect becomes less prominent. The difference of MAEM estimation was obtained at around 5%, with the element size at  $1/40^{\text{th}}$  of the width of the member for this shear dominated problem.

For  $\nu = 0.2$  case (Figure 3.5a), the results were slightly affected by the number of connecting spring pairs, and as the mesh got finer, this effect vanished. For this problem, in which shear is dominant and no significant rotations in the elements, the effect of the connecting spring number was less significant. Similar to the cantilever column problem in Section 3.2.1, the minor difference in results for the coarsest mesh with respect to different spring pairs was due to the rotation of elements. When  $\nu = 0.33$  (Figure 3.5b), the number of spring pairs did not affect the results. Since shear springs vanished in the numerical model (for  $\nu = 0.33$ ), the applied loading was directly transferred to the bottom layers by diagonal springs. Hence, these springs cannot cause rotation on an element.

Regardless of Poisson's ratio and the number of spring pairs between the elements, the difference decreased with decreasing element size. Although the relative error of FEM models was less than MAEM, the behavior of this shear dominated problem could be simulated with less than 1% difference for very small element sizes of  $1/200^{\text{th}}$  of the member width. For the shear dominant problems, the spring pair number has a negligible effect on the results, and the displacement estimation mainly depends on the mesh density. The top displacements were obtained well for the element sizes smaller than  $1/40^{\text{th}}$  of the width of the member. For this example, an increase in the mesh density from  $1/40^{\text{th}}$  to  $1/200^{\text{th}}$  of the member width led to an increase in the DOF number from 4680 to 76320; accordingly, the computational cost increased from 2 sec to 60 sec.

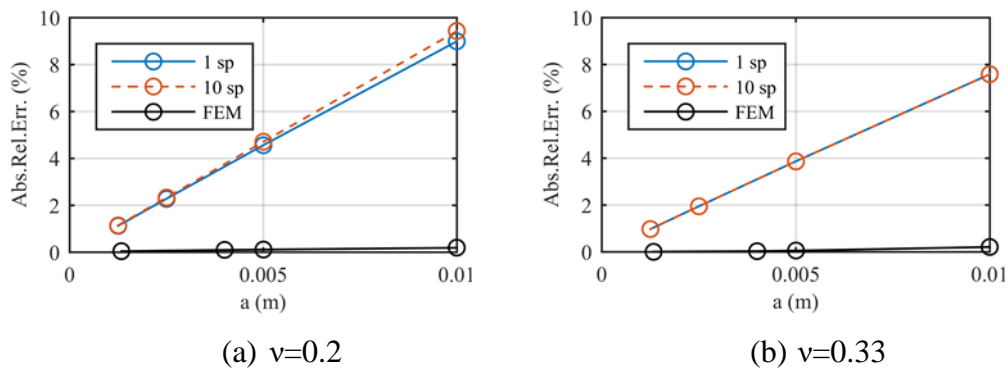


Figure 3.5 Shear wall problem

Next, the simple bare concrete frame problem (Figure 3.3b), simulating a bending dominant behavior, was solved with MAEM, and the results were compared to the FEM analyses. Similar to the previous case, four models with 0.05 m, 0.025 m, 0.0125 m, and 0.00625 m element length were formed, and the absolute relative difference of the top displacement with respect to the 'converged' FEM result was computed for each case (Figure 3.6). As explained above, the difference between the results of a coarse and fine mesh of an identical structure was higher in MAEM compared to FEM due to the differences in the boundary condition definitions in

these two methodologies. Similar to the shear dominant case, for this problem as well, as the mesh got finer, the difference in the results decreased, irrespective of  $\nu$  and spring pair number. The difference of MAEM estimation was obtained at around 5%, with the element size at  $1/10^{\text{th}}$  of the width of the column for this bending dominated problem.

For  $\nu = 0.2$  case (Figure 3.6a), error decreased significantly by increasing spring pair number, especially for coarse meshes. Since this was a more slender problem than the shear wall example, element rotations occurred, so the increase in spring pair number enabled to capture the bending behavior more correctly. When  $\nu$  was 0.33, however, (Figure 3.6b), the number of spring pairs did not affect the results for this problem as well. As the shear springs were not present, the applied loading was directly transferred to the bottom layers by diagonal springs. Therefore, these springs cannot cause rotation on an element.

The relative differences of MAEM models were higher than FEM models for the coarse meshes; however, as the mesh got finer, the solutions of the two models converged, and the tip displacement could be obtained with approximately 1% difference in MAEM solutions for very small elements sizes ( $1/40^{\text{th}}$  of the column width). For the bending dominant problems, the displacement estimation depends both on the spring number and the mesh density. Especially for the coarse meshes, the increase of spring pairs decreased the difference in the displacement prediction. When the total spring number was increased by 5 times, the duration for the stiffness matrix assembly increased by approximately 20%. The top displacements were obtained well for the element sizes smaller than  $1/10^{\text{th}}$  of the width of the column with 10 spring pairs. For this problem, the decrease in the element size from 0.025 m to 0.00625 m led to an increase in the DOF number from 10989 to 176445; accordingly, the computational cost increased from 5 sec to 300 sec.

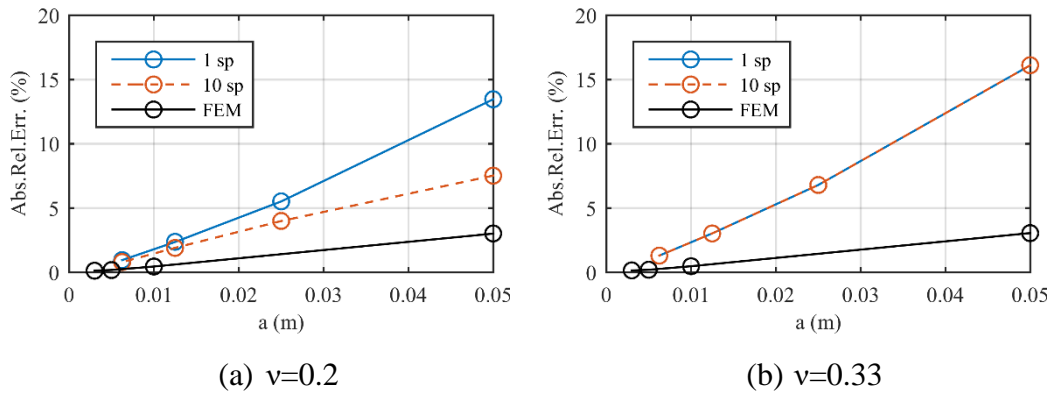


Figure 3.6 Tall frame problem

The solution times of FEM and MAEM were compared for this frame problem as well. In the FEM model with a 0.005 m element size, corresponding to 282294 DOF, the solution time was less than a minute. In a comparable MAEM model with a mesh size of 0.00625 m and 176445 DOF, the solution time was approximately 5 minutes. The difference in the solution times was due to the assembly of the stiffness matrix in MAEM: In the MAEM solution algorithm, the stiffness matrix is assembled with contributions from each spring pair. For the aforementioned model with 10 spring pairs connecting each interface, a total of 1.3 million springs are obtained, increasing the workload.

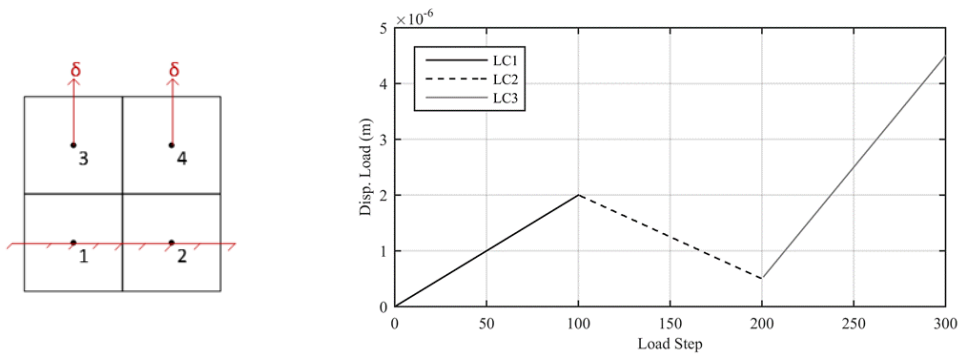
Investigating Figure 3.5 and Figure 3.6, it can be concluded that MAEM exhibits a linear convergence rate compared to the FEM, which has a quadratic convergence rate. Although the convergence rate of MAEM is slower than FEM, the results are acceptable in the available computation capacity.

### 3.4 Validation of the Modified Applied Elements in the Nonlinear Range

#### 3.4.1 Direct Tension Simulation

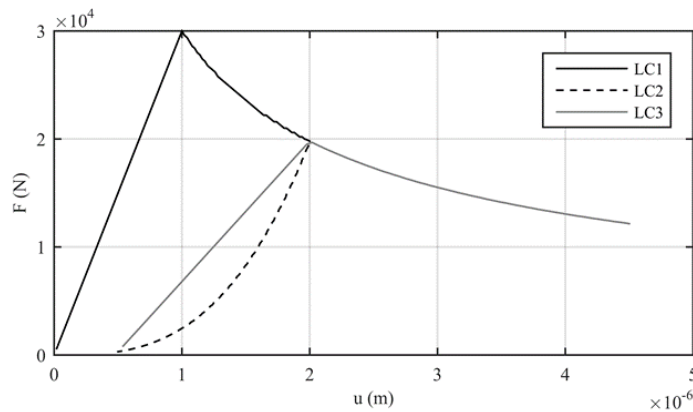
The implementation of the nonlinear material model, namely the Maekawa tension softening model, is validated first in this section at the element level for the plane

stress configuration. The behavior of the 1D normal springs in loading, unloading, and reloading behavior is demonstrated using a simple model consisting of 4 modified applied elements (Figure 3.7a). The modified applied element size was 0.01 m, and the thickness was taken as 1 m. 10 connecting spring pairs were modeled between elements. The compressive behavior of the normal springs was assumed linear; shear springs were assumed to behave linearly for this simulation as well. The modulus of elasticity and Poisson's ratio were taken as 15 GPa and 0.0, respectively. The bottom nodes were fixed, and displacement was prescribed to the top nodes in the y-direction in three different load cases. The cracking strain,  $\varepsilon_t$ , was assigned as  $1 \times 10^{-4}$  with the softening parameter,  $c$ , taken as 0.6. A high  $\varepsilon_{ult} = 0.1$  was chosen such that none of the springs failed. The solution was performed using the Newton-Raphson method with a displacement tolerance of 0.1%. The loading protocol and, accordingly, the force-displacement response obtained from the simulation are presented in Figure 3.7b and Figure 3.7c, respectively. In the first loading case (LC1), after  $\varepsilon_t$  was reached (corresponding to  $1 \times 10^{-6}$  m displacement), softening started. Then the nonlinear unloading as defined in the material model was observed (LC2), in the final load case (LC3), straight reloading was modeled and the system continued with the nonlinear tension softening behavior (Figure 3.7c). It can be concluded in Figure 3.7 that the implemented material model was able to simulate the loading, unloading, and reloading branches with the use of the proposed modified applied element methodology.



(a) Model

(b) Loading protocol



(c) Load-displacement response

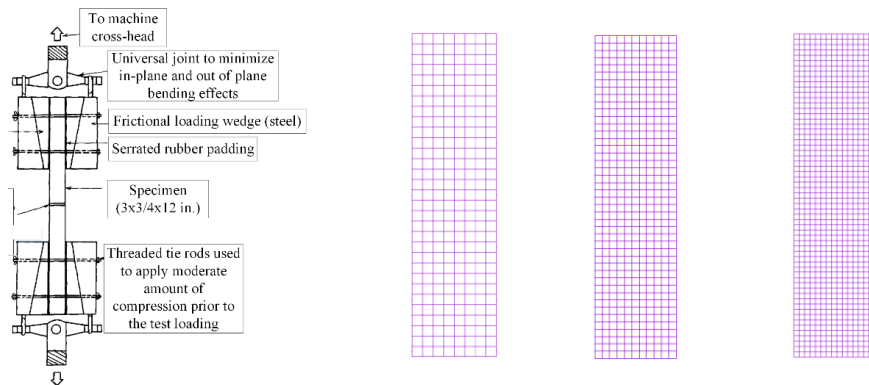
Figure 3.7 Direct tension simulation

### 3.4.2 Uniaxial Tension Test

The accurate modeling of concrete structures regarding the tensile behavior requires the simulation of the complete response of concrete, i.e., the inclusion of the post-peak softening response. In order to investigate this response, a series of experiments were conducted by Gopalaratnam & Shah (1985) on plain concrete specimens. In this study, the direct tension test conducted by Gopalaratnam & Shah (1985) on a 76 mm (L), 305 mm (H), and 19 mm (W) rectangular concrete prism was simulated in the static nonlinear setting (Figure 3.8a). At mid-height, the specimen had 13 mm long, 3 mm wide notches at both sides. The tensile strength, modulus of elasticity, and the fracture energy of the specimen were reported as 3.41 MPa, 29.1 GPa, and

54 N/m, respectively. The measurements in the experiment were taken with a gauge length of 83 mm.

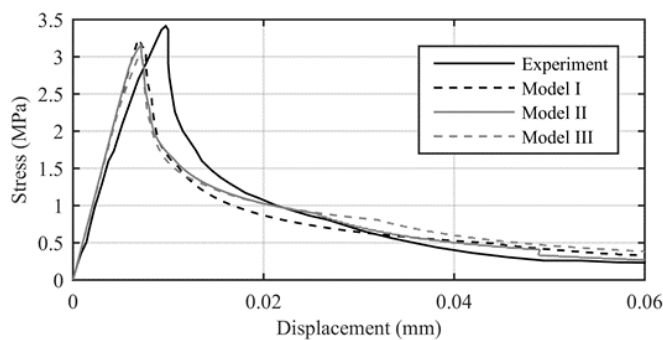
Three MAEM models with different mesh densities, 0.010 m (Model I), 0.007 m (Model II), and 0.005 m (Model III), were used in plane stress simulations with 720, 1419, and 2880 degrees of freedom, respectively, with 10 spring pairs between elements (Figure 3.8b-d). The notch was simulated by removing the vertical and diagonal connections between the elements at notch locations. The stress-displacement curves for the whole range of loading and the crack scheme were compared to the test results.



(a) Experimental setup

(b) Model I (c) Model II (d) Model III

(Gopalaratnam & Shah, 1985)



(e) Stress-displacement response

Figure 3.8 Uniaxial tension test

Displacement was applied to the system until failure. The solution was performed using the arc-length method with a displacement tolerance of 0.1%. Maekawa tension softening model was utilized for the normal and diagonal springs with an ultimate strain,  $\varepsilon_{ult}$ , of 0.008, 0.007, and 0.012; the softening parameter  $c$ , was calculated as 0.66, 0.50, and 0.45 for Model I, Model II, and Model III, respectively, in accordance with the mesh size and the given fracture energy. This tension behavior was employed to normal and diagonal springs. Shear springs were brittle: after the exceedance of cracking strain,  $\varepsilon_t$  in the normal spring of the spring pair, the shear spring lost its resistance, corresponding to no shear retention in the crack. The springs in compression were assumed to behave linearly. The results were compared to experimental counterparts in Gopalaratnam & Shah (1985), showing the stress at the notch location versus elongation of the specimen over the gauge length. The displacement differences of the closest points to the gauge length of the experiment were calculated. The displacements of points at the left, midpoint, and right end of the specimen at the measurement locations were recorded, and the average of the displacement differences over the gauge length was computed. The results of the simulations compared well with the experiment, capturing the tensile strength and the softening trend; accordingly, the fracture energy of the models was calculated as 52 N/m, 53 N/m, and 56 N/m for Models I, II, and III, respectively (Figure 3.8e). The crack schemes replicated the experiment forming a straight crack between the two notches.

It is worth mentioning to discuss the effects of nonlinear Maekawa tension softening material model parameters on the post-peak response. This material model is simply defined with respect to two parameters, the softening parameter,  $c$ , and the ultimate tensile strain,  $\varepsilon_{ult}$ . The softening parameter quantifies the post-peak behavior of the curve, and when the ultimate tensile strain is reached, the springs no longer carry any force. The fracture energy,  $G_f$ , is obtained in accordance with the element size based on the parameters  $c$  and  $\varepsilon_{ult}$ . Ideally,  $\varepsilon_{ult}$  should be selected based on uniaxial tension tests, corresponding to the strain level for the springs such that when this ultimate level is reached, springs can no longer carry any force. Then,  $c$  can be computed for



the prescribed  $G_f$  and  $\varepsilon_{ult}$  values. In the numerical models,  $\varepsilon_{ult}$  depends on the mesh size, and as the element size is decreased,  $\varepsilon_{ult}$  should be increased to get the same displacement level such that the spring cannot carry the load anymore (i.e., spring has no capacity to carry any load). Then, the  $c$  value should be adjusted accordingly to represent the desired  $G_f$ . In addition to the change in  $\varepsilon_{ult}$  with respect to the element size,  $c$  is adjusted in accordance with the mesh size. Given that the area under the stress-strain curve is characterized by the fracture energy divided by the mesh size, for the same  $G_f$ , the area should be larger for finer meshes. Therefore, for smaller element sizes, in addition to the increase in  $\varepsilon_{ult}$ ,  $c$  should be selected smaller (corresponding to a less brittle softening curve that increases the area under the stress-strain curve). Then, the shape of the post-peak curve of the experimental results may not be represented well for small element sizes (less than 5 mm, according to the uniaxial tension test simulations conducted in this study). Despite such drawbacks of the softening behavior, the employed material model has its simplicity by defining the post-peak shape with a single parameter,  $c$ .

### **3.4.3 Splitting Tension Test**

The second validation in the nonlinear range was conducted by simulation of the splitting tension test. In order to estimate the tensile strength of concrete, which is an essential parameter in the analyses of concrete structures, splitting tests on cylindrical specimens are generally preferred over the direct uniaxial tension experiments due to complexities in performing such tests. A variety of splitting tension tests with different strengths and geometries were carried out by Malárics & Müller (2010) to investigate the relationship between the splitting tensile strength and the compressive and uniaxial tensile strengths. The splitting tests were performed per the standard DIN EN 12390-6 (2001). In this study, the experiment on the 150mmx300mm cylindrical specimen was used for validation (Malárics & Müller, 2010). The Young's modulus, tensile strength, fracture energy, and Poisson's ratio were reported as 28 GPa, 2.5 MPa, 90 N/m, and 0.2, respectively.

Three MAEM models in plane stress condition were generated with element sizes 0.010m (Model I), 0.005m (Model II), and 0.001m (Model III), leading to 533, 2014, and 52397 degrees of freedom, respectively, with 10 normal-shear spring pairs between each element (Figure 3.9). The widths of the load-bearing strip were 10mm for all models (Malárics & Müller, 2010). Maekawa tension softening model was utilized for the normal and diagonal springs with the ultimate strain ( $\epsilon_{ult}$ ) values of 0.01, 0.02, and 0.075, and softening parameter values ( $c$ ) of 0.43, 0.37, and 0.22 for Model I, Model II, and Model III, respectively, computed based on the reported fracture energy. Shear springs were modeled as brittle, while compressive behavior was assumed to be elastic.

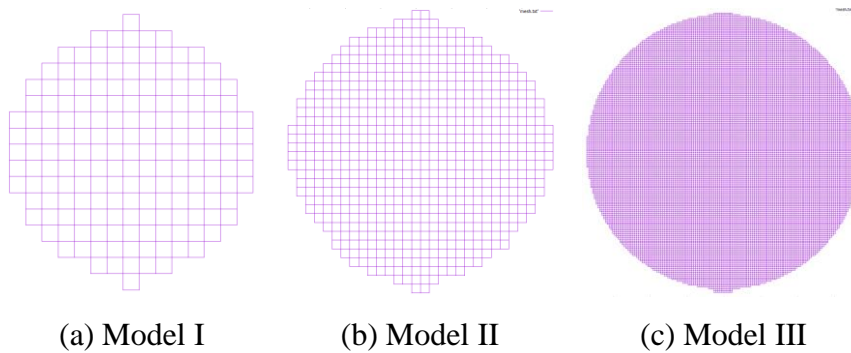


Figure 3.9 Splitting tension test models

Displacement controlled loading was applied to the bearing strip to a total downward displacement of 0.15 mm with the use of the modified Newton-Raphson algorithm with a constant initial stiffness for the determination of internal forces and displacements. The displacement tolerance in the solutions was taken as 0.1%. The splitting tensile strength,  $f_{t,sp}$ , was estimated from the theory of elasticity formulation (Equation (3.2)), with  $F_u$  being the ultimate load, and  $D$  and  $L$  are the diameter and length of the specimen, respectively. Accordingly, the estimated splitting tensile strengths were calculated as 1.70 MPa, 1.76 MPa, and 1.80 MPa, for Model I, Model II, and Model III, respectively. In the simulations, there were

limitations for modeling the contact in between the load bearing strips and the specimen, and stress localization occurred for the coarser meshes that affected the overall behavior. Nevertheless, as the mesh density increased, stress localization reduced; accordingly, a better estimation of the splitting capacity was made. The results were parallel to the outcomes of Malárics & Müller (2010): As the mesh got finer, the splitting tensile strength capacity increased. Furthermore, the researchers investigated the relationship of direct tensile strength,  $f_{t,uni}$ , and split tensile strength and defined a parameter  $A$  as the ratio of the direct tensile strength to the splitting tensile strength (Equation (3.3)). For normal strength concrete, this ratio ranged from 1.1 to 1.3 (Malárics & Müller, 2010). In the most refined mesh of MAEM (Model III),  $A$  was obtained as 1.33, which is in the upper bound of the range reported by Malárics & Müller (2010).

$$f_{t,sp} = \frac{2F_u}{\pi DL} \quad (3.2)$$

$$A = \frac{f_{t,uni}}{f_{t,sp}} \quad (3.3)$$

#### 3.4.4 Push-Over Loading Problem of a Notched Model Concrete Dam

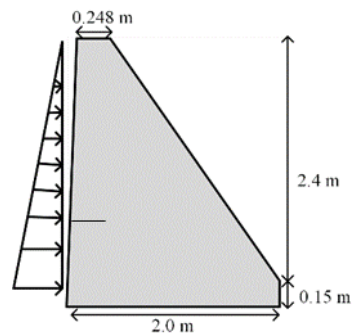
The next validation study was conducted by simulation of the response of a 1:40 scaled concrete gravity dam specimen (Carpinteri et al., 1992) under monotonically increasing hydrostatic loading. In the experimental work, two specimens with heights of 2.4 m, and upstream and downstream slopes of 0.03 and 0.7, respectively, were tested. In order to prescribe the location of crack initiation on the specimen, a 15 cm and a 30 cm deep notch was cut on the upstream face of the dam at the height of 0.6 m from the base for the first and second models, respectively (Figure 3.10a). Displacement controlled experiments using the controlling parameter as the crack mouth opening displacement (CMOD) at the notch were carried out. The tensile strength and modulus of elasticity of the specimen were reported as 3.6 MPa and

35.7 GPa, respectively. The load-displacement curves from the test, as well as the reported propagation of the crack, were used as benchmark results for MAEM analyses. The experiment on the second model with a 30 cm deep notch was simulated in this study.

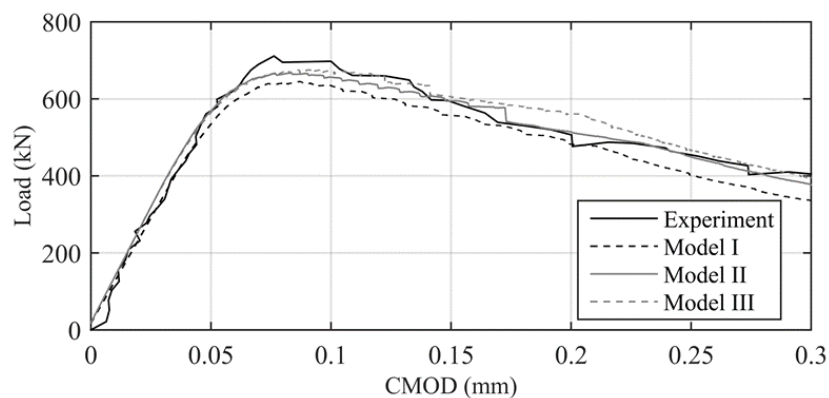
Similar to the previous problems, the analyses were conducted in the plane stress configuration for models with different mesh densities, Model I, Model II, and Model III, with element sizes of 0.05 m, 0.03 m, and 0.02 m, respectively. Model I and Model II had 3549 and 10005 DOF, respectively; whereas, the DOF number in the most refined model (Model III) was 22341. All models had 10 spring pairs connecting each element. The notch was simulated by merely deleting the interface springs connecting the elements at the notch locations. In accordance with Carpinteri et al. (1992), the modulus of elasticity and, accordingly, the tensile strength was increased by 1.58 and 1.53, respectively, to remediate the low initial stiffness and capacity of the model. The fracture energy and Poisson's ratio were assumed as 184 N/m and 0.1, respectively, as reported. The softening parameter,  $c$ , was calculated as 0.85, 0.68, and 0.55 for Model I, Model II, and Model III, respectively, in accordance with the fracture energy value; the ultimate strain at the tensile range,  $\varepsilon_{ult}$ , was assumed as 0.003, 0.0055, and 0.007, respectively, for the three models. Shear springs were again assumed to be brittle, and the compression response was linear.

A triangular hydrostatic force was applied, and the solution was performed with the arc-length method, where the controlling nodes were the opposite sides of the notch. In the simulations, both the displacement and force tolerances were selected as 0.1%. The corresponding load-crack mouth opening displacement and the cracking patterns in the specimen are compared in Figure 3.10 for Models I, II, and III. The final capacity was slightly underestimated with the coarse mesh but captured well when the mesh was finer (Model III) (Figure 3.10b). The coarse model led to a straight crack pattern, similar to a previous study using the fictitious crack model with finite element method (Shi et al., 2003), which is inconsistent with the experimental result

shown with the red dashed line (Figure 3.10c). The finer meshes (Model II and III) remediated this issue (Figure 3.10c). The final deformed shapes of MAEM models clearly showing the discrete nature of crack can be seen in Figure 3.10d. The obtained crack propagation was less than that of the experiment for all MAEM models. The penetration of the cracking in the laboratory testing could be attributed to the changes in the loading conditions during the experiment before the structural failure (Shi et al., 2003). Accordingly, the MAEM cracking results were similar to previous studies using smeared crack models with the finite element technique, predicting a shorter crack length (Bhattacharjee & Léger, 1994; Soysal et al., 2016).

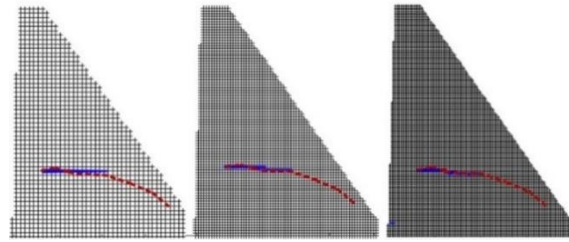


(a) Dimensions and loading of the specimen

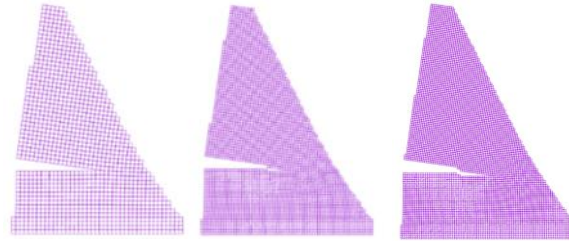


(b) Load vs. CMOD graph

Figure 3.10 MAEM results of push-over loading problem



(c) Model I-II-III Cracking patterns



(d) Model I-II-III Deformed shapes

Figure 3.10 (Continued) MAEM results of push-over loading problem

### 3.5 Validation of the Mixed u/p Fluid Finite Elements

#### 3.5.1 Water Tank under Self-Weight

The first problem used for the validation of the implement mixed u/p fluid elements is a water tank under its self-weight (Özmen, 2016). The example problem is presented in Figure 3.11a, with the width and height of the tank as 1 m and 5 m, respectively. The bottom was fixed in the vertical direction, whereas the sides of the water tank were restrained in the horizontal direction. The Poisson's ratio, density, and acoustic wave speed of water were taken as 0.4999, 1000 kg/m<sup>3</sup>, and 1440 m/s, respectively. The pressures,  $P$ , from the theoretical solution,  $P(z) = \rho g z$  were compared with the result of the developed computed program at the locations of pressure degrees of freedom, as indicated in Chapter 2, where  $\rho$ ,  $g$  and  $z$  stand for the density of water, the gravitational acceleration, and depth measured from the top,

respectively. The pressure results are compared in Figure 3.11b; the obtained pressures matched the theoretical solution well.

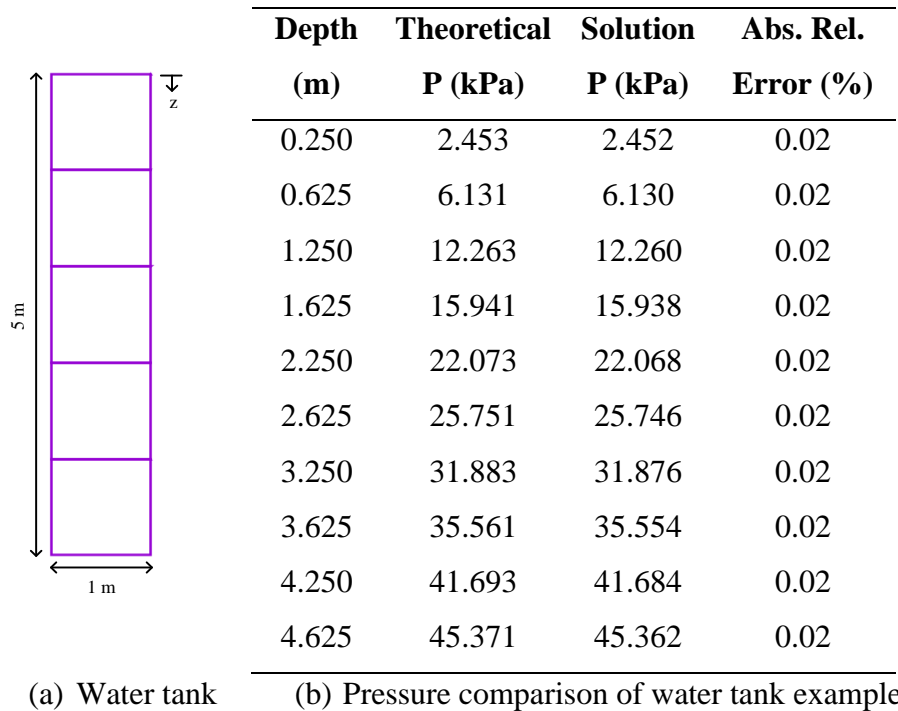
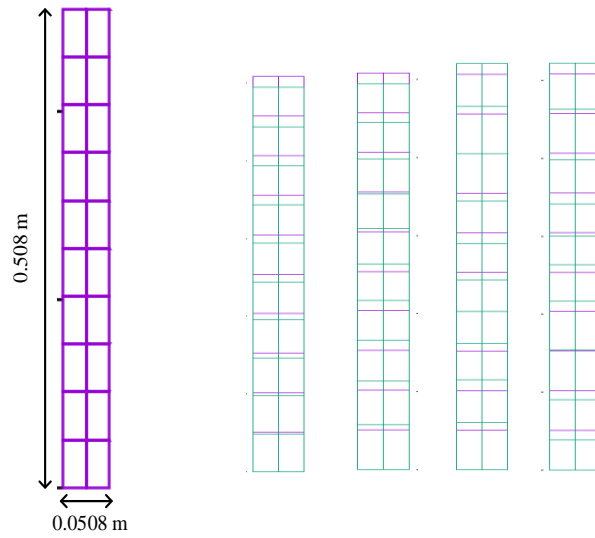


Figure 3.11 Water tank example under self-weight

### 3.5.2 Modal Analysis of a Water Column

The next verification problem for displacement/pressure based mixed finite element is the modal analysis of a water column investigated by Wang & Bathe (1997). The model constituted for the water column is presented in Figure 3.12a. It can be seen that the width and height are 0.0508 m and 0.508 m, respectively. The water column was meshed with 20 elements, as shown in Figure 3.12a. Similar to the previous example, the bottom of the column was restrained in the vertical direction and the sides in the horizontal direction. In accordance with Wang & Bathe (1997), the density and acoustic wave speed of water were taken as  $999 \text{ kg/m}^3$  and  $1477.22 \text{ m/s}$ ,

respectively. An almost incompressible fluid was assumed by modeling the Poisson's ratio as 0.4999. The first four mode shapes and the frequencies are compared to the analytical solution in Figure 3.12b and Figure 3.12c, respectively. The eigenvalues were estimated correctly.



(a) Water column

(b) Mode shapes

<b>Mode #</b>	<b>Analytical <math>w</math> (rad/s)</b>	<b>Solution <math>w</math> (rad/s)</b>	<b>Abs. Rel. Error (%)</b>
1	4567.74	4568.26	0.01
2	13703.2	13705.68	0.02
3	22838.7	22852.91	0.06
4	31974.2	32038.59	0.20

(c) Frequency comparison

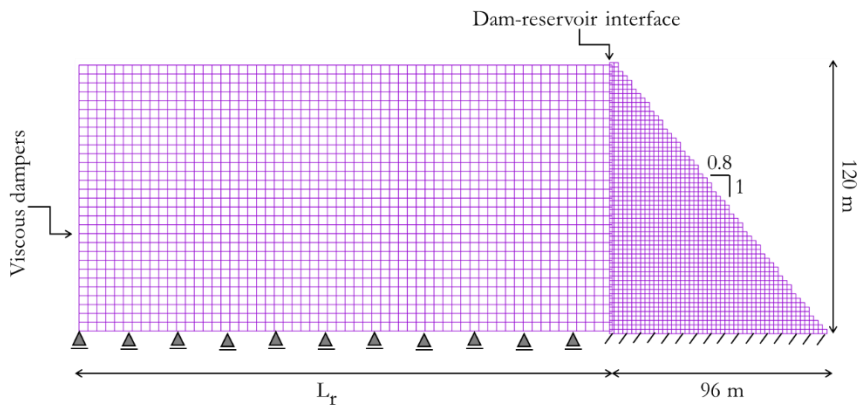
Figure 3.12 Modal analysis of a water column



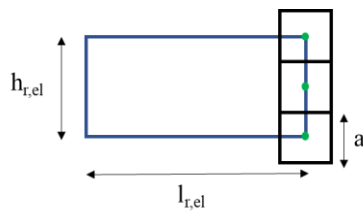
### 3.6 Frequency Response of a Full-Scale Dam-Reservoir System

The frequency response of a full-scale dam-reservoir system was investigated to validate MAEM and FEM working together. The dam body was modeled with modified applied elements in the plane stress setting, while the reservoir elements were modeled with u/p based mixed finite elements. To this end, an idealized concrete gravity dam-reservoir system, as given in Fenves & Chopra (1987), was analyzed (Figure 3.13a). The dam had a vertical upstream, and the downstream had a slope of H/V ratio of 0.8. Both dam ( $H_d$ ) and reservoir height ( $H_r$ ) were modeled as 120 m, with a unit thickness. In order to investigate the effect of reservoir length,  $L_r$ , three different models with  $L_r$  240 m, 480 m and 720 m, corresponding to  $2H_d$ ,  $4H_d$  and  $6H_d$ , respectively were constituted. The aspect ratio of finite elements was also varied as 1, 3, and 4, corresponding to 4 m, 12 m, and 16 m, respectively, for the largest element size,  $l_{r,el}$  (Figure 3.13b). The modulus elasticity, Poisson's ratio, and density of the dam concrete were taken as 22.4 GPa, 0.2, and 2483 kg/m<sup>3</sup>, respectively. The acoustic wave speed, Poisson's ratio, and density of water were modeled as 1477.2 m/s, 0.499, and 1000 kg/m<sup>3</sup>, respectively. The mass and stiffness proportional Rayleigh damping coefficients for the dam body were taken as 1 and 0.001, respectively, corresponding to 5% damping at 2 Hz and 14 Hz. For the reservoir, on the other hand, the mass and stiffness proportional Rayleigh damping coefficients were 0.2 and 0.0015, respectively, producing 5% damping at 0.5 Hz and 10 Hz. At the far end of the reservoir, viscous dampers were modeled to simulate the Sommerfeld radiation condition (Bouaanani & Lu, 2009). At the dam-reservoir interface, a constraint was introduced to have the identical displacement at the dam and reservoir in the horizontal direction. In order to ensure this condition, at each node of the fluid element, a modified applied element was modeled at the intersection (Figure 3.13b). In this figure, the black squares with side length  $a$  represent the dam body, the blue rectangle represents one reservoir element, and the nodes at the interface are shown with green. The main advantage of such discretization is that no interface elements are required, and the constraint can be easily defined. With this

discretization, however, the height of one fluid element,  $h_{r,el}$ , should be twice the size of the modified applied element:  $h_{r,el} = 2a$ .



(a) Dam-reservoir model



(b) Dam-reservoir interface

Figure 3.13 Full-scale dam reservoir system

The frequency response of the dam-reservoir system was compared to the validated solutions that were obtained using the computer code EAGD84 with the aforementioned properties and a hysteretic damping coefficient of  $\eta=0.10$  over the whole frequency range (equivalent to 5% damping ratio). The frequency-domain response of the dam-reservoir system is solved for small amplitude, irrotational motion of water, assuming linearly compressible fluid domain with negligible viscosity in this software, considered to be the benchmark for validating other techniques in time and frequency domain (Løkke & Chopra, 2017; Lotfi et al., 1987). The frequency response with MAEM, on the other hand, was obtained by estimating

the linear, time-invariant transfer function, in the frequency domain, for the frequency response function for the crest acceleration of the dam-reservoir system. In order to achieve this, a triangular unit pulse acceleration with 0.02 s duration was applied to the system in the horizontal direction until 60 s, and the transfer function between the applied pulse acceleration and the output crest acceleration was estimated (Figure 3.14). The dynamic analyses were performed with the implemented implicit time-stepping scheme, with a time increment of 0.01 s.

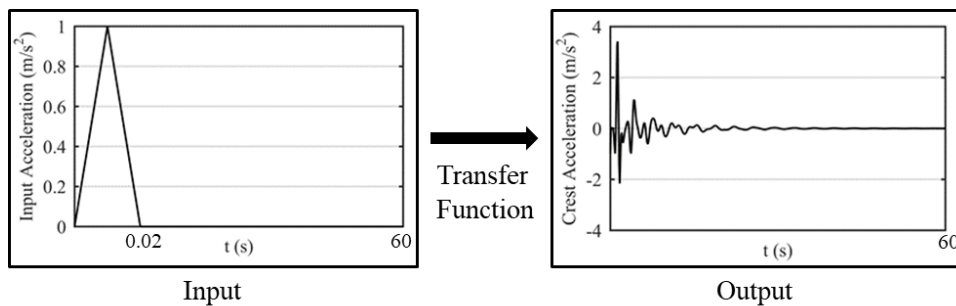
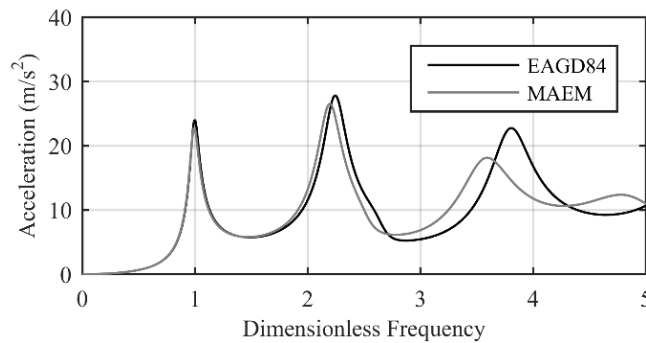


Figure 3.14 Transfer function estimation

Firstly, the frequency response of solely the dam body was compared for the horizontal crest acceleration with MAEM and EAGD84 computer codes (Figure 3.15a). The x-axis of this figure was normalized with respect to the first frequency of the dam body (3.4 Hz) without modeling the reservoir. For the empty reservoir case, the three distinct natural frequencies could be observed clearly. The MAEM results were quite close to EAGD84 results for the 1<sup>st</sup> and 2<sup>nd</sup> modes. For the 3<sup>rd</sup> mode, however, some discrepancy was observed (Figure 3.15a) due to the differences in mesh sizes of both models and the damping ratio specifications of the two methods. Since EAGD84 works in the frequency domain, a hysteretic damping factor of 0.10, which corresponds to a 5% damping ratio, could be specified along a frequency range. In contrast, Rayleigh damping was specified in MAEM; therefore,

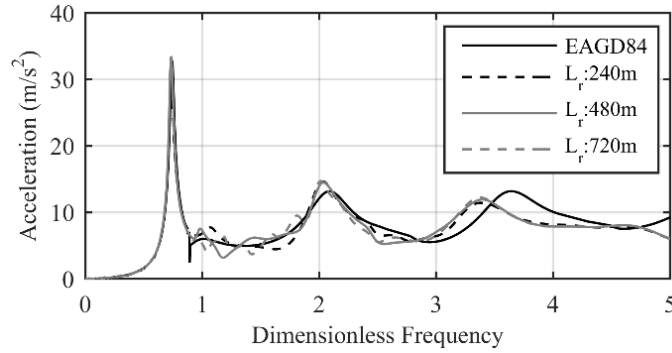
5% damping could not be specified at each mode, and hence the amplitude of the 3<sup>rd</sup> mode was obtained lower.

Next, the results of MAEM and EAGD84 solutions with the reservoir were compared in Figure 3.15b. It should be noted that the reservoir length was modeled as 480 m in EAGD84. In order to investigate the length of the reservoir on the frequency response, three MAEM models with 240 m, 480 m, and 720 m reservoir lengths were modeled utilizing finite elements having aspect ratio 1 (corresponding to 4 m element side length). It could be seen that all three models generally captured the trend in the frequency response well. Due to the reservoir, a sharp increase of the first peak and reduction in the second and third peaks could be simulated. In addition, all periods were elongated. Although the first peak was estimated lower for  $L_r = 240\text{ m}$  case, even with modeling of the reservoir two times the dam height, the frequency response function appears reasonable. However, some small peaks/oscillations between the first two frequencies were observed in the frequency response again due to the limitations of Rayleigh damping. Furthermore, the magnitudes of these small oscillations near the first peak increased with decreasing  $L_r$ , as the reservoir could curl more easily, forming local modes.



(a) Dam body

Figure 3.15 Frequency response comparison



(b) Dam-reservoir system

Figure 3.15 (Continued) Frequency response comparison

The influence of the size and aspect ratio of the u/p mixed element was investigated as well, in Figure 3.16, for the three reservoir lengths, with elements having three different aspect ratios. The aspect ratio was calculated by  $l_{r,el}/h_{r,el}$  (Figure 3.13b). As the modified applied element size was 2 m, all models had a finite element height,  $h_{r,el}$ , of 4 m. For the models with aspect ratio 1, 3, and 4, the corresponding finite element length,  $l_{r,el}$ , were 4 m, 12 m, and 16 m, respectively. The last two values are actually larger than the maximum size of 10m suggested in the literature (Lysmer & Kuhlemeyer, 1969, Bouaanani & Lu, 2009), which is one-twelfth of the considered smallest wavelength,  $H_r = C_r/f_{max}$ , calculated using the maximum frequency of interest and the acoustic wave speed. (The natural frequency of a full reservoir,  $\omega_0$ , was computed as  $\omega_0 = \pi C_r/(2H_r)$  using the acoustic wave speed of reservoir,  $C_r = 1477.2 \text{ m/s}$ , and reservoir height,  $H_r = 120 \text{ m}$ , and the maximum frequency,  $f_{max}$ , was considered as  $f_{max} = 2\omega_0/\pi$ ).

The frequency response functions given in Figure 3.16 show that an increase in the aspect ratio of the elements affected the third mode only; as the largest finite element size increased, the third peak decreased regardless of the reservoir length. Even when the maximum element size was 16 m, greater than the calculated 10 m limit, the 9-node element worked fine, similar to the findings of Bouaanani & Lu (2009). It can be concluded that for the dam-reservoir simulations, the results are satisfactory even

when the extent of the reservoir is taken as twice the dam height, together with finite elements having an aspect ratio of 4, exceeding the computed maximum size of the largest finite element.

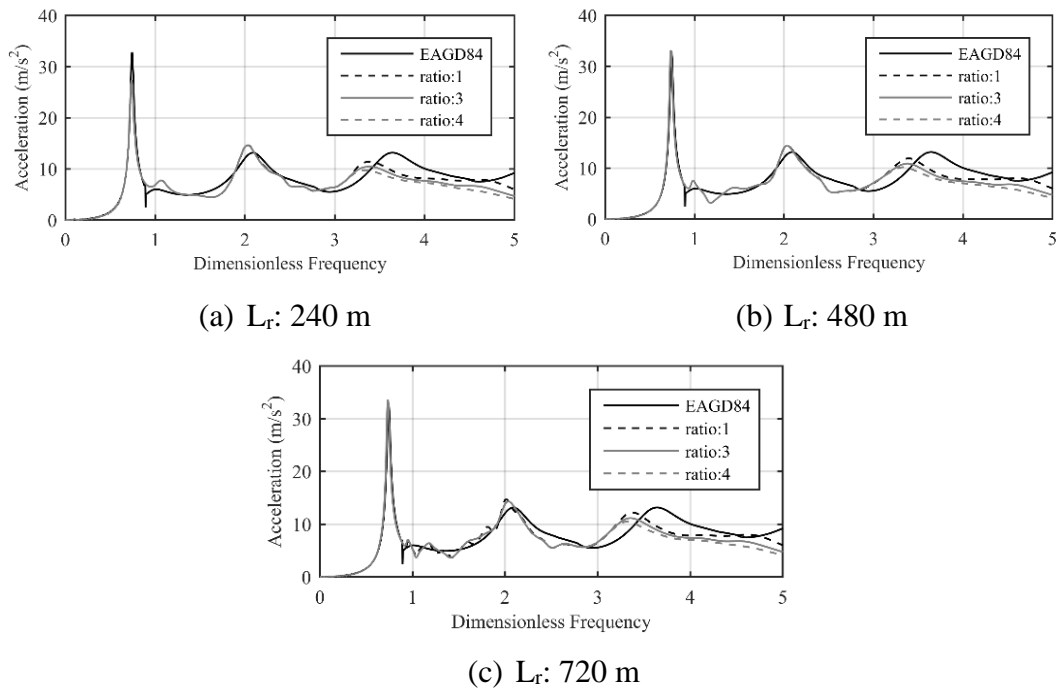


Figure 3.16 Effect of largest finite element size

### 3.7 Nonlinear Dynamic Analysis of Koyna Dam-Reservoir System

Given that the verification of the dam-reservoir systems was conducted successfully in the linear range, the next validation case was selected as the nonlinear dynamic analysis of the Koyna Dam. This dam suffered severe damage during the 1967 Koyna event (Chopra & Chakrabarti, 1973) and was used in several studies for comparing the cracking scheme and validation of the nonlinear material models (Bhattacharjee & Léger, 1994; Calayir & Karaton, 2005b; Wang et al., 2015). It can be seen from Figure 3.17a that cracking occurred at the base of the upstream face and the abrupt

slope change in the downstream side, completely penetrating through the dam body and forming a separate rigid body on the top. The reported cracking patterns were observed on the front of the dam; actually, cracks cannot be observed on the lateral faces of monoliths since access is not possible. The well-documented case serves as a benchmark for validating the analysis tools and reservoir-dam interaction model.

The nonlinear dynamic analysis of the non-overflow monolith of Koyna Dam was performed using the explicit central difference method. The dam, in a plane stress setting, was constituted with modified applied element sizes of 1 m, and the reservoir, with a length of 320 m, was modeled with 2 m x 8 m fluid finite elements (Figure 3.17c). The Young's modulus, Poisson's ratio, density, and tensile strength of the dam were assumed as 31027 MPa, 0.2, 2643 kg/m<sup>3</sup>, and 3 MPa, respectively. For the reservoir, the Poisson's ratio, density, and acoustic wave speed of water were assumed as 0.4999, 1000 kg/m<sup>3</sup>, and 1440 m/s, respectively. For the explicit solution, the stiffness multipliers for mass scaling were selected as  $\alpha = 1 \times 10^{-6}$  and  $\alpha = 2 \times 10^{-6}$  for the dam-reservoir and viscous dampers, respectively. Accordingly, explicit time-stepping with  $\Delta t = 2 \times 10^{-4}$  could be used by applying both the horizontal and the vertical components of the recorded Koyna motion simultaneously. For the transient analysis, 3% mass and stiffness proportional Rayleigh damping at the first and third modes of the structure was utilized. The explicit nonlinear dynamic analysis was conducted after applying the self-weight of the structure. The ultimate strain on normal springs was assumed as  $\varepsilon_{ult} = 0.01$ , with the softening parameter adjusted for proper representation of the fracture energy. As before, compressive behavior was assumed elastic, while the shear springs ceased resistance after the exceedance of the tensile strain limit,  $\varepsilon_t$ . The fracture energy was taken as 250 N/m, with the softening parameter  $c = 50$ .

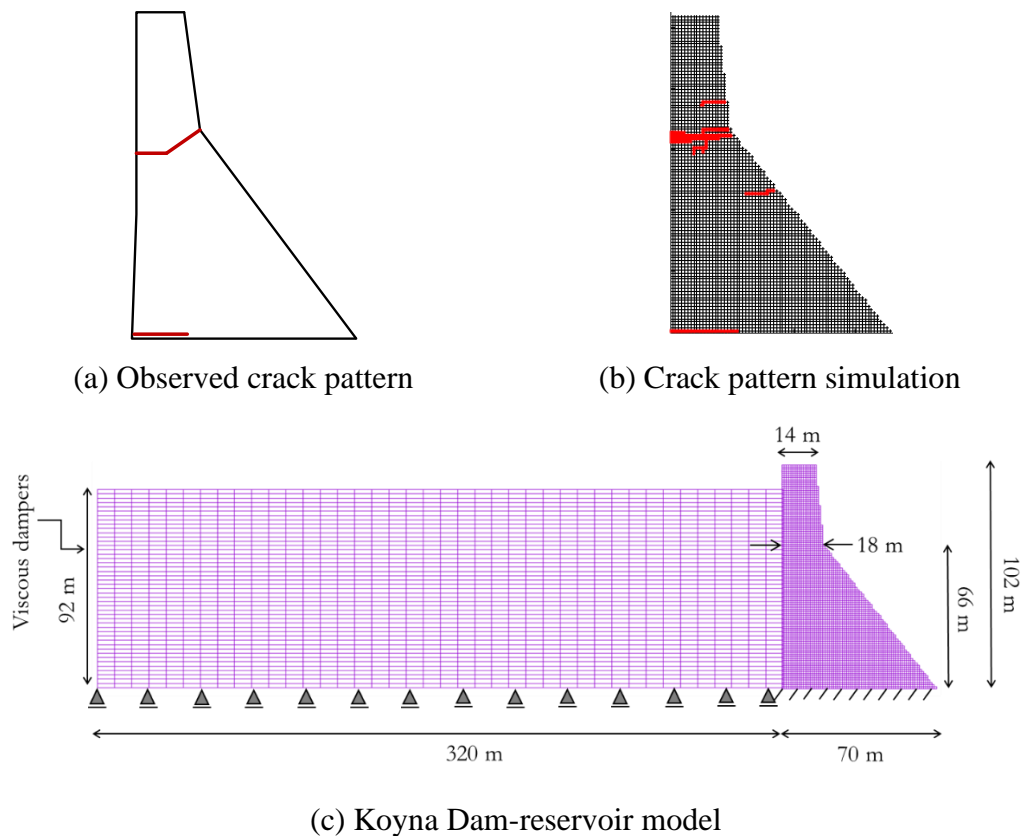


Figure 3.17 Cracking pattern of Koyna Dam

The final cracking pattern of the MAEM solution, given for 0.5 mm crack width, is presented in Figure 3.17b. The localized cracking at the heel of the dam and the downstream side of the monolith where there is a slope change was observed, together with some additional cracks at the downstream face of the dam. These additional cracks emerged from the mesh discretization, where stress localizations occurred. The cracking pattern was compatible with the actual damage on the Koyna Dam.

### 3.8 The Effect of Poisson's Ratio on Results

The influence of Poisson's ratio on the mechanical behavior of brittle materials has not been widely recognized. Although, as early as 1970, Timoshenko et al. (1970)



proposed the beam theory in which the stress of a beam under bending depends on Poisson's ratio, the effects more prominent in continuum structures (compared to slender members) were rarely studied. A closed-form solution of tensile stresses depending on  $\nu$  was derived by Hu et al. (2004) for the split tensile test, and it was found out that at the center of a particle, the tensile stresses differed by 28% for a range of Poisson's ratio 0.0-0.5. It was reported that the deformation field of an elastic plate was affected by the Poisson's ratio such that the deformation was into a saddle shape for positive Poisson's ratio and a convex shape for auxetic solids, having a negative Poisson's ratio (Lakes, 2017). An analytical solution for the longitudinal wave speed through a rectangular slab conducted by Lim (2019) showed that the wave speed increased with increasing Poisson's ratio. Several numerical studies were conducted on steel and rock materials to investigate the effect of Poisson's ratio on the fracture behavior of such materials. A nonlinear static study was conducted utilizing a uni-bond dual-parameter peridynamic model to investigate the effect of  $\nu$  on the deformation and fracture behavior of steel plates (Huang et al., 2019). It was concluded that when a plate was subjected to uniaxial and biaxial loading, the fracture initiation time and crack propagation path was highly dependent on  $\nu$ ; more damage was also likely to occur for materials with higher  $\nu$  (Huang et al., 2019). Utilizing bonded discrete element method, a rock cutting problem was simulated for two different Poisson's ratio, showing that with different Poisson's ratios, different fracture length and fragmentation were obtained (Zhao et al., 2019).

In the discrete element methods, the effect of Poisson's ratio is often ignored. The formulations usually allow the representation of a distinct value, such as  $\nu = 0$  for the original applied element method (Meguro & Tagel-Din, 2000),  $\nu = 0.25$  for 3D and plain strain cases, and  $\nu = 0.33$  for plane stress case for the lattice models (Zhao et al., 2011). These restrictions on  $\nu$  results in limitations for the accurate simulation of elastic deformations and elastic waves (Madan, 2019). Acknowledging the Poisson's effect on the behavior of structures, to model this mechanical behavior within a variety of range, research has been conducted to break the limitation of the specific Poisson's ratio. The Poisson's effect was represented indirectly through

uniaxial concrete test simulations by modifying the normal and shear stiffnesses, which increased the lateral deformation in the numerical model (Nagai et al., 2004). Several studies were conducted considering the particle packing and particle size distribution to be able to represent the Poisson's effect in the discrete methods. For the simulation of granular media under compression, the effect of the particle size distribution of granular packings was investigated through statistical methods, and when the particle diameters were normally distributed, the Poisson's ratio in the 3D simulations lied in the range 0.25-0.30 (Wiącek & Molenda, 2014). It was shown in another study that the particle packing affected the Poisson's ratio significantly; for a weakly jammed packing, the Poisson's ratio could be simulated with the upper boundary of 0.35 and lower boundary of -0.5, enabled to model auxetic materials as well (Kumar et al., 2016). A wider span of attainable Poisson's ratio ( $-0.1 < \nu < 0.5$ ) was obtained with a random-packed particle model together with shear interaction factor (Zhao et al., 2019). A variety of Poisson's ratio ( $0.1 \leq \nu \leq 0.33$ ) could be simulated by modifying the peridynamic method with the introduction of tangential stiffness to develop the uni-bond dual-parameter peridynamic model (Huang et al., 2019). An analytical study, also compared with numerical models, to determine the limits of Poisson's ratio was conducted by Eliáš (2020) on isotropic, arbitrary geometry models in the statistical sense, and the model geometry with Voronoi tessellation obtained the widest Poisson's ratio limits. Recently, a modified rigid body spring model was suggested directly modeling the Poisson's ratio without an increase in the computational cost (Mehrpay et al., 2020). Similarly, the particular modification to the applied element methodology provides the opportunity to investigate the effect of Poisson's ratio on such a discrete body model directly. In the following sections, for the same MAEM validation studies given above in the plane stress setting, the effect of Poisson's ratio on the response is investigated.

### 3.8.1 Linear Static Analysis of a Cantilever Column

Linear static analysis of continuum media and the estimation of the corresponding displacement field in the small displacement range is likely where the Poisson's ratio matters the most significantly. The prediction of the lateral expansion at the tip of the cantilever obtained directly because of the Poisson's effect due to an axial load (Case I in Figure 3.1a) was first investigated by comparison to the theoretical result obtained by the Poisson's ratio formula  $\nu = -\varepsilon_t/\varepsilon_l$ , with transverse strain,  $\varepsilon_t$  and lateral strain,  $\varepsilon_l$  for the Poisson's ratios of 0.1, 0.2, 0.3 and 0.4 (Figure 3.18) with 10 connecting spring pairs. It should be noted that when Poisson's ratio is greater than  $1/3$ , the shear springs have negative stiffness in the model. In accordance with Zhao et al. (2011), for modeling elastic solids, negative shear springs produce good results (Figure 3.18). The representation of the Poisson's ratio in the model improved with an increase in mesh density as expected, validating the theoretical approach. Lateral displacement could be simulated with approximately 7% error with the fine mesh.

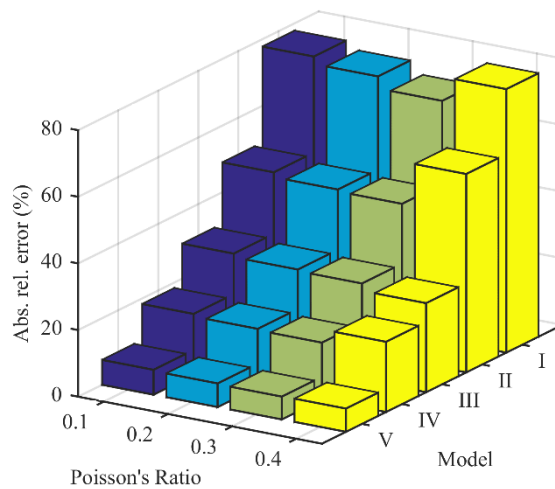


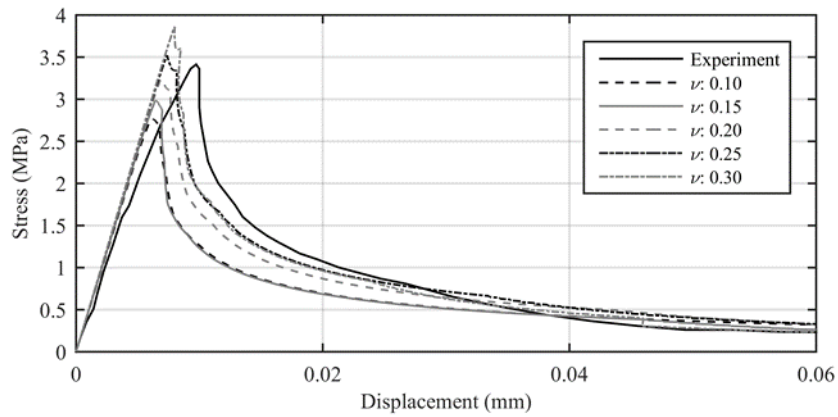
Figure 3.18 Lateral displacement comparison for axial loading

Poisson's ratio affects the stress distribution in a continuum with complex boundary conditions; in this sense, it affects the nonlinear behavior indirectly. The effects of the Poisson ratio on the cracking behavior observed in the validation tests are examined below.

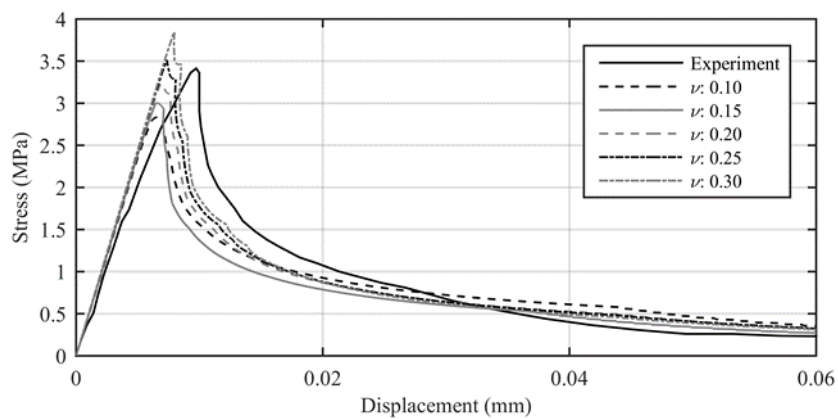
### 3.8.2 Uniaxial Tension Test

The effect of Poisson's ratio on the nonlinear behavior of plain concrete structures was first investigated in the context of the uniaxial tension test investigated in Section 3.4.2. Analyses were conducted on Model I, with 10 mm element size, for a variation of Poisson's ratio in the  $\nu = 0.2 \pm 0.1$  range with 0.05 increments, i.e., for  $\nu = 0.10, 0.15, 0.20, 0.25, 0.30$ . According to the fracture energy formulation, for the same parameters  $c$  and  $\varepsilon_{ult}$ , as  $\nu$  increases,  $G_f$  also increases. Therefore, in order to eliminate the variability of  $G_f$  and focus the response based only on the change of  $\nu$ , the simulations for this test were conducted for a constant  $G_f$ . Indeed, the same  $G_f$  with respect to different  $\nu$  can be obtained by changing  $c$  and  $\varepsilon_{ult}$  with two alternatives. For the first case,  $c$  is kept constant, and as  $\nu$  increased,  $\varepsilon_{ult}$  is decreased. Conversely, in the second case, for a constant  $\varepsilon_{ult}$ ,  $c$  is increased with increasing  $\nu$ . In the first case, the softening parameter,  $c$ , was kept constant as 0.66 and the ultimate tensile strain,  $\varepsilon_{ult}$ , was adjusted to obtain identical fracture energy in all models. The  $\varepsilon_{ult}$  for  $\nu=0.10, 0.15, 0.20, 0.25,$  and  $0.30$  were taken as 0.012, 0.010, 0.008, 0.006, and 0.005, respectively. Conversely, in the second case, analyses were conducted under a constant  $\varepsilon_{ult} = 0.008$  and varying  $c$  accordingly as 0.55, 0.61, 0.66, 0.70, and 0.75, for  $\nu=0.10, 0.15, 0.20, 0.25,$  and  $0.30$ , respectively. In all of the analyses, similar to the  $\nu = 0.2$  case, a joining crack between the notches was observed. The stress-displacement behavior, on the other hand, was affected by the material parameter  $\nu$  (Figure 3.19). When  $c$  was kept constant, and  $\varepsilon_{ult}$  was adjusted accordingly, as  $\nu$  increased, the structural capacity estimation was higher (Figure 3.19a). For this simulation, similarly, the capacity increased as  $\nu$  increased, for the constant  $\varepsilon_{ult}$  case (Figure 3.19b). In both analyses, the increase in  $\nu$  led to an increase

in the capacity; however, for the constant  $\varepsilon_{ult}$  case, the capacity difference between  $\nu=0.10$  and  $0.30$  was obtained slightly less than the first case with a constant  $c$ .



(a) Constant  $c$  analyses



(b) Constant  $\varepsilon_{ult}$  analyses

Figure 3.19 Stress-displacement response for different  $\nu$

### 3.8.3 Splitting Tension Test

The effect of modeling the Poisson's ratio in the discrete nonlinear setting was next investigated using the splitting tension test. For the third model with 1 mm mesh size, the material parameters  $c$  and  $\varepsilon_{ult}$  were kept constant as 0.22 and 0.075,

respectively, to consider the variation of  $G_f$ , as well, so that different fracture energy would lead to different estimations of the splitting tensile strengths with respect to varying Poisson's ratio. Accordingly, as the Poisson's ratio increased, fracture energy also increased. Similar to the previous problem, a variety of Poisson's ratio in the  $\nu = 0.2 \pm 0.1$  range with 0.05 increments were studied. The splitting tensile strengths,  $f_{t,sp}$ , were again calculated according to Equation (3.2) are presented in Table 3.1. The results showed that similar to the uniaxial tension test, for this simulation, the capacity was directly affected by  $\nu$ , as well. However, the computed splitting capacity increased with a decrease in  $\nu$ , in contrast with the previous simulation. The capacity in this test, with a relatively more brittle ending compared to the other tests, apparently does not depend on the ultimate capacity of the material.

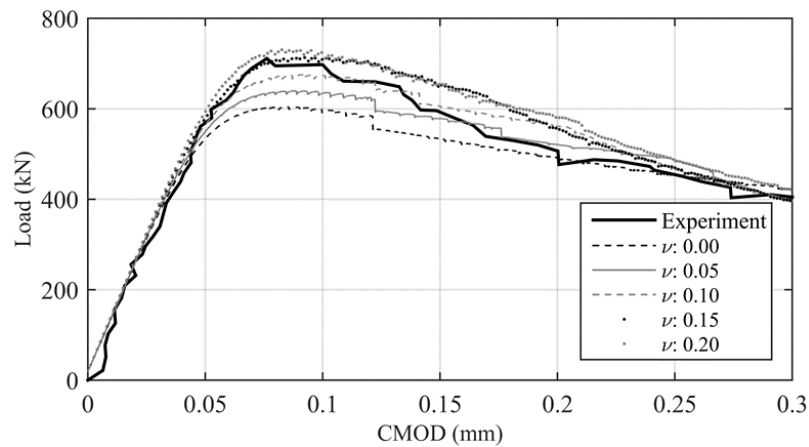
Table 3.1 Splitting tensile strengths for different Poisson's ratio

$\nu$	0.10	0.15	0.20	0.25	0.30
$f_{t,sp}$ (MPa)	2.24	1.89	1.80	1.72	1.68

### 3.8.4 Push-Over Loading Problem of a Notched Model Concrete Dam

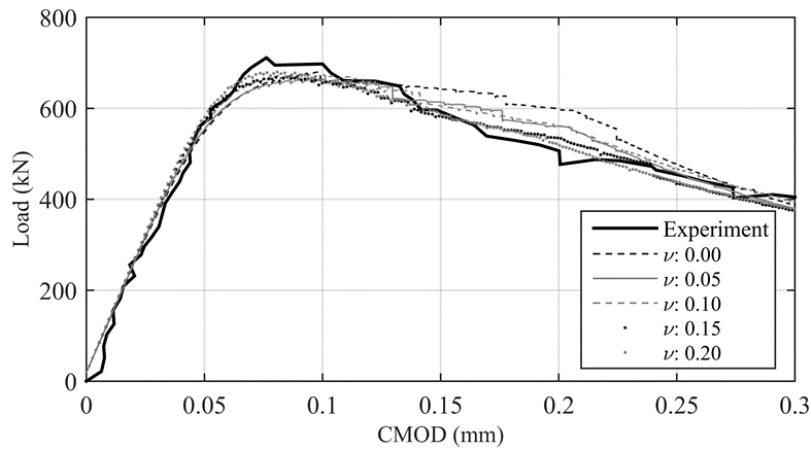
The nonlinear response of the notched model concrete dam subjected to push-over loading was investigated as well to study the effect of Poisson's ratio on the load-CMOD behavior and the final deformation. For the most refined mesh (Model III with 0.02 m element size), two sets of analyses were conducted by keeping the fracture energy constant to focus the response based only on the change of  $\nu$ , for the Poisson range  $\nu = 0.1 \pm 0.1$  with 0.05 increments, i.e., for  $\nu = 0.00, 0.05, 0.10, 0.15, 0.20$ . The same  $G_f$  with respect to the Poisson range can be obtained by changing  $c$  and  $\epsilon_{ult}$  with two alternatives. For the first case,  $c$  is kept constant, and as  $\nu$  increased,  $\epsilon_{ult}$  is decreased. Conversely, in the second case, for a constant  $\epsilon_{ult}$ ,  $c$  is increased with increasing  $\nu$ . In the first case,  $c$  was kept as 0.55, and

according to the fracture energy,  $\varepsilon_{ult}$  were taken as 0.0120, 0.0090, 0.0070, 0.0054, and 0.0045 for  $\nu=0.00, 0.05, 0.10, 0.15,$  and  $0.20,$  respectively. In second case, on the other hand, analyses were conducted for  $\varepsilon_{ult} = 0.007$  and  $c$  was accordingly taken as 0.46, 0.51, 0.55, 0.61 and 0.65, for  $\nu=0.00, 0.05, 0.10, 0.15,$  and  $0.20,$  respectively. The load vs. CMOD graphs are presented in Figure 3.20. For the first analysis case with a constant  $c$ , the increase in  $\nu$  led to increased capacity (Figure 3.20a). For the second case under the same  $\varepsilon_{ult}$ , on the other hand, although a slight increase in the capacity was obtained as  $\nu$  increased, the capacities were estimated closely (Figure 3.20b), unlike the uniaxial tension test results. In addition, in Figure 3.21, the deformed shapes, scaled by 500, at the end of the simulation are given. In all models, inclined cracking was observed, similar to the experimental observation.



(a) Constant  $c$  analyses

Figure 3.20 Load-CMOD response for different  $\nu$



(b) Constant  $\epsilon_{ult}$  analyses

Figure 3.20 (Continued) Load-CMOD response for different  $\nu$

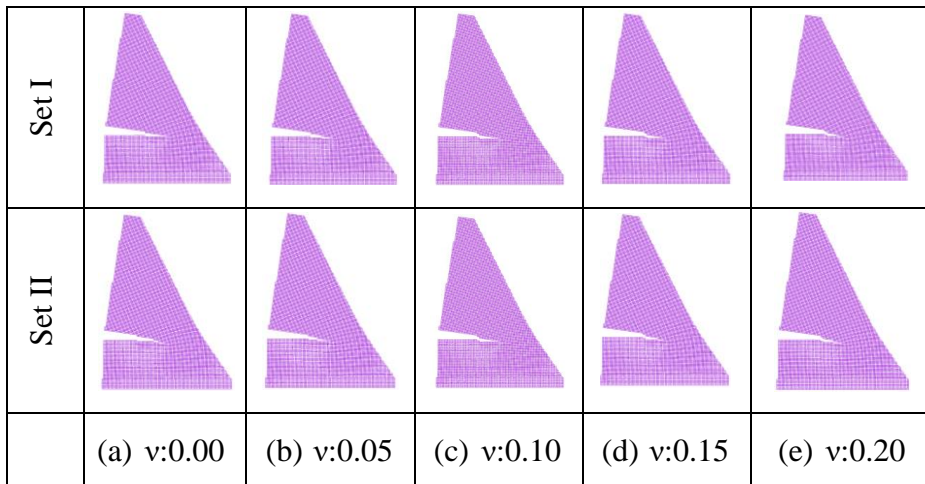


Figure 3.21 Deformed shapes for different  $\nu$

In the fracture energy formulation,  $G_f$  and  $\nu$  were proportionally related, and the increase in  $\nu$  led to an increase in  $G_f$ . The effect of Poisson's ratio was shown to increase the fracture energy for materials such as metallic glasses (Tandaiya et al., 2008); however, as there are no experiments on this issue in concrete, the fracture energy  $G_f$  was kept constant for varying Poisson's ratio in the uniaxial tension and push-over loading simulations. For the split tension test, the same softening parameters were utilized for varying  $\nu$ ; even for theoretically higher  $G_f$  values for



higher Poisson's ratios, the capacities were obtained lower, unlike the previous simulations. The capacity in this test, with a relatively more brittle ending compared to the other tests, apparently does not depend on the ultimate capacity of the material.

### 3.9 Computational Aspects of MAEM

The computation times with respect to the element sizes and the number of spring pairs were investigated for a nonlinear dynamic problem constituted with MAEM. To this end, the Koyna dam body was modeled with modified applied elements, ignoring the reservoir effects, and analyzed using the nonlinear explicit dynamic solver for an input acceleration having a duration of 1 second. In the plane stress setting, three models with different element sizes, 2 m (Model I), 1 m (Model II), and 0.5 m (Model III), were used in the simulations with 2715, 10959, and 43680 degrees of freedom, respectively. In order to investigate the effect of the number of connecting springs between elements on the run times, each model was analyzed with 1, 3, 5, 10, and 20 spring pairs. Accordingly, for each spring pair connecting the elements, the total spring numbers, including the diagonal springs, are presented in Table 3.2 for the three models. It can be seen from this table that as the element size is halved, the total number of springs is increased four times.

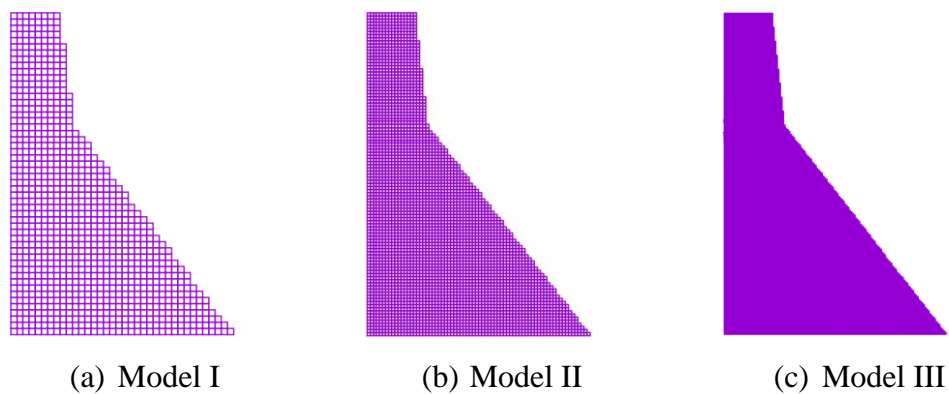


Figure 3.22 Koyna Dam models

Table 3.2 Total spring numbers

Spring Pair #	Total Spring Number		
	Model I	Model II	Model III
1	3530	14430	57876
3	7118	28978	115988
5	10706	43526	174100
10	19676	79896	319380
20	37616	152636	609940

The solution times with respect to the number of spring pairs for an input earthquake with a 1-second duration is given in Figure 3.23 for the models. The performance analyses were conducted on a system with Intel Core i7 3.40 GHz processor and 16 GB RAM using Windows 10 operating system. In all models, the increase of the number of spring pairs from 1 to 20 (i.e., the total spring number is increased by approximately 10 times) increased the computational cost approximately 1.7 times. For a constant spring pair number, on the other hand, as the mesh got finer (i.e., as the element size is halved and the number of degrees of freedom increased roughly four times), on average, the solution time increased 4.7 times.

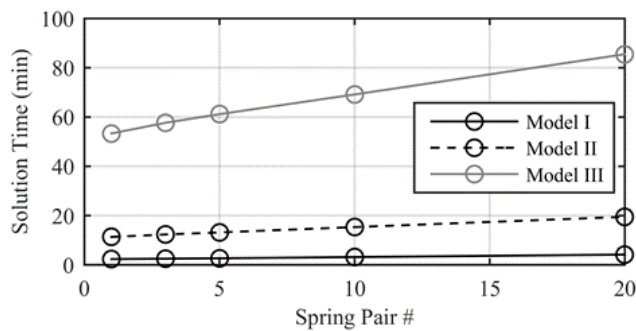


Figure 3.23 Solution time comparison

### **3.10 Summary**

In this chapter, a set of validation tests were conducted to verify the proposed modified applied element method and the implemented displacement/pressure based mixed finite reservoir. After the modified applied elements were validated in the linear setting for a cantilever column under different types of loadings, the convergence rate of the proposed methodology was investigated by solving a shear wall and a frame problem loaded laterally. The verification of modified applied elements in the nonlinear static setting was then conducted by a direct tension simulation first to show the nonlinear loading, unloading, reloading branches of the implemented material model. Next, experimental studies in the literature were studied by simulating the uniaxial tension test of a rectangular concrete prism, splitting tension test of a cylindrical concrete specimen, and the push-over loading of a scaled dam experiment in the literature. The fluid elements, on the other hand, were validated in static and modal analysis first, then the behavior of the coupled modified applied-finite elements system was investigated by performing frequency response analysis accounting for the fluid-structure interaction. The nonlinear response of Koyna Dam-reservoir system was also investigated to verify the coupling of modified applied-finite elements in the nonlinear dynamic setting by means of crack simulation on the dam body. Finally, the simulation of the Poisson's effect was validated in a separate section, along with the investigation of the Poisson's effect on the capacity and cracking behavior in different loading scenarios in the same validation tests. The results of these studies are summarized as follows:

#### **3.10.1 Summary – Linear Validations**

- The robustness of MAEM was verified for static linear elastic problems of a cantilever column under different types of loadings. As expected, the error in predicting the results compared to the theoretical solutions decreased with

increasing mesh density. Moreover, the error decreased when the number of springs between elements increased.

- The normal and shear stress distribution at the base, along the width of the laterally loaded cantilever column, was investigated, and it was shown that the theoretical normal stress distribution could be obtained by even a coarse mesh. Moreover, the presence of shear springs in MAEM enabled the simulation of shear effects. The shear stress in between any two modified applied elements was constant. Accordingly, by making the mesh more refined, the theoretical shear stress distribution could be captured.
- The number of spring pairs had effects on linear static problems, depending on the type of the problem, mesh density, and the Poisson's ratio. For the case of  $\nu=0.2$ , when the slenderness effect was less (the shear wall problem) in which shear is dominant, and no significant rotations occur in the elements, the effect of the connecting spring number was less significant. Conversely, for a more slender problem such as the cantilever column and tall frame problems, error decreased significantly by increasing spring pair number, especially for coarse meshes. For the  $\nu=0.33$  case, on the other hand, the spring pair number (i.e., for 1 and 10 spring pairs) did not affect the results for both shear wall and tall frame problems. In this case, shear springs vanished in the numerical model; therefore, the applied loading was directly transferred to the bottom layers by diagonal springs. Hence, these springs cannot cause rotation on an element.
- The theoretical representation of accounting for the Poisson's effect in the modified applied element methodology, as presented in Chapter 2, was verified in linear static problems in this section. The proposed methodology showed superiority over discrete methods that ignore the Poisson's effect or able to model only a fixed Poisson's value with identical elements. The lateral expansion of the cantilever column was also affected by the mesh density, similar to the estimation of tip displacements, such that as the element size got smaller, the representation of Poisson's ratio was better.

- The convergence rate of MAEM was also investigated through linear static problems of laterally loaded shear wall and frame problems by comparing the results with FEM solutions. The difference between the results of a coarse and fine mesh of an identical structure was higher in MAEM compared to FEM. The main reason for this difference is the boundary condition definitions in FEM and MAEM. In FEM, boundary conditions are assigned to a joint; therefore, the restrictions for the degrees of freedom influence only the points. Conversely, in MAEM, the degrees of freedom are located at the centroids of the elements, so when a boundary condition is assigned to a single element, the movement of the whole rigid element is restricted. This effect is especially significant for coarse meshes, as in this case, a larger part of the structure is restricted to move. By making the mesh finer, however, this effect becomes less prominent. The difference of MAEM estimation was obtained at around 5%, with the element size at  $1/40^{\text{th}}$  of the width of the member for a shear dominated problem. A similar difference (5%) was obtained for element size at  $1/10^{\text{th}}$  of the member size in a problem dominated by bending. The difference in the solution for both approaches were around 1% for very small element sizes ( $1/200^{\text{th}}$  and  $1/40^{\text{th}}$  of member width, respectively). It was demonstrated that MAEM exhibited a linear convergence rate, which is acceptable in the available computational capacity.
- The computational cost of MAEM models was investigated in the linear static solution of a shear wall and a frame problem using the PARDISO solver. Making the mesh finer led to an increase in both the spring and DOF numbers. For the shear wall problem, when the total number of elements was increased from 1600 to 25600, both the DOF and total spring numbers increased approximately 16 times; the solution time increased 30 times. For the frame problem, on the other hand, a similar increase in the DOF (16 times, 3679 to 58879 elements) led to a 60 fold increase in the computational cost. The input-output times appear to be effective in the computational cost.

- The solution times of FEM and MAEM were compared for the frame problem. In the FEM model with a 0.005 m element size, corresponding to 282294 DOF, the solution time was less than 1 minute. In a comparable MAEM model with a mesh size of 0.00625 m and 176445 DOF, the solution time was approximately 5 minutes. The difference in the solution times was due to the assembly of the stiffness matrix in MAEM: In the MAEM solution algorithm, the stiffness matrix is assembled with contributions from each spring pair. For the aforementioned model with 10 spring pairs connecting each interface, a total of 1.3 million springs are obtained, increasing the workload.
- The implemented fluid finite elements were verified by comparing the pressure distribution of a water tank under its self-weight with the theoretical solution. Moreover, the modal properties of a water column were estimated correctly compared to the analytical solution. By utilizing the fluid finite elements, water compressibility and viscosity could be included in the simulations, in contrast to the full acoustic pressure or potential based solutions.
- The coupling of the proposed modified applied elements with the implemented fluid finite elements was evaluated in detail with the frequency response analysis of an idealized full-scale dam-reservoir system. In this model, the applicability of the radiation boundary condition to represent the loss of energy by the outgoing waves at the far end of the reservoir was shown. The effects of the reservoir length and the maximum size of the finite element through this length were also evaluated. The implemented fluid elements, together with the radiation boundary condition, showed that the dam-reservoir interaction was captured well using a reservoir length just two times the dam height modeled with fluid elements having large sizes and relatively high aspect ratios.

### 3.10.2 Summary – Nonlinear Validations

- Direct tension simulation on a simple MAEM model showed that the nonlinear Maekawa tension softening material model to the springs was implemented successfully. The nonlinear softening started at the specified strain, and the nonlinear loading, unloading, and reloading branches were clearly modeled.
- The verification of MAEM in the nonlinear setting was demonstrated by employing the nonlinear Maekawa tension softening material model. This material model is simply defined with respect to two parameters, the softening parameter,  $c$ , and the ultimate tensile strain,  $\epsilon_{ult}$ . The softening parameter quantifies the post-peak behavior of the curve, and when the ultimate tensile strain is reached, the springs no longer carry any force. The fracture energy,  $G_f$ , is obtained in accordance with the element size based on the parameters  $c$  and  $\epsilon_{ult}$ . Ideally,  $\epsilon_{ult}$  should be selected based on uniaxial tension tests, corresponding to the strain level for the springs such that when this ultimate level is reached, springs can no longer carry any force. Then,  $c$  can be computed for the prescribed  $G_f$  and  $\epsilon_{ult}$  values. In the numerical models,  $\epsilon_{ult}$  depends on the mesh size, and as the element size is decreased,  $\epsilon_{ult}$  should be increased to get the same displacement level such that the spring cannot carry the load anymore (i.e., spring has no capacity to carry any load). Then, the  $c$  value should be adjusted accordingly to represent the desired  $G_f$ . In addition to the change in  $\epsilon_{ult}$  with respect to the element size,  $c$  is adjusted in accordance with the mesh size. Given that the area under the stress-strain curve is characterized by the fracture energy divided by the mesh size, for the same  $G_f$ , the area should be larger for finer meshes. Therefore, for smaller element sizes, in addition to the increase in  $\epsilon_{ult}$ ,  $c$  should be selected smaller (corresponding to a less brittle softening curve that increases the area under the stress-strain curve). Then, the shape of the post-peak curve of the experimental results may not be represented well for small element sizes (less

than 5 mm, according to the uniaxial tension test simulations conducted in this study). Despite such drawbacks of the softening behavior, the employed material model has its simplicity by defining the post-peak shape with a single parameter,  $c$ .

- Through the nonlinear simulations, the Maekawa material model was introduced to the normal springs only (horizontal, vertical, and diagonal). Shear springs, on the other hand, were assumed to be brittle. When the tensile strength of the normal spring was reached, the stiffness and force terms of the corresponding shear spring pair were eliminated. The verifications under various loading types, such as direct tension, indirect tension, bending, and earthquake loading, showed that this assumption on the behavior of shear springs was acceptable.
- The nonlinear analyses of the uniaxial tension test on a rectangular concrete prism showed that the capacity, softening trend, and therefore, the fracture energy of the specimen could be simulated close to the reported experimental results. The parameters of the implemented tension softening material model,  $c$  and  $\epsilon_{ult}$ , were computed in accordance with the element sizes of the numerical models that were able to represent the reported global material parameters,  $E$ ,  $\nu$ , and  $G_f$ . Furthermore, similar to the experimental observations, a complete crack between the notches of the specimen was observed.
- The proposed methodology, MAEM utilizing the Maekawa tension softening material model, was verified by modeling the splitting tension test of a cylindrical concrete specimen. Three numerical models were constituted with different mesh densities, and the splitting tensile strengths were computed for each model. Following the researchers' proposal for the relationship between direct tensile strength and splitting tensile strength, the calculated splitting tensile strengths were evaluated. In the MAEM simulations, there were limitations for modeling the contact in between the load bearing strips and the specimen, and stress localization occurred for the coarser meshes that



affected the overall behavior. Nevertheless, as the mesh density increased, stress localization reduced; accordingly, a better estimation of the splitting capacity was made.

- In addition to direct and indirect tension loadings, another loading type to validate the nonlinear static solution of MAEM was the simulation of the push-over experiment of a scaled concrete dam. Similar to the previous problems, the material model parameters,  $c$  and  $\varepsilon_{ult}$  were computed with respect to the element sizes of the numerical models and were able to represent the reported global material parameters,  $E$ ,  $\nu$ , and  $G_f$ . The capacity and softening behavior were simulated well as the mesh got finer. Moreover, the cracking scheme, in accordance with the experimental outcomes, was obtained with the fine meshes that were able to simulate the inclined cracking.
- The Koyna Dam-reservoir system under the horizontal and vertical components of the Koyna Earthquake was modeled to validate the dynamic analysis of MAEM. In the model, the nonlinear tension softening material model was assigned to the dam body, and the fluid elements were utilized together with the radiation boundary condition. The solution was conducted by employing explicit nonlinear algorithm utilizing the mass scaling method. The cracking simulation of the dam body compared well with the actual observed damage; however, some additional cracks at the downstream face of the dam were also observed. These additional cracks emerged from the mesh discretization, where stress localizations occurred.
- The effect of Poisson's ratio on the nonlinear response of structures was investigated for the uniaxial tension test on a rectangular concrete prism, splitting tension test of a cylindrical concrete specimen, and push-over experiment of a scaled concrete dam test. According to the fracture energy formulation, for the same parameters  $c$  and  $\varepsilon_{ult}$ , as  $\nu$  increases,  $G_f$  also increases. Therefore, in order to eliminate the variability of  $G_f$  and focus the response based only on the change of  $\nu$ , the simulations for the uniaxial

tension and push-over tests were conducted for a constant  $G_f$ . Indeed, the same  $G_f$  with respect to different  $\nu$  can be obtained by changing  $c$  and  $\varepsilon_{ult}$  with two alternatives. For the first case,  $c$  is kept constant, and as  $\nu$  increased,  $\varepsilon_{ult}$  is decreased. Conversely, in the second case, for a constant  $\varepsilon_{ult}$ ,  $c$  is increased with increasing  $\nu$ . It was shown that Poisson's ratio had an apparent effect on the capacity of structures. For the uniaxial tension test simulation, when  $c$  was kept constant, and  $\varepsilon_{ult}$  was adjusted accordingly, as  $\nu$  increased, the structural capacity estimation was higher. For this simulation, similarly, the capacity increased as  $\nu$  increased, for the constant  $\varepsilon_{ult}$  case. For the push-over loading, the same modeling approaches mentioned above were conducted as well. Under a constant  $c$ , the capacity was estimated higher for higher  $\nu$ . For the second case conducted under the same  $\varepsilon_{ult}$ , the effect of  $\nu$  was not as evident as in the uniaxial tension simulation. Although a slight increase in the capacity was obtained as  $\nu$  increased, the capacities were estimated closely. The splitting tension test simulations, on the other hand, were conducted by keeping  $c$  and  $\varepsilon_{ult}$  constant to consider the variation of  $G_f$ , as well. Accordingly, as  $\nu$  increased,  $G_f$  also increased. The results showed that for this simulation, the capacity was directly affected by  $\nu$ , as well. However, the computed splitting capacity increased with a decrease in  $\nu$ , in contrast with the above two simulations.

- In the fracture energy formulation, the  $G_f$  and  $\nu$  were proportionally related, and the increase in  $\nu$  led to an increase in  $G_f$ . The effect of Poisson's ratio was shown to increase the fracture energy for materials such as metallic glasses; however, as there are no experiments on this issue in concrete, the fracture energy  $G_f$  was kept constant for varying Poisson's ratio in the uniaxial tension and push-over loading simulations. For the split tension test, the same softening parameters were utilized for varying  $\nu$ ; even for theoretically higher  $G_f$  values for higher Poisson's ratios, the capacities were obtained lower, unlike the previous simulations. The capacity in this test,

with a relatively more brittle ending compared to the other tests, apparently does not depend on the ultimate capacity of the material.

- The computational aspects of MAEM were investigated on Koyna dam body model utilizing nonlinear explicit dynamic solver for an earthquake with one-second duration. Three models with different mesh densities were formed, and each model was analyzed with five different spring pair numbers. Accordingly, for a given mesh, when the total spring number was increased by approximately 10 times, the computational cost increased approximately 1.7 times. On the other hand, when the element size was halved and the number of degrees of freedom increased four times, the solution time increased approximately 4.7 times showing linear scaling for the explicit solver.



## CHAPTER 4

### NONLINEAR BEHAVIOR OF CONCRETE AND ROLLER- COMPACTED CONCRETE GRAVITY DAM-RESERVOIR SYSTEMS DURING SEISMIC EXCITATION

#### 4.1 Introduction

Extensive validation studies were conducted for the verification of modified applied element, fluid finite element, and the coupling of these two elements in the preceding chapter, showing that MAEM models are capable of representing the behavior of concrete structures both in the linear and nonlinear range. Hence, the implemented nonlinear material model can be used to investigate the occurrence of damage on dam monoliths. The verification of the displacement/pressure based mixed finite element and its coupling with MAEM was also successfully demonstrated in Chapter 3, leading to the study herein to examine the nonlinear behavior of 100 m high dam monolith-reservoir system under seismic actions by performing incremental dynamic analysis (IDA).

The prediction of the nonlinear behavior of gravity dams under seismic actions is challenging. First of all, there should be a clear damage indicator to quantify the performance limits of such structures based on the cracking on these systems. The parameters used as damage indicators should properly relate to the severity of damage that the dam has undergone. Another important point in investigating the nonlinear behavior of gravity dams is establishing the numerical model properly to produce reliable results. The tool to construct the numerical model needs to be capable of representing the nonlinear behavior adequately. While the finite element method (FEM) is a commonly utilized tool to predict damage on concrete dam bodies, diffused cracking patterns has been reported as a significant disadvantage in fracture simulation. Another limitation of FEM is that the layered structure of roller-

compacted concrete (RCC) cannot be modeled directly, leading to simulations in which these weak layers are ignored or smeared to the model. These limitations of FEM, on the other hand, can be overcome by utilizing discrete element-based methods that simulate the discrete fracture phenomenon properly on concrete and RCC gravity dams. Using such a discrete technique enables modeling the effect of lift joints of RCC directly as well. Given that work regarding setting performance limits on RCC dams are limited, it will be possible to quantify the damage to investigate the nonlinear behavior of RCC dams under seismic actions with the used methodology.

To this end, the seismic performances of identically shaped concrete and RCC dam monoliths were evaluated using incremental dynamic analysis (IDA) technique in this study. This commonly used procedure, to determine a relationship between intensity measures (IM) of ground motions and engineering demand parameters of the structure, is conducted using several ground motions that are incrementally scaled to a desired level. Hence, IDA enables investigating the effect of different ground motion characteristics, as a variety of motions are selected and scaled at various levels enabling the investigation of the effect of ground motion properties on the nonlinear behavior of structure quantified in terms of demand parameters. The damage quantification of gravity dams can be made considering several demand parameters obtained as the output of dynamic analyses, with cracking of the system as the main concern in the behavior. Along with the limit states based on the extent of cracking towards the core of the dam, the use of a discrete element technique allowed the use of crack width based measures for the first time in this study. The relationship between ground motion intensity measures and crack widths on the system were studied. In addition to the damage assessment within the seismic event, the post-earthquake performance was also be quantified by considering the residual crack openings and the leakage estimations through these cracks at the base and at the upstream surface. These numerical indicators enabled the introduction of a crack width related assessment of the seismic performance of these dams.

In this chapter, first, the numerical models used in the study are introduced. Two coupled dam-reservoir systems were formed utilizing MAEM and fluid elements to simulate the dam body and reservoir, respectively. A concrete gravity and an RCC gravity dam having identical geometries for the dam body were evaluated. The concrete gravity dam was modeled with homogenous material properties throughout the dam body. On the other hand, the effect of lift joints was taken into account in the RCC gravity dam by modeling the lift joints with lower strength. In order to assess the performance of these systems under seismic actions, IDA was conducted on a ground motion set comprised of 21 motions, each scaled to 17 different intensity levels leading to 357 nonlinear transient analyses for each model. The comparison for the seismic performance of a concrete and an RCC dam and the quantification of damage was made under the same input motions. After the utilized ground motion set is explained together with the IDA procedure, the fragility analysis and the limit states used to construct these fragility functions are introduced, giving way to the analyses.

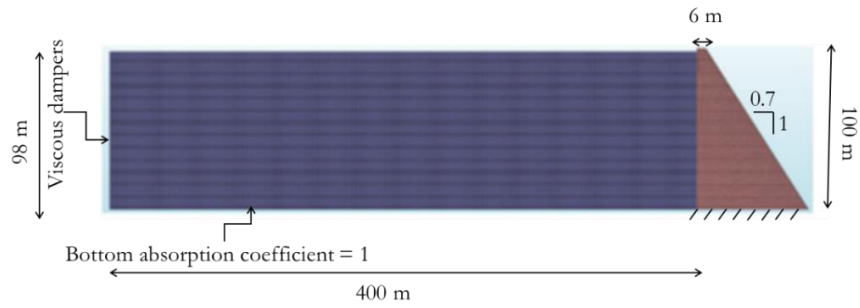
The first set of analyses presented in this chapter are those for the concrete dam whose results were compared with counterparts based on FEM. The cracking schemes and fragility curves were investigated in detail, accounting for different modeling approaches on the nonlinear analysis results. Next, IDA analyses conducted on the MAEM model for the RCC dam is presented. The cracking distribution of the dam body was compared with that of the concrete dam model. The evolution of damage and the discrete crack propagation on the dam body for the two models were investigated thoroughly. The damage on the dam body for the two MAEM models was compared qualitatively and quantitatively utilizing fragility curves considering the extent of cracks. In addition to the fragility functions, crack widths on the upstream faces of the dam monoliths were computed as a new damage indicator. The variation of the maximum base and total crack widths were studied to set a relationship between ground motion IMs and the damage on the dam bodies. Lastly, the leakage through the upstream cracks was estimated related to the residual opening of the crack as well as crack geometrical properties like depth and length.

The effect of residual crack widths on the leakage estimations was studied considering 4 different residual crack width factors. The results of the analyses based on several performance indicators were shown with mean quantities and bounds on the mean summarizing the comprehensive time history results.

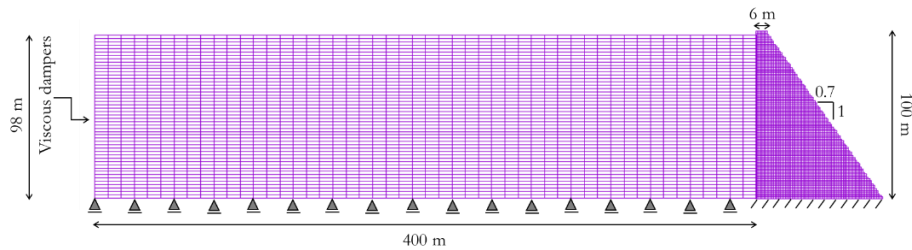
## **4.2 Simulation Models**

A typical 100 m tall monolith was investigated in the plane stress configuration with a vertical upstream face and a slope of 0.7H/1V at the downstream face, having a crest length of 6 m (Figure 4.1). Since the dam-foundation interaction is beyond the scope of this research, fixed base boundary conditions were applied, and only dam-reservoir interaction was accounted for in the simulations. The reservoir elevation was assumed as 98 m, with roller supports at the base, corresponding to a bottom absorption coefficient of 1.0. At the far end of the reservoir, Sommerfeld radiation boundary condition was applied. The Young's Modulus, Poisson's ratio, mass density of concrete, tensile strength, and fracture energy were assumed as 28 GPa, 0.2, 2400 kg/m<sup>3</sup>, 2.4 MPa, and 200 N/m, respectively. In MAEM models, the reservoir was modeled as a nearly incompressible fluid with Poisson's ratio, acoustic wave speed, and density of water as 0.4999, 1438.66 m/s, and 1000 kg/m<sup>3</sup>, respectively. It should be noted that, at the dam-reservoir interface, a constraint was introduced to have the identical displacement at the dam and reservoir in the horizontal direction. Additional modeling details regarding the FEM and two MAEM models are presented in the following sections.

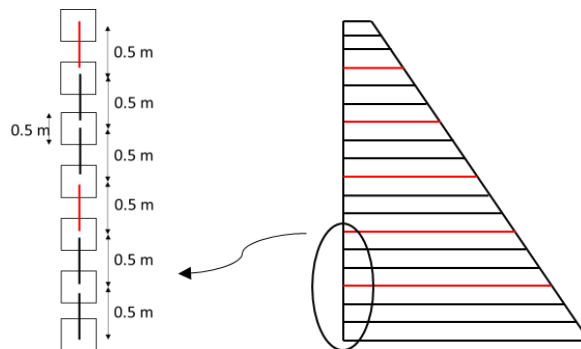




(a) FEM model



(b) MAEM model



(c) Sketch for RCC dam modeling

Figure 4.1 Dam-reservoir models

#### 4.2.1 Finite Element Method Model

The MAEM model results for a concrete dam modeling approach for the dam body were compared with FEM model results (Figure 4.1a) of a previous study conducted by Soysal et al. (2016). In this former study, the general-purpose finite element program DIANA was used (TNO DIANA, 2014). The element size of the dam was

approximately 0.7 m, while the fluid elements were modeled with 2.4 m length and 0.4 m height. Having a length of 400 m, the reservoir was modeled using compressible fluid elements with pressure degrees of freedom. The nonlinearity of concrete was modeled with the total strain rotating smeared crack approach. Mass and stiffness proportional Rayleigh damping corresponding to 6% damping ratio in the first and third modes of the structure was used. In the nonlinear implicit transient analyses, a time increment of 0.005 sec was utilized, and the solution time for 40 steps (0.2 sec) was 1.5 minutes.

#### **4.2.2 Modified Applied Element Method Model I**

The first MAEM model was constituted in accordance with the FEM model to enable making a direct comparison for the different modeling approaches on the results. The modified applied elements in the plane stress setting had a size of 1 m; following this size and taking the aspect ratio as 4, the fluid elements were modeled as 8 m x 2 m, rather coarsely than FEM. The reservoir length was 400 m, and the same mass and stiffness proportional Rayleigh damping coefficients were utilized as in the FEM model. The softening parameter,  $c$ , and ultimate strain,  $\varepsilon_{ult}$ , of Maekawa tension softening model were 13 and 0.01, respectively, leading to 200 N/m fracture energy for this mesh size. This tension behavior was employed to normal and diagonal springs. Shear springs were brittle: after the exceedance of cracking strain,  $\varepsilon_t$  in the normal spring of the spring pair, the shear spring lost its resistance, corresponding to no shear retention in the crack. The springs in compression were assumed to behave linearly. 10 connecting springs between each element were modeled with 32157 DOF. The nonlinear dynamic analyses were conducted utilizing the explicit nonlinear solution scheme with a time increment of 0.0002 sec. To ensure numeric stability, mass scaling was applied to the system with the stiffness multipliers as  $\alpha = 1e - 6$  and  $\alpha = 2e - 6$  for the dam-reservoir and viscous dampers, respectively. It should be noted that the solution time for 1000 steps (0.2 sec) was 6 minutes, and the shortest and longest motions had 45000 and 222500 steps, respectively.

A comparison of the cracking schemes between the plane stress and plane strain solutions for this model, together with the effect of the number of connecting spring pairs on the damage prediction and solution times, are presented in Appendix A. The analyses herein were conducted with plane stress assumption given the expansion joints separating concrete gravity dams to 10 - 20m wide individual monoliths.

#### **4.2.3 Modified Applied Element Method Model II**

In the second MAEM model, the effect of lift joints was taken into account by considering a weak zone in every 1 m throughout the height of the dam (USACE, 2000). Therefore, the modified applied element size was decreased to 0.5 m so that following each 1 m high connection (corresponding to 3 rows of modified applied elements), a weak layer was introduced (schematically shown in Figure 4.1c, red lines illustrating the lift joints). Following USACE recommendations (USACE, 2000), the tensile strength of lift joints was assumed as 1.4 MPa and fracture energy as 110 N/m. Hence, the nonlinear tension model parameters  $c$  and  $\epsilon_{ult}$  were taken as 1.7 and 0.1, respectively, for the lift joints; for the remaining parts  $c$  and  $\epsilon_{ult}$  were 2.5 and 0.1, respectively, corresponding to 200 N/m fracture energy for 0.5 m modified applied element size. In order to decrease the computational cost, the reservoir length was decreased to 200 m, and the size of the fluid elements was 8 m x 1 m. Similar to Model I, the Maekawa tension softening model was employed to normal and diagonal springs, while shear springs were brittle and the compression behavior was elastic. The number of connecting spring pairs between each element was 10 with 69165 DOF in the model. It should be noted that, as will be discussed in the following section, the decrease of reservoir length from 400 m to 200 m had a negligible effect on the response of the dam-reservoir system. The utilized Rayleigh damping coefficients were identical to Model I. Stiffness multipliers for the mass scaling were identical as well. Nonlinear dynamic analyses were conducted with explicit nonlinear solution algorithm with a time increment of 0.0002 sec. As the

mesh was finer in this model, the solution time for 1000 steps (0.2 sec) was obtained higher than Model I at 10 minutes.

#### 4.2.4 Modal Properties of FEM and MAEM Models

The modal properties of the two above MAEM models were obtained by conducting frequency response analyses. Similar to the analyses conducted in Chapter 3, a short duration pulse in the horizontal direction was applied to the MAEM system, and according to the output crest acceleration, a transfer function was estimated. In Figure 4.2, Model I (concrete dam) corresponds to the first MAEM model with 1 m modified applied element size and 400 m reservoir length, and Model II (RCC dam) is the second model having 0.5 m modified applied element size, 200 m reservoir length with different fluid finite element size. Regardless of this discretization, it can be seen from Figure 4.2 that the frequency responses of the two models were very close to each other. The first three frequencies were identical, and there were only slight differences in the peaks of the three distinct modes. Therefore, these two models can be used as tools to make a direct comparison between MAEM models.

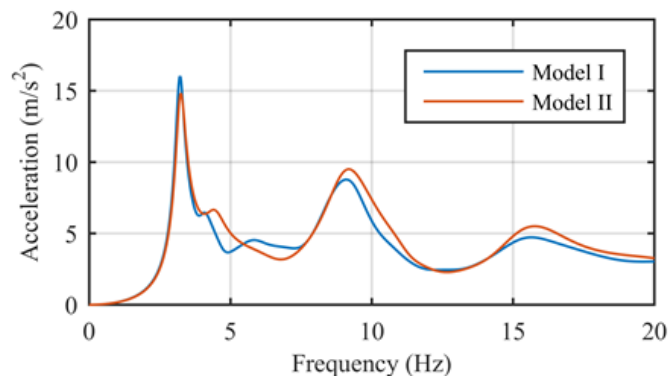


Figure 4.2 Frequency response comparison of MAEM models

The first three periods of FEM and the two MAEM models are tabulated in Table 4.1. In the first mode, the period of MAEM models was obtained 7% higher than the FEM model; in contrast, the third period was underestimated by approximately 30% in MAEM. The main difference in the periods between FEM and MAEM can be attributed to utilizing different formulations for the reservoir and modeling approaches of the dam body.

Table 4.1 Modal properties of FEM and MAEM models

	Period (s)		
	FEM	MAEM Model I	MAEM Model II
Mode 1	0.29	0.31	0.31
Mode 2	0.11	0.11	0.11
Mode 3	0.09	0.06	0.06

### 4.3 Analysis Technique

#### 4.3.1 Incremental Dynamic Analysis

Incremental dynamic analysis (IDA) is a commonly used procedure to determine a relationship between intensity measures of ground motions and engineering demand parameters of the structures (Vamvatsikos & Cornell, 2002). In this method, the ground motions are scaled with a positive scaling factor, increasing incrementally to a desired level (Vamvatsikos & Cornell, 2002). A wide range of intensity measures (IM) can be selected, such as the peak ground acceleration (PGA), peak ground velocity (PGV), and 5% damped spectral acceleration at the first mode period of the structure ( $S_a(T_1, 5\%)$ ) for buildings and dams (Armstrong et al., 2020; Hariri-Ardebili & Saouma, 2015; Vamvatsikos & Cornell, 2002). The engineering demand parameter (EDP), on the other hand, is a response parameter obtained from the output

of dynamic analysis results based on the user's objectives and constraints. Commonly utilized EDPs for the design and evaluation of structures are maximum roof displacement, base shear, drift ratio, sliding damage state, crest acceleration, and displacement (Hariri-Ardebili & Saouma, 2016; Segura et al., 2019; Sevieri et al., 2020). The relationship between damage on the dam body and the crest displacement is not clear, as shown in Soysal et al. (2016), and an EDP based on the crack profile of the dam body was proposed. This criterion, based on the limit states established according to the consequences and severity of the damage, was also used in this work in conjunction with the IDA analysis.

In order to make a direct comparison with FEM results, IDA was performed on the two MAEM models with the same set of 21 ground motions (Soysal et al., 2016). A variety of motions were selected to investigate the effect of different ground motion characteristics at various scale levels. The ground motions, taken from the Pacific Earthquake Engineering Research (PEER) database, were recorded on rock (type A of USGS) or stiff soil (type B of USGS). Per FEMA440, near-fault motions with epicentral distances of 2 to 39 km were selected, having large magnitudes ranging from 6 to 7.6 (Table 4.2). IDA was performed by scaling the ground motions such that the spectral acceleration at the first natural period of the dam-reservoir system was in the range of 0.2g to 1.0g, with 0.05g increments (Figure 4.3). These target levels led to scale factors of 0.1-6.1. Although limits on scale factors were suggested to be between 0.25-4 (Krinitzsky & Marcuson, 1983), for earthquake magnitudes between 6.4-7.4, a limitation regarding the scale factors was not applicable (Iervolino & Cornell, 2005).

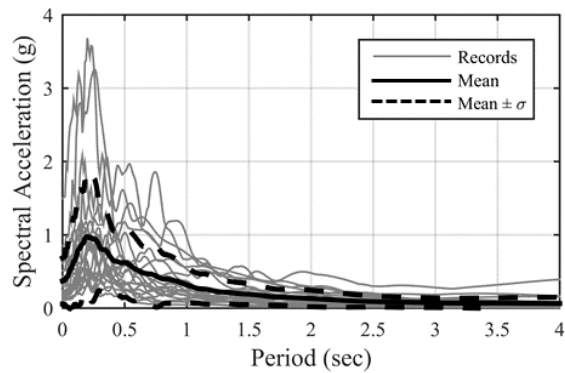


Figure 4.3 Acceleration response spectra of the selected ground motions

Table 4.2 Selected ground motions for IDA

No.	Earthquake Name	Component	M <sub>w</sub>	PGA (g)	USGS soil type
1	Imperial Valley, 1979	315°	6.5	0.204	B
2	San Fernando, 1971	90°	6.6	0.110	B
3	San Fernando, 1971	270°	6.6	0.136	B
4	Landers, 1992	0°	7.3	0.171	B
5	Loma Prieta, 1989	0°	6.9	0.512	B
6	Loma Prieta, 1989	67°	6.9	0.357	B
7	Loma Prieta, 1989	270°	6.9	0.244	B
8	Morgan Hill, 1984	90°	6.2	0.292	B
9	Northridge, 1994	360°	6.7	0.514	B
10	Düzce, 1061 Lamont	E	7.1	0.134	B
11	Manjil, Abbar	Lng.	7.37	0.5146	B
12	Tabas	Trn.	7.35	0.8518	A
13	Loma Prieta, Gilroy	337°	6.9	0.325	B
14	Northridge, Burbank-Hw Rd.	330°	6.7	0.163	B
15	Northridge, 24088 Pacoima	360°	6.7	0.433	B
16	Spitak	0°	6.8	0.199	B

Table 4.2 (Continued) Selected ground motions for IDA

17	Cape Mendocino 1992	0°	7.1	1.497	A
18	Chi-Chi, Taiwan, 1999	E	7.6	0.133	A
19	Kocaeli-Gebze, 1999	0°	7.4	0.244	A
20	Kocaeli-İzmit, 1999	90°	7.4	0.22	A
21	Palm Springs, 1986	270°	6.0	0.612	A

### 4.3.2 Fragility Analysis

The IDA results were interpreted to quantify the damage on the dam body by utilizing fragility functions for the FEM, MAEM concrete, and MAEM RCC models. Fragility curves specify the probability of exceeding certain limit states of a structure as a function of ground motion intensity measure, IM (Baker, 2015). A fragility function is usually described by a lognormal cumulative distribution function as given in Equation (4.1) (Baker, 2015).

$$P(C|IM = x) = \Phi\left(\frac{\ln x - \theta}{\beta}\right) \quad (4.1)$$

where  $P(C|IM = x)$  gives the probability that a ground motion with  $IM = x$  will cause the structure to exceed a particular limit state,  $\Phi()$  is the standard normal cumulative distribution function,  $\theta$  stands for the median of the fragility function, and  $\beta$  is the standard deviation of  $\ln IM$ .

The maximum likelihood estimation method was utilized for the derivation of fragility curves. The estimates of  $\theta$  and  $\beta$ , denoted as  $\hat{\theta}$  and  $\hat{\beta}$ , are maximized by maximizing the log of the likelihood function (Equation (4.2)) (Baker, 2015).

$$\{\hat{\theta}, \hat{\beta}\} = \max_{\theta, \beta} \sum_{i=1}^m \left\{ \ln \binom{n_i}{z_i} + z_i \ln \Phi\left(\frac{\ln x_i - \theta}{\beta}\right) + (n_i - z_i) \ln \left(1 - \Phi\left(\frac{\ln x_i - \theta}{\beta}\right)\right) \right\} \quad (4.2)$$



where  $z_i$  is the number of exceeding a specific limit out of  $n_i$  ground motions, and  $x_i$  is the IM of the ground motion.

### **4.3.3 Limit States**

The fragility curves are constructed based on several limit states. The quantification of damage for dams is a significant challenge, as in the case of buildings, a widely accepted and used parameter such as the drift ratio is not applicable for such structures. Cracking on the dam body is crucial to assess the seismic performance; hence, the geometry and propagation of cracks have to be considered while defining the limit states. In this study, the limit states proposed by Soysal et al. (2016) were used. The fragility curves were derived with respect to the four limit states defined as limited damage (LS1), moderate damage (LS2), severe damage (LS3), and rigid block formation (LS4) states. The dam is in LS1 when the upstream base crack exceeded the foundation drains -which were assumed to be located at 20% of the base width from the upstream face-, which may result in an increase in seepage on the dam body. LS2 state corresponds to body cracking in addition to the base crack of LS1, cracks remaining in the upstream and downstream limits, as shown in Figure 4.4. The limit for the upstream face was chosen such that no tension would occur due to the hydrostatic forces, self-weight, and uplift forces. For the downstream side for LS2, a sliding factor of safety of 2.0 was used. Severe damage state (LS3) was defined for the cases in which the cracks exceeded the limits defined in LS2. The final limit state (LS4) for constructing the fragility functions is the state when the upstream and downstream cracks are joined (Figure 4.4).

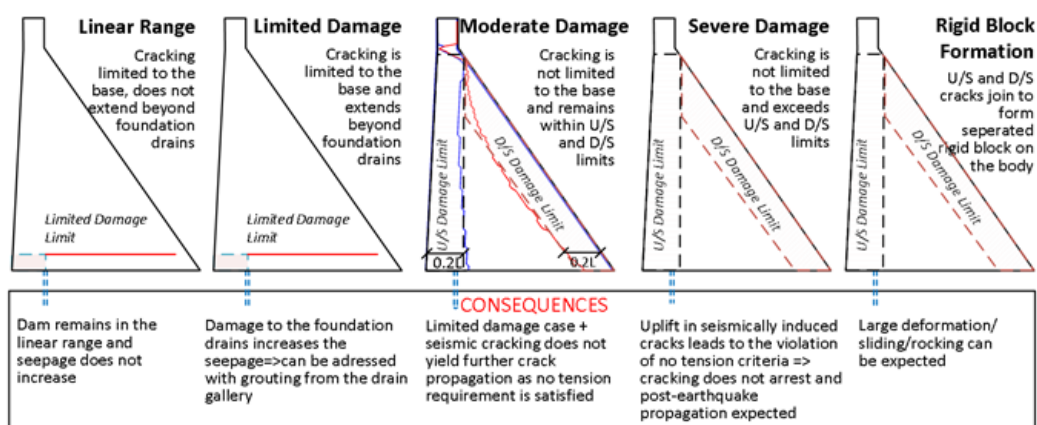


Figure 4.4 Graphical description of limit states (Soysal et al., 2016)

#### 4.4 Results from the Incremental Dynamic Analysis

For MAEM Model I (corresponding to concrete dam) and MAEM Model II (corresponding to RCC dam), IDA was performed by conducting 357 nonlinear transient analyses for each model. Throughout these analyses, the fluid pressure within the cracks was neglected in accordance with the suggestions of detailed experimental and numerical studies conducted on the problem (Javanmardi et al., 2005a, 2005b). The simulation of the fluid pressure inside the cracks is a highly complex issue. As the uplift pressures might have a larger effect on the crack closing mode than the crack opening case (Javanmardi et al., 2005a), the crack openings might be underestimated in this study.

The damage on the dam body, as it was previously mentioned, was quantified in terms of the crack profiles. Therefore, both the active and inactive cracks were considered by calculating the maximum strain that each spring had experienced throughout the analysis, and the cracking schemes were constituted based on these overall maximum strains that each spring had undergone.

Figure 4.5 presents the cracking scheme comparison for FEM, MAEM concrete (indicated as MAEM I), and MAEM RCC (MAEM II) models presented for selected

results corresponding to low, medium, and high damage; the output cracks for all motions in all scales are given in Appendix B (Figure B.1). A crack width of 0.35 mm was selected (Soysal et al., 2016), corresponding to strain limits of  $5 \times 10^{-4}$ ,  $3.5 \times 10^{-4}$ , and  $7 \times 10^{-4}$  for FEM, MAEM Model I, and MAEM Model II, respectively. For all modeling approaches, cracks were initiated at the upstream base of the dam. Then, in the concrete dams (FEM and MAEM Model I), cracks occurring at the downstream face tended to propagate approximately with  $45^\circ$  inclination. However, cracks occurring at the upstream face propagated in a horizontal direction. For RCC dams, on the other hand, as weak horizontal layers existed, cracks at the upstream and downstream sides of the dam propagated horizontally. As the lift joints were considered in the simulations, RCC dams were subjected to more cracking, especially at the upstream side of the dam (Figure 4.5).

The detailed comparison of FEM and MAEM Model I, and MAEM Model I, and MAEM Model II are provided below for sample analyses.

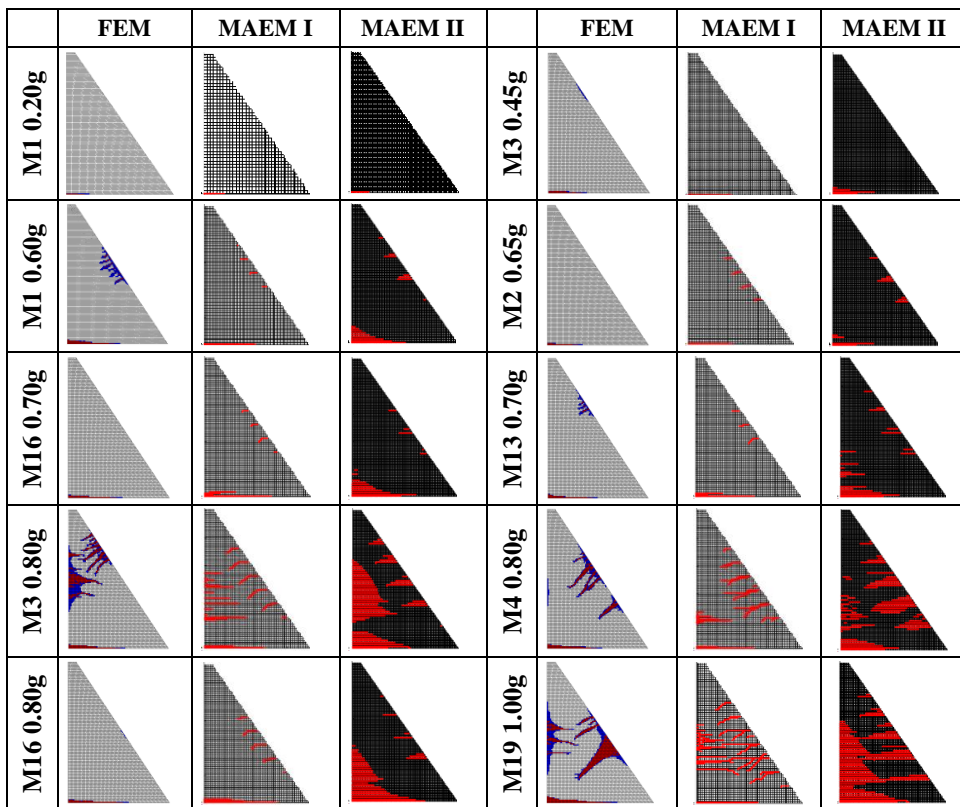


Figure 4.5 Cracking scheme comparison for FEM and MAEM models for selected results

MAEM enables the determination of post-earthquake damage state in a straightforward manner. Therefore, for MAEM Model I, the post-earthquake damage state of the concrete dam-reservoir system was evaluated in terms of the crack profiles (Appendix C).

#### 4.4.1 Comparison of MAEM and Finite Element Simulations

The prediction of damage on the concrete dam body through crack simulation was investigated extensively in the literature utilizing FEM. The obtained crack patterns displayed diffusion, which causes difficulties with setting performance limits on these structures. On the other hand, discrete element-based techniques, such as the proposed MAEM, enable discrete crack propagation simulation naturally. In this

section, the comparison of FEM and MAEM concrete gravity dam models was conducted to show that the proposed methodology has an advantage over continuum-based methods for the nonlinear simulations by obtaining discrete crack patterns. This advantage enables setting performance limits on gravity dams considering crack propagation and opening using MAEM.

For the concrete gravity dam cross-section, when FEM and MAEM Model I were compared in terms of cracking profiles, it was observed that the MAEM model exhibited much less smearing than FEM. Especially at the downstream face, discrete crack propagation could be clearly simulated (Figure 4.5 and Figure B.1: Motion 1 – Scale 0.60g, Motion 9 – Scale 0.80g, Motion 15 – Scale 0.75g, Motion 21 – Scale 0.75g). However, in the MAEM model, due to discretization of the inclined downstream face with rectangular elements, additional cracks, due to stress concentrations at the discretized points, compared to the FEM model were also observed, these cracks initiated at much earlier scales (Figure 4.5 and Figure B.1: Motion 2 – Scale 0.65g, Motion 4 – Scale 0.65g, Motion 10 – Scale 0.70g, Motion 16 – Scale 0.70g), and as the ground motion scale increased, the cracks propagated (Figure 4.5 and Figure B.1: Motion 2 – Scale 0.80g, Motion 4 – Scale 0.75g, Motion 10 – Scale 0.80g, Motion 16 – Scale 0.80g). Generally, cracks at the upstream side of the dam propagated more in the MAEM model; whereas, the cracks were smeared in FEM, leading to less propagation (Figure 4.5 and Figure B.1: Motion 3 – Scale 0.80g, Motion 9 – Scale 0.80g, Motion 12 – Scale 0.80g, Motion 19 – Scale 0.90g). For some motions, upstream cracks observed in MAEM were not present in FEM due to the differences in the reservoir elements and modeling approaches (Figure 4.5 and Figure B.1: Motion 4 – Scale 0.80g, Motion 19 – Scale 0.85g). Essentially, smearing could be highly decreased with the use of a discrete method such as the proposed modified applied element method. As smearing was decreased, cracks propagated more, leading to a conclusion that the FEM model could produce less conservative results for design purposes compared to a discrete model.

The computational cost of the MAEM and FE methods are different. The FEM analyses were performed with implicit solution scheme with a solution time step

( $\Delta t = 0.005 \text{ s}$ ) 25 times greater than those in MAEM ( $\Delta t = 0.0002 \text{ s}$ ) utilizing an explicit time stepping requiring much smaller  $\Delta t$ . The solution times for 1000 steps were approximately 35 minutes and 6 minutes for FEM and MAEM, respectively. As a much higher solution time step can be specified for FEM analysis utilizing implicit solution algorithm, the FEM solution time was observed to be 4 times faster than the MAEM run time. However, this should be qualified on MAEM analysis having  $1/25^{\text{th}}$  of the time step of the FEM in the same analysis.

In addition to the cracking profiles, the fragility curves for the four aforementioned limit states were generated for MAEM Model I and were also compared to the fragility curves constructed based on the previously conducted FEM results (Figure 4.6). The fragility functions were constituted by selecting the spectral acceleration at the dam-reservoir system's first natural period as the intensity measure of the motion. For instance, for an earthquake producing a spectral acceleration of 0.5g at the dam-reservoir system's first natural period, the probability of exceeding limit states LS1 and LS2 were 99% and 3%, respectively, for the FEM model; the exceedance probabilities of LS3 and LS4 were close to 0% (Figure 4.6a). For the same spectral intensity, MAEM Model I estimated these probabilities as 99%, 16%, less than 1%, and close to 0%, for LS1, LS2, LS3, and LS4, respectively (Figure 4.6b).

The fragility curves obtained using the FEM and MAEM models are compared in Figure 4.6c to Figure 4.6f for all four limit states. For LS1, very high differences were observed between the two models as the fragility curves were very steep (Figure 4.6c). For LS2, the probability of obtaining an identical damage state was generally 40% higher in the MAEM model, excluding the very low and very high intensity range (Figure 4.6d). For LS3, this difference reduced to 20% (Figure 4.6e). The fragility curves for LS4 state showed that, up to 0.9g spectral acceleration, the probability of exceedance was estimated close in both models, and the probability value was less than 15%. For 1.0g spectral acceleration, the difference between MAEM and FEM estimate was 20%; for higher intensities up to the very high intensity range, MAEM prediction of this damage state was generally 30% higher

than the FEM (Figure 4.6f). Figure 4.6c to Figure 4.6f show that, at almost every intensity level, the probability of observing damage was predicted higher in the MAEM model, between 20-40%, compared to the fragility curves constructed based on the previously conducted FEM simulations. Longer discrete cracks were obtained in MAEM models compared to FEM with smeared cracking: consequently, fragility curves moved left, indicating a more severe damage situation for MAEM compared to the FEM model.

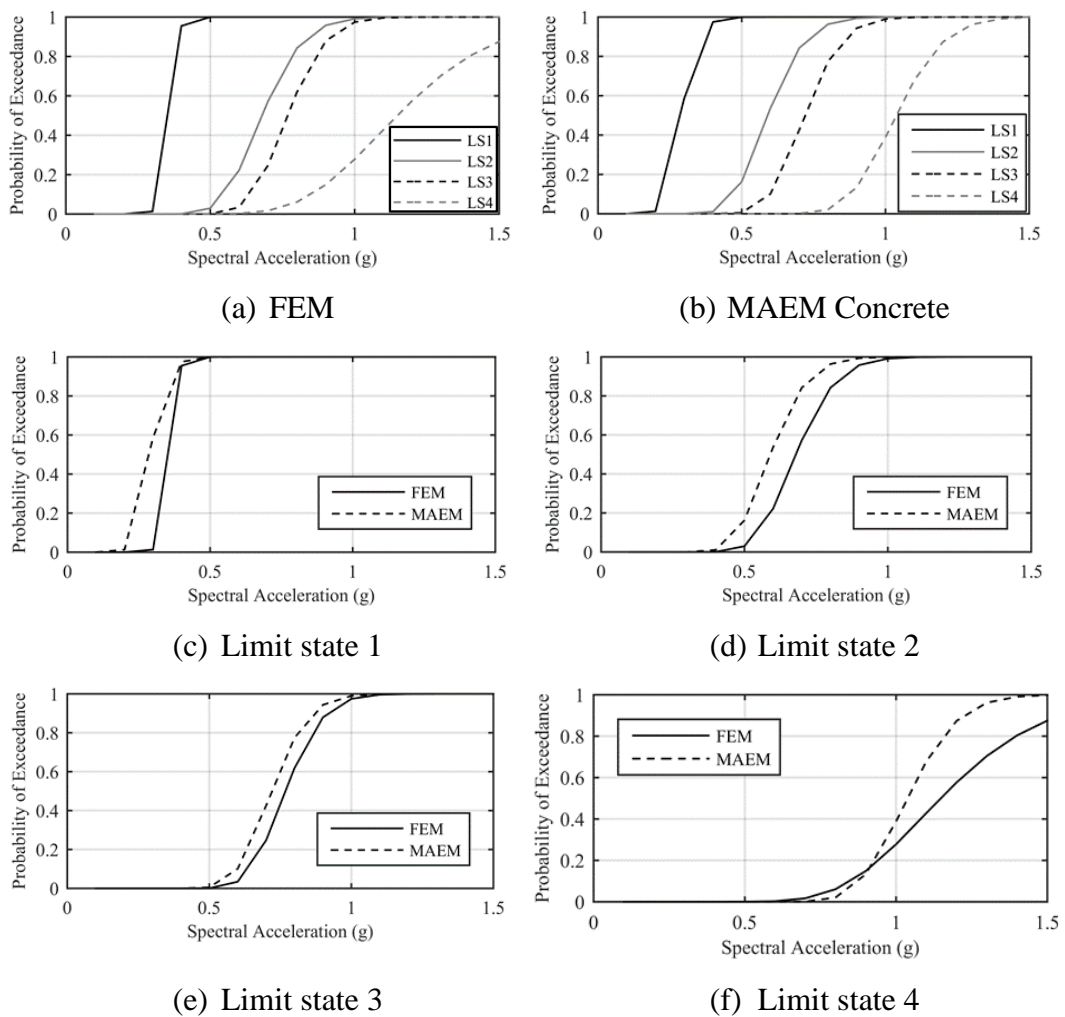


Figure 4.6 Fragility curves for FEM and MAEM Model I

#### 4.4.2 Comparison of the Gravity Dam vs. RCC Dam with Weak Joints

RCC gravity dams have a significant difference in the construction methodology, differentiating them from the concrete gravity dams. These dams are constructed in thin horizontal layers (lifts), ranging from 0.15 m to 1 m, compacted by rollers, creating weak zones between each construction layer. Despite these weak lift joints, the modeling of RCC dams was conducted in a similar fashion to the concrete dams in the literature. In this part of the study, the seismic performances of a concrete and an RCC monolith with an identical geometry were compared in detail, considering the effect of lift joints in the numerical model of RCC.

The results from MAEM Model I (concrete) and MAEM Model II (RCC), modeled by considering the weak layers due to the lift joints during the construction, were first compared quantitatively. For motions with low intensity (Figure 4.5 and Figure B.1: Scale 0.20g – 0.45g), similar behavior was observed for concrete and RCC dams; limited damage at the upstream base was observed. However, as the ground motion intensity increased, significant damage, especially at the upstream side of the RCC dam, occurred (Figure 4.5 and Figure B.1: Motion 1 – Scale 0.60g, Motion 3 – Scale 0.65g, Motion 13 – Scale 0.70g, Motion 14 – Scale 0.80g, Motion 16 – Scale 1.00g). The lift joints also affected the cracking at the downstream face; the existence of weak layers induced more cracking in Model II (Figure 4.5 and Figure B.1: Motion 1 – Scale 0.75g, Motion 4 – Scale 0.80g, Motion 7 – Scale 0.80g, Motion 15 – Scale 0.80g, Motion 17 – Scale 1.00g). Some extreme damage cases were observed as well (Figure 4.5: Motion 3 – Scale 1.00g, Motion 4 – Scale 1.00, Motion 16 – Scale 1.00g, Motion 19 – Scale 1.00g). When the cracking profiles were compared, the RCC dam was observed to be more prone to cracking compared to the concrete counterpart.

For Motion 6 – Scale 0.80g, the evolution of damage by means of crack widths exceeding 0.35 mm and the deformed shapes were investigated step by step for the two MAEM models. Damage first occurred in the upstream base of the dam; the base crack initiation and closing can be seen in Figure 4.7 between  $t=2.22$  s and 2.36 s.



The RCC dam model had more damage than the concrete dam model due to the weak lift joints spaced at every 1 m elevation. At  $t=2.86$  s, downstream body cracking initiated in both models with maximum propagation at  $t=2.90$  s. Between  $t=3.02$  s and  $t=3.20$  s, the cracking shifted to the upstream face. The existing crack at the base propagated more towards the core of the dam, and additional cracks at the body of the dam at the upstream side were observed. At the next cycle, at  $t=3.26$  s, additional damage to the downstream face was seen in both models exhibiting increased cracking compared to  $t=2.86$  s. In all of the cases, the effect of lift joints could be clearly observed; the RCC dam was always subjected to more damage than the concrete dam (Figure 4.7).

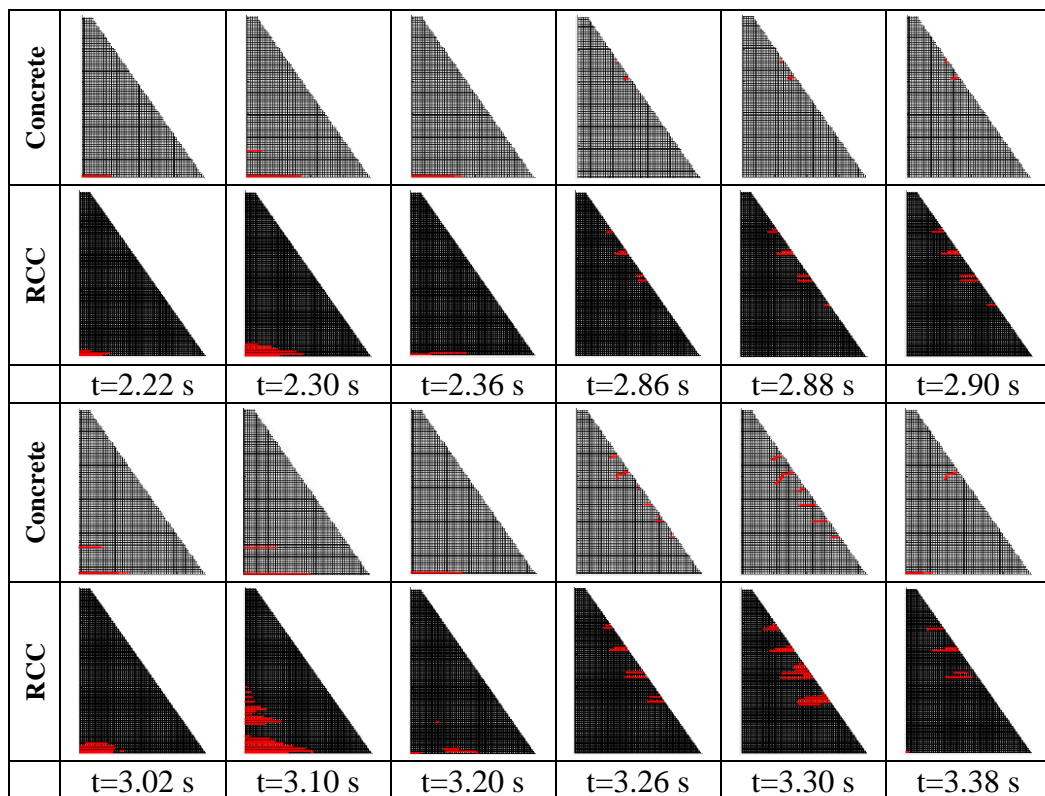


Figure 4.7 Cracking schemes of MAEM models at selected times

The deformed shapes of both models at  $t=3.10$  s and  $t=3.30$  s were investigated as well to observe the element separation occurring at the dam body (Figure 4.8). In

this figure, the displacements of the dam body were scaled by 500 to illustrate the element separation clearly. The deformed shapes of MAEM Model I and II are presented in Figure 4.8a and c, respectively, at  $t=3.10$  s, corresponding to cracking at the upstream face of the dam. The separation between the elements in both models at the upstream faces of the dams is clearly shown. The separation in the RCC model was less than the concrete dam as more elements were damaged in the RCC case. The deformations at the downstream sides of the dams at  $t=3.30$  s are given in Figure 4.8b and d for concrete and RCC dams, respectively. The separation between the elements on the concrete dam was once again more pronounced than the RCC dam model.

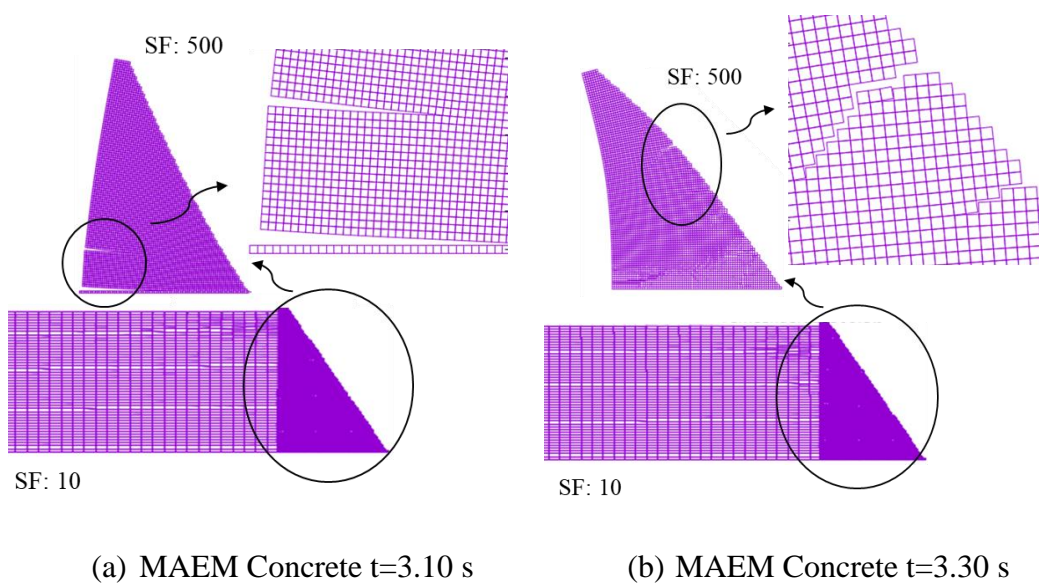


Figure 4.8 Deformed shapes of MAEM models at selected times

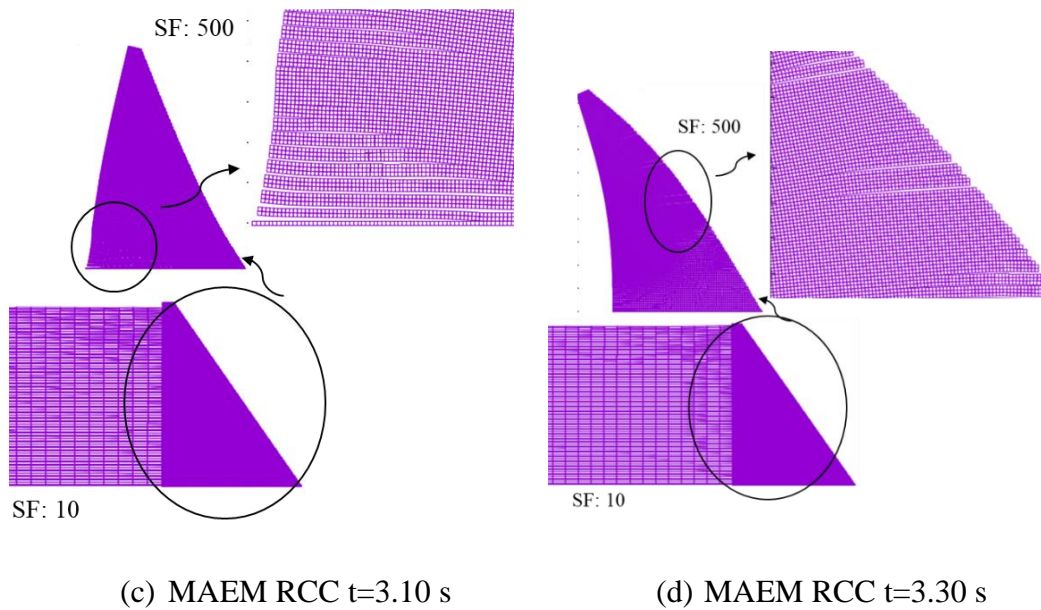


Figure 4.8 (Continued) Deformed shapes of MAEM models at selected times

The fragility curves for LS1 to LS4 limit states are presented in Figure 4.9a and Figure 4.9b, respectively, for MAEM Model I and II by selecting the spectral acceleration at the dam-reservoir system's first natural period as the intensity measure of the motion. For the concrete dam, at 0.5g spectral acceleration, at the dam-reservoir system's first natural period, the probability of exceeding limit states LS1, LS2, LS3, and LS4 were 99%, 16%, less than 1%, and close to 0%, respectively. For the same spectral intensity, these probabilities were determined higher for the RCC case as 99%, 36%, 2%, and close to 0%, respectively.

The corresponding comparison for both systems at individual damage states is presented in Figure 4.9c to Figure 4.9f. For LS1, unlike the other three limit states, the probability of obtaining the same damage state was generally 20% higher in Model I (Figure 4.9c), as a single base crack occurred and propagated more in the concrete dam (Figure 4.8a), unlike the RCC case in which many cracks at the weak layers within the heel took place (Figure 4.8c). For the remaining limit states, the probability of exceeding damage on the RCC model was more than the corresponding value for the concrete dam (Figure 4.9d - Figure 4.9f). For LS2,

between 0.4g – 0.8g spectral accelerations, the probability of exceedance for the RCC dam was estimated 20% to 35% higher compared to the concrete dam. For intensities higher than 0.8g, both models converged to 100% probabilities (Figure 4.9d). For LS3, when the very low and very high intensity ranges were excluded, the probability of obtaining the identical damage was generally 25% higher in the RCC model (Figure 4.9e). For the last limit state (LS4), up to 0.8g, the exceedance probabilities were less than 3% for both dams. At higher intensities levels of 1.0g – 1.1g, the difference between RCC and concrete estimate was 15%, and converged to 100% eventually, for very high intensity levels (Figure 4.9f). Figure 4.9c to Figure 4.9f show that, excluding LS1, more damage was expected to occur in the RCC dam, between 15% - 35%, compared to the concrete dam having identical geometry. Taking into account the lift joints, cracking initiated at early stages in RCC dams, and these cracks propagated into the zones defined in the limit states before the concrete dam. Accordingly, the probability of exceeding the limit states was considerably higher for the RCC dam considering the lift joints in the analytical model.

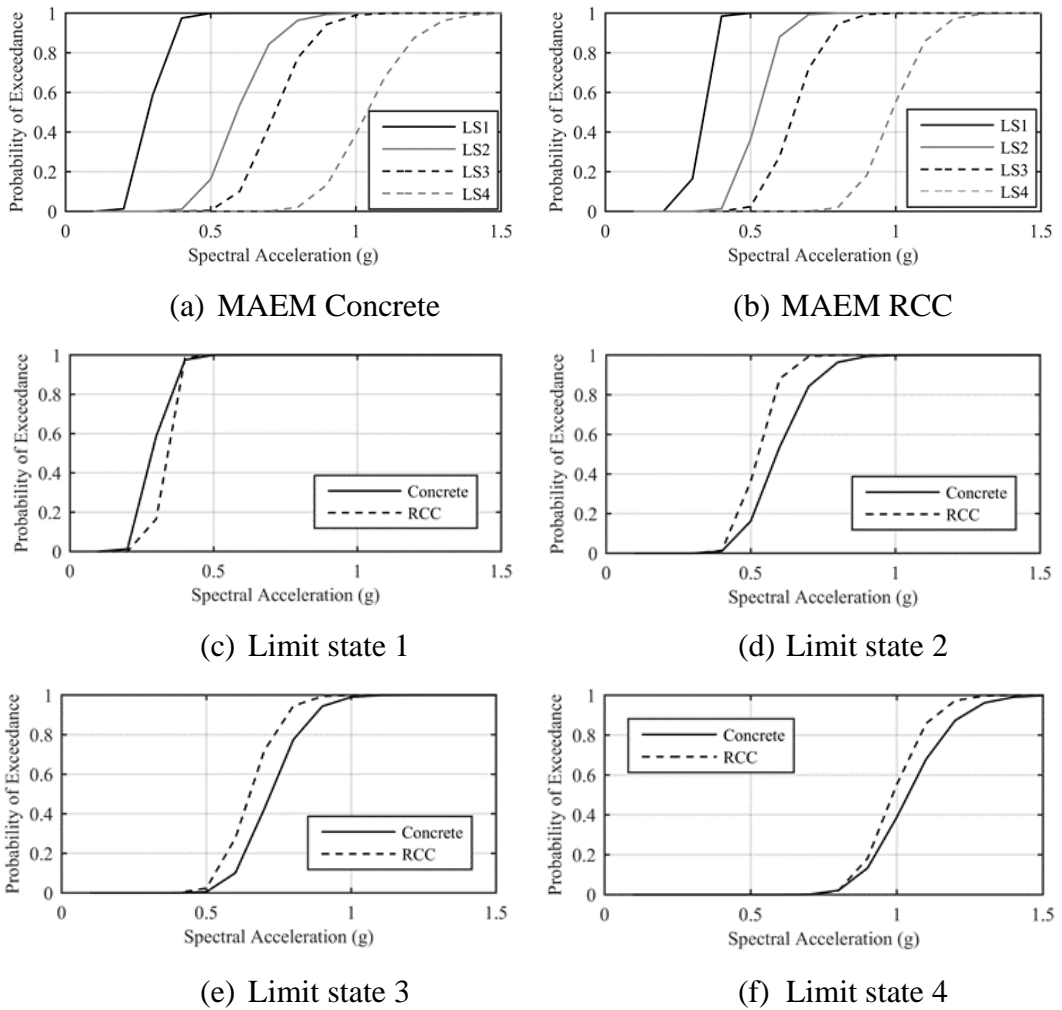


Figure 4.9 Fragility curves for MAEM Model I and II

#### 4.4.3 Cracking in the Upstream Face as a Performance Indicator

The limit states, as given above, represent an evaluation of the damage expected on a dam outlining a) the damage pattern and its evolution with seismic intensities and b) the comparative performance between two systems. However, they do not provide a measurable basis as observation of cracking on monoliths is not straightforward. Moreover, the consequences of the damage are hard to quantify except for expected poor structural performance for loading after a strong earthquake event. A direct

consequence of an earthquake event is the seepage through the dam due to the cracking on the load-bearing surface. Cracking on the upstream face is, therefore, a primary concern in these systems, which can be used as a performance criterion in evaluating the performance of new and existing systems. The finite element technique is deficient for evaluating the discontinuities on the surface as such: smeared crack methods distributed the cracking to a large region on the surface, while discrete crack modeling would require a large number of predefined remeshing operations for cracks emerging on the upstream surface. The use of the modified applied element technique provides an opportunity to investigate the cracking on the upstream face as a performance quantity, which can further be linked to seepage through the monolith after an event. In this section, the seismic performance of concrete and RCC dams, treated above with limit state criteria, is investigated through the use of upstream cracking as a seismic demand on these systems using the FEM and two MAEM models.

For the FEM model, the limitations given above only allow the determination of cumulative crack width on the surface of a model with crack width estimations based on the crack strains on each element on the upstream face. Crack strains were estimated at four Gauss points within an element. The crack width for this element at the upstream face was obtained through averaging the crack strains of the two Gauss points near the upstream face; cracks larger than 0.35 mm were considered for the cumulative calculation. The total maximum crack width at the upstream face of the dam was computed by integrating the crack strains as such through the entire upstream face. The base crack width was obtained by integrating this value for two elements at the base with a total height of approximately 1.5 m. The total crack strains were transformed into the total maximum crack widths by multiplying with the finite element size.

For the MAEM models, a sample cracking scheme obtained at the upstream face of the chosen monolith is shown in Figure 4.10a. Crack width time history can be obtained for each crack  $w_i$  between the discrete elements, as well as the corresponding length of penetration ( $L$ ). A number of smaller cracks on the upstream

face can be as important as a large localized crack. For evaluating the importance of the cracks, the maximum opening in the crack ( $w_{max}$ ) was chosen. It should be noted that similar to the limit for the minimum crack width shown in the crack profiles, minimum crack width of 0.35 mm was selected while calculating the maximum crack widths, i.e., crack openings smaller than 0.35 mm were ignored similar to the crack width calculations of the FEM model. The base crack on such systems is usually the most important and prevalent feature of the damage. For each transient analysis, the maximum crack width at the upstream base ( $w_{max,b}$  in Figure 4.10a) and the summation of maximum crack widths for each crack ( $w_{max,i}$ ) that occurred in the upstream side of the dams, i.e.,  $w_{max,b} + w_{max,1} + \dots + w_{max,n}$ , were computed.

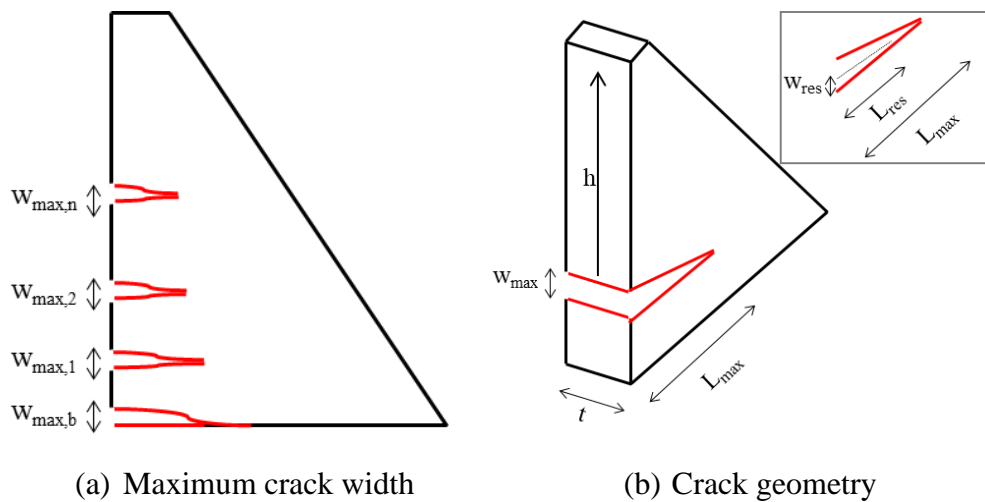
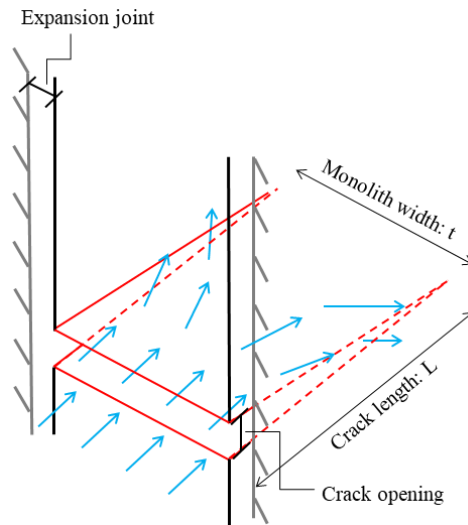


Figure 4.10 Crack width and leakage amount estimations



(c) Leakage amount estimation

Figure 4.10 (Continued) Crack width and leakage amount estimations

In Figure 4.11, the maximum crack width at the base and the total maximum crack width at the upstream side of the dams are presented with respect to the spectral acceleration of the ground motion at the dam-reservoir system's first natural period for each motion and each scale, together with the mean (solid black line) and mean  $\pm$  one standard deviation (dotted black line), for the two concrete models constructed with FEM and MAEM, and for the MAEM RCC dam model. It should be noted that although the maximum crack width of each upstream crack might occur at different times, for simplicity, the total maximum crack width at the upstream face was calculated by summing up all the maximum widths that occurred in each crack during the earthquake excitation.



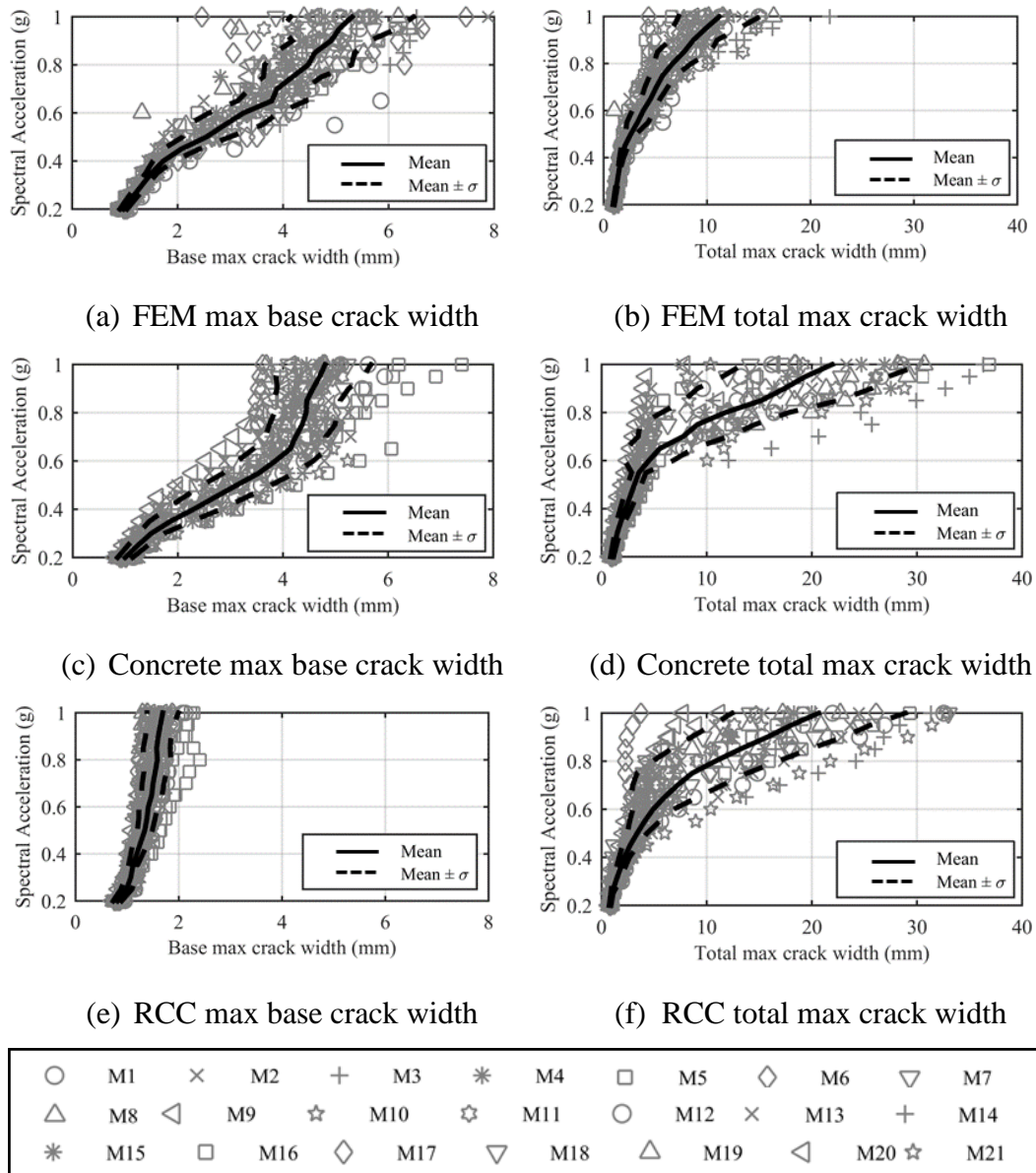


Figure 4.11 Maximum crack widths

The mean values of the maximum base crack opening for the two concrete dams, calculated from 21 events, were 1 mm at 0.2g spectral acceleration level, increasing to nearly 5 mm at Sa=1.0g, both for FEM (Figure 4.11a) and MAEM (Figure 4.11c) models. The localized cracking behavior at the base was estimated similarly for the two different modeling methodologies; the crack widths were obtained similarly in FEM and MAEM. For the RCC dam with the same section, the corresponding range

was much less, varying between 0.8 mm to 1.7 mm for loading levels of  $S_a=0.2g$  and  $1.0g$ , respectively. (Figure 4.11e). The corresponding behavior is apparent when the deformed shapes of the two models are investigated in Figure 4.8a and Figure 4.8c. For the concrete dam, high tensile stresses occurred at the base due to the boundary condition definition at that part, leading to the formation of a base crack. As earthquake cycles hit the dam to open cracks in the upstream face, the base crack width increased. On the other hand, for the RCC dam, the existence of weak layers at 1 m intervals forced the formation of new cracks close to the base; therefore, the increase of the base crack opening was less for this case. The variation in the maximum base crack widths was also much more substantial for the concrete dam compared to the RCC counterpart. While other cracks occurred as well, the damage at the upstream can be said to be concentrated at the base for the concrete gravity dam.

The total maximum crack widths on the upstream face obtained from the 21 earthquake events scaled to identical spectral accelerations are presented in Figure 4.11b, Figure 4.11d, and Figure 4.11f for the FEM concrete, MAEM concrete, and the MAEM RCC dams, respectively. The mean crack widths for the 21 events as well the one standard deviation bound around the mean are shown on the same figures. In the chosen range of loading, the mean of total maximum crack width varied between 1 – 11 mm, 1 – 22 mm, and 0.8 – 20.6 mm for the FEM and MAEM concrete, and MAEM RCC dams, respectively. The smearing of cracks in the FEM model led to an underestimation of the total maximum crack widths with respect to the MAEM concrete dam; hence, similar to the crack propagation comparison, the results for this damage measure provided less conservative results. Conversely, when the two MAEM models were compared, the envelope of total crack width on the upstream face was similar. The number of cracks for the RCC dams was more than the concrete dam, as shown in the crack scheme comparison for the concrete and RCC models in Figure 4.5. The total maximum crack widths of the two models converged for the lower number of cracks with higher widths (MAEM concrete dam) and more cracks but with smaller widths (MAEM RCC dam).

According to RILEM TC 104 (1991), the severity of damage with respect to crack width in non-reinforced concrete is classified into four categories as very mild (crack width  $< 1$  mm), mild (crack width between 1 – 10 mm), moderate (crack width between 10 – 20 mm), and severe moderate (crack width between 20 – 25 mm). Based on this classification, the maximum opening of a single crack for all three models can be characterized as a mild damage state. However, the upstream surface is directly in contact with reservoir water and subject to hydrostatic forces; as such, the detrimental effects of cracking may be much more severe (Pekau & Zhu, 2008).

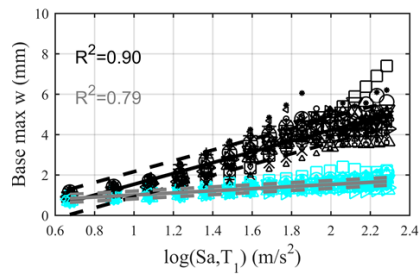
#### **4.4.4 Cracking on Monoliths: Relationship to Seismic Intensity Measures**

IDA is performed utilizing various ground motions that are scaled to different intensity levels; hence, it enables the investigation of the effect of ground motion properties on the nonlinear behavior of structures. Accordingly, in this section, the relationship between damage accumulation on the concrete and RCC monoliths and the input ground motions was investigated in order to assess the major characteristics of the motion that has an influence on the damage evolution on the dam bodies. The damage measure was selected as the maximum base crack width and the total maximum crack width at the upstream face of the monoliths, and the relationship of these demand quantities with the selected intensity measures (IM) was shown. The spectral acceleration,  $S_a(T_1,5\%)$ , the spectral velocity,  $S_v(T_1,5\%)$ , peak ground acceleration, PGA, peak ground velocity, PGV, Arias Intensity,  $I_A$ , specific energy density,  $S_E$ , spectral acceleration at the second period,  $S_a(T_2,5\%)$ , and maximum incremental velocity, MIV are common intensity measures used to characterize the ground motions. Among these IMs,  $S_a(T_1,5\%)$ ,  $S_v(T_1,5\%)$ , and  $S_a(T_2,5\%)$  are structure-dependent spectral IMs, as these are derived from the response spectrum of ground motion based on the natural periods of the structure. PGA, PGV,  $I_A$ ,  $S_E$ , and MIV are categorized as ground motion dependent IMs. PGA and PGV represent the peak values of ground motion. While  $I_A$  is a measure of dissipated energy per unit mass in an elasto-plastic system (Arias, 1970),  $S_E$  measures the total energy of

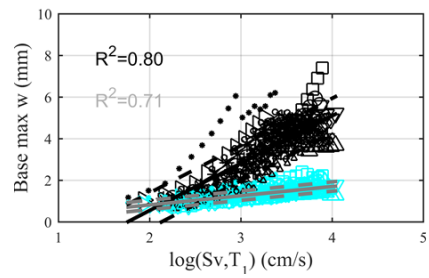
a ground motion. MIV is defined as the maximum area under the acceleration time history of a ground motion between two successive zero-crossings (Kurama & Farrow, 2003).

The relationship between the intensity measures and the damage on concrete gravity and RCC gravity dams was investigated first by selecting the EDP as the maximum width of the crack at the base of the monoliths. For the selected IMs, the correlation of damage on the monoliths was investigated for 21 events at 17 different scales in Figure 4.12. In this figure, the black markers represent the results of the concrete dam, while the results of the RCC dam are illustrated with cyan markers. In addition, the mean and mean  $\pm$  one standard deviation estimations are drawn with solid and dashed lines to show the variations in the estimations, respectively, together with the correlation coefficient ( $R^2$ ) of damage with the natural logarithm of the IMs. The statistical estimations for the concrete and RCC dams are indicated in black and gray colors, respectively.

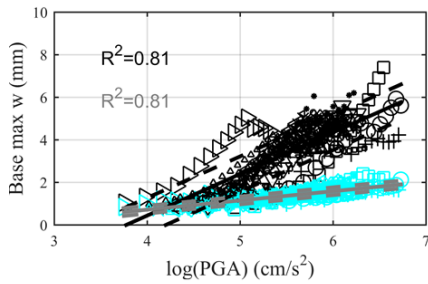
The highest correlation ( $R^2 = 0.90$ ) between the maximum base crack width and an IM was obtained for the spectral acceleration at the first period of the dam for the concrete dam model. PGA, spectral velocity, Arias Intensity, and the second mode spectral acceleration had a fairly high correlation with the damage as well. Given that high dispersions occurred for estimations with respect to PGV, specific energy density, and MIV, these quantities were not very effective indicators for the quantification of the selected damage level on the concrete gravity dam. For the RCC dam, on the other hand, the correlations with maximum base crack width were obtained lower than its concrete dam counterpart for all selected IMs. The highest correlation coefficient was obtained as  $R^2 = 0.81$  for the PGA. Similar to the concrete dam, acceptable correlation with damage was attained for the first mode spectral acceleration, Arias Intensity, spectral velocity, and the second mode spectral acceleration. For the remaining IMs, i.e., the PGV, specific energy density, and MIV, a clear relationship could not be set for the RCC case either. Using a single IM of the ground motion, the maximum base crack width could be predicted with the first mode spectral acceleration and PGA for the concrete and RCC dams, respectively.



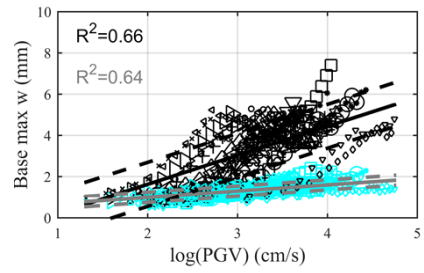
(a)  $S_a(T_1, 5\%)$  ( $m/s^2$ )



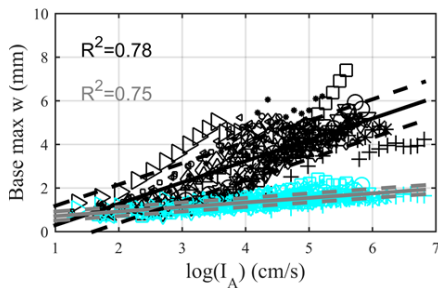
(b)  $S_v(T_1, 5\%)$  ( $m/s^2$ )



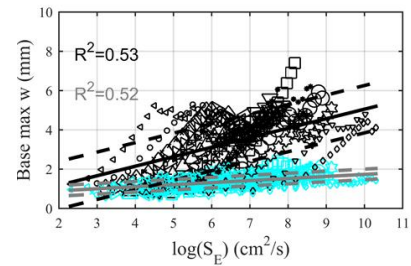
(c) PGA ( $cm/s^2$ )



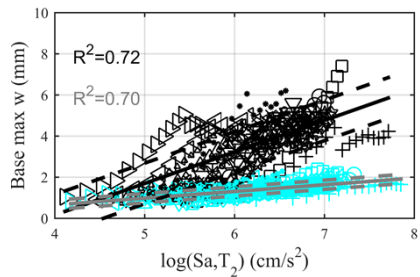
(d) PGV ( $cm/s$ )



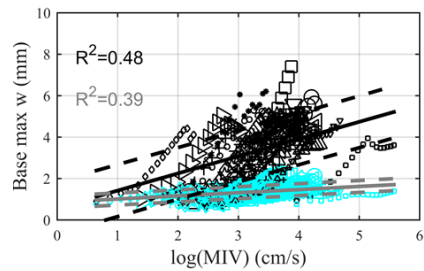
(e) Arias Intensity ( $cm/s$ )



(f) Specific energy density ( $cm^2/s^2$ )



(g)  $S_a(T_2, 5\%)$  ( $m/s^2$ )



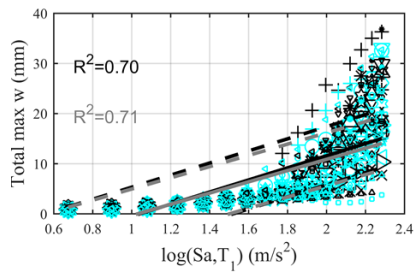
(h) MIV ( $cm/s$ )

○ Motion 1	* Motion 4	▷ Motion 7	▷ Motion 10
× Motion 2	□ Motion 5	◊ Motion 8	☆ Motion 11
+ Motion 3	◇ Motion 6	◊ Motion 9	☆ Motion 12
○ Motion 13	* Motion 16	▽ Motion 19	
× Motion 14	◊ Motion 17	△ Motion 20	
+ Motion 15	◊ Motion 18	◄ Motion 21	

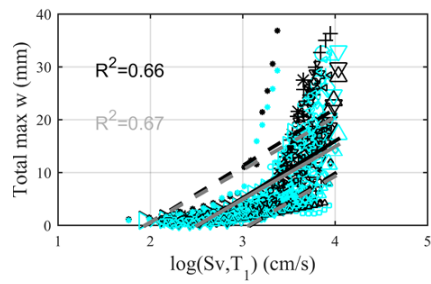
Figure 4.12 Intensity measures vs. maximum base crack width (black concrete dam, cyan RCC dam)

Next, similar to the above case, the relationship between the total maximum crack width on the upstream face and the ground motion intensity measures were investigated (Figure 4.13). Similar to Figure 4.12, the results for the concrete and RCC dam models are represented with black and cyan markers, respectively. In addition to the mean estimations (solid lines), the variation in the estimations was shown via mean  $\pm$  one standard deviation that are shown with dashed lines, together with the correlation coefficient ( $R^2$ ) of damage with the natural logarithm of the IMs. The statistical estimations for the concrete dam and RCC dams are indicated in black and gray colors, respectively.

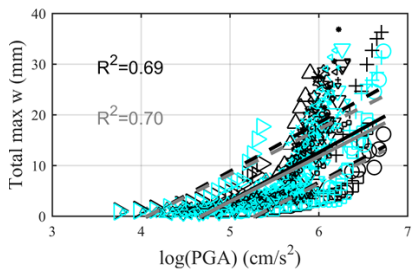
The total maximum crack width of the concrete dam could be predicted fairly with the spectral acceleration at the first period of the dam and Arias Intensity, both having correlation coefficients of 0.70. A similar correlation could be made with PGA, the second mode spectral acceleration, and the spectral velocity. On the other hand, there was a weak relationship between the total maximum crack width on the concrete dam and the IMs PGV, MIV, and the specific energy density. The total maximum crack width on the RCC dam could also be predicted fairly with the first mode spectral acceleration of the dam, and PGA, with correlation coefficients of 0.71, and 0.70, respectively. Similar predictions could be made with the Arias Intensity, spectral velocity, and the second mode spectral acceleration. The trends for the relation between the total maximum crack width on the RCC dam were similar to the concrete dam when the IMs PGV, specific energy density, and MIV were considered; they were all weakly correlated with the damage.



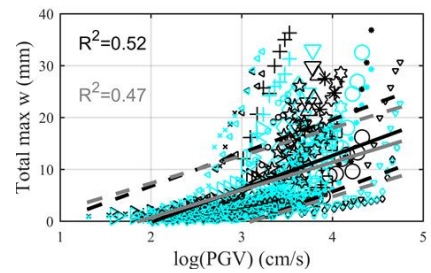
(a)  $S_a(T_{1,5\%})$  ( $m/s^2$ )



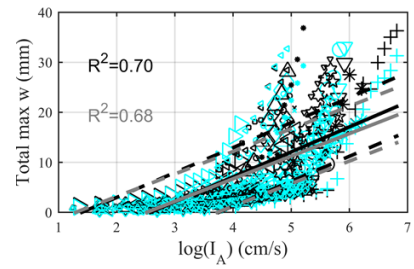
(b)  $S_v(T_{1,5\%})$  ( $m/s^2$ )



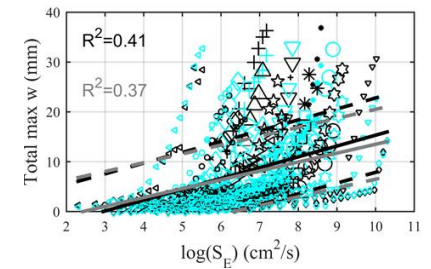
(c) PGA ( $cm/s^2$ )



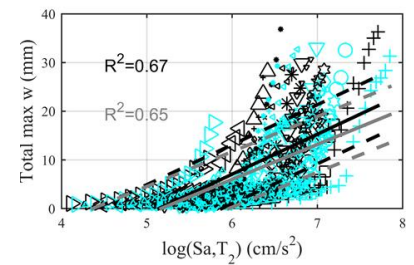
(d) PGV ( $cm/s$ )



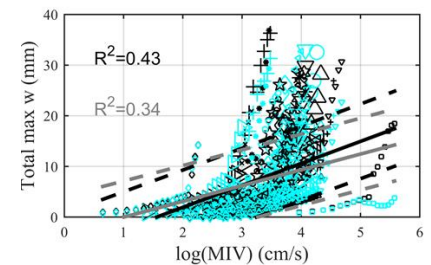
(e) Arias Intensity ( $cm/s$ )



(f) Specific energy density ( $cm^2/s^2$ )



(g)  $S_a(T_{2,5\%})$  ( $m/s^2$ )



(h) MIV ( $cm/s$ )

○ Motion 1	* Motion 4	◇ Motion 7	▽ Motion 10
× Motion 2	□ Motion 5	◇ Motion 8	☆ Motion 11
+ Motion 3	◇ Motion 6	◇ Motion 9	◇ Motion 12
○ Motion 13	* Motion 16	▽ Motion 19	
× Motion 14	○ Motion 17	△ Motion 20	
* Motion 15	◇ Motion 18	◁ Motion 21	

Figure 4.13 Intensity measures vs. total maximum crack width (black concrete dam, cyan RCC dam)

The variation of damage with respect to the considered IMs was much less for the maximum base crack width compared to the total maximum crack width at the upstream face. Accordingly, the correlation coefficients were always obtained higher for the maximum base crack width, both for concrete and RCC dams. For the majority of cases, the damage estimates for concrete dams were more successful compared to RCC dams with higher  $R^2$  factors. Using a single IM of the ground motion, the maximum base crack width could be best predicted with the first mode spectral acceleration and PGA for the concrete and RCC dams, respectively. A comparable high correlation between the studied IMs and the total crack width on the upstream face was not obtained. It should be noted that these results are obtained for the studied single dam geometry with a single set of material properties. As each gravity dam is one of a kind of structure with different geometry and material properties, the relationship between the EDPs and IMs can be generalized by considering different geometries with various material properties, which is left for further work.

Another factor to consider while evaluating damage is the relationship between face cracking and the post-earthquake seepage in the monoliths. A further quantification is therefore attempted in the form of prediction of leakage from cracking in the upstream face of the monolith as given below.

#### **4.4.5 Leakage through a Monolith as a Performance Indicator**

Seepage is defined as the flow of water through the foundation or abutments of hydraulic structures, whereas; leakage is defined as the flow of water through cracks, joints, or openings in dams (Atkinson et al., 2014). Since leakage in cracks is an important parameter to evaluate the seepage behavior of a dam that is directly related to the dam safety, the water flow through each upstream crack in MAEM models was computed to estimate the leakage through the monolith. The leakage through a dam is a damage indicator: it is also measurable and used directly to assess the health of the system after serious events.



The seepage flow,  $Q$ , of a concrete dam body is calculated with respect to three components, namely seepage flow due to hydrostatic pressure,  $Q_h$ , ambient temperature,  $Q_T$  and unexpected irreversible behavior with time,  $Q_\theta$  (Equation (4.3)). (J. Hu et al., 2018).

$$Q = Q_h + Q_T + Q_\theta \quad (4.3)$$

It was reported that the  $Q_\theta$  component did not play a significant role in the leakage amount. Similarly, the seepage flows in non-cracked concrete (a component of  $Q_h$ ) did not affect the leakage amount considerably. Observed over a 10-year period, the leakage amount of an RCC dam in China was affected most by the annual amplitude of local temperature variations,  $Q_T$ , and the penetrating cracks in the dam body, which is a component of  $Q_h$  (J. Hu et al., 2018). Accordingly, in this study, the leakage amount was calculated considering the cracks in the upstream face of the dam models, for the post-earthquake state, under a constant average temperature of 15 °C. While the hydraulic conductivity of cracked concrete is several orders of magnitude greater than that of the non-cracked concrete (J. Hu et al., 2018), seepage is not considered in the attempt here as seepage through mass concrete is negligible compared to flow through leakage pathways.

For a straight and smooth, ideal crack, the water flow is expressed by the cubic law as given in Equation (4.4). (Aldea et al., 2000).

$$q = \frac{gt}{12\nu} \frac{\Delta h}{L} w^3 \quad (4.4)$$

where  $q$  is the seepage velocity,  $g$  is the gravitational acceleration,  $\Delta h$  is the change in water head,  $L$  is the crack length in the flow direction,  $t$  is the crack length perpendicular to the flow direction,  $w$  is the crack width, and  $\nu$  is the kinematic viscosity (Figure 4.10b).

It was shown in the literature that the cracks in concrete are tortuous and rough rather than straight and smooth; therefore, a modification to Equation (4.4) is made via the correction factor,  $\xi$ , to consider the crack morphology (Equation (4.5)). In this study,  $\xi$  was selected as 0.10, in accordance with Aldea et al. (2000).

$$q = \frac{gt}{12\nu} \frac{\Delta h}{L} w^3 \xi \quad (4.5)$$

A schematic sketch for the upstream crack geometry and the leakage calculations are presented in Figure 4.10b and Figure 4.10c, respectively. During the analytical simulations, as presented, a number of cracks were obtained at the upstream faces of the sample monoliths. The leakage amount for a given crack was estimated using  $w = w_{res}$ , i.e. the residual crack width  $w_{res}$  as the primary factor in Equation (4.5). The residual crack width was assumed as a factor of the maximum crack width,  $w_{max}$  due to uncertainties in the process as well as computational limitations. One important limitation is, as mentioned before, the fluid pressure within the cracks was neglected in the analysis: compared to the global behavior, this could affect the residual crack opening. Research into the crack pressures (Javanmardi et al., 2005a, 2005b, Pekau & Zhu, 2006) yielded a complex behavior: the uplift pressures might have an effect on the crack closing mode than the crack opening case (Javanmardi et al., 2005a). Another particular difficulty is the damage to the crack surfaces in these systems with large aggregate sizes. Accordingly, the crack openings are likely underestimated in this study, prompting a parametric consideration of the crack width based on the maximum opening.

For each crack, based on the residual opening,  $w_{res}$ , the length of the crack in the flow direction,  $L_{res}$ , was also computed (Figure 4.10b). The flow of water through the cracks for a single dam monolith is presented in Figure 4.10c as a representative sketch. For a dam monolith with thickness,  $t$ , the water penetrates through the cracks and exits at the vertical expansion joints between the two monoliths in zero head condition. In the absence of an estimate for such a seepage path, the leakage formula

given in Equation (4.5) has been used to obtain an estimate for the flow through this crack. The leakage amount for the base crack and the total leakage amount for all upstream cracks were calculated to evaluate the post-seismic behavior of the concrete and RCC dams accordingly. For these calculations, the width of the monolith was assumed as 20 m determining the crack length perpendicular to the flow direction,  $t$ , as 20 m. As stated, the correction factor for crack morphology,  $\xi$ , and the kinematic viscosity of water,  $\nu$ , at 15 °C were taken as 0.10 and  $1.1384 \times 10^{-6} \text{ m}^2/\text{s}$ , respectively.

The leakage in cracks is an important parameter to evaluate the seepage behavior of a dam, which is directly related to dam safety (J. Hu et al., 2018). Therefore, in addition to the leakage amount at the base, the total leakage amount at the upstream cracks were evaluated for MAEM models with discrete cracks, as well. In Figure 4.14, the leakage amount estimations for concrete and RCC models are given for the base crack and the total leakage in all upstream cracks, assuming a residual crack width,  $w_{res} = 0.2w_{max}$ , together with the mean (solid black line) and mean  $\pm$  one standard deviation (dotted black line) leakage amounts. On average, the base leakage (Figure 4.14a) and the total leakage (Figure 4.14b), obtained by summing up the leakage amount in each upstream crack for the concrete dam, were estimated in the ranges 0.1 – 3.7 l/s and 0.1 – 7.9 l/s, respectively. For a critical leakage amount of 1.0 l/s, at the base of the concrete dam, on average, significant leakage was expected to occur for low ground motion intensities, for spectral acceleration ( $S_a$ ) greater than 0.45g. With this residual opening, mean leakage values as high as 4 l/s were expected at the base when  $S_a$  was greater than 0.7g. It should be noted that remedial issues were taken immediately for a leakage amount of 4 l/s for an RCC dam located in China (J. Hu et al., 2018), indicating the severity of the above leakage estimations for the seismic safety of the gravity dam.

For the RCC dam, the leakage amounts with respect to the same residual crack width factor 0.2 were estimated considerably less than the concrete dam. The mean base (Figure 4.14c) and total leakage (Figure 4.14d) for this case were obtained as 0.07 –

0.2 l/s and 0.08 – 0.9 l/s, respectively, indicating leakage more than 1.0 l/s occurring from the upstream face for spectral accelerations higher than  $1.0g S_a$ . For the base crack, important leakage that would endanger the post-seismic safety of the dam was not expected. For the RCC dam, the base and the total leakage amounts were estimated at nearly  $1/20^{\text{th}}$  and  $1/10^{\text{th}}$  of the concrete dam, respectively.

Investigating the leakage estimations at the base and at the upstream face of the dams, it was observed that although more cracking was expected to occur on the RCC dam, the leakage estimations were considerably less. This is due to the fact that in the RCC dam, individual crack widths were lower, and the lengths of the cracks were higher, which in turn led to a decrease in the seepage velocity for the leakage amount estimations. The concrete dam, on the other hand, was subjected to more leakage, both at the base and at the upstream face: significant leakage amounts were obtained. From the point of leakage estimations, it can be concluded that a concrete dam would be more susceptible to leakage after an earthquake compared to an RCC counterpart.

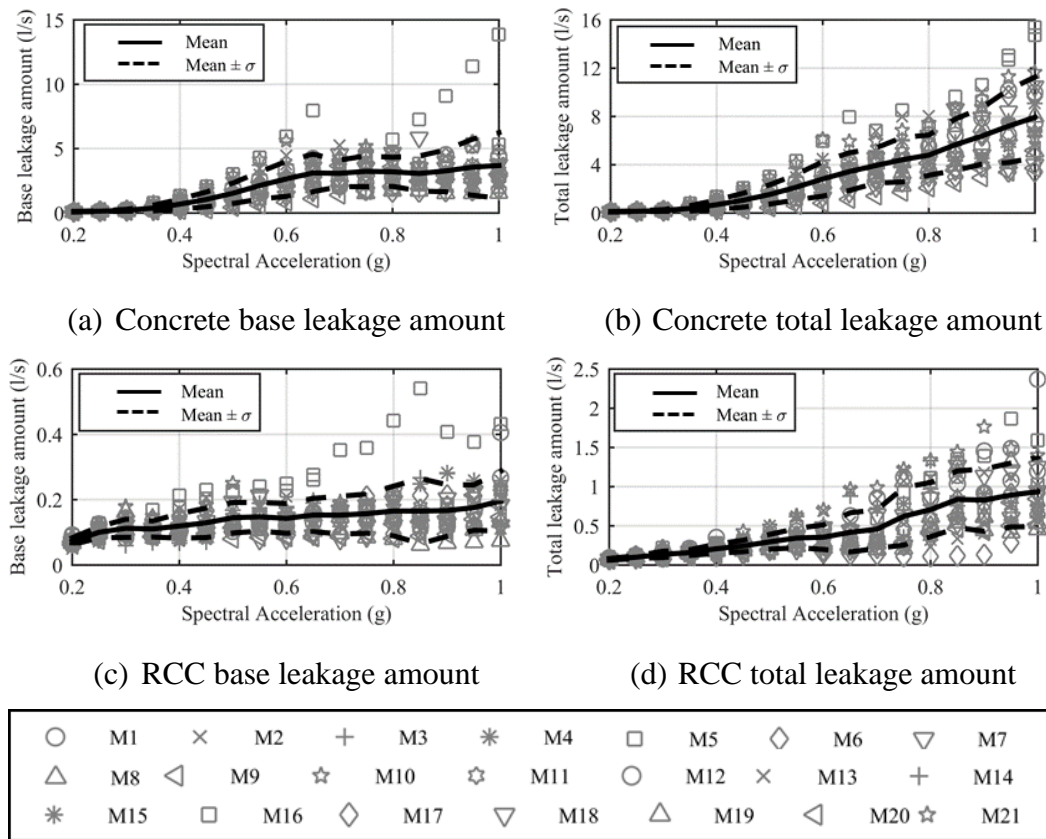
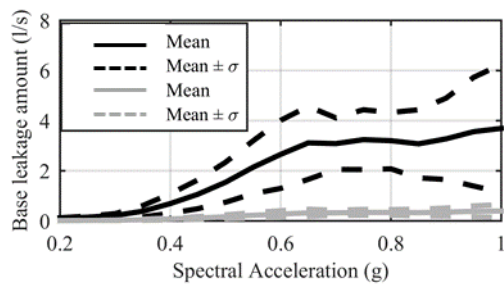


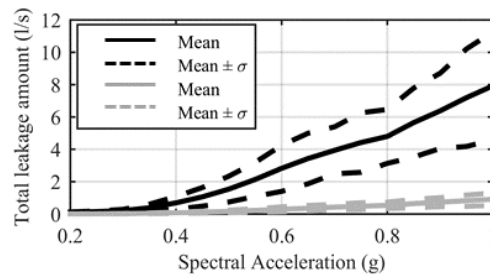
Figure 4.14 Leakage amount estimations for residual crack factor 0.2

In order to investigate the effect of residual crack width,  $w_{res}$ , the same leakage calculations were conducted for different residual crack width factors of 0.2, 0.1, 0.05, and 0.01, i.e.,  $w_{res} = 0.2w_{max}$ ,  $w_{res} = 0.1w_{max}$ ,  $w_{res} = 0.05w_{max}$ , and  $w_{res} = 0.01w_{max}$ , respectively (Figure 4.15). The comparison of leakage amount regarding only  $w_{res} = 0.2w_{max}$ , and  $w_{res} = 0.1w_{max}$  are presented in Figure 4.15, as the leakage estimations were obtained considerably less for residual crack width factors 0.05 and 0.01. The leakage estimation decreased significantly as the residual crack width decreased. The mean base leakage amount ranges for the concrete dam were calculated as 0.1 – 3.7 l/s, 0.01 – 0.4 l/s, 0.002 – 0.05 l/s, and  $0.1 \times 10^{-4}$  –  $3.8 \times 10^{-4}$  l/s, respectively, for residual crack width factors 0.2, 0.1, 0.05, and 0.01 (Figure 4.15a). The leakage amount of 1 l/s was exceeded only for the residual crack width factor of 0.2 at the base of the concrete dam. For the RCC dam, mean base

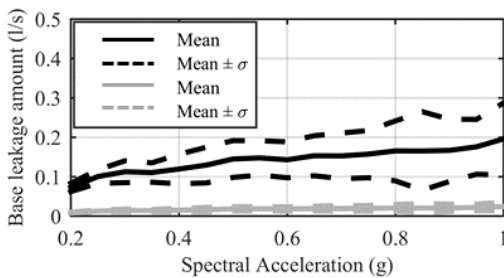
leakage amount ranges were estimated as 0.07 – 0.2 l/s, 0.01 – 0.02 l/s, 0.001 – 0.003 l/s, and  $0.9 \times 10^{-5} - 2.4 \times 10^{-5}$ , for residual crack width factors 0.2, 0.1, 0.05, and 0.01, respectively (Figure 4.15c). In addition to the base leakage estimations, the total leakage amount at the upstream cracks was compared for the same residual crack width factors: for the concrete dam, flow ranges of 0.1 – 7.9 l/s, 0.01 – 0.9 l/s, 0.002 – 0.1 l/s, and  $0.1 \times 10^{-4} - 9 \times 10^{-4}$  l/s, respectively, was obtained for residual crack width factors 0.2, 0.1, 0.05, and 0.01 (Figure 4.15b). For  $S_a$  greater than 0.45g, the critical leakage amount, 1 l/s, was expected to occur when  $w_{res} = 0.2w_{max}$ . Even for the residual crack width factor of 0.1, critical leakage might be expected at the upper bound of  $S_a$  for the concrete dam. Conversely, for the RCC dam, the average total leakage amounts were within the bounds 0.08 – 0.9 l/s, 0.01 – 0.1 l/s, 0.001 – 0.01 l/s,  $0.09 \times 10^{-4} - 1.2 \times 10^{-4}$  l/s, for residual crack width factors 0.2, 0.1, 0.05, and 0.01, respectively (Figure 4.15d).



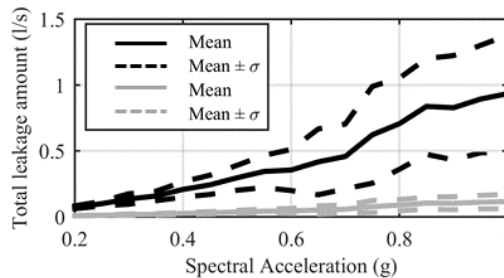
(a) Concrete base leakage amount



(b) Concrete total leakage amount



(c) RCC base leakage amount

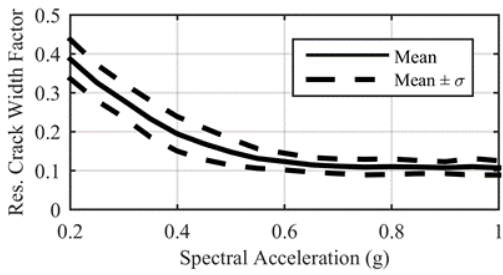


(d) RCC total leakage amount

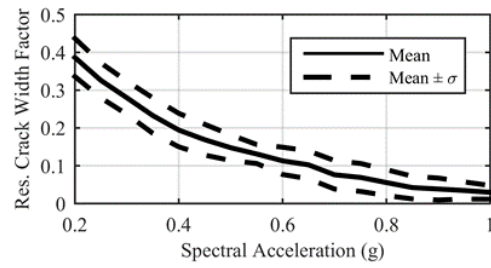
Figure 4.15 Mean leakage amount comparison of residual crack width factor 0.2 (black) and 0.1 (gray)

Concrete and roller-compacted concrete gravity dams appear to yield very different estimates regarding post-earthquake leakage. Much less leakage is expected in roller-compacted concrete monolith due to disbursed cracking in lift joints and smaller crack openings compared to concentrated cracks in the concrete counterpart. On the other hand, as the leakage estimation is highly affected by the residual crack opening, the breaking of contact regions and residual material penetrating inside the crack from the reservoir during strong shaking appear to be the primary determinants of the leakage. The behavior of these two materials can be different in this sense as well: the more heterogeneous nature of RCC material may lead to higher residual opening not adequately defined in the concrete constitutive models.

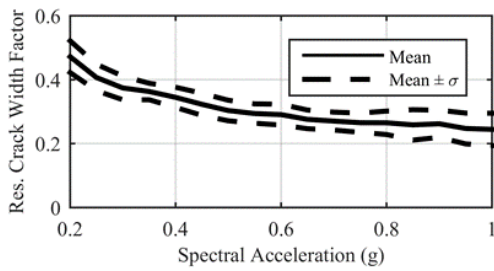
The leakage estimations, as presented above, is highly affected by the residual crack widths since the water flow is proportionally related to the cube of the crack width (Equation (4.4)). In order to quantify the residual estimates used above, crack openings obtained at the end of the dynamic simulations were calculated, and the residual crack width factor was obtained by dividing these numbers by the maximum crack width (i.e.,  $w_{res}/w_{max}$ ). These factors were computed for the base and total upstream cracks, both for the concrete and RCC dams, at different spectral acceleration levels. The mean and mean  $\pm$  one standard deviation residual factors, obtained henceforth, are presented in Figure 4.16. The results show, in spite of the large maximum openings during the motion, some cracks on the upstream face closed: similar residual crack opening divided by larger, increasing crack width with  $S_a$  led to the curves given in Figure 4.16b and d. The base crack, on the other hand, remained open due to the static load. For the base cracks, on average, residual crack width factors were obtained as 0.1 and 0.3 for the concrete and RCC dams, respectively. A residual factor of 0.1 appears to be a good upper bound on the response on the total crack width for both systems. The real response is likely higher due to the residual reservoir pressure in the crack.



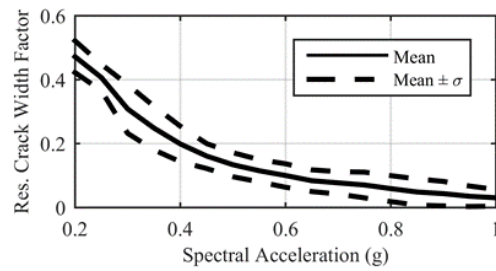
(a) Concrete base



(b) Concrete total



(c) RCC base



(d) RCC total

Figure 4.16 Computed residual crack width factors

## 4.5 Summary

In this chapter, the nonlinear seismic behavior of gravity dam-reservoir systems was investigated by conducting incremental dynamic analysis (IDA) to quantify damage levels on these systems based on various outputs obtained through discrete cracks. Two MAEM models, having identical geometries for the dam body, were constituted for investigating the nonlinear performance of concrete and roller-compacted concrete gravity dams separately. The concrete gravity dam was modeled with the same material properties throughout the dam body. On the other hand, the effect of lift joints was taken into account in the RCC gravity dam by modeling the lift joints with lower strength. IDA was conducted on a ground motion set comprised of 21 motions, each scaled to 17 different intensity levels leading to 357 nonlinear transient analyses for each model. The seismic performance of a concrete dam monolith was evaluated first by considering various parameters such as the extent of cracks, the



maximum crack widths, and the corresponding leakage estimates. The results from the modified applied element modeling of the monolith were compared with the finite element method (FEM) results using crack patterns and fragility curves, accounting for different modeling techniques on the nonlinear results. The performance of this conventional concrete gravity dam was compared to the roller compacted counterpart by considering the lift joints to properly simulate RCC dam behavior, with the same geometry using fragility curves. The crack distribution, evolution of damage, and the separation of elements on the dam body for MAEM models were investigated thoroughly. In addition to the comparison of the damage on models using fragility curves based on the extent of damage, crack widths on the upstream faces of the dam monoliths were computed as a new damage indicator. The maximum base and the total maximum crack widths in the upstream face of the dams were compared to investigate the severity of damage that these structures were subjected to with respect to crack width. Furthermore, the variation of the maximum base and total crack widths were studied to set a relationship between ground motion IMs and the damage on the dam bodies. To this end, 8 different structure and ground motion dependent IMs were used. Lastly, the leakage through the upstream cracks was estimated using residual opening of the cracks as well as the crack geometrical properties like depth and length. The results of the analyses based on several performance indicators were shown with mean quantities and bounds on the mean summarizing the comprehensive time history results. The following conclusions were drawn from the analyses:

- The IDA results were first investigated by means of observed crack profiles in the FEM and two MAEM models. Both the active and inactive cracks were taken into account, and the limit for the minimum crack width shown in the crack profiles was chosen as 0.35 mm in all three models. For all modeling approaches, cracks were initiated at the upstream base of the dam. In the concrete dams (FEM and MAEM Model I), cracks occurring at the downstream face tended to propagate approximately with 45° inclination. However, cracks occurring at the upstream face propagated in a horizontal

direction. On the other hand, as weak horizontal layers existed for the RCC dam, cracks at the upstream and downstream sides of the dam propagated horizontally. As the lift joints were considered in the simulations, the RCC dam was subjected to more cracking, especially at the upstream side of the dam.

- The IDA results were next compared for FEM and MAEM concrete models based on the observed crack profiles in more detail. In general, the smearing of cracks occurring in the FEM model was eliminated using a discrete approach, such as the proposed MAEM model. Especially at the downstream face of the dam, the discrete crack propagation could be clearly simulated with MAEM. A disadvantage that could be attributed to the MAEM model for the modeling of concrete dams was that due to the discretization of the inclined downstream face with rectangular elements, stress concentrations at the discretized points occurred. Therefore, compared to the FEM model, additional cracks were observed. However, this modeling is appropriate for RCC dams as the downstream slope is layered as in the model. At the upstream side of the dam, the cracks propagated more in MAEM than in the FEM. Smearing was highly decreased in the MAEM model leading to further propagation of cracking. Consequently, the FEM model led to unsafe results compared to a discrete model in terms of crack propagation.
- The solution time of MAEM was found to be 4 times that of the FEM model due to the differences in the nonlinear dynamic solvers. As implicit solution scheme was utilized for the FEM model: the solution time step was 25 times the corresponding value for the MAEM model with the explicit integration algorithm. Although the computational cost of MAEM and explicit integration was 4 times higher than FEM, discrete crack propagation could be obtained.
- The fragility curves of the FEM and MAEM concrete models were obtained for four limit states based on damage propagation towards the dam core. The probability of damage was obtained smaller at almost every intensity level

with the FEM model based on the smeared crack model. For the MAEM model, at almost every intensity level, the probability of observing damage was predicted 20% to 40% higher than the FEM model. Accordingly, the fragility curves moved left, indicating more risk to these systems at the identical seismic intensity measures.

- The solution times of the MAEM concrete model for a 1-second duration of ground motion were investigated with five different spring pair numbers. The increase in the number of spring pairs from 1 to 20 led to an increase in the computational cost approximately 1.2 times. It was observed that the reservoir finite elements had a significant contribution to the solution times.
- The comparison of seismic performances of the concrete and the RCC dam constituted with MAEM was also made by initially investigating the cracking schemes. For smaller motion intensities, when the damage was limited to the upstream base, similar crack profiles were observed for the concrete and RCC dams. However, for larger motions, the weakness of the lift joints considerably affected the cracking at the downstream face. The RCC dam suffered considerably more cracks compared to an identical geometry monolithic concrete dam.
- The comparison of the fragility curves of the monolithic concrete dam and the RCC dam showed the probability of exceeding the damage states was more for the RCC dam as expected due to weak lift joints. The only exception was for the first limit state representing the initiation of damage in the system with very limited cracking at the base. The probability of exceeding LS1 was generally calculated 20% higher in the concrete dam compared to the RCC counterpart as a single base crack occurred in the model; in contrast, in the RCC dam, many cracks at the weak layers within the heel were observed. For the other limit states, at almost every intensity level, the likelihood of exceeding the same damage state was approximately 15%-35% higher for the RCC.

- As a new damage indicator, the maximum crack width at the base and the total maximum crack width at the upstream side of the dam were computed. For the maximum crack width calculations, the minimum crack width was chosen as 0.35 mm, in accordance with the minimum crack width shown in the crack profiles.
- The comparison of the total crack widths from the FEM and MAEM models for the concrete gravity dam showed similar results for base cracks. The total maximum crack width, on the other hand, was estimated 50% less by the FEM model compared to the MAEM model for the concrete dam for high ground motion intensities that produced significant damage, leading to less conservative results.
- The results of the analysis for the RCC and concrete gravity dams with identical cross-sections were compared using the MAEM models. The maximum base crack opening for the RCC dam was obtained 80% to 35% less than the concrete counterpart for the 0.2g – 1.0g loading range quantified in terms of  $S_a$ . The variation in the maximum base crack width with respect to seismic intensity was also much more substantial for the concrete dam compared to the RCC counterpart. When the mean of total crack widths on the upstream face was compared, the envelope was similar for both sections. The total maximum crack widths of the two models converged for the lower number of cracks with higher widths (concrete) and more cracks but with smaller widths (RCC).
- The relationship between ground motion IMs and damage on the concrete gravity and RCC gravity dams were investigated by selecting the maximums of the base crack and total crack width as EDPs. The studied 8 IMs showed that the maximum base crack width could be predicted better with less variance compared to the overall upstream crack width for the two models. Utilizing a single IM of the ground motion, the maximum base crack width could be best predicted with the first mode spectral acceleration and PGA for the concrete and RCC dams, respectively. A comparable high correlation

between the total crack width at the upstream side and the investigated IMs were not obtained for either of the simulated systems.

- The leakage through the upstream cracks for the concrete and RCC models were compared by assuming a residual crack width after a seismic event, as 20% of the maximum crack width, concerning the base and total cracks. For the concrete dam, on average, leakage over 1 l/s was expected to occur at the base for  $S_a$  greater than 0.45g. Moreover, mean leakage values as high as 4 l/s were expected at the base crack when  $S_a$  was greater than 0.7g. Conversely, for the RCC dam, the mean base and total leakage amounts were estimated nearly at 1/20<sup>th</sup> and 1/10<sup>th</sup> of the concrete dam, respectively. For this case, leakage over 1 l/s was attained at 1.0g  $S_a$  over the whole upstream face. In the RCC dam, although cracking was more spread, the leakage estimations at the base and in total were considerably less than the concrete dam since the widths of these individual cracks were lower, and their lengths were higher, which in turn led to a decrease in the seepage velocity for the leakage amount estimation.
- The residual crack width has a significant effect on the leakage estimations. Calculations with respect to 4 different residual crack widths showed that as the residual crack widths decreased, the estimated leakage amounts decreased significantly. For the RCC dam, leakage over 1 l/s was not expected to occur for residual crack width factors less than 0.2. As the leakage estimation is highly affected by the residual crack opening, the breaking of contact regions and residual material penetrating inside the crack from the reservoir during strong shaking can be the primary determinants of the leakage.
- The residual crack widths were calculated according to the crack openings obtained at the end of the dynamic simulations for concrete and RCC dam-reservoir systems. Accordingly, a residual crack width factor of 0.1 appeared to be a good upper bound on the response on the total crack width for both systems. The real response, however, is likely higher due to the residual

reservoir pressure within the cracks, as the fluid pressure within the cracks was neglected in this study.

- The seismic performance of concrete dam-reservoir systems was evaluated based on the severity of the cracking defined in terms of the distribution of cracking, the extent of cracking as well as the nature of cracking as allowed by the definition of crack width in the MAEM model. When considered based on the extent and propagation of cracking, the RCC dam was subjected to more severe damage than the concrete dam at the same seismic intensity. When the evaluation was made with respect to the nature of cracking, i.e., considering the crack width at the base, higher damage was observed for the concrete section. On the other hand, the cumulative consideration of the damage on the upstream face expressed in terms of the envelope of the total maximum crack widths yielded similar metrics for the RCC and concrete dams. The estimated leakage amount, depending on the cube of the crack width and to a lesser amount on the crack length, showed cracking on a concrete dam can be more critical compared to the RCC dam due to the concentration of damage at the base crack.

## CHAPTER 5

### SUMMARY, CONCLUSIONS AND FUTURE EXTENSIONS

#### 5.1 Executive Summary

A discrete element-based methodology called the modified applied element method was developed, accurately simulating the linear and nonlinear behavior of plain concrete structures. The existing applied element method was first modified to obtain a robust methodology and enable the representation of a variety of Poisson's ratio, unlike many discrete techniques that ignore the Poisson's effect or use a fixed Poisson's value. In order to show that this mathematical model can be used to simulate physical phenomena, and therefore, can be used as a prediction tool, extensive validation studies were performed. These validation tests were conducted for linear and nonlinear response cases with the goal of demonstrating the robustness of the methodology. The implemented cyclic, hysteretic, nonlinear concrete tension material model was shown to be capable of representing the nonlinear response of concrete structures by modeling experimental studies under various loading conditions such as direct tension, indirect tension, bending, and earthquake loading with a stable analysis response. In order to accurately simulate the dam-reservoir systems, a displacement/pressure based mixed fluid finite element was implemented as well, coupling the modified applied elements with fluid finite elements. These elements were validated alone and coupled with the modified applied element method, MAEM, successfully, showing these tools can be used together in simulation of the behavior of gravity dams.

The assessment of the behavior of concrete gravity dams under seismic actions is challenging. First of all, numerical models producing reliable results in cracking of this brittle material is required. Secondly, clear damage indicators to quantify the performance of these systems are not available. While the finite element method

(FEM) is a commonly utilized tool to predict damage on concrete dam bodies, diffused cracking patterns has been reported as a significant disadvantage in fracture simulation, which can be overcome by utilizing discrete element-based methods. Accordingly, the MAEM model, as validated in the linear range, as well as the nonlinear range for brittle cracking, was used in this study to determine the seismic performances of identically shaped concrete and roller-compacted concrete (RCC) monoliths. Incremental dynamic analysis (IDA), taking into account the effect of different ground motion characteristics, was used to establish damage indicators appropriate to these monolithic brittle structures, with cracking of the system as the main concern in the behavior. Using a discrete element based technique allowed the use of crack width based damage indicators for the first time in this study, along with the limit states based on the extent of cracking towards the core of the dam. IDA also enabled the investigation of the relationship between ground motion intensity measures and the crack widths on the system. The quantification of damage at the post-earthquake state was studied by considering the residual crack openings and the leakage estimations through these cracks at the base and at the upstream surface. The damage indicators defined as such take the performance-based seismic assessment of gravity dams one step ahead with good correlations to commonly used seismic intensity measures.

## **5.2 Summary**

In Chapter 1, an introduction to the work and the literature review on numerical methods for simulation of cracking, the influence of dam-reservoir interaction on the seismic behavior of concrete dams, and the nonlinear analyses of concrete dams are presented. The majority of the conducted research on the nonlinear seismic response of concrete dams focused on determining the damage on the dam body with the finite element method (FEM). FEM has a significant disadvantage: the use of the smeared crack technique leads to diffused cracking patterns. The weak layers of roller-compacted concrete (RCC) dams, state of the art for gravity dams, can also not be



modeled directly in FEM. While ease of use is well-accepted, the results based on a continuum approach preclude the definition of clear performance-based metrics for gravity dams. The limitations of the FEM were the motivations for this study; accordingly, a robust discrete element based tool, the modified applied element method (MAEM), was developed to accurately simulate the behavior of concrete monoliths in the linear and nonlinear ranges. The discrete nature of the methodology enables the nonlinear seismic investigation based on discrete cracks and the use of corresponding metrics for damage quantification on gravity dams.

In Chapter 2, the theoretical background of this work is presented. In this chapter, the proposed MAEM technique, the theory, and formulation in the linear and nonlinear ranges are introduced. A major contribution presented in this chapter is the theoretical representation of accounting for Poisson's effect. In order to model the fluid-structure interaction problems, the implemented fluid finite element and radiation boundary conditions at the far end of the reservoir are explained. A detailed explanation regarding the implementation of the methodology in a computer program written in FORTRAN language is presented. The linear and nonlinear static solvers, linear implicit and explicit dynamic solvers, and nonlinear explicit dynamic solvers that were implemented are explained, together with the utilization of the mass scaling procedure and the loading type definitions in the computer program.

In Chapter 3, extensive validation tests for the modified applied elements, fluid finite elements, and the coupling of these discrete and finite elements are presented. The robustness of MAEM was demonstrated through linear static analysis of a cantilever column under various loading types. Then the convergence rate of the proposed methodology was determined by solving linear static problems of a laterally loaded shear wall problem, in which shear is dominant, and a bending dominant frame loaded in a similar fashion. Next, the loading, unloading, and reloading branches of the implemented nonlinear material model was demonstrated, and several validation tests of experimental works in the literature were carried out. The simulated experimental works such as the uniaxial tension test of a rectangular concrete prism, splitting tension test of a cylindrical concrete specimen, and the push-over loading

of a scaled dam experiment in the nonlinear setting showed that the implemented nonlinear material model was capable of simulating the cracking and global load-displacement behavior of plain concrete structures successfully. After the verification of MAEM, the implemented fluid elements were validated by calculating the pressure distribution of a water tank under its self-weight; in addition, the modal properties of a water column were estimated correctly. Then, the coupling of MAEM and reservoir finite elements, together with the radiation boundary condition, was investigated by performing frequency response analysis. The results showed that the coupling of the two methods was successful in the linear range. In the nonlinear range, Koyna Dam-reservoir system was investigated. Employing an explicit solution algorithm showed that the crack simulation on the dam body could be simulated well, verifying the coupling of modified applied-finite elements using an explicit nonlinear solution algorithm utilizing the mass scaling technique. An important outcome in this chapter is the demonstration of the effect of Poisson's ratio on the simulation results. For the same nonlinear MAEM validation tests, the effect of Poisson's ratio on the capacity and the cracking behavior under different loading scenarios together with the influence of material parameters were shown.

In Chapter 4, the nonlinear behavior of gravity dam-reservoir systems, coupling the modified applied elements and reservoir finite elements, was investigated thoroughly under seismic actions. A concrete gravity and an RCC gravity dam having identical geometries for the dam body were evaluated using two MAEM models. The concrete gravity dam was modeled with homogenous material properties throughout the dam body. The effect of lift joints was taken into account in the RCC gravity dam by modeling the lift joints with lower strength. In order to assess the performance of the gravity dams under seismic loads, IDA was conducted on a ground motion set comprised of 21 motions, each scaled to 17 different intensity levels leading to 357 nonlinear transient analyses for each model. The analyses conducted for the concrete dam were first compared to FEM results for the same section, showing the effect of different modeling approaches on the analysis outcomes. Then, IDA was performed on the second MAEM model by considering the lift joints to properly simulate RCC

dam behavior. The comparison of the model outcomes for the FEM, MAEM concrete, and MAEM RCC dams were conducted first using qualitative results: later, two quantitative approaches were used to establish the differences. The first of these approaches were based on limit states depending on the propagation of cracking within the body and the foreseen consequences. The second, the new introduction in this work, is based on the direct calculation of the crack widths on the upstream faces of the dam monoliths as a new damage indicator. The relationship between the maximum base/total upstream crack widths and the ground motion IMs were studied, leading to a substantial correlation in the response compared to poor correlations in damage indicators like crest displacement commonly used in FEM models. The crack widths on the upstream face were further used to predict the leakage through the upstream cracks, a direct performance measure after an earthquake. The results of the analyses based on several performance indicators were shown with mean quantities and bounds on the mean summarizing the comprehensive time history results.

### **5.3 Concluding Remarks**

The main conclusions of this study are as follows:

#### **I. Validation Studies, Linear:**

- The robustness of the developed analysis framework was verified in a linear setting with respect to mesh refinement (number of elements) and mesh detail (number of spring pairs) using displacements and stresses for a range of problems. Increase in mesh density and detail brings in additional accuracy at the cost of computation, as expected.
- The proposed methodology showed superiority over discrete methods in the small displacement range by its ability to model the Poisson effect accurately, compared to other techniques that ignore or can only include it using

randomly distributed element sizes and corresponding special meshes in the model.

- The number of spring pairs affected the results of bending and shear dominated linear static problems depending on the Poisson's ratio. For the specific  $\nu=0.33$  case, as the shear springs vanish from the model, rotations are eliminated; hence, identical results are obtained irrespective of the spring number.
- The convergence rate of the proposed technique was shown to be linear. For bending and shear dominated problems, modeling components with elements at  $1/40^{\text{th}}$  and  $1/200^{\text{th}}$  of the component width was shown to decrease the error in displacement predictions to less than 1%, which is acceptable in the available computational capacity.
- The difference between the results of a coarse and fine mesh of an identical structure was higher in MAEM compared to FEM due to the boundary condition definitions in these models. In FEM, boundary conditions are assigned to joints; conversely, in MAEM, boundary conditions restrain the movement of a whole rigid element; this effect is reduced by making the mesh finer.
- The coupling of the proposed modified applied elements with the implemented fluid finite elements was evaluated in detail with the frequency response analysis of an idealized full-scale dam-reservoir system. The dam-reservoir interaction was captured well using a reservoir length just two times the dam height modeled with the implemented fluid elements having large sizes and relatively high aspect ratios decreasing the computational cost.

## **II. Validation Studies, Non-Linear:**

- MAEM utilizing the Maekawa tension softening material model was verified in the nonlinear setting with respect to mesh density for a range of problems with various loading types. The overall behavior was simulated well with the increase in the mesh density.

- The post-peak parameters of the implemented Maekawa tension model, the softening parameter,  $c$ , and the ultimate tensile strain,  $\varepsilon_{ult}$ , should be selected based on the desired fracture energy,  $G_f$ , in accordance with the mesh size. For smaller element sizes, in addition to the increase in  $\varepsilon_{ult}$ ,  $c$  should be selected smaller (corresponding to a less brittle softening curve that increases the area under the stress-strain curve). The shape of the post-peak curve of the experimental results may not be represented well for very small element sizes (less than 5 mm, according to the uniaxial tension test simulations conducted in this study).
- The nonlinear Maekawa material model was introduced to the normal springs only. Shear springs, on the other hand, were assumed to be brittle such that when the tensile strength of the normal spring was reached, the stiffness and force terms of the corresponding shear spring pair were eliminated. The verifications under various loading types showed that this assumption on the behavior of shear springs is acceptable.
- The effect of Poisson's ratio on the nonlinear response of structures was investigated for a range of problems with various loading types. In the fracture energy formulation, the  $G_f$  and  $\nu$  were proportionally related, and the increase in  $\nu$  led to an increase in  $G_f$ . Excluding the splitting tension test, the analyses conducted under a constant  $G_f$  led to higher capacities for higher  $\nu$ . For the splitting tension test, in the simulations,  $G_f$  increased with increasing  $\nu$ ; however, the capacities were obtained lower. The capacity in this test, with a relatively more brittle ending compared to the other tests, apparently does not depend on the ultimate capacity of the material.

### **III. Nonlinear Behavior of Dam-Reservoir Systems:**

- The crack profile comparison for the FEM and MAEM models of concrete gravity dams showed the clear effects of the smearing of cracks in the FEM model, which was eliminated using the proposed MAEM model.

Consequently, the FEM model led to unsafe results compared to a discrete model in terms of crack propagation.

- A disadvantage of the MAEM models for modeling the concrete dams was the stress concentrations at the discretized points in downstream, leading to more cracking compared to FEM models. However, this modeling is appropriate for RCC dams as the downstream slope is layered as in the model.
- The fragility curves of the FEM and MAEM concrete models, obtained for limit states based on damage propagation towards the dam core, showed that the probability of damage was obtained smaller at almost every intensity level with the FEM model based on the smeared crack model. As discrete and more propagated cracks were obtained for the MAEM model, observing damage was 20% to 40% higher; accordingly, the fragility curves moved left, indicating more risk to these systems at the identical seismic intensity measures.
- The solution times of MAEM models in the nonlinear dynamic setting showed that the computational cost was directly affected by the mesh density and number of spring pairs. When the element size was halved and the number of DOF increased four times, the solution time increased approximately 4.7 times showing linear scaling in the explicit solver. Increasing the number of springs connecting the elements affects the run times far less: increasing connection springs from 1 to 20 led to 1.2 and 1.7 folds increase in the computational cost for a dam-reservoir system and a dam only model, respectively.
- The computational cost of conducting nonlinear transient analysis using explicit integration and MAEM models was four times higher than a corresponding analysis conducted with FEM using implicit integration. Although the cost was 4 times higher, discrete crack propagation could be obtained with MAEM. The analyses were also linearly scalable.

- The crack profile comparison of MAEM models for the concrete and RCC dams showed the effect of weakness of the lift joints in the RCC dam, especially for motions with large intensities. The RCC dam suffered considerably more cracks compared to an identical geometry monolithic concrete dam.
- The fragility curves of the monolithic concrete dam and the RCC dam showed that the probability of exceeding the first limit state with very limited cracking at the base was calculated 20% higher in the concrete dam compared to the RCC counterpart since a single base crack occurred in the concrete model. In contrast, in the RCC dam, many cracks at the weak layers within the heel were observed. For the other limits, the probability of exceeding the damage states was 15% to 35% more for the RCC dam, as expected due to weak lift joints.
- The cracking on the monolith was used as a damage measure with the presentation of a new damage indicator in the form of the maximum crack width at the base and the total maximum crack width at the upstream side of the dam. The fluid pressure within the cracks was neglected; accordingly, the crack openings might be underestimated in this study. Still, with the use of MAEM, cracking can be used as a direct indicator of expected damage for these systems practically.
- The comparison of the total crack widths from the FEM and MAEM models for the concrete gravity dam yielded similar results for base cracks. Conversely, the total maximum crack width was estimated 50% less by the FEM model compared to the MAEM model for high ground motion intensities that produced significant damage, leading to less conservative results.
- The mean maximum base crack opening for the RCC dam was obtained 80% to 35% less than the concrete dam for the 0.2g – 1.0g loading range quantified in terms of  $S_a$ . The variation in the maximum base crack width regarding seismic intensity was also much more substantial for the concrete

dam than the RCC counterpart. A single base crack occurred in the concrete model led to an increase in the base crack width more compared to the RCC dam, in which many cracks at the weak layers within the heel were observed.

- The mean of total maximum crack widths on the upstream face was similar for both sections. The total maximum crack widths of the two models converged for the lower number of cracks with higher widths (concrete dam) and more cracks but with smaller widths (RCC dam).
- The relationship between ground motion IMs and damage on the concrete gravity and RCC gravity dams were investigated by selecting the maximums of the base crack and total crack width as a damage measure. The maximum base crack width could be predicted well with first mode spectral acceleration and PGA for the concrete and RCC dams, respectively. A comparable high correlation between the maximum total crack width at the upstream side and the investigated IMs were not obtained.
- The leakage through the upstream cracks for the concrete and RCC models were compared by assuming a residual crack width after a seismic event. For residual cracking at 20% of the maximum crack width, significant leakage was predicted for concrete dams for  $S_a$  greater than 0.45g. For the RCC dam, leakage was estimated at 1/10<sup>th</sup> of the concrete dam. The nature of cracking in the RCC dam rendered the leakage behavior very different compared to concrete dams: although damaged less in a comparable event, leakage is more for a concrete monolith.
- As the residual crack widths decreased, the estimated leakage amounts decreased significantly for both models. As the leakage estimation is highly affected by the residual crack opening, the breaking of contact regions and residual material penetrating inside the crack from the reservoir during strong shaking can be the primary determinants of the leakage.
- The residual crack widths calculated according to the crack openings obtained at the end of the dynamic simulations for MAEM dam-reservoir systems showed that a residual crack width factor of 0.1 appeared to be a



good upper bound for predicting post-earthquake crack width from the maximum crack width for high ground motion intensities. The real opening, however, is likely higher due to the residual reservoir pressure within the cracks.

- The seismic performance of gravity dam-reservoir systems was evaluated based on the severity of the cracking defined in terms of the distribution of cracking, the extent of cracking as well as the nature of cracking as allowed by the definition of crack width in the MAEM model. When considered based on the extent and propagation of cracking, the RCC dam was subjected to more severe damage than the concrete dam at the same seismic intensity. When the evaluation was made with respect to the nature of cracking, i.e., considering the crack width at the base, higher damage was observed for the concrete section. On the other hand, the cumulative consideration of the damage on the upstream face expressed in terms of the envelope of the total maximum crack widths yielded similar metrics for the RCC and concrete dams. The estimated leakage amount showed cracking on a concrete dam can be more critical compared to the RCC dam due to the concentration of damage at the base crack.

#### **5.4 Future Extensions**

Some avenues of future study for establishing a performance-oriented dam engineering using MAEM are given below:

- With a focus on the nonlinear behavior, the dam-foundation interaction was not considered within the scope of this dissertation. Foundation-structure interaction significantly affects the dynamic characteristics of these systems. The foundation interaction should be introduced into the dynamic problem in order to account for the effect of radiation damping and foundation behavior on the nonlinear behavior of these systems simulated using such a discrete element tool.

- The fluid pressure within the cracks was not considered in this study. Previous studies indicate a complex picture on the effect of fluid pressure on cracking on dam systems. As multi-scale models with current computational capacities are not possible, these could be introduced using heuristic models based on crack face velocities. The effects on the damage accumulation on concrete monoliths can be important to quantify.
- Large deformation and contact formulation were not included in the implemented nonlinear dynamic solver within this study. The stability of crest of dams at neck portions (i.e., dams with an abrupt slope change in the downstream face such as the Koyna Dam) under strong earthquake could be investigated regarding the collapse process of dams by simulating element separation in the transient analyses.
- The vertical ground motions were not considered within the scope of the analysis in this dissertation. High-quality vertical ground motions are increasingly being included in the ground motion databases: with the improved knowledge, design provisions for buildings are updated to include the effects in the analyses. The effects are not clearly known for dams with very short periods and should be further studied, especially with regard to severe damage conditions.
- Rayleigh damping with mass and stiffness proportional parts were used in the transient analyses of this study. For the nonlinear dynamic solver, the damping matrix was formed with respect to the initial linear stiffness matrix, and the damping matrix was kept constant throughout the simulations. This is a significant limitation if high damping ratios due to radiation damping may be required in models with foundations as the damping forces might reach unrealistically high values for higher velocity gradients due to the initial stiffness in a softening element affecting behavior. Enhanced damping algorithms should be implemented to modulate the effects of Rayleigh damping in explicit analyses with radiation damping.

- Two IMs were found to correlate well with the damage on the concrete and RCC gravity dams with respect to the maximum base crack width; however, more work appears to be required for defining new IMs correlating better the total crack width at the upstream face of concrete and RCC dams.
- The residual crack widths were calculated as a percentage of the maximum crack widths throughout the seismic analyses within the scope of this dissertation. Studies on residual crack width estimations were conducted for reinforced concrete members relating the residual crack widths to maximum crack widths, member forces, and load cycles. The relationship of residual crack width with respect to the ground motion characteristics, such as the intensity and the number of cycles, in addition to the maximum crack widths, can be worthwhile to study.
- The seismic response of the gravity dams was evaluated, assuming a homogeneous distribution of materials throughout the dam bodies in this study. Concrete is a heterogeneous material; the randomness of material properties such as the tensile strength and fracture energy could be included by spatially correlated statistical distributions to investigate the effects on the damage accumulation on huge structures such as dams.
- The investigation of the nonlinear behavior of gravity dams was conducted considering a single geometry and single material property within the scope of this dissertation. The quantification of the performance of these systems can be made by parametric studies considering various dam geometries (different dam height, downstream slope) and a variety of material properties (various tensile strength and fracture energy) to assess the influence of these parameters on the damage prediction.
- The investigation of the behavior of gravity dams was conducted using a single geometry in this work. Points of slope change and neck regions, much less common in RCC dams compared to older concrete gravity dams, were ignored. The effect of these regions of stress concentration on crack based performance assessment needs to be investigated.

The modified applied element technique can be improved to address a range of problems along with improvement in the modeling of dam monoliths.

- A non-uniform discretization of modified applied elements can be introduced so that the mesh could be formed by considering different sized square elements instead of a uniform mesh. With this approach, the thickness of the weak layers for RCC dam simulations could be much smaller. Moreover, by increasing the mesh size for non-critical portions of the model, the computational cost would decrease.
- Elements with different geometries, such as rectangles or triangles, may be useful. Elements having different geometries can be beneficial to construct meshes for arbitrary domains.
- The modified applied element method has the advantage of direct use of the load-displacement diagram from a uniaxial tension test, especially for smaller element sizes. The post-peak shape and ultimate displacement at which tensile forces cease are the critical parameters. A compilation of data from well-documented uniaxial test studies should be done in order to provide sample model curves in the model.
- The shear retention in inclined cracking has not been considered within the scope of this dissertation. Shear retention and its effect can be introduced into the model, coupling the normal and shear spring pairs accordingly. The effects on inclined cracking and energy release at the crack should be investigated.
- The compression behavior was assumed as linear in this study. A nonlinear compression material model can be implemented to simulate a cyclic, hysteretic, nonlinear response for cases in which compressive stresses are high.
- The computational time of the MAEM solutions was observed to be high as each spring's contribution is calculated separately for stiffness and force terms. Accordingly, the computational cost can be decreased by optimization within the algorithms as well as possible parallelization of the code.

## REFERENCES

- Akpinar, U., Aldemir, A., & Binici, B. (2013). Different analysis strategies for roller compacted concrete dam design. *Advanced Structured Materials*. [https://doi.org/10.1007/978-3-642-32295-2\\_9](https://doi.org/10.1007/978-3-642-32295-2_9)
- Aldea, C. M., Ghandehari, M., Shah, S. P., & Karr, A. (2000). Estimation of water flow through cracked concrete under load. *ACI Structural Journal*. <https://doi.org/10.14359/9289>
- Alembagheri, M., & Seyedkazemi, M. (2015). Seismic performance sensitivity and uncertainty analysis of gravity dams. *Earthquake Engineering & Structural Dynamics*. <https://doi.org/10.1002/eqe.2457>
- Alembagheri, Mohammad, & Ghaemian, M. (2013). Seismic assessment of concrete gravity dams using capacity estimation and damage indexes. *Earthquake Engineering and Structural Dynamics*. <https://doi.org/10.1002/eqe.2196>
- Arias, A. (1970). A measure of earthquake intensity. In *Seismic Design for Nuclear Power Plants*.
- Arıcı, Y., Binici, B., & Aldemir, A. (2014). Comparison of the expected damage patterns from two- and three-dimensional nonlinear dynamic analyses of a roller compacted concrete dam. *Structure and Infrastructure Engineering*. <https://doi.org/10.1080/15732479.2012.753921>
- Armstrong, R., Kishida, T., & Park, D. S. (2020). Efficiency of ground motion intensity measures with earthquake-induced earth dam deformations. *Earthquake Spectra*. <https://doi.org/10.1177/8755293020938811>
- ASI. (2014). *Extreme Loading for Structures v3.1*.
- Atkinson, R. O., Chastain, J. T., Huston, S. M., & Lofton, E. (2014). *Training Aids for Dam Safety: Inspection of Concrete and Masonry Dams*. United States. Department of Homeland Security.
- Ayari, M. L., & Saouma, V. E. (1990). A fracture mechanics based seismic analysis of concrete gravity dams using discrete cracks. *Engineering Fracture Mechanics*. [https://doi.org/10.1016/0013-7944\(90\)90233-7](https://doi.org/10.1016/0013-7944(90)90233-7)
- Baker, J. W. (2015). Efficient analytical fragility function fitting using dynamic structural analysis. *Earthquake Spectra*. <https://doi.org/10.1193/021113EQS025M>
- Barenblatt, G. I. (1962). The Mathematical Theory of Equilibrium Cracks in Brittle Fracture. *Advances in Applied Mechanics*. [https://doi.org/10.1016/S0065-2156\(08\)70121-2](https://doi.org/10.1016/S0065-2156(08)70121-2)
- Bathe, K. J. (1996). Finite Element Procedures. In *Englewood Cliffs New Jersey*.

- Bathe, K. J., & Hahn, W. F. (1979). On transient analysis of fluid-structure systems. *Computers and Structures*. [https://doi.org/10.1016/0045-7949\(79\)90109-3](https://doi.org/10.1016/0045-7949(79)90109-3)
- Bažant, Z. P., Tabbara, M. R., Kazemi, M. T., & Pyaudier-Cabot, G. (1990). Random particle model for fracture of aggregate or fiber composites. *Journal of Engineering Mechanics*. [https://doi.org/10.1061/\(ASCE\)0733-9399\(1990\)116:8\(1686\)](https://doi.org/10.1061/(ASCE)0733-9399(1990)116:8(1686))
- Belytschko, T. (1980). Fluid-structure interaction. *Computers and Structures*. [https://doi.org/10.1016/0045-7949\(80\)90121-2](https://doi.org/10.1016/0045-7949(80)90121-2)
- Belytschko, T., Chen, H., Xu, J., & Zi, G. (2003). Dynamic crack propagation based on loss of hyperbolicity and a new discontinuous enrichment. *International Journal for Numerical Methods in Engineering*. <https://doi.org/10.1002/nme.941>
- Bernier, C., Monteiro, R., & Paultre, P. (2016). Using the conditional spectrum method for improved fragility assessment of concrete gravity dams in Eastern Canada. *Earthquake Spectra*. <https://doi.org/10.1193/072015EQS116M>
- Bernier, C., Padgett, J. E., Proulx, J., & Paultre, P. (2016). Seismic Fragility of Concrete Gravity Dams with Spatial Variation of Angle of Friction: Case Study. *Journal of Structural Engineering (United States)*. [https://doi.org/10.1061/\(ASCE\)ST.1943-541X.0001441](https://doi.org/10.1061/(ASCE)ST.1943-541X.0001441)
- Bhattacharjee, S. S., & Léger, P. (1993). Seismic cracking and energy dissipation in concrete gravity dams. *Earthquake Engineering & Structural Dynamics*. <https://doi.org/10.1002/eqe.4290221106>
- Bhattacharjee, Sudip S., & Léger, P. (1994). Application of NLFM models to predict cracking in concrete gravity dams. *Journal of Structural Engineering (United States)*. [https://doi.org/10.1061/\(ASCE\)0733-9445\(1994\)120:4\(1255\)](https://doi.org/10.1061/(ASCE)0733-9445(1994)120:4(1255))
- Bouaanani, N., & Lu, F. Y. (2009). Assessment of potential-based fluid finite elements for seismic analysis of dam-reservoir systems. *Computers and Structures*. <https://doi.org/10.1016/j.compstruc.2008.10.006>
- Bybordiani, M., & Arıçı, Y. (2017). The use of 3D modeling for the prediction of the seismic demands on the gravity dams. *Earthquake Engineering and Structural Dynamics*. <https://doi.org/10.1002/eqe.2880>
- Calayir, Y., & Karaton, M. (2005a). A continuum damage concrete model for earthquake analysis of concrete gravity dam-reservoir systems. *Soil Dynamics and Earthquake Engineering*. <https://doi.org/10.1016/j.soildyn.2005.05.003>
- Calayir, Y., & Karaton, M. (2005b). Seismic fracture analysis of concrete gravity dams including dam-reservoir interaction. *Computers and Structures*. <https://doi.org/10.1016/j.compstruc.2005.02.003>
- Carpinteri, A., Valente, S., Ferrara, G., & Imperato, L. (1992). Experimental and

- Numerical Fracture Modelling of a Gravity Dam. *Special Publication*. <https://doi.org/10.14359/4582>
- Chávez, J. W., & Fenves, G. L. (1995). Earthquake response of concrete gravity dams including base sliding. *Journal of Structural Engineering (United States)*. [https://doi.org/10.1061/\(ASCE\)0733-9445\(1995\)121:5\(865\)](https://doi.org/10.1061/(ASCE)0733-9445(1995)121:5(865))
- Chen, D. H., Yang, Z. H., Wang, M., & Xie, J. H. (2019). Seismic performance and failure modes of the Jin'anqiao concrete gravity dam based on incremental dynamic analysis. *Engineering Failure Analysis*. <https://doi.org/10.1016/j.engfailanal.2019.02.018>
- Chen, H. C., & Taylor, R. L. (1990). Vibration analysis of fluid–solid systems using a finite element displacement formulation. *International Journal for Numerical Methods in Engineering*. <https://doi.org/10.1002/nme.1620290402>
- Chopra, A. K. (1986). *EARTHQUAKE ANALYSIS OF CONCRETE DAMS*.
- Chopra, A. K. (2015). *Dynamics of Structures Theory and Applications to Earthquake Engineering* (4th editio). Pearson Education Limited.
- Chopra, Anil K, & Chakrabarti, P. (1973). The Koyna Earthquake and the Damage to Koyna Dam. *Bulletin of the Seismological Society of America*.
- Coffield, A., & Adeli, H. (2016). Irregular steel building structures subjected to blast loading. *Journal of Civil Engineering and Management*. <https://doi.org/10.3846/13923730.2015.1073172>
- Cook, R. D., Malkus, D. S., Plesha, M. E., & Witt, R. J. (2001). *Concepts and Applications of Finite Element Analysis* (4th Editio). Wiley. <https://doi.org/10.1115/1.3264300>
- CSI. (2017). CSI Analysis Reference Manual. In *CSI: Berkeley (CA, USA): Computers and Structures INC*.
- Cundall, P. A. (1971). A computer model for simulating progressive large-scale movements in blocky rock systems. *Proceedings of the Symposio of the International Society of Rock Mechanics, Nancy 2*.
- de Borst, R., Crisfield, M. A., Remmers, J. J. C., & Verhoosel, C. V. (2012). Non-Linear Finite Element Analysis of Solids and Structures: Second Edition. In *Non-Linear Finite Element Analysis of Solids and Structures: Second Edition*. <https://doi.org/10.1002/9781118375938>
- Demirel, E., & Aydin, I. (2016). Numerical Simulation and Formulation of Wave Run-Up on Dam Face due to Ground Oscillations Using Major Earthquake Acceleration Records. *Journal of Engineering Mechanics*. [https://doi.org/10.1061/\(ASCE\)EM.1943-7889.0001077](https://doi.org/10.1061/(ASCE)EM.1943-7889.0001077).
- DIN EN 12390-6 (2001). Testing hardened concrete, part 6: Tensile splitting strength of test specimens. Berlin: Beuth.

- Dinu, F., Dubina, D., & Marginean, I. (2015). Improving the structural robustness of multi-story steel-frame buildings. *Structure and Infrastructure Engineering*. <https://doi.org/10.1080/15732479.2014.927509>
- Domínguez, J., & Maeso, O. (1993). Earthquake analysis of arch dams. II dam-water-foundation interaction. *Journal of Engineering Mechanics*. [https://doi.org/10.1061/\(ASCE\)0733-9399\(1993\)119:3\(513\)](https://doi.org/10.1061/(ASCE)0733-9399(1993)119:3(513))
- Dongre, A., & Ramancharla, P. K. (2012). Comparative Study of Inelastic Behavior of RC Frame With and Without Brick Infill Using Applied Element Method. *ISET Golden Jubilee Symposium on Earthquake Engineering*.
- Dugdale, D. S. (1960). Yielding of steel sheets containing slits. *Journal of the Mechanics and Physics of Solids*. [https://doi.org/10.1016/0022-5096\(60\)90013-2](https://doi.org/10.1016/0022-5096(60)90013-2)
- Ehab, M., Salem, H., Mostafa, H., & Yehia, N. (2014). Earthquake Pounding Effect on Adjacent Reinforced Concrete Buildings. *International Journal of Computer Applications*.
- Eliáš, J. (2020). Elastic properties of isotropic discrete systems: Connections between geometric structure and Poisson's ratio. *International Journal of Solids and Structures*. <https://doi.org/10.1016/j.ijsolstr.2019.12.012>
- Espandar, R., & Lotfi, V. (2003). Comparison of non-orthogonal smeared crack and plasticity models for dynamic analysis of concrete arch dams. *Computers and Structures*. [https://doi.org/10.1016/S0045-7949\(03\)00083-X](https://doi.org/10.1016/S0045-7949(03)00083-X)
- Everstine, G. C. (1981). A symmetric potential formulation for fluid-structure interaction. In *Journal of Sound and Vibration*. [https://doi.org/10.1016/0022-460X\(81\)90335-7](https://doi.org/10.1016/0022-460X(81)90335-7)
- FEAST. (2015). *FEAST Eigenvalue Solver*.
- Felippa, C. A., & Ohayon, R. (1990). Mixed variational formulation of finite element analysis of acoustoelastic/slosh fluid-structure interaction. *Journal of Fluids and Structures*. [https://doi.org/10.1016/0889-9746\(90\)90036-5](https://doi.org/10.1016/0889-9746(90)90036-5)
- Fenves, G., & Chopra, A. K. (1985). Effects of reservoir bottom absorption and dam-water-foundation rock interaction on frequency response functions for concrete gravity dams. *Earthquake Engineering & Structural Dynamics*. <https://doi.org/10.1002/eqe.4290130104>
- Fenves, G., & Chopra, A. K. (1987). Simplified Earthquake Analysis of Concrete Gravity Dams. *Journal of Structural Engineering*. [https://doi.org/10.1061/\(asce\)0733-9445\(1987\)113:8\(1688\)](https://doi.org/10.1061/(asce)0733-9445(1987)113:8(1688))
- Fok, K. L., & Chopra, A. K. (1986a). Earthquake analysis of arch dams including dam-water interaction, reservoir boundary absorption and foundation flexibility. *Earthquake Engineering & Structural Dynamics*.



<https://doi.org/10.1002/eqe.4290140202>

- Fok, K. L., & Chopra, A. K. (1986b). Hydrodynamic and foundation flexibility effects in earthquake response of arch dams. *Journal of Structural Engineering (United States)*. [https://doi.org/10.1061/\(ASCE\)0733-9445\(1986\)112:8\(1810\)](https://doi.org/10.1061/(ASCE)0733-9445(1986)112:8(1810))
- Fok, K. L., & Chopra, A. K. (1987). Water compressibility in earthquake response of arch dams. *Journal of Structural Engineering (United States)*. [https://doi.org/10.1061/\(ASCE\)0733-9445\(1987\)113:5\(958\)](https://doi.org/10.1061/(ASCE)0733-9445(1987)113:5(958))
- Gao, H., & Klein, P. (1998). Numerical simulation of crack growth in an isotropic solid with randomized internal cohesive bonds. *Journal of the Mechanics and Physics of Solids*. [https://doi.org/10.1016/S0022-5096\(97\)00047-1](https://doi.org/10.1016/S0022-5096(97)00047-1)
- Ghaedi, K., Jameel, M., Ibrahim, Z., & Khanzaei, P. (2016). Seismic analysis of Roller Compacted Concrete (RCC) dams considering effect of sizes and shapes of galleries. *KSCE Journal of Civil Engineering*. <https://doi.org/10.1007/s12205-015-0538-2>
- Ghanaat, Y. (2004). Failure modes approach to safety evaluation of dams. *13th World Conference on Earthquake Engineering*.
- Gingold, R. A., & Monaghan, J. J. (1977). Smoothed particle hydrodynamics - Theory and application to non-spherical stars. *Monthly Notices of the Royal Astronomical Society*.
- Gopalaratnam, V. S., & Shah, S. P. (1985). SOFTENING RESPONSE OF PLAIN CONCRETE IN DIRECT TENSION. *Journal of the American Concrete Institute*. <https://doi.org/10.14359/10338>
- Hall, J. F., & Chopra, A. K. (1983). Dynamic analysis of arch dams including hydrodynamic effects. *Journal of Engineering Mechanics*. [https://doi.org/10.1061/\(ASCE\)0733-9399\(1983\)109:1\(149\)](https://doi.org/10.1061/(ASCE)0733-9399(1983)109:1(149))
- Hariri-Ardebili, M. A., & Saouma, V. (2015). Quantitative failure metric for gravity dams. *Earthquake Engineering and Structural Dynamics*. <https://doi.org/10.1002/eqe.2481>
- Hariri-Ardebili, M. A., & Saouma, V. E. (2016). Probabilistic seismic demand model and optimal intensity measure for concrete dams. *Structural Safety*. <https://doi.org/10.1016/j.strusafe.2015.12.001>
- Hariri-Ardebili, M. A., Seyed-Kolbadi, S. M., Saouma, V. E., Salamon, J., & Rajagopalan, B. (2018). Random finite element method for the seismic analysis of gravity dams. *Engineering Structures*. <https://doi.org/10.1016/j.engstruct.2018.05.096>
- Hariri-Ardebili, Mohammad Amin, Saouma, V. E., & Porter, K. A. (2016). Quantification of seismic potential failure modes in concrete dams. *Earthquake Engineering and Structural Dynamics*. <https://doi.org/10.1002/eqe.2697>

- Helmy, H., Hadhoud, H., & Mourad, S. (2015). Infilled masonry walls contribution in mitigating progressive collapse of multistory reinforced concrete structures according to UFC guidelines. *International Journal of Advanced Structural Engineering*. <https://doi.org/10.1007/s40091-015-0094-5>
- Helmy, H. M., Elfouly, A. K., & Salem, H. M. (2012). Numerical simulation of demolition of Perna Seca hospital using the applied element method. *Structures Congress 2012 - Proceedings of the 2012 Structures Congress*. <https://doi.org/10.1061/9780784412367.026>
- Helmy, H., Salem, H., & Mourad, S. (2012). Progressive collapse assessment of framed reinforced concrete structures according to UFC guidelines for alternative path method. *Engineering Structures*. <https://doi.org/10.1016/j.engstruct.2012.03.058>
- Hu, G., Wang, Y., Xie, P., & Pan, Z. (2004). Tensile strength for splitting failure of brittle particles with consideration of poisson's ratio. *China Particuology*. [https://doi.org/10.1016/s1672-2515\(07\)60067-0](https://doi.org/10.1016/s1672-2515(07)60067-0)
- Hu, J., Ma, F., & Wu, S. (2018). Comprehensive investigation of leakage problems for concrete gravity dams with penetrating cracks based on detection and monitoring data: A case study. *Structural Control and Health Monitoring*. <https://doi.org/10.1002/stc.2127>
- Huang, X., Li, S., Jin, Y., Yang, D., Su, G., & He, X. (2019). Analysis on the influence of Poisson's ratio on brittle fracture by applying uni-bond dual-parameter peridynamic model. *Engineering Fracture Mechanics*. <https://doi.org/10.1016/j.engfracmech.2019.106685>
- Ibarhim, A., Salim, H., & Rahman, N. A. (2012). Progressive collapse of post-tensioned box girder bridges under blast loads using applied element method. *Structures Congress 2012 - Proceedings of the 2012 Structures Congress*. <https://doi.org/10.1061/9780784412367.201>
- Iervolino, I., & Cornell, C. A. (2005). Record selection for nonlinear seismic analysis of structures. *Earthquake Spectra*. <https://doi.org/10.1193/1.1990199>
- Javanmardi, F., Léger, P., & Tinawi, R. (2005a). Seismic structural stability of concrete gravity dams considering transient uplift pressures in cracks. *Engineering Structures*. <https://doi.org/10.1016/j.engstruct.2004.12.005>
- Javanmardi, F., Léger, P., & Tinawi, R. (2005b). Seismic Water Pressure in Cracked Concrete Gravity Dams: Experimental Study and Theoretical Modeling. *Journal of Structural Engineering*. [https://doi.org/10.1061/\(asce\)0733-9445\(2005\)131:1\(139\)](https://doi.org/10.1061/(asce)0733-9445(2005)131:1(139))
- Jiang, S. Y., & Du, C. Bin. (2012). Seismic stability analysis of concrete gravity dams with penetrated cracks. *Water Science and Engineering*. <https://doi.org/10.3882/j.issn.1674-2370.2012.01.010>

- Karbassi, A., & Nollet, M. J. (2008). Application of the applied element method to the seismic vulnerability evaluation of existing buildings. *Proceedings, Annual Conference - Canadian Society for Civil Engineering*.
- Karbassi, A., & Nollet, M. J. (2013). Performance-based seismic vulnerability evaluation of masonry buildings using applied element method in a nonlinear dynamic-based analytical procedure. *Earthquake Spectra*. <https://doi.org/10.1193/1.4000148>
- Kawai, T. (1986). *No Title Recent Developments of the Rigid Body and Spring Model (RBSM) in Structural Analysis* (pp. 226–237). Seiken Seminar Text Book, The University of Tokyo.
- Kernicky, T. P., Whelan, M. J., Weggel, D. C., & Rice, C. D. (2015). Structural identification and damage characterization of a masonry infill wall in a full-scale building subjected to internal blast load. *Journal of Structural Engineering (United States)*. [https://doi.org/10.1061/\(ASCE\)ST.1943-541X.0001158](https://doi.org/10.1061/(ASCE)ST.1943-541X.0001158)
- Keys, R. A., & Clubley, S. K. (2017). Establishing a predictive method for blast induced masonry debris distribution using experimental and numerical methods. *Engineering Failure Analysis*. <https://doi.org/10.1016/j.engfailanal.2017.07.017>
- Khalil, A. A. (2012). Enhanced modeling of steel structures for progressive collapse analysis using the applied element method. *Journal of Performance of Constructed Facilities*. [https://doi.org/10.1061/\(ASCE\)CF.1943-5509.0000267](https://doi.org/10.1061/(ASCE)CF.1943-5509.0000267)
- Kotsubo, S. (1957). DYNAMIC WATER PRESSURE ON DAMS DUE TO IRREGULAR EARTHQUAKES. *Transactions of the Japan Society of Civil Engineers*. [https://doi.org/10.2208/jscej1949.1957.47\\_38](https://doi.org/10.2208/jscej1949.1957.47_38)
- Krinitzsky, E. L., & Marcuson, W. F. (1983). PRINCIPLES FOR SELECTING EARTHQUAKE MOTIONS IN ENGINEERING DESIGN. *Bulletin of the Association of Engineering Geologists*. <https://doi.org/10.2113/gseegeosci.xx.3.253>
- Küçükarslan, S., Coşkun, S. B., & Taşkın, B. (2005). Transient analysis of dam-reservoir interaction including the reservoir bottom effects. *Journal of Fluids and Structures*. <https://doi.org/10.1016/j.jfluidstructs.2005.05.004>
- Kumar, R., Rommel, S., Jauffrès, D., Lhuissier, P., & Martin, C. L. (2016). Effect of packing characteristics on the discrete element simulation of elasticity and buckling. *International Journal of Mechanical Sciences*. <https://doi.org/10.1016/j.ijmecsci.2016.02.009>
- Kurama, Y. C., & Farrow, K. T. (2003). Ground motion scaling methods for different site conditions and structure characteristics. *Earthquake Engineering and Structural Dynamics*. <https://doi.org/10.1002/eqe.335>

- Lakes, R. S. (2017). Negative-Poisson's-Ratio Materials: Auxetic Solids. *Annual Review of Materials Research*. <https://doi.org/10.1146/annurev-matsci-070616-124118>
- Lau, D. T., & Wibowo, H. (2010). Seismic progressive collapse analysis of reinforced concrete bridges by applied element method. *Proceedings of the 12th International Conference on Engineering, Science, Construction, and Operations in Challenging Environments - Earth and Space 2010*. [https://doi.org/10.1061/41096\(366\)287](https://doi.org/10.1061/41096(366)287)
- Lee, J., & Fenves, G. L. (1998). A plastic-damage concrete model for earthquake analysis of dams. *Earthquake Engineering and Structural Dynamics*. [https://doi.org/10.1002/\(SICI\)1096-9845\(199809\)27:9<937::AID-EQE764>3.0.CO;2-5](https://doi.org/10.1002/(SICI)1096-9845(199809)27:9<937::AID-EQE764>3.0.CO;2-5)
- Léger, P. (2007). Reducing the earthquake induced damage and risk in monumental structures: Experience at école polytechnique de Montreal for large concrete dams supported by hydro-Quebec and Alcan. *NATO Security through Science Series C: Environmental Security*. [https://doi.org/10.1007/978-1-4020-5656-7\\_11](https://doi.org/10.1007/978-1-4020-5656-7_11)
- Lilliu, G., & van Mier, J. G. M. (2003). 3D lattice type fracture model for concrete. *Engineering Fracture Mechanics*. [https://doi.org/10.1016/S0013-7944\(02\)00158-3](https://doi.org/10.1016/S0013-7944(02)00158-3)
- Lim, T. C. (2019). Longitudinal wave speed in rectangular slabs with mixed restraints in lateral directions. *Proceedings of the Institution of Civil Engineers: Engineering and Computational Mechanics*. <https://doi.org/10.1680/jencm.19.00008>
- Liu, W., & Hong, J. W. (2012). Discretized peridynamics for linear elastic solids. *Computational Mechanics*. <https://doi.org/10.1007/s00466-012-0690-1>
- Løkke, A., & Chopra, A. K. (2017). Direct finite element method for nonlinear analysis of semi-unbounded dam–water–foundation rock systems. *Earthquake Engineering and Structural Dynamics*. <https://doi.org/10.1002/eqe.2855>
- Lotfi, V., Roesset, J. M., & Tassoulas, J. L. (1987). A technique for the analysis of the response of dams to earthquakes. *Earthquake Engineering & Structural Dynamics*. <https://doi.org/10.1002/eqe.4290150405>
- Lucy, L. B. (1977). A numerical approach to the testing of the fission hypothesis. *The Astronomical Journal*. <https://doi.org/10.1086/112164>
- Lupoae, M., Baciuc, C., Constantin, D., & Puscau, H. (2012). Aspects Concerning Progressive Collapse of a Reinforced Concrete Frame Structure with Infill Walls. *World Conference on Engineering*.
- Lupoae, Marin, & Bucur, C. (2009). Use of applied element method to simulate the collapse of a building. *SISOM 2009 and Session of the Commission of*

*Acoustics, Bucharest 28-29 May.*

- Lysmer, J., & Kuhlemeyer, R. (1969). Finite Dynamic Model For Infinite Media. *Journal of the Engineering Mechanics Division.*
- Madan, N. (2019). *New formulation of the discrete element method with deformable particles.* INSTITUTE OF FUNDAMENTAL TECHNOLOGICAL RESEARCH POLISH ACADEMY OF SCIENCES.
- Maekawa, K., Okamura, H., & Pimanmas, A. (2003). Non-Linear Mechanics of Reinforced Concrete. In *Non-Linear Mechanics of Reinforced Concrete.* <https://doi.org/10.1201/9781482288087>
- Maeso, O., & Dominguez, J. (1993). Earthquake analysis of arch dams. I: Dam-foundation interaction. *Journal of Engineering Mechanics.* [https://doi.org/10.1061/\(ASCE\)0733-9399\(1993\)119:3\(496\)](https://doi.org/10.1061/(ASCE)0733-9399(1993)119:3(496))
- Malárics, V., & Müller, H. S. (2010). Evaluation of the Splitting Tension Test for Concrete from A Fracture Mechanical Point of View. In *Fracture Mechanics of Concrete and Concrete Structures-Assessment, Durability, Monitoring and Retrofitting of Concrete Structures-B.H. Oh, et al., Eds, Seoul.*
- Malomo, D., Pinho, R., & Penna, A. (2019). Applied Element Modelling of the Dynamic Response of a Full-Scale Clay Brick Masonry Building Specimen with Flexible Diaphragms. *International Journal of Architectural Heritage.* <https://doi.org/10.1080/15583058.2019.1616004>
- Mansouri, A., Neshaei, M., & Aghajany, R. (2011). Fracture analysis of concrete gravity dam under earthquake induced loads. *Journal of Applied Sciences and Environmental Management.* <https://doi.org/10.4314/jasem.v15i2.68515>
- Medina, F., Dominguez, J., & Tassoulas, J. L. (1990). Response of dams to earthquakes including effects of sediments. *Journal of Structural Engineering (United States).* [https://doi.org/10.1061/\(ASCE\)0733-9445\(1990\)116:11\(3108\)](https://doi.org/10.1061/(ASCE)0733-9445(1990)116:11(3108))
- Meguro, K., & Tagel-Din, H. (1997). A New Simplified and Efficient Technique for Fracture Behavior Analysis of Concrete Structures. *Fracture Mechanics of Concrete Structures Proceedings FRAMCOS-3.*
- Meguro, K., & Tagel-Din, H. (2000). Applied element method for structural analysis: Theory and application for linear materials. *Structural Engineering/Earthquake Engineering.* [https://doi.org/10.2208/jscej.2000.647\\_31](https://doi.org/10.2208/jscej.2000.647_31)
- Meguro, K., & Tagel-Din, H. (2001). Applied element simulation of RC structures under cyclic loading. *Journal of Structural Engineering.* [https://doi.org/10.1061/\(ASCE\)0733-9445\(2001\)127:11\(1295\)](https://doi.org/10.1061/(ASCE)0733-9445(2001)127:11(1295))
- Meguro, K., & Tagel-Din, H. (2002). Applied Element Method Used for Large Displacement Structural Analysis. *Journal of Natural Disaster Science.*

- Mehrpay, S., Wang, Z., & Ueda, T. (2020). Development and application of a new discrete element into simulation of nonlinear behavior of concrete. *Structural Concrete*. <https://doi.org/10.1002/suco.201900059>
- Mirzabozorg, H., & Ghaemian, M. (2005). Non-linear behavior of mass concrete in three-dimensional problems using a smeared crack approach. *Earthquake Engineering and Structural Dynamics*. <https://doi.org/10.1002/eqe.423>
- Mirzabozorg, H., & Kianoush, M. R. (2008). Seismic Safety Evaluation of Concrete Dams Using Damage Mechanics Approach. *The 14th World Conference on Earthquake Engineering*.
- Morand, H., & Ohayon, R. (1979). Substructure variational analysis of the vibrations of coupled fluid–structure systems. Finite element results. *International Journal for Numerical Methods in Engineering*. <https://doi.org/10.1002/nme.1620140508>
- Nagai, K., Sato, Y., & Ueda, T. (2004). Mesoscopic simulation of failure of mortar and concrete by 2D RBSM. *Journal of Advanced Concrete Technology*. <https://doi.org/10.3151/jact.2.359>
- Ngo, D., & Scordelis, A. C. (1967). Finite element analysis of reinforced concrete beams. *Journal of ACI*, 64, 152–163.
- Olovsson, L., Simonsson, K., & Unosson, M. (2005). Selective mass scaling for explicit finite element analyses. *International Journal for Numerical Methods in Engineering*. <https://doi.org/10.1002/nme.1293>
- Olson, L. G., & Bathe, K. J. (1983). A study of displacement-based fluid finite elements for calculating frequencies of fluid and fluid-structure systems. *Nuclear Engineering and Design*. [https://doi.org/10.1016/0029-5493\(83\)90130-9](https://doi.org/10.1016/0029-5493(83)90130-9)
- Olson, L. G., & Bathe, K. J. (1985). Analysis of fluid-structure interactions. a direct symmetric coupled formulation based on the fluid velocity potential. *Computers and Structures*. [https://doi.org/10.1016/0045-7949\(85\)90226-3](https://doi.org/10.1016/0045-7949(85)90226-3)
- Omidi, O., Valliappan, S., & Lotfi, V. (2013). Seismic cracking of concrete gravity dams by plastic-damage model using different damping mechanisms. *Finite Elements in Analysis and Design*. <https://doi.org/10.1016/j.finel.2012.08.008>
- Özmen, S. (2016). *Implicit Monolithic Parallel Solution Algorithm for Seismic Analysis of Dam-Reservoir Systems*. Middle East Technical University.
- Pandey, B. H., & Meguro, K. (2004). Simulation of brick masonry wall behavior under in-plane lateral loading using applied element method. *13th World Conference on Earthquake Engineering, Vancouver, BC, Canada, August*.
- PARDISO. (2018). *User Guide*.
- Pekau, O. A., & Yuzhu, C. (2004). Failure analysis of fractured dams during

- earthquakes by DEM. *Engineering Structures*.  
<https://doi.org/10.1016/j.engstruct.2004.05.019>
- Pekau, O. A., & Zhu, X. (2006). Seismic behaviour of cracked concrete gravity dams. *Earthquake Engineering and Structural Dynamics*.  
<https://doi.org/10.1002/eqe.542>
- Pekau, O. A., & Zhu, X. (2008). Effect of Seismic Uplift Pressure on the Behavior of Concrete Gravity Dams with a Penetrated Crack. *Journal of Engineering Mechanics*. [https://doi.org/10.1061/\(asce\)0733-9399\(2008\)134:11\(991\)](https://doi.org/10.1061/(asce)0733-9399(2008)134:11(991))
- Polizzi, E. (2009). Density-matrix-based algorithm for solving eigenvalue problems. *Physical Review B - Condensed Matter and Materials Physics*.  
<https://doi.org/10.1103/PhysRevB.79.115112>
- Raparla, H. B., & Ramancharla, P. K. (2012). *Nonlinear Large Deformation Analysis of RC Bare Frames Subjected to Lateral Loads*.
- Rashid, Y. R. (1968). Analysis of prestressed concrete pressure vessels. *Nucl.Eng.Des.*
- Remmers, J. J. C., de Borst, R., & Needleman, A. (2008). The simulation of dynamic crack propagation using the cohesive segments method. *Journal of the Mechanics and Physics of Solids*. <https://doi.org/10.1016/j.jmps.2007.08.003>
- RILEM TC 104. (1991). Damage classification of concrete structures. The state of the art report of RILEM Technical Committee 04-DCC activity. *Materials and Structures*, 24(142), 253–259.
- Rots, J. G. (1988). *Computational Modeling of Concrete Fracture*. Delft University of Technology.
- SAP2000. (2017). *SAP2000 (Version 20)*. Computers and Structures, Inc. (CSI).
- Segura, R., Bernier, C., Monteiro, R., & Paultre, P. (2019). On the seismic fragility assessment of concrete gravity dams in eastern Canada. *Earthquake Spectra*.  
<https://doi.org/10.1193/012418EQS024M>
- Sevieri, G., De Falco, A., & Marmo, G. (2020). Shedding light on the effect of uncertainties in the seismic fragility analysis of existing concrete dams. *Infrastructures*. <https://doi.org/10.3390/infrastructures5030022>
- Shi, Z., Suzuki, M., & Nakano, M. (2003). Numerical analysis of multiple discrete cracks in concrete dams using extended fictitious crack model. *Journal of Structural Engineering*. [https://doi.org/10.1061/\(ASCE\)0733-9445\(2003\)129:3\(324\)](https://doi.org/10.1061/(ASCE)0733-9445(2003)129:3(324))
- Silling, S. A. (2000). Reformulation of elasticity theory for discontinuities and long-range forces. *Journal of the Mechanics and Physics of Solids*.  
[https://doi.org/10.1016/S0022-5096\(99\)00029-0](https://doi.org/10.1016/S0022-5096(99)00029-0)

- Simion, A., & Dragomir, C. S. (2013). The Simulation of an Industrial Building Demolition. *Urbanism, Architecture, Constructions*, 4(2), 67–74.
- Simo, J. C., Oliver, J., & Armero, F. (1993). An analysis of strong discontinuities induced by strain-softening in rate-independent inelastic solids. *Computational Mechanics*. <https://doi.org/10.1007/BF00372173>
- Skrikerud, P. E., & Bachmann, H. (1986). Discrete crack modelling for dynamically loaded, unreinforced concrete structures. *Earthquake Engineering & Structural Dynamics*. <https://doi.org/10.1002/eqe.4290140209>
- Smyrou, E., Priestley, M. J. N., & Carr, A. J. (2011). Modelling of elastic damping in nonlinear time-history analyses of cantilever RC walls. *Bulletin of Earthquake Engineering*. <https://doi.org/10.1007/s10518-011-9286-y>
- Sommerfeld, A. (1949). Partial Differential Equations in Physics. In *Partial Differential Equations in Physics*. New York: Academic Press. <https://doi.org/10.1016/b978-0-12-654658-3.x5001-0>
- Soysal, B. F., Binici, B., & Arici, Y. (2016). Investigation of the relationship of seismic intensity measures and the accumulation of damage on concrete gravity dams using incremental dynamic analysis. *Earthquake Engineering and Structural Dynamics*, 45(5). <https://doi.org/10.1002/eqe.2681>
- Strouboulis, T., Copps, K., & Babuška, I. (2000). The generalized finite element method: An example of its implementation and illustration of its performance. *International Journal for Numerical Methods in Engineering*. [https://doi.org/10.1002/\(SICI\)1097-0207\(20000320\)47:8<1401::AID-NME835>3.0.CO;2-8](https://doi.org/10.1002/(SICI)1097-0207(20000320)47:8<1401::AID-NME835>3.0.CO;2-8)
- Sun, D., & Ren, Q. (2016). Seismic damage analysis of concrete gravity dam based on wavelet transform. *Shock and Vibration*. <https://doi.org/10.1155/2016/6841836>
- Tagel-Din, H., & Meguro, K. (1999). Applied Element Simulation for Collapse Analysis of Structures. *Bulletin of Earthquake Resistant Structure*, 32.
- Tagel-Din, H., & Meguro, K. (2000). Applied element method for dynamic large deformation analysis of structures. *Structural Engineering/Earthquake Engineering*. [https://doi.org/10.2208/jscej.2000.661\\_1](https://doi.org/10.2208/jscej.2000.661_1)
- Tandaiya, P., Ramamurty, U., Ravichandran, G., & Narasimhan, R. (2008). Effect of Poisson's ratio on crack tip fields and fracture behavior of metallic glasses. *Acta Materialia*. <https://doi.org/10.1016/j.actamat.2008.08.018>
- Tekie, P. B., & Ellingwood, B. R. (2003). Seismic fragility assessment of concrete gravity dams. *Earthquake Engineering and Structural Dynamics*. <https://doi.org/10.1002/eqe.325>
- Timoshenko, S. P., Goodier, J. N., & Abramson, H. N. (1970). Theory of Elasticity



- (3rd ed.). *Journal of Applied Mechanics*. <https://doi.org/10.1115/1.3408648>
- TNO DIANA (2014). *Diana User's manual, R. 9.5*.
- USACE. (2000). *Roller-Compacted Concrete*.
- USACE. (2003). TIME-HISTORY DYNAMIC ANALYSIS OF CONCRETE HYDRAULIC STRUCTURES. *EM 1110-2-6051*.
- Vamvatsikos, D., & Allin Cornell, C. (2002). Incremental dynamic analysis. *Earthquake Engineering and Structural Dynamics*. <https://doi.org/10.1002/eqe.141>
- Van Mier, J. G. M. (1997). *Fracture process of concrete, assessment of material parameters for fracture models*. Boca Rotan, FL: CRC Press.
- Wang, G., Lu, W., Zhou, C., & Zhou, W. (2015). The influence of initial cracks on the crack propagation process of concrete gravity dam-reservoir-foundation systems. *Journal of Earthquake Engineering*. <https://doi.org/10.1080/13632469.2015.1021407>
- Wang, X., & Bathe, K. J. (1997). Displacement/pressure based mixed finite element formulations for acoustic fluid-structure interaction problems. *International Journal for Numerical Methods in Engineering*. [https://doi.org/10.1002/\(SICI\)1097-0207\(19970615\)40:11<2001::AID-NME152>3.0.CO;2-W](https://doi.org/10.1002/(SICI)1097-0207(19970615)40:11<2001::AID-NME152>3.0.CO;2-W)
- Westergaard, H. M. (1933). Water pressures on dams during earthquakes. *Trans. ASCE*.
- Wiącek, J., & Molenda, M. (2014). Effect of particle size distribution on micro-and macromechanical response of granular packings under compression. *International Journal of Solids and Structures*. <https://doi.org/10.1016/j.ijsolstr.2014.06.029>
- Wilson, E. L., & Khalvati, M. (1983). Finite elements for the dynamic analysis of fluid-solid systems. *International Journal for Numerical Methods in Engineering*. <https://doi.org/10.1002/nme.1620191105>
- Zangar, C. N. (1959). *Hydrodynamic pressure on dams due to horizontal earthquake effects*. Engineering Monograph, U.S. Bureau of Reclamation 11.
- Zhang, S., Wang, G., Pang, B., & Du, C. (2013). The effects of strong motion duration on the dynamic response and accumulated damage of concrete gravity dams. *Soil Dynamics and Earthquake Engineering*. <https://doi.org/10.1016/j.soildyn.2012.11.011>
- Zhao, G. F., Fang, J., & Zhao, J. (2011). A 3D distinct lattice spring model for elasticity and dynamic failure. *International Journal for Numerical and Analytical Methods in Geomechanics*. <https://doi.org/10.1002/nag.930>

Zhao, G. F., Yin, Q., Russell, A. R., Li, Y., Wu, W., & Li, Q. (2019). On the linear elastic responses of the 2D bonded discrete element model. *International Journal for Numerical and Analytical Methods in Geomechanics*. <https://doi.org/10.1002/nag.2858>

Zhong, H., Li, X. Y., & Lin, G. (2012). Analyses of failure modes-based seismic fragility of gravity dams. *Dalian Ligong Daxue Xuebao/Journal of Dalian University of Technology*.

## APPENDICES

### A. Cracking Scheme and Run Time Comparisons

A comparison on the cracking schemes between the plane stress and plane strain solutions for MAEM Model I, corresponding to the concrete dam-reservoir system (Figure 4.1), with 10 connecting spring pairs were made for Motion 6 – Scale 1.00g by utilizing the explicit nonlinear solution scheme (Figure A.1). Some minor differences exist for the cracks at upstream and downstream faces. These differences can be neglected for the performance prediction, as the crack locations and propagation were obtained similarly for both solutions.

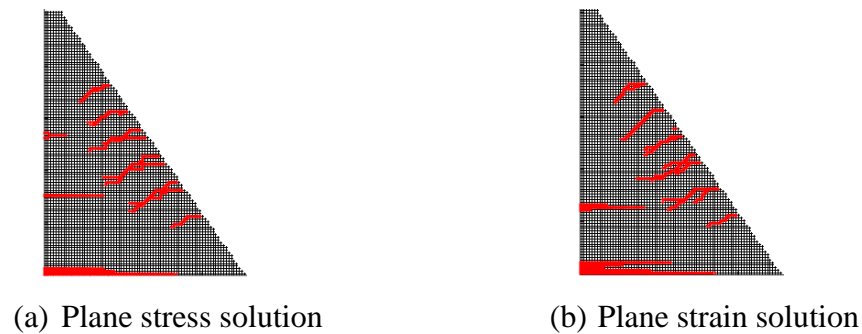


Figure A.1 Cracking schemes of MAEM models

For the plane stress solutions, the effect of the number of connecting spring pairs on the damage prediction and the solution times were also studied for the same model under the same motion (Motion 6 – Scale 1.00g). The dam-reservoir model consisted of 4197 modified applied elements, 2450 reservoir finite elements; in total, there were 14196 nodes with 32157 DOF. The total number of springs, including the diagonal springs, were 16326, 32758, 49190, 90270, and 172430 for 1, 3, 5, 10, and 20 springs, respectively. For spring pairs more than 1 (i.e., 3, 5, 10, and 20 spring pairs), the cracking schemes were almost identical (Figure A.2). On the other hand, for a single spring pair connecting the elements from the centroids, somewhat

different cracking was observed (Figure A.2a). The main reason for this difference is insufficient modeling of rotational stiffness with 1 spring pair: the theoretical rotational stiffness is attained as the number of spring pairs between the elements increase (Meguro & Tagel-Din, 2000).

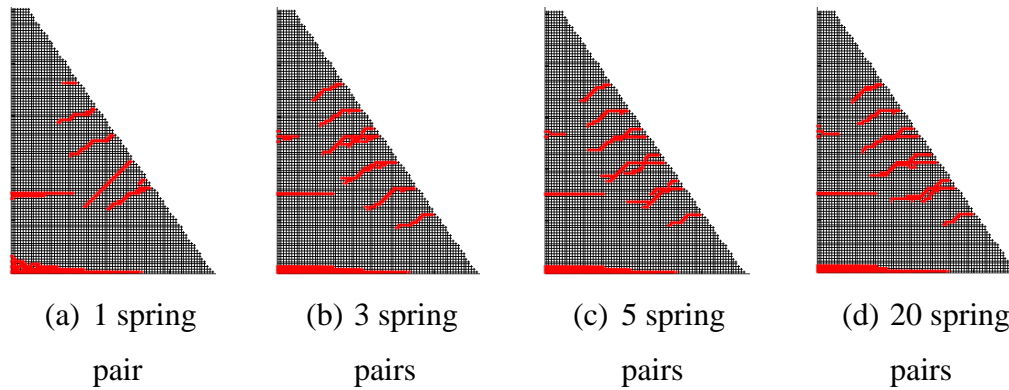


Figure A.2 Cracking schemes of MAEM models with different spring numbers

The solution times for the above simulations were compared for a 1-sec duration of the ground motion on a system comprised of Intel Core i7 3.40 GHz processor and 16 GB RAM with Windows 10 operating system. The computational cost increased as the spring pair number increased. The run times were 1830 sec, 1880 sec, 1890 sec, 1960 sec, and 2120 sec, respectively, for analyses with 1, 3, 5, 10, and 20 spring pairs used between the elements. The increase in the number of spring pairs from 1 to 20 led to 1.2 folds increase in the computational cost. The increase in the run time with respect to the number of spring pairs was more prominent (1.7 times) for the Koyna dam body solutions consisting of only modified applied elements (Section 3.9). For the dam-reservoir system investigated in this part, it was observed that the reservoir finite elements had a significant contribution to the solution time, reducing this effect.

## B. Incremental Dynamic Analyses Results

The crack schemes obtained from the incremental dynamic analyses performed in Chapter 4 are given below. The results for the FEM, MAEM concrete (indicated as MAEM I), and the MAEM RCC (MAEM II) models are presented for each motion at each scale level in Figure B.1. The figures show all of the cracked elements within the time history, corresponding to a total (envelope) damage map.

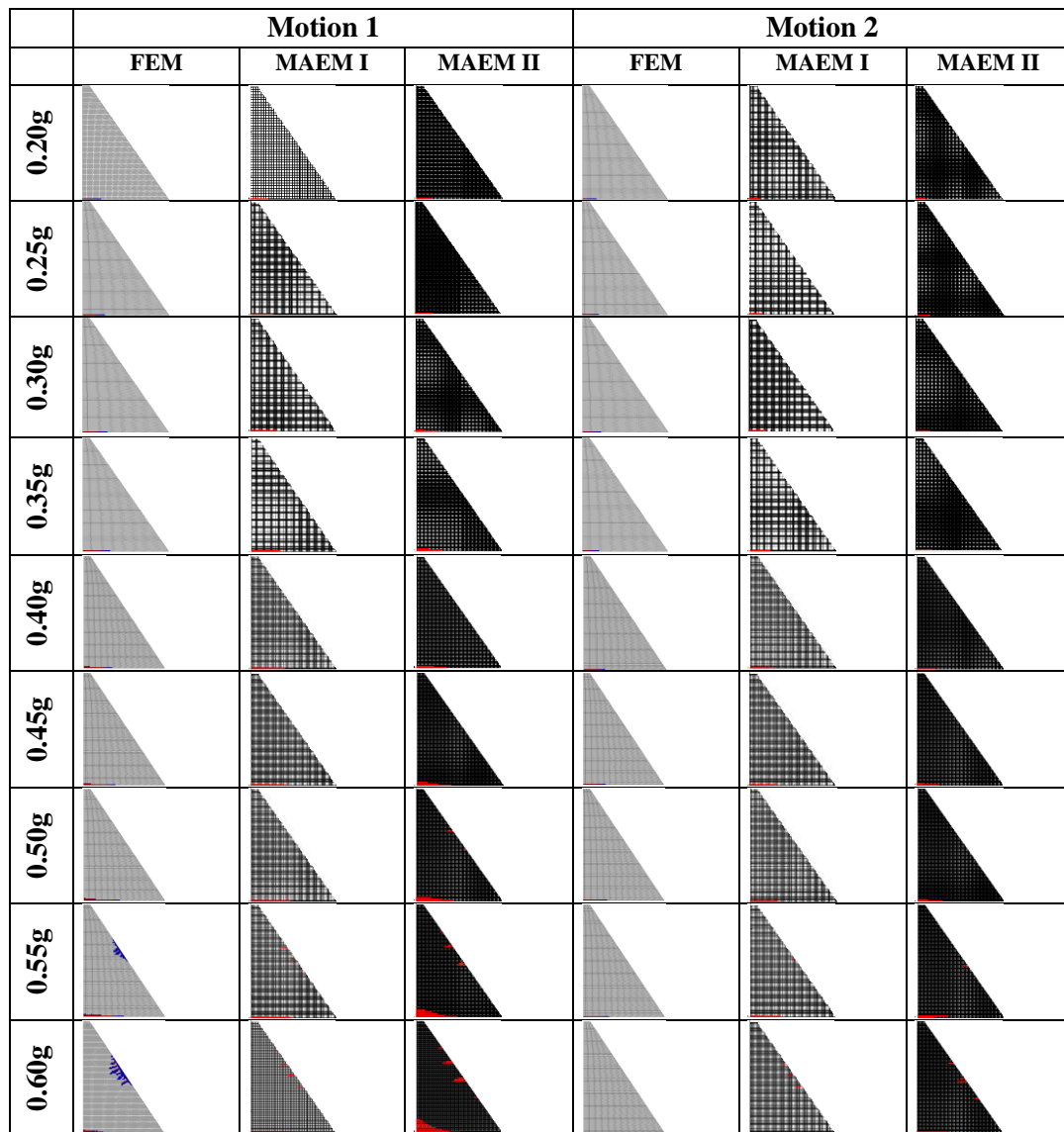


Figure B.1 Cracking scheme comparison for FEM and MAEM models

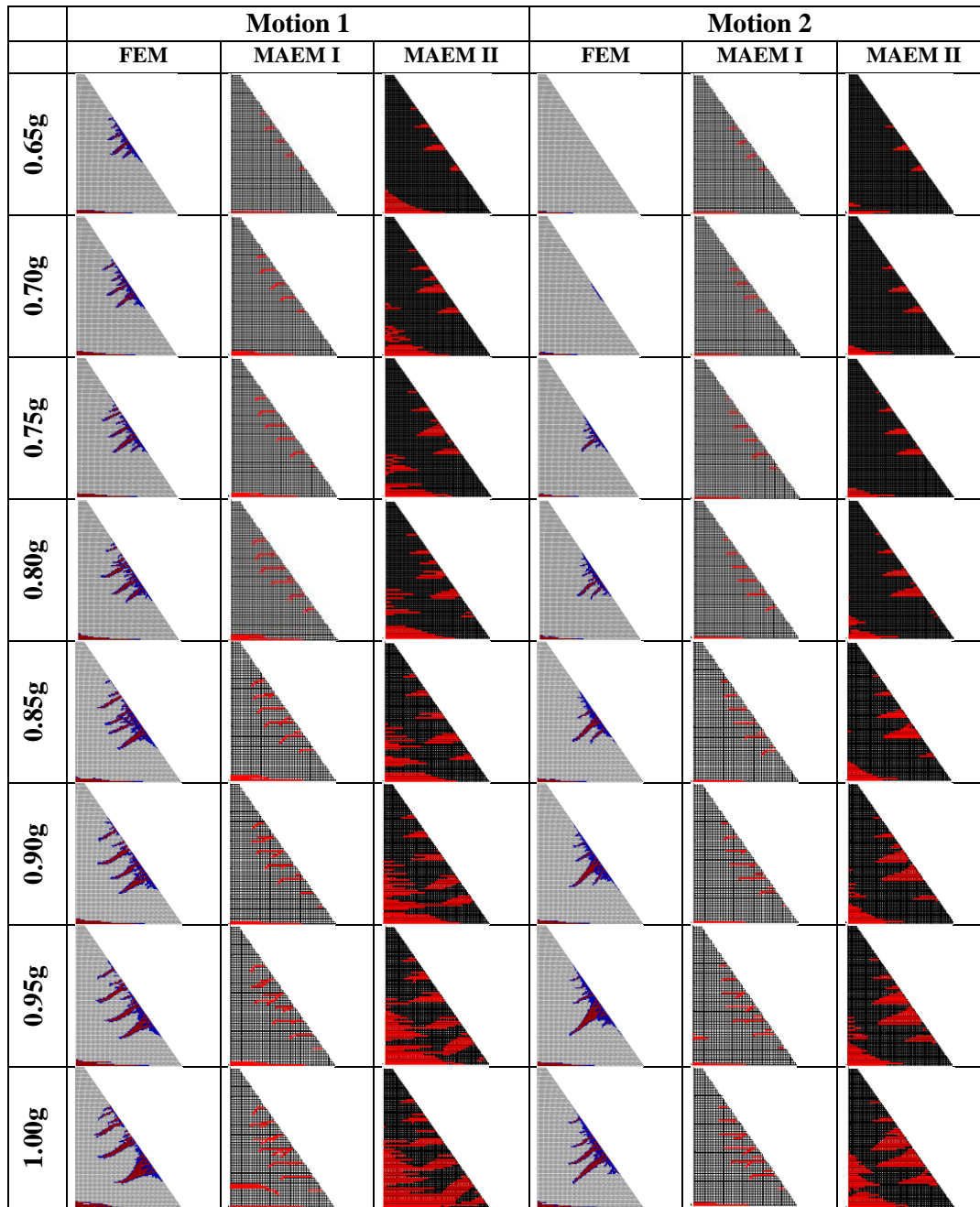


Figure B.1 (Continued) Cracking scheme comparison for FEM and MAEM models



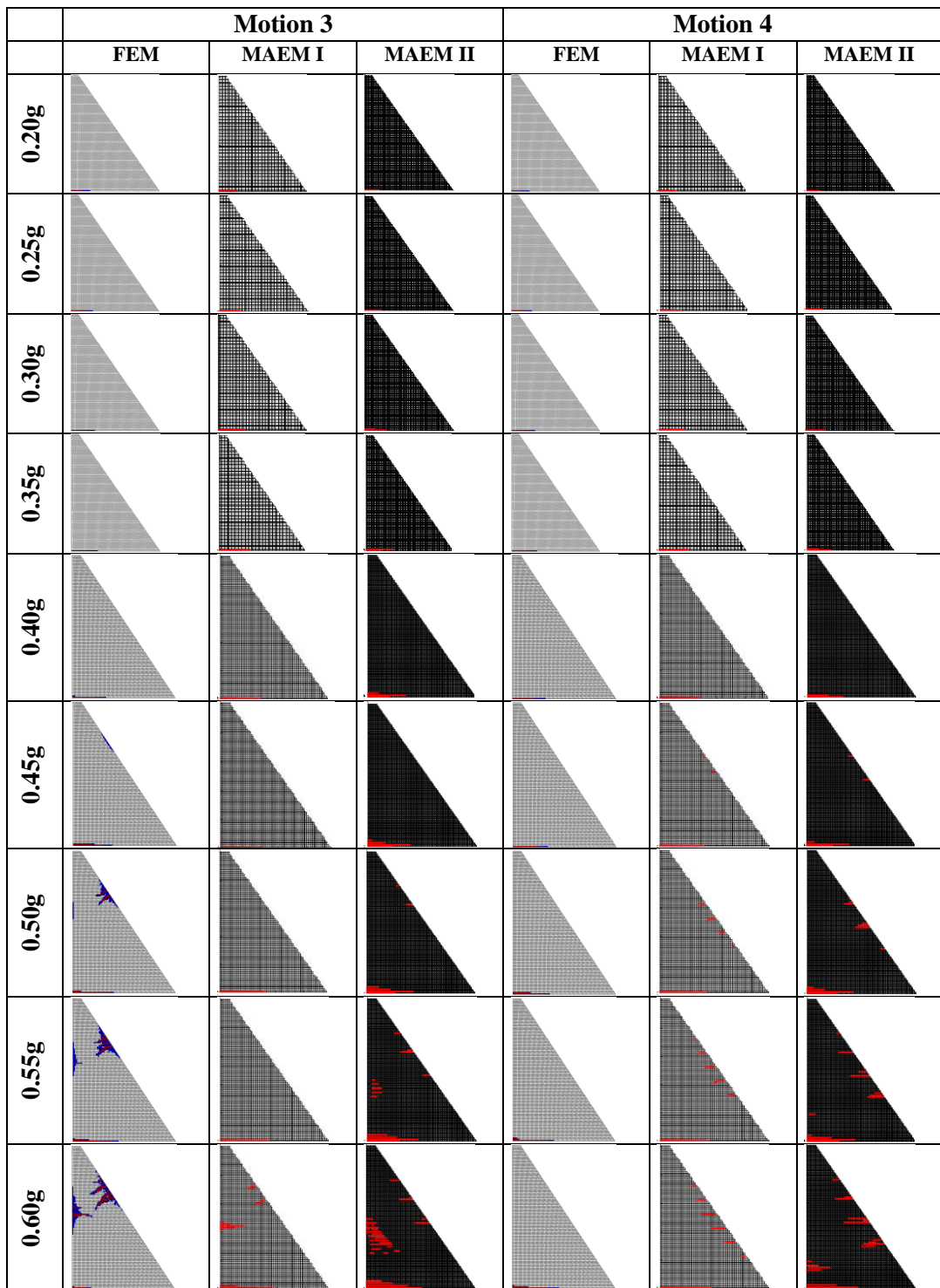


Figure B.1 (Continued) Cracking scheme comparison for FEM and MAEM models

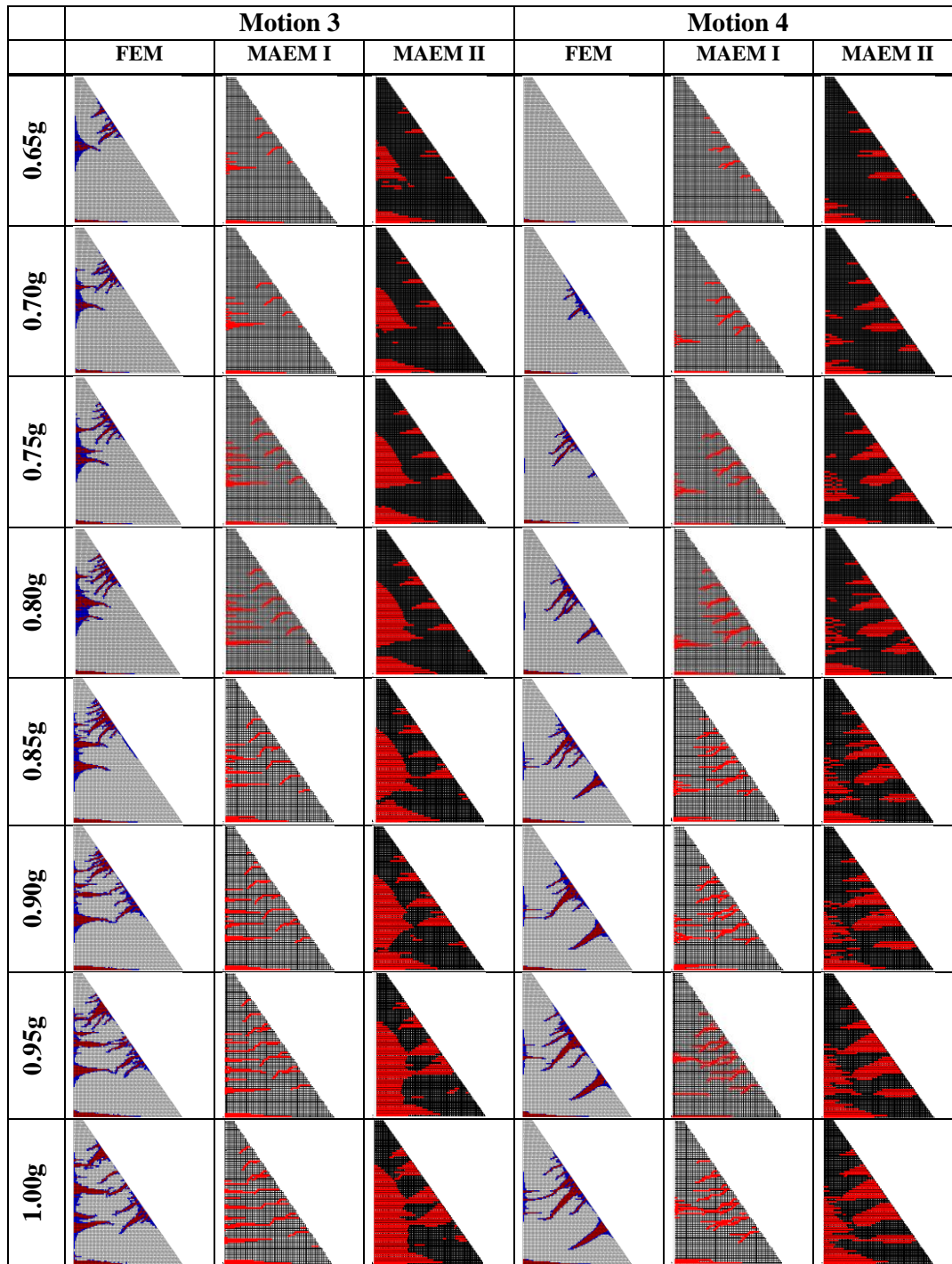


Figure B.1 (Continued) Cracking scheme comparison for FEM and MAEM models



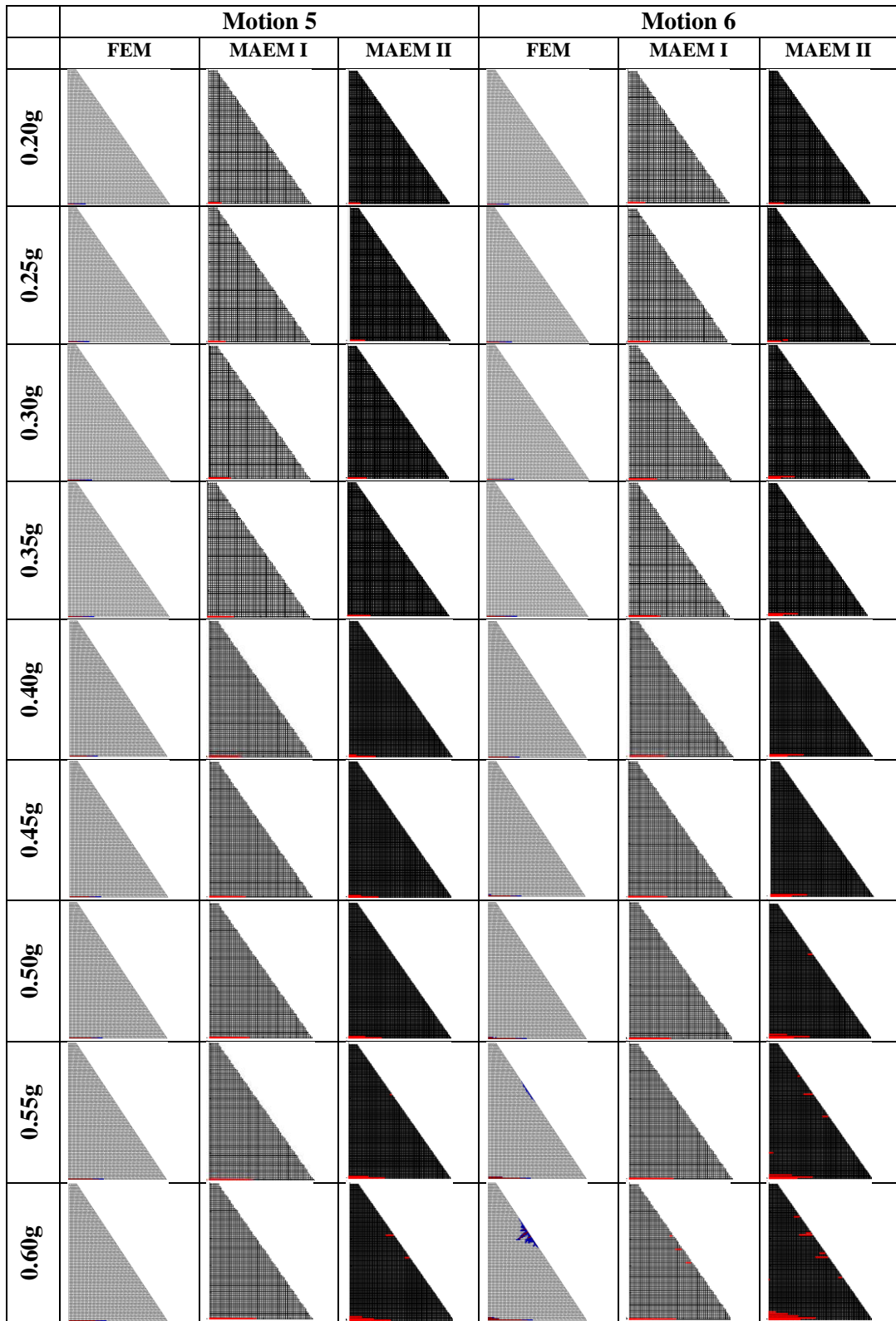


Figure B.1 (Continued) Cracking scheme comparison for FEM and MAEM models

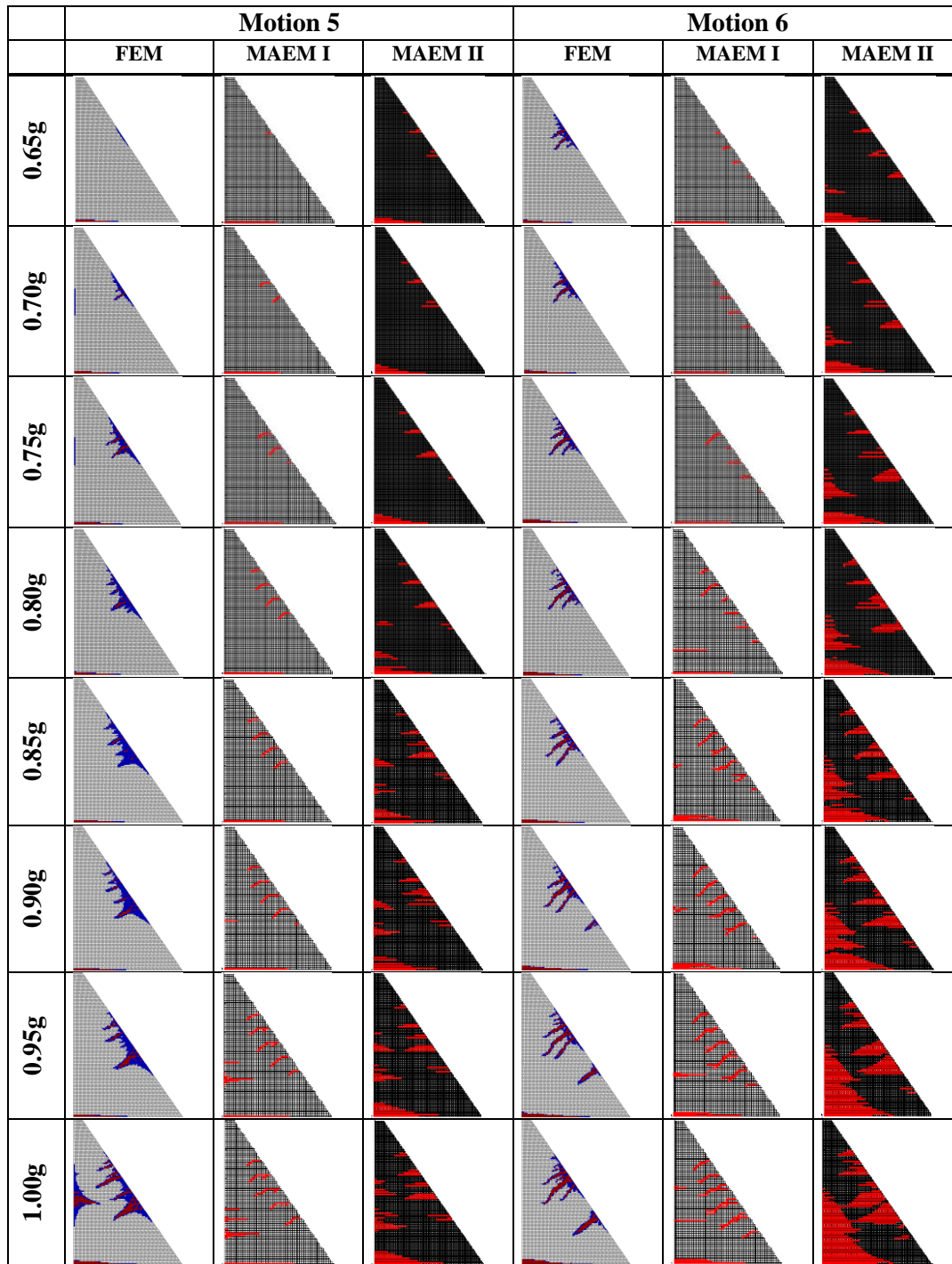


Figure B.1 (Continued) Cracking scheme comparison for FEM and MAEM models

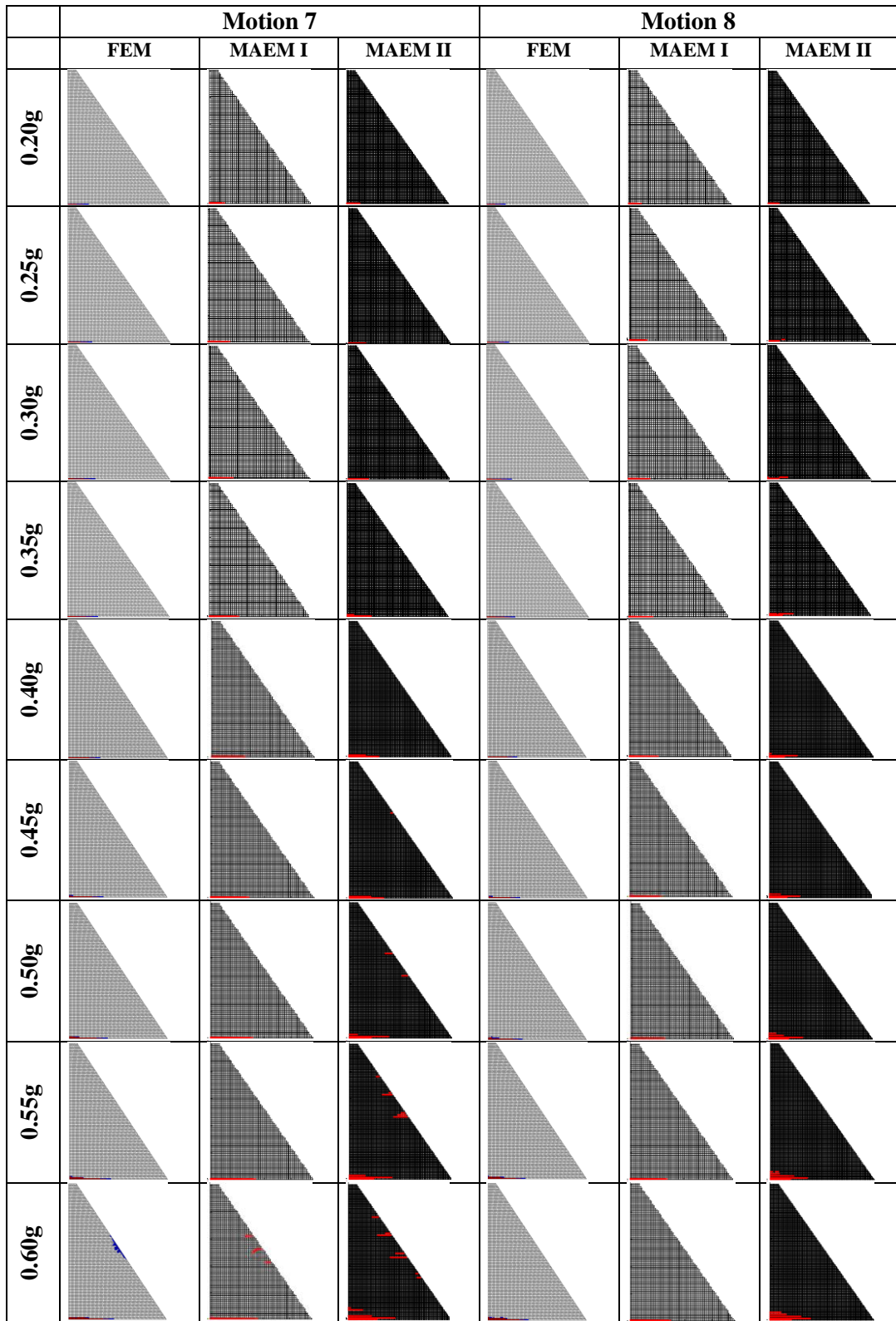


Figure B.1 (Continued) Cracking scheme comparison for FEM and MAEM models



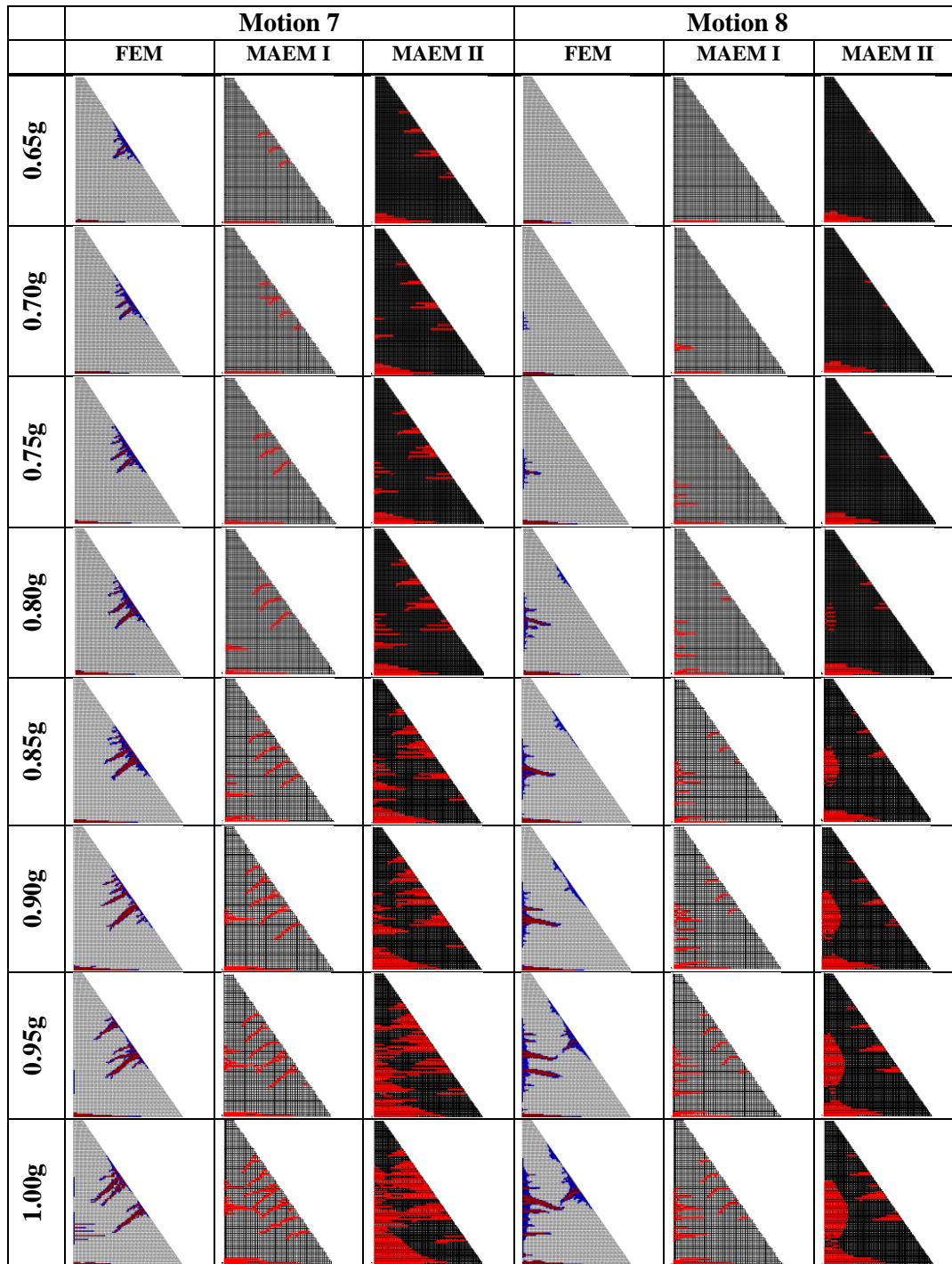


Figure B.1 (Continued) Cracking scheme comparison for FEM and MAEM models

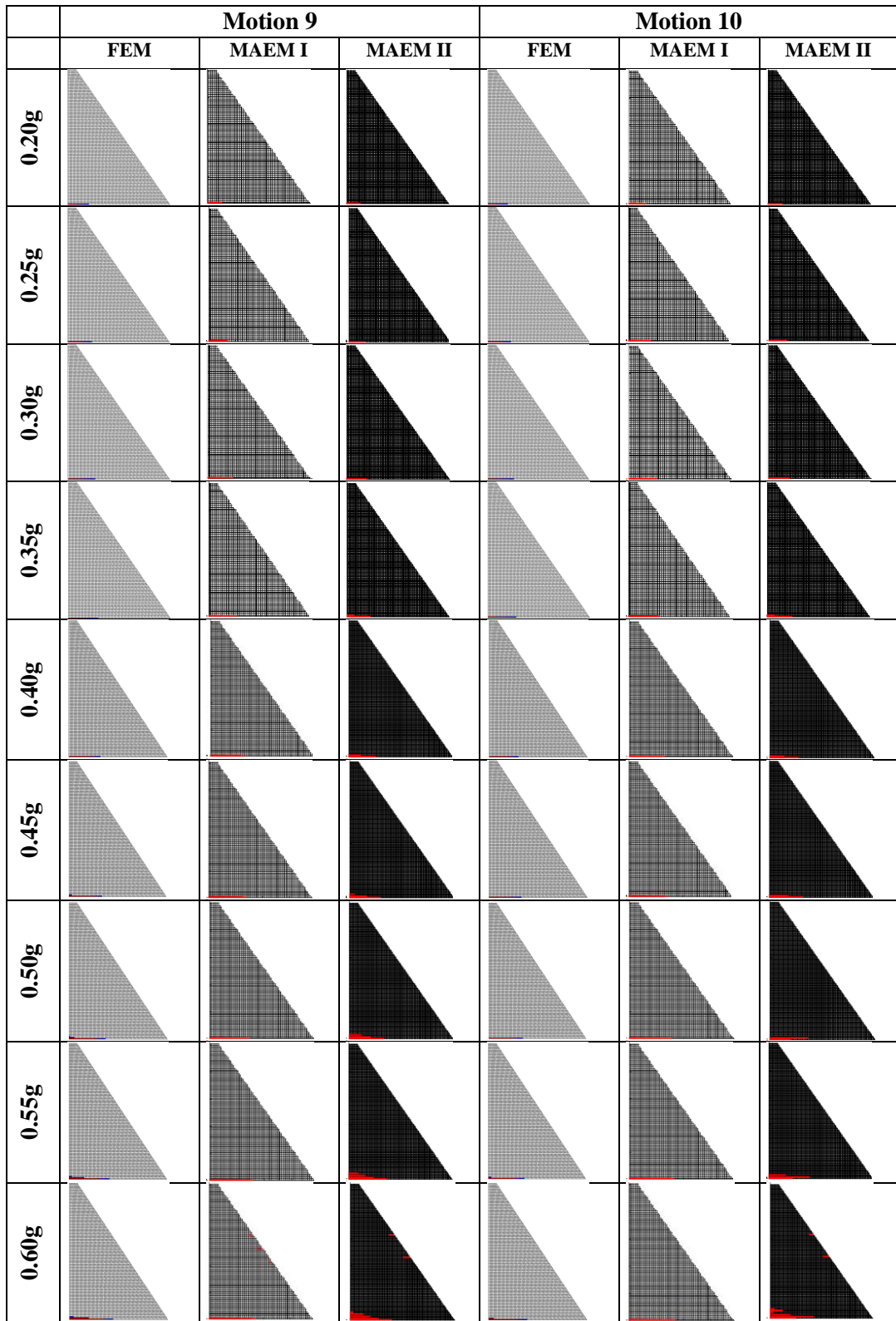


Figure B.1 (Continued) Cracking scheme comparison for FEM and MAEM models

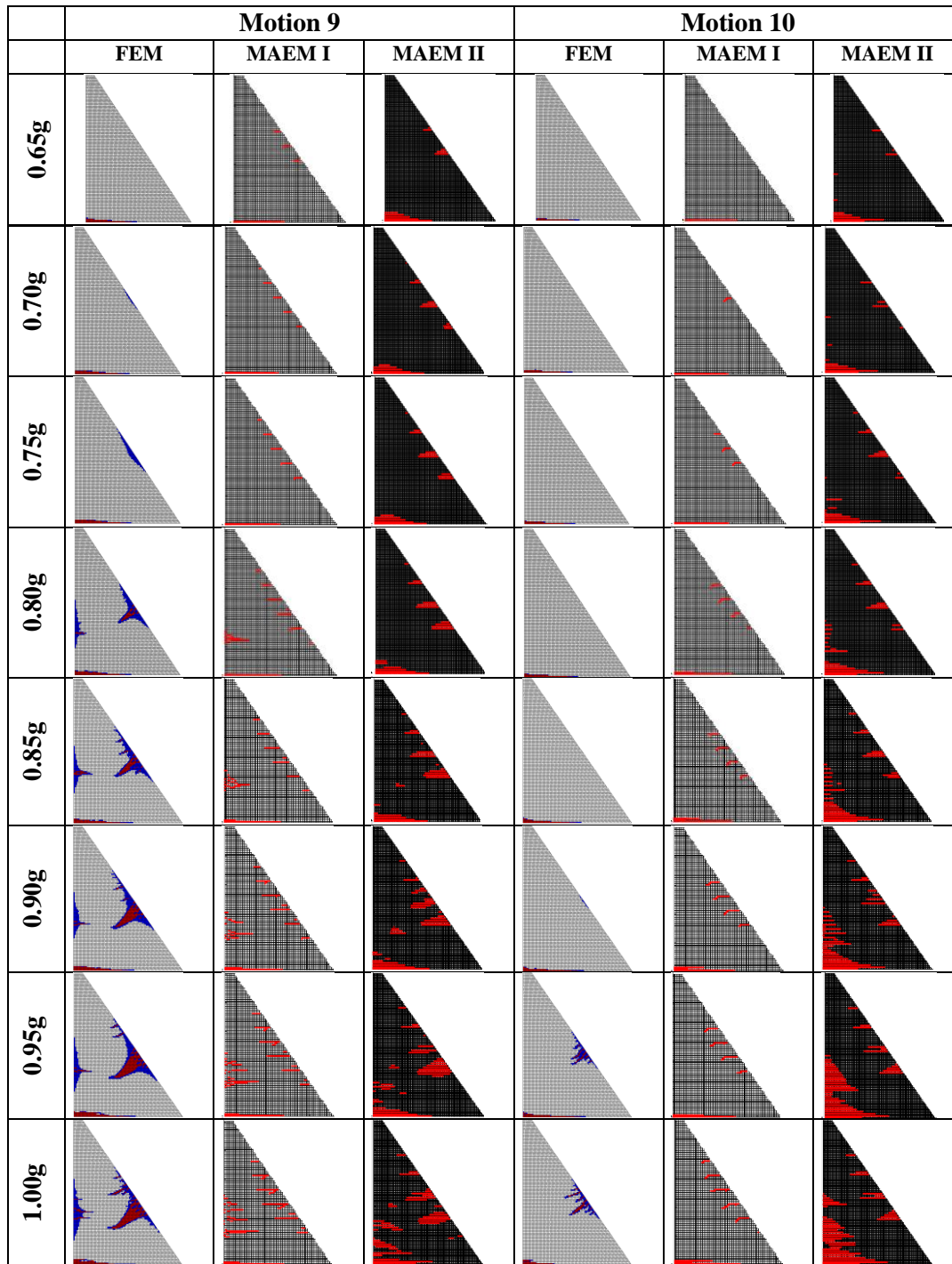


Figure B.1 (Continued) Cracking scheme comparison for FEM and MAEM models



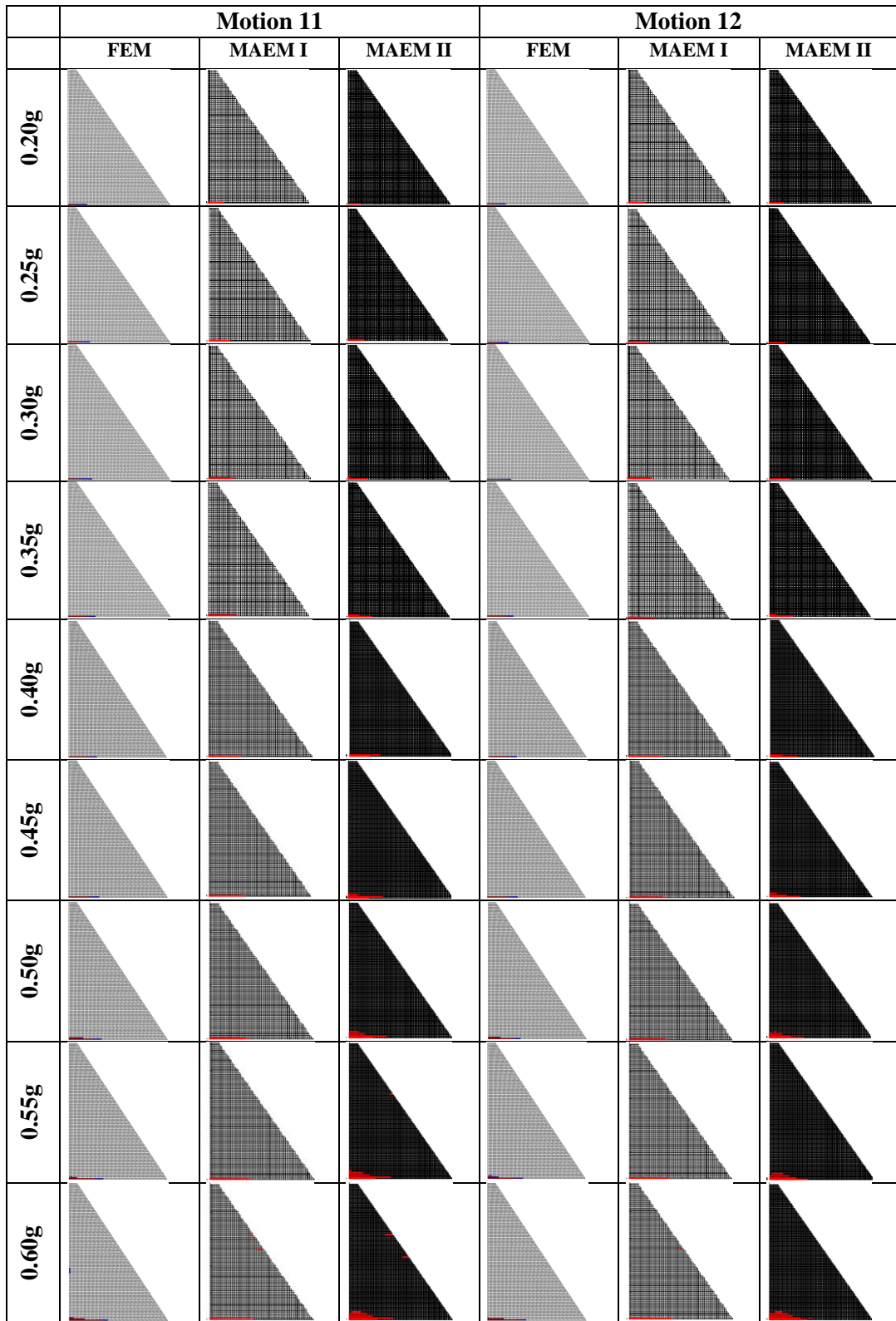


Figure B.1 (Continued) Cracking scheme comparison for FEM and MAEM models

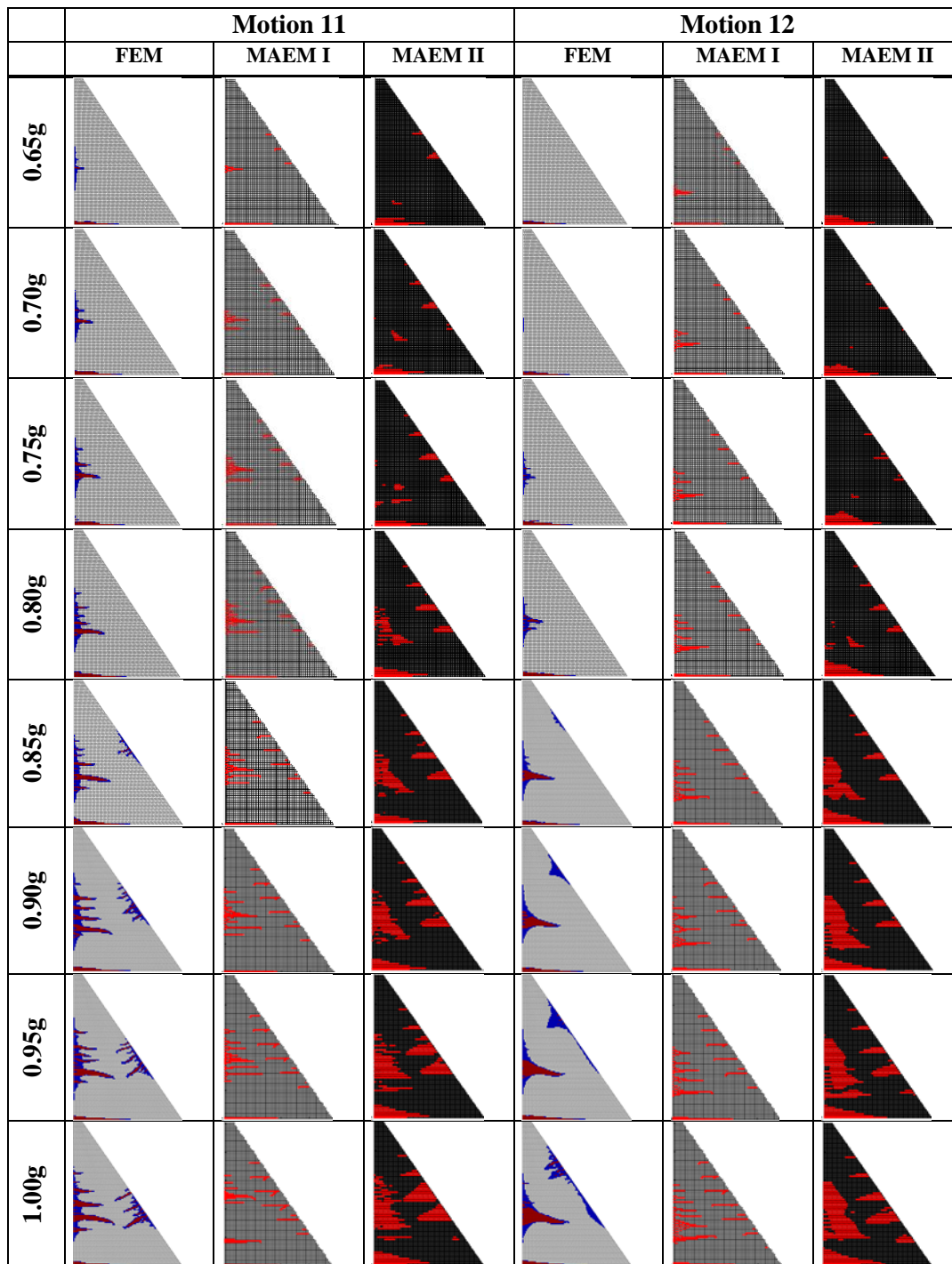


Figure B.1 (Continued) Cracking scheme comparison for FEM and MAEM models



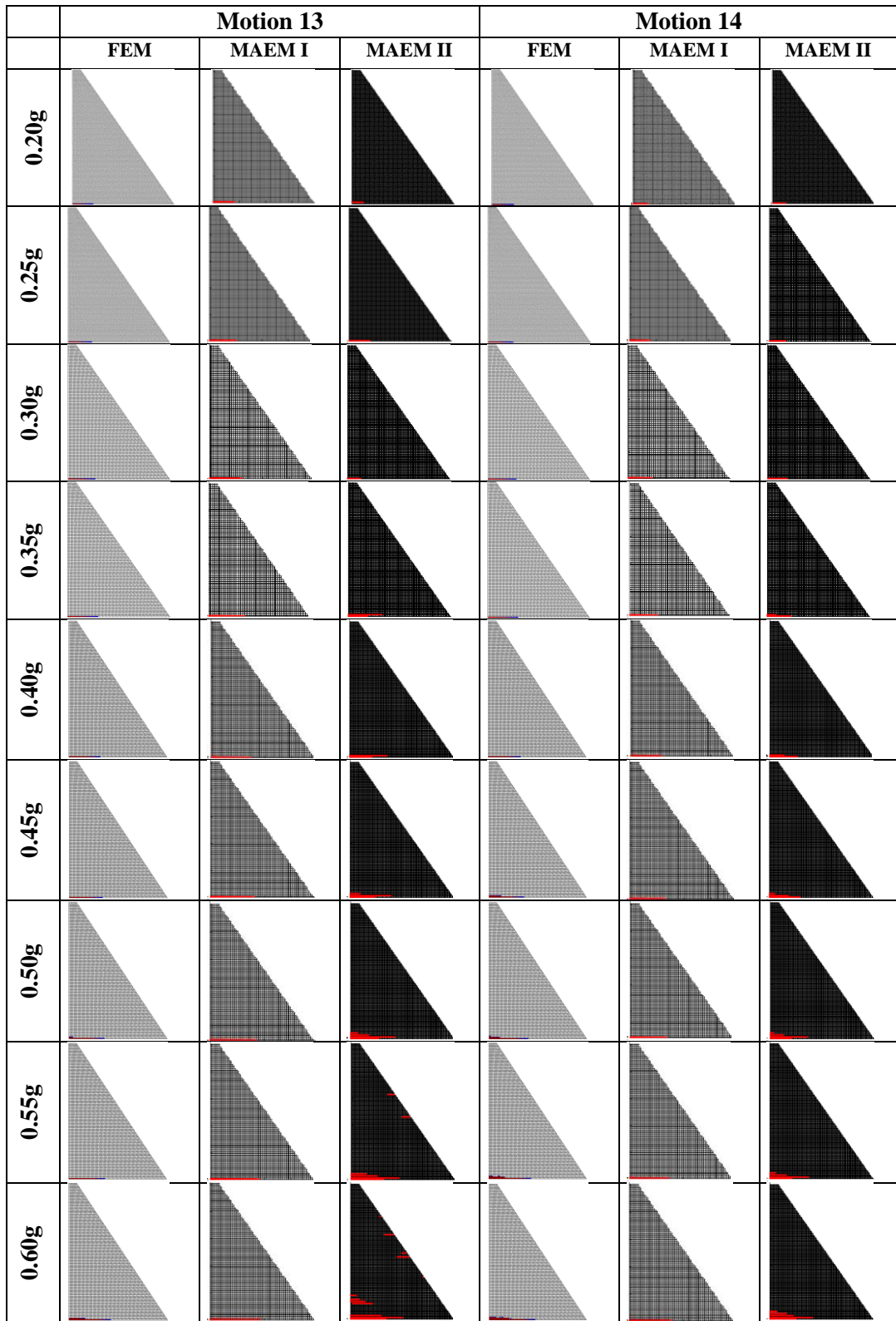


Figure B.1 (Continued) Cracking scheme comparison for FEM and MAEM models

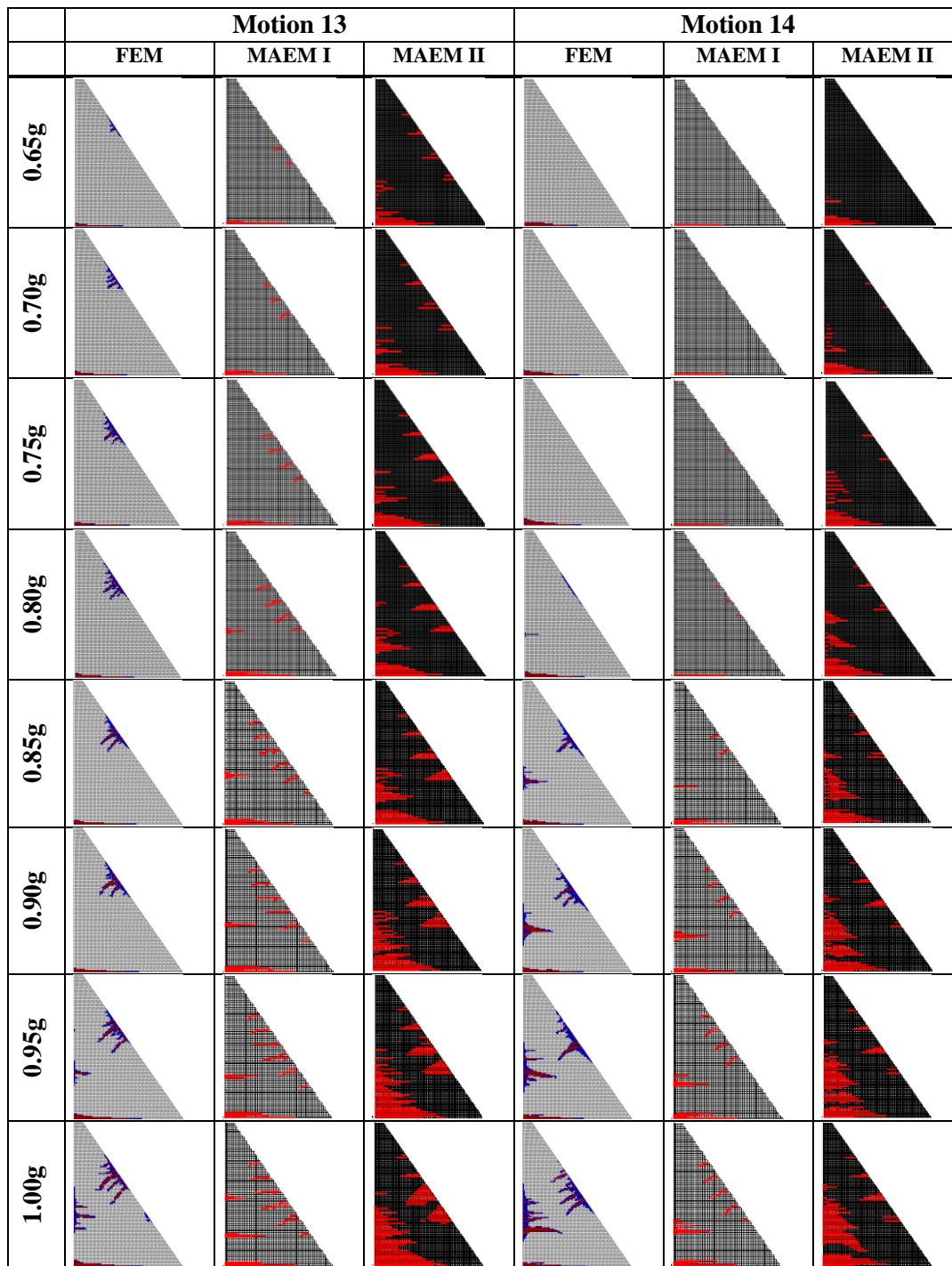


Figure B.1 (Continued) Cracking scheme comparison for FEM and MAEM models

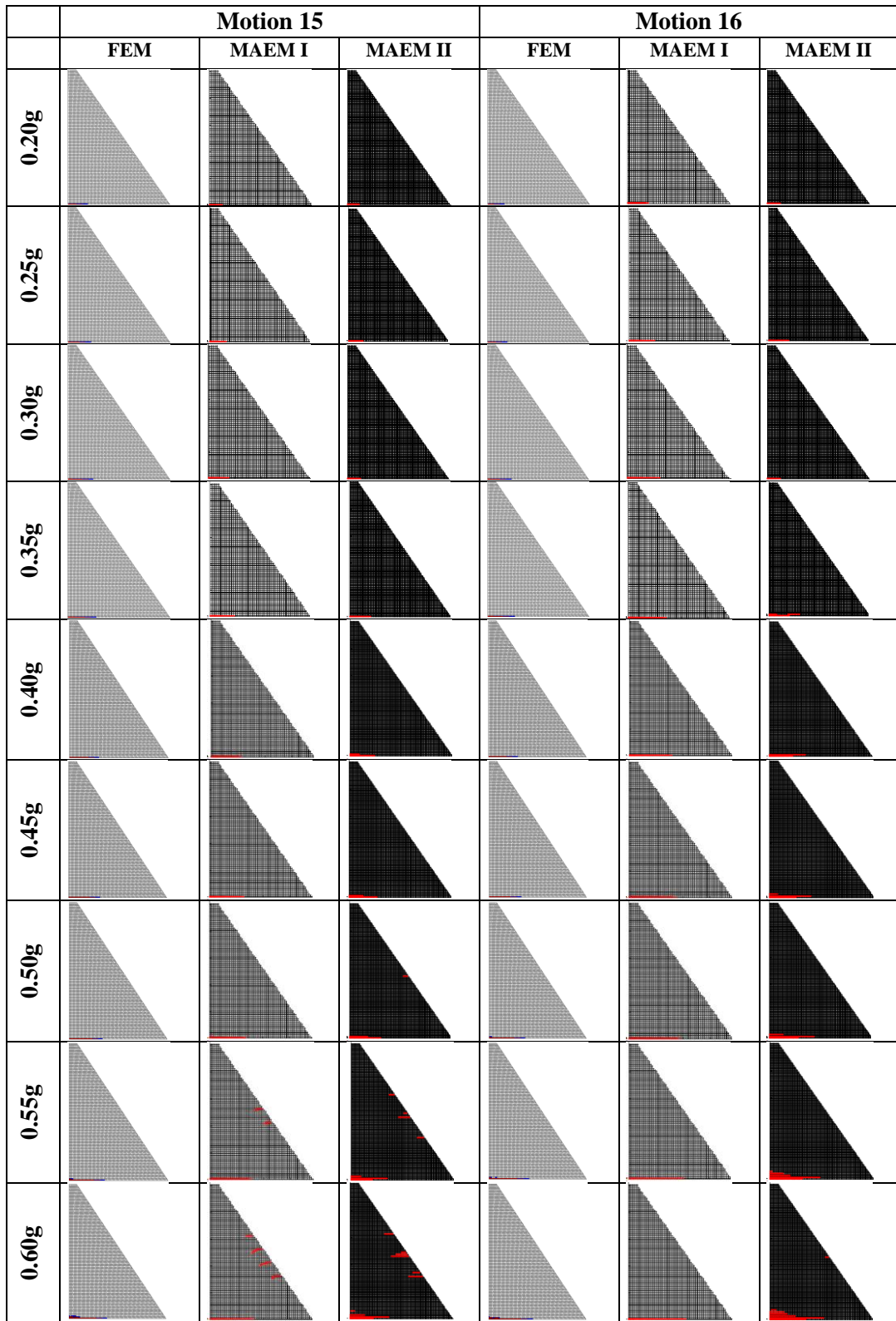


Figure B.1 (Continued) Cracking scheme comparison for FEM and MAEM models



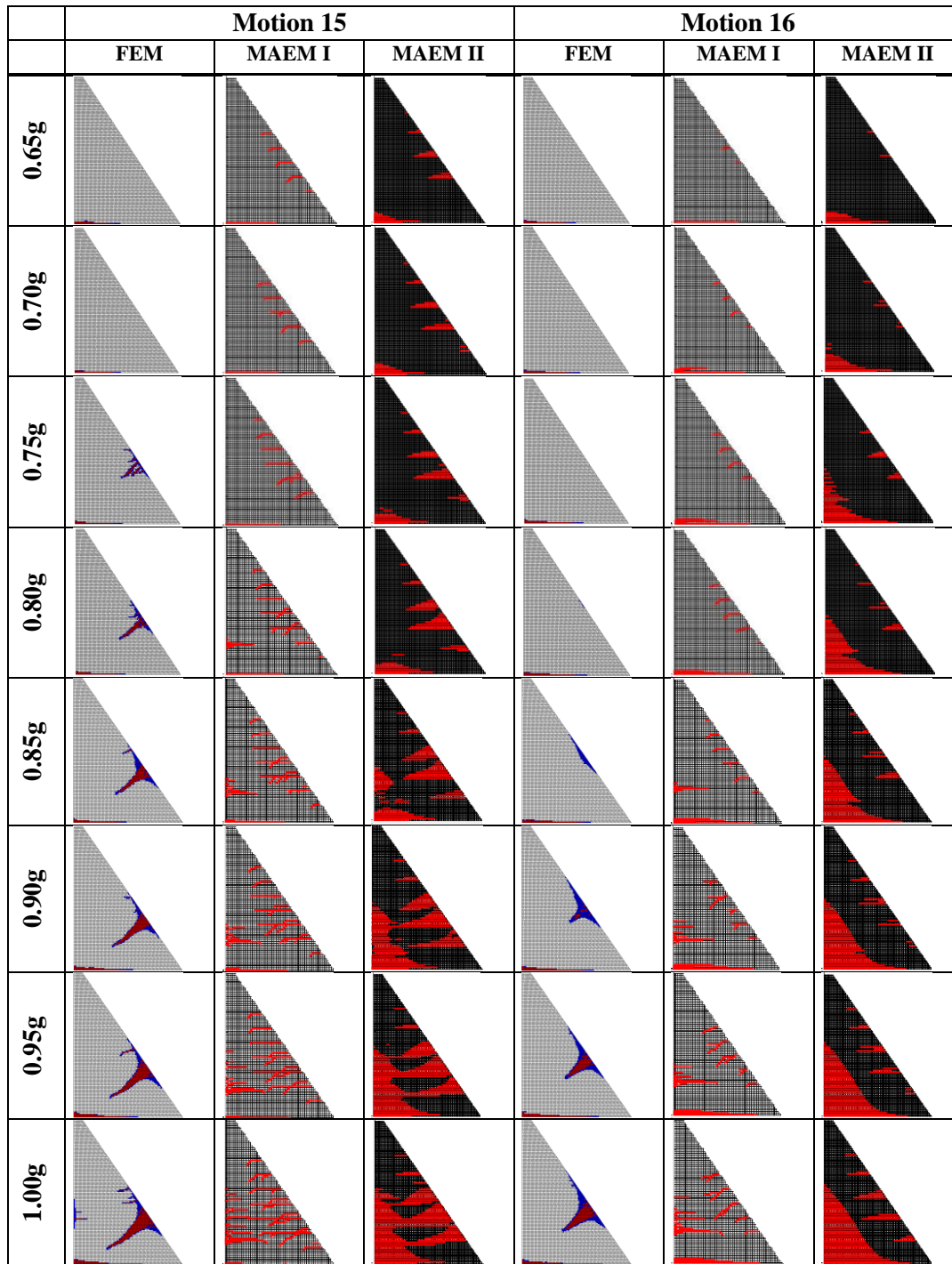


Figure B.1 (Continued) Cracking scheme comparison for FEM and MAEM models

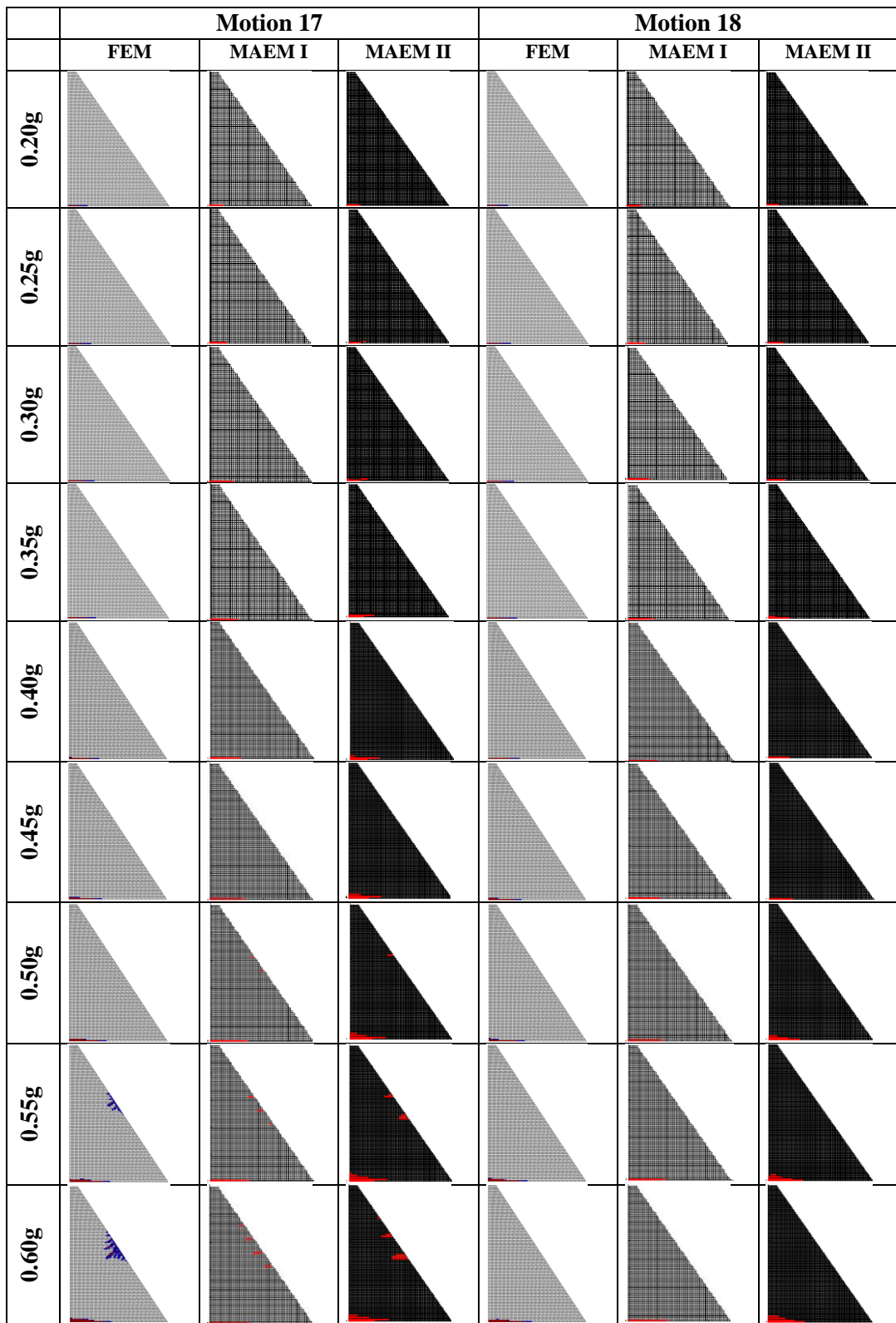


Figure B.1 (Continued) Cracking scheme comparison for FEM and MAEM models

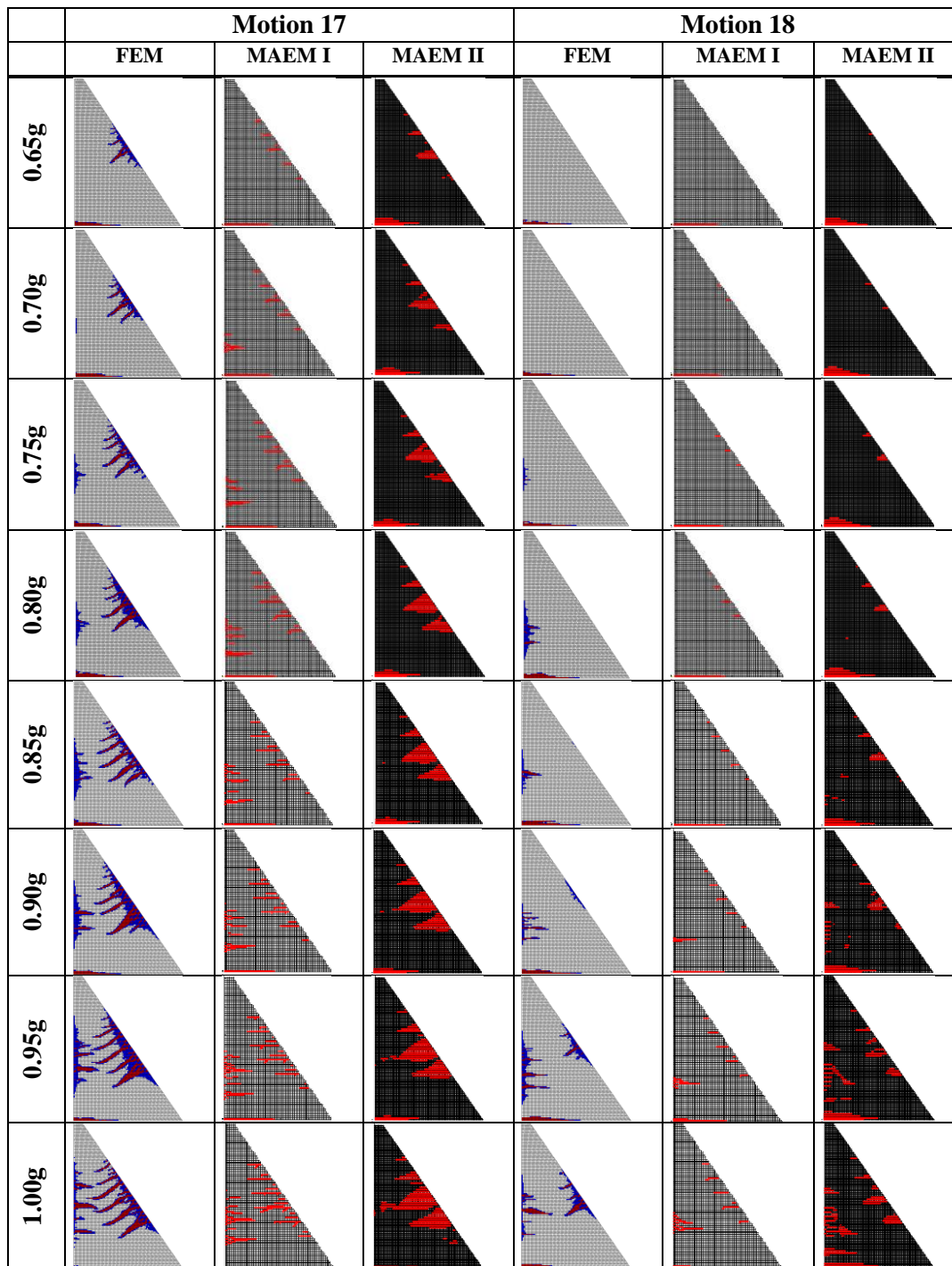


Figure B.1 (Continued) Cracking scheme comparison for FEM and MAEM models



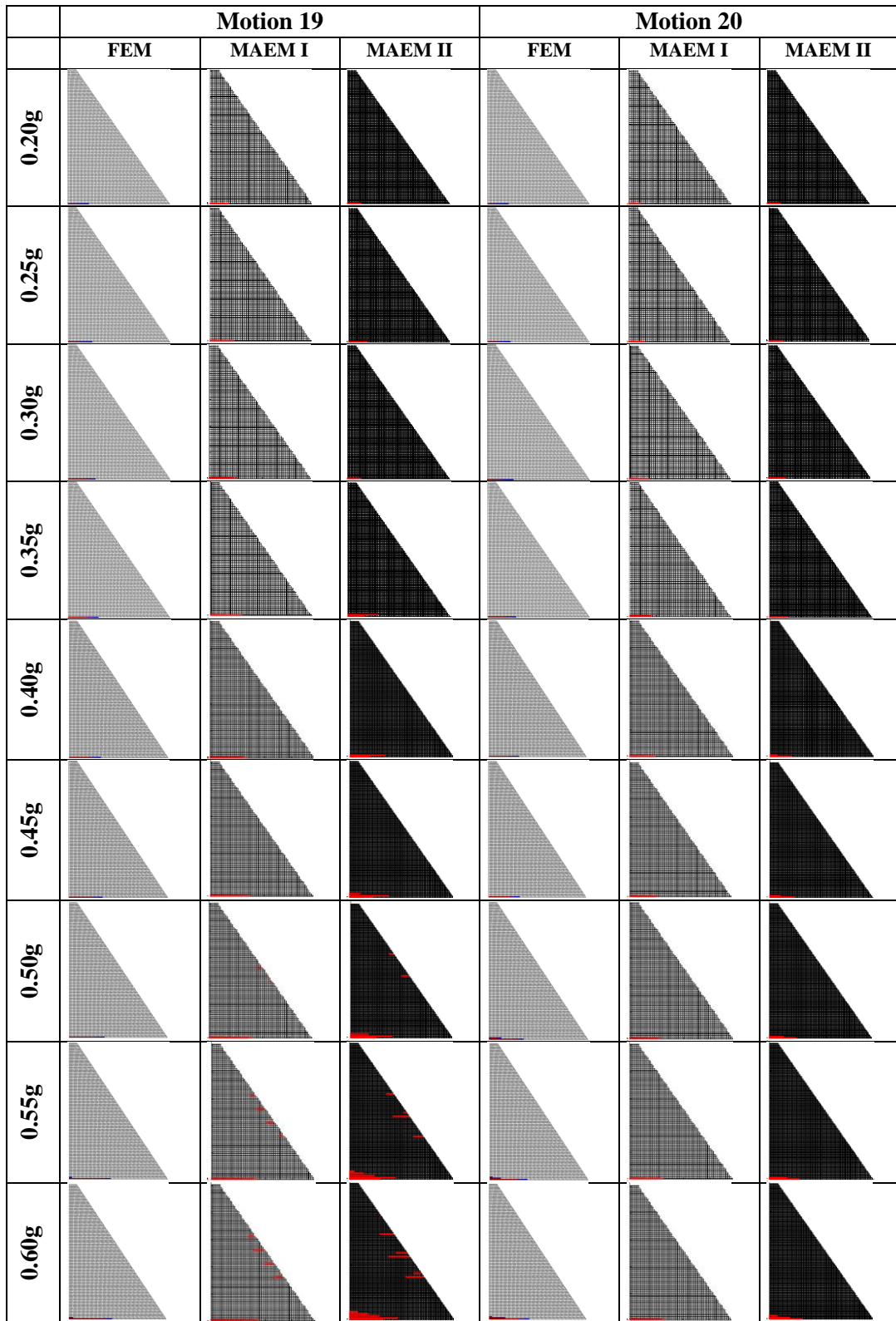


Figure B.1 (Continued) Cracking scheme comparison for FEM and MAEM models

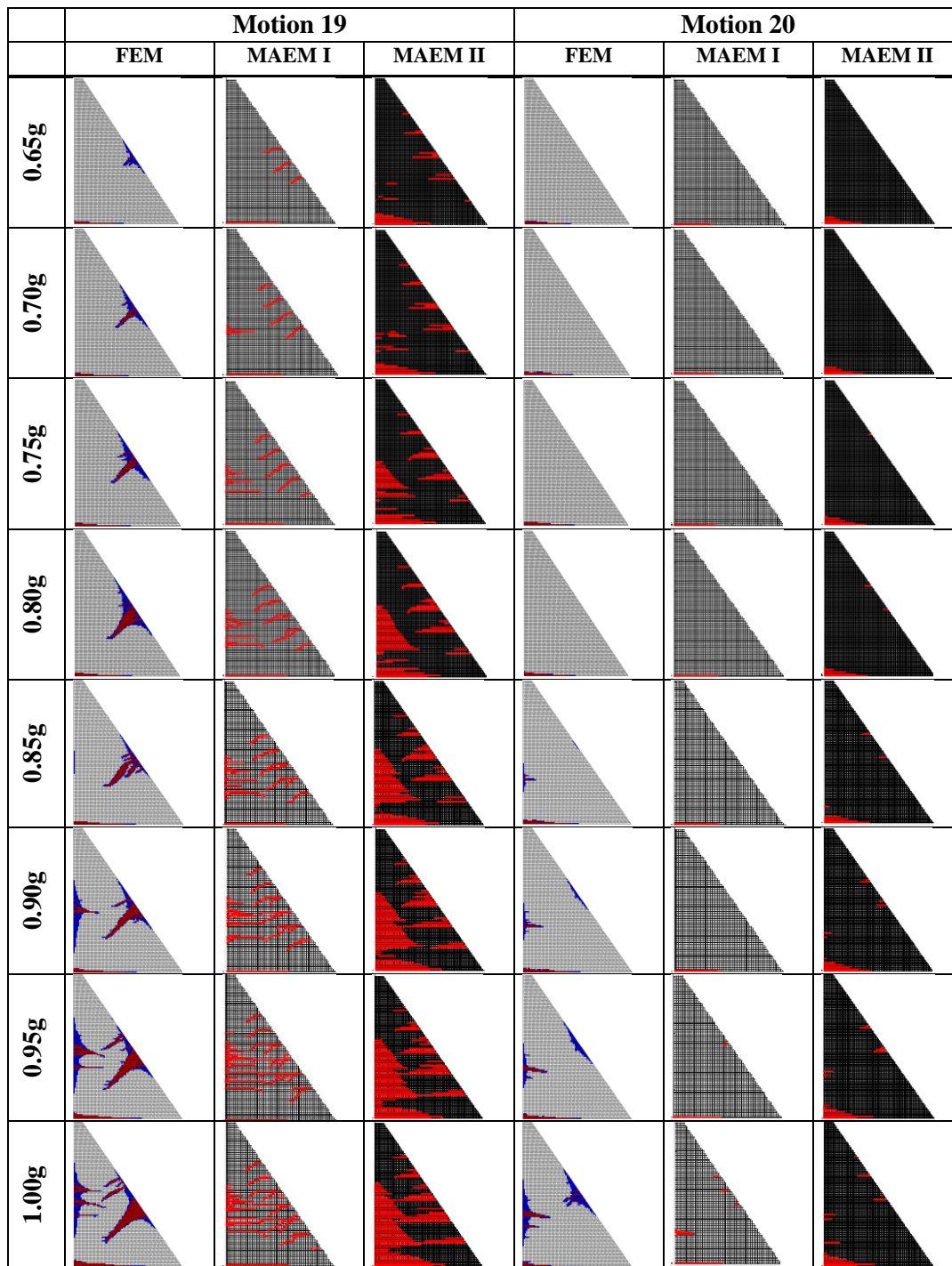


Figure B.1 (Continued) Cracking scheme comparison for FEM and MAEM models



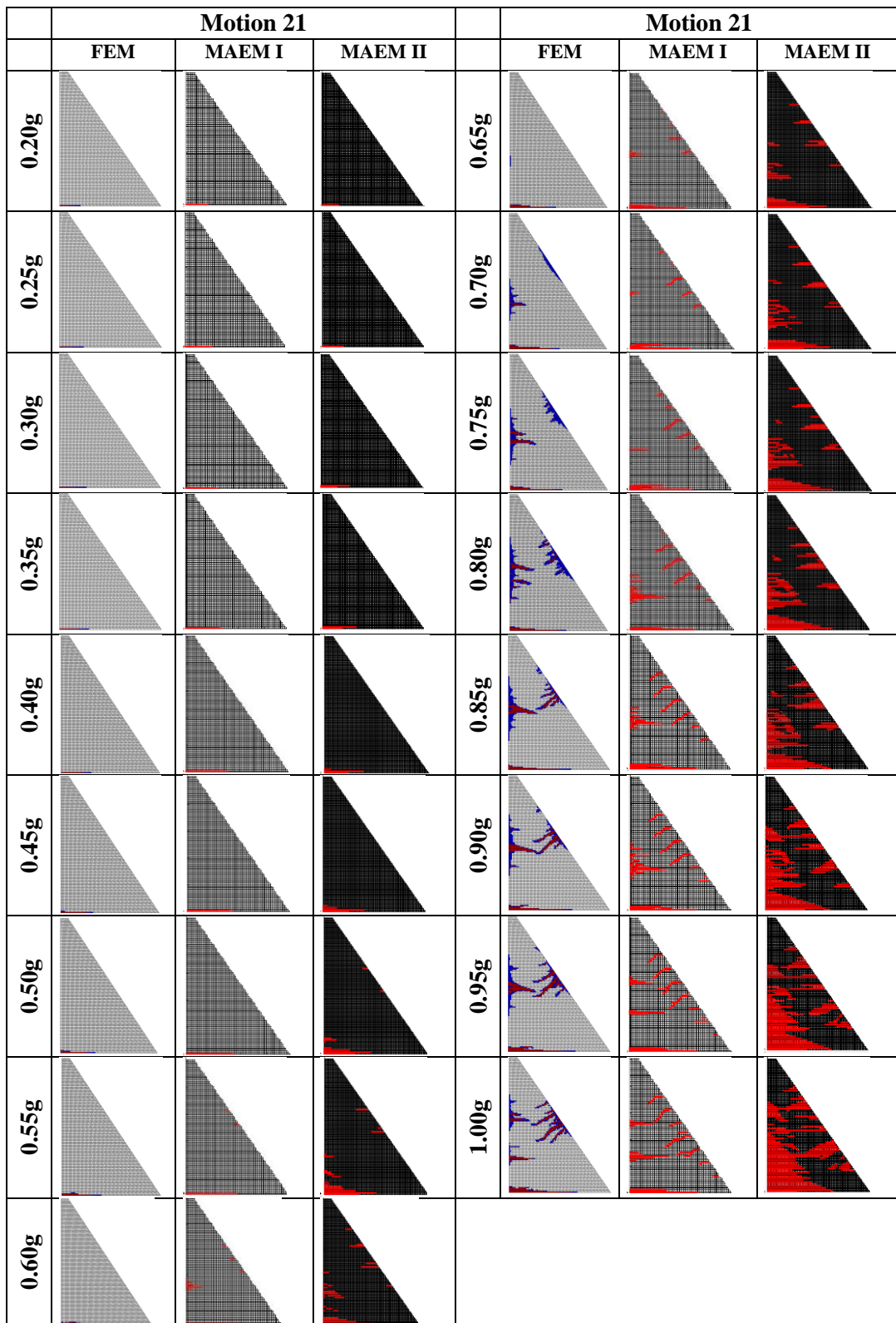


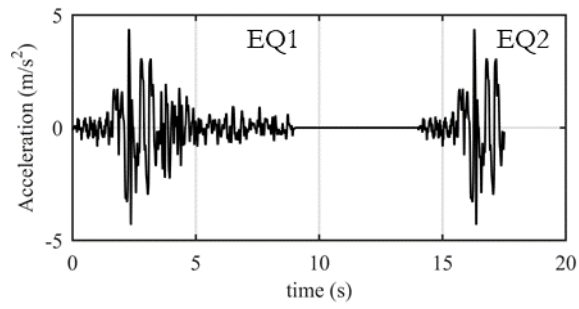
Figure B.1 (Continued) Cracking scheme comparison for FEM and MAEM models



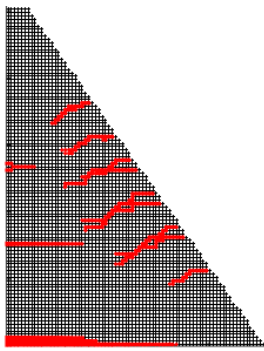
### **C. Assessment of the Use of Damaged State Models for Determination of the Post-Earthquake Response**

The use of post-earthquake damaged state of MAEM models for the determination of the response of the system for additional demands was evaluated in this section. To this end, two analyses were conducted. In the first analysis (Analysis I), Motion 6 – Scale 1.00g was applied to the system as EQ1; after the motion was damped-out, a second earthquake (EQ2) was applied (Figure C.1a). Accordingly, the cracking profiles at the end of the first (Figure C.1b) and second earthquakes (Figure C.1c) were obtained. For the second analysis (Analysis II), zero tensile strength was assigned to the damaged springs for the connections that were damaged after the first earthquake of the first analysis (Figure C.1b). Consequently, the behavior in the compression range was simulated, but the tensile forces could not be carried. Then, analysis under the second earthquake (EQ2) was conducted with these weak connections, and the cracking scheme was obtained (Figure C.1d).

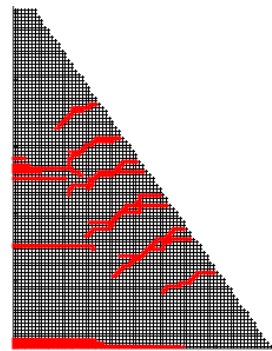
It can be seen from Figure C.1 that only minor differences exist for the cracks at the upstream and downstream faces of the dams after EQ2; crack propagation was obtained similarly for both solutions for this example. In contrast to the finite element models in which such an approach would be very cumbersome, the discrete nature of MAEM enables the use of post-earthquake damage state for further evaluation in a straightforward manner, as described above.



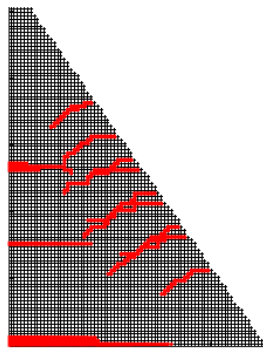
(a) Applied ground motions



(b) Analysis I: Cracking at the end of EQ1



(c) Analysis I: Cracking at the end of EQ2



(d) Analysis II: Cracking at the end of EQ2

Figure C.1 Damaged State Modeling with MAEM

## CURRICULUM VITAE

### PERSONAL INFORMATION

Surname, Name: Soysal Albostan, Berat Feyza  
Nationality: Turkish (TC)  
Date and Place of Birth: 23 March 1989, Altındağ  
Marital Status: Married  
Phone: +90 532 447 40 54  
email: e155113@metu.edu.tr

### EDUCATION

Degree	Institution	Year of Graduation
MS	METU Civil Engineering	2014
BS	METU Civil Engineering	2011
High School	Milli Piyango Anadolu High School, Ankara	2006

### WORK EXPERIENCE

Year	Place	Enrollment
2020-Present	Çankaya University Dept. of Civil Eng.	Part-time Instructor
2011-2020	METU Dept. of Civil Eng.	Research Assistant
2010 July	Kolin İnşaat	Intern Eng. Student
2009 July	METU Dept. of Civil Eng.	Intern Eng. Student

### FOREIGN LANGUAGES

Advanced English, Beginner German

### PUBLICATIONS

#### Peer Reviewed International Journal Papers:

1. **Soysal, B.F.**, Ay, B.Ö., Arıcı, Y. (2017). An Investigation of the Ground Motion Scaling Procedures for the Nonlinear Seismic Analyses of Concrete Gravity Dams, Journal of Earthquake Engineering, doi: 10.1080/13632469.2017.1342298.

2. **Soysal, B.F.**, Binici, B., Arıcı, Y. (2016). Investigation of the Relationship of Seismic Intensity Measures and the Accumulation of Damage on Concrete Gravity Dams using Incremental Dynamic Analysis, *Earthquake Engineering and Structural Dynamics*, 45: 719-737. doi: 10.1002/eqe.2681.

#### **Peer Reviewed National Journal Papers:**

1. Akansel, V.H., **Soysal, B.F.**, Kadaş, K., Gülkan, H.P. (2020). An Evaluation of the 2018 Seismic Hazard Map of Turkey on the Basis of Spectrum Intensity, *Turk. J. Earthq. Res.*, 2(2), 115-137, <https://doi.org/10.46464/tdad.737433>.

#### **International Conference Papers:**

1. Akansel, V.H., **Soysal, B.F.**, Kadaş, K., Gülkan, P. (2019). An Evaluation of the 2019 Seismic Hazard Map of Turkey on the Basis of Spectrum Intensity, 5th International Conference on Earthquake Engineering and Seismology, Ankara.

2. **Soysal, B.F.**, Arıcı, Y. (2019). Modelling from Elastic Range to Failure Level Using the Modified Applied Element Method, 5th International Conference on Earthquake Engineering and Seismology, Ankara.

3. **Soysal, B.F.**, Tuncay, K., Arıcı, Y. (2019). Analyses of Dam-Reservoir Systems Using the Coupled Modified Applied – Finite Element Methods, 5th International Conference on Earthquake Engineering and Seismology, Ankara.

4. Kadaş, K., **Soysal, B.F.**, Akansel, V.H., Mazılıgüney, L., Yakut, A. (2019). Comparison of 2007 and 2019 Seismic Hazard Maps Based on Spectrum Intensities and Corresponding Engineering Demands – A Case Study with RC School Buildings in Istanbul, 5th International Conference on Earthquake Engineering and Seismology, Ankara.

5. Mazılıgüney, L., Akansel, V.H., **Soysal, B.F.**, Kadaş, K., Yakut, A. (2019). Seismic Risk Assessment of School Buildings on the Basis of Recent Turkish Seismic Hazard Map, 6th International Earthquake Symposium, Kocaeli.

6. **Soysal, B.F.**, Arıcı, Y., Binici, B., Tuncay, K. (2017). Comparison of the Overlapping Lattice and the Finite Element Approaches for the Prediction of the Collapse State of Concrete Gravity Dams, 4th International Conference on Earthquake Engineering and Seismology, Eskişehir.

7. **Soysal, B.F.**, Arıcı, Y., Binici, B., Tuncay, K. (2017). Simulation of Damage Propagation on Massive Concrete Structures, the Overlapping Lattice Model vs. the Finite Element Approach, 4th International Conference on Earthquake Engineering and Seismology, Eskişehir.

8. **Soysal, B.F.**, Ay, B.Ö., Arıcı, Y. (2017). Evaluation of Motion Selection and Scaling for the Nonlinear Seismic Analysis of Concrete Gravity Dams, 4th International Conference on Earthquake Engineering and Seismology, Eskişehir.
9. **Soysal, B.F.**, Ay, B.Ö., Arıcı, Y. (2017). Evaluation of the Ground Motion Scaling Procedures for Concrete Gravity Dams, Procedia Engineering, 199: 844-849, doi: 10.1016/j.proeng.2017.09.014, EURODDN 2017, Rome, Italy.
10. **Soysal, B.F.**, Aydın, B.B., Tuncay, K., Arıcı, Y., Binici, B. (2017). Overlapping Lattice Simulation of Concrete Gravity Dam Collapse Scenarios, COMPDYN 2017, Rhodes, Greece.
11. **Soysal, B.F.**, Arıcı, Y. (2016). Seismic Fragility Assessment of Concrete Gravity Dams using Incremental Dynamic Analysis, 12th International Congress on Advances in Civil Engineering, İstanbul.
12. **Soysal, B.F.**, Arıcı, Y. (2016). Quantification of the Damage States and Levels on Concrete Gravity Dams using Seismic Intensity Measures, 1st International Conference on Natural Hazards and Infrastructure, Chania, Greece.
13. **Soysal, B.F.**, Arıcı, Y. (2015). The Use of Nonlinear Analyses Tools for the Structural Design of Concrete Dams, Symposium Hydropower '15, Stavanger.
14. **Soysal, B.F.**, Arıcı, Y. (2014). Nonlinear Behavior of Concrete Gravity Dams, 11th International Congress on Advances in Civil Engineering, İstanbul.
15. **Soysal, B.F.**, Arıcı, Y. (2014). Incremental Dynamic Analysis of a Gravity Dam, Tenth U.S. National Conference on Earthquake Engineering, Anchorage, Alaska.

#### **National Conference Papers:**

1. **Soysal, B.F.**, Arıcı, Y. (2015). Artımlı Dinamik Analiz Yöntemi ile Beton Ağırlık Barajlardaki Hasar Belirlenmesi, 3. Türkiye Deprem Mühendisliği ve Sismoloji Konferansı, İzmir.
2. **Soysal, B.F.**, Arıcı, Y. (2015). Beton Ağırlık Barajların Sismik Davranışını Etkileyen Parametreler, 3. Türkiye Deprem Mühendisliği ve Sismoloji Konferansı, İzmir.
3. **Soysal, B.F.**, Arıcı, Y. (2013). Sarsma Tablası Testi ile Beton Barajların Doğrusal Olmayan Analiz Parametreleri Kalibrasyonu, 2. Türkiye Deprem Mühendisliği ve Sismoloji Konferansı, Hatay.

#### **HOBBIES**

Pilates, Cooking, Travel, Movies